Title
Design Guidelines of Printing Processes to Improve Electrical and Mechanical Properties for Haptics and Robotics

Author
Zhai, Yichen

Publication Date
2021

UNIVERSITY OF CALIFORNIA SAN DIEGO

Design Guidelines of Printing Processes to Improve Electrical and Mechanical Properties for Haptics and Robotics

A dissertation submitted in partial satisfaction of the requirements for the degree
Doctor of Philosophy

in

Electrical Engineering (Intelligent Systems, Robotics and Control)

by

Yichen Zhai

Committee in charge:

Professor Tse Nga Ng, Chair
Professor Shengqiang Cai
Professor Darren J. Lipomi
Professor Yu-Hwa Lo
Professor Sheng Xu

2021

The Dissertation of Yichen Zhai is approved, and it is acceptable in quality and form for publication on microfilm and electronically.

University of California San Diego

2021

DEDICATION

To my family

EPIGRAPH

The way ahead is long and has no ending,
yet high and low I will search with my will unbending.
—Qu Yuan

TABLE OF CONTENTS

LIST OF FIGURES

LIST OF TABLES

ACKNOWLEDGEMENTS

First of all, I appreciate my advisor, Professor Tse Nga Ng for her endless supports over my whole Ph. D. career. I value all the ideas, inspirations and research conditions she has provided to realize my wish of making innovations. I fully appreciate her utmost tolerance on my frequent arguments of different views, and her trust in my works of using whatever newly designed approaches and self-made strange machines to challenge whosever published results. Without the free academic environment that she has provided, I would not be able to have the current results and complete the degree. Besides daily research, I would also acknowledge her enlightenment on writing skills, human relationship and academic integrity, which will be my valuable harvest on the way forward.

I would like to appreciate my parents who gave me great mental and funding supports. They gave me fully freedom and no pressure on the pursuit of any degrees, which helped me to pursue the novel ideas and truth without any concerns.

I would like to give many thanks to the friends and the precious time we spent on the land and sea, the time we spent on the Pacific coast to think about the reality and future. Also, I would remember the friends in New Jersey and the long days we sat on the side Hudson River and watched the day and night lights of the Big Apple.

Appreciation is given to all the lab members for being a part of my safari in academics.

Among all the collaborators, special appreciation is given to Prof. Kye-si Kwon from Soonchunhyang University. Thanks for the printer he has made that led me to the way of research, and thanks for the encouragement that once I started to change the research field and build the new printer, there is no turning back. Indeed, the way to the truth and endless technology has no turning back. Special appreciation is given to Prof. Shengqiang Cai, Dr. Zhijian Wang and Zijun Wang for leading us to the way of printing LCE, which gave me a totally new and amazing field of research. This consists the most fruitful part of this dissertation through Chapter 3~5. Appreciation is given to Dr. Jiyeon Lee for the impedance calculation and simulation works in the wireless sensor project, and Dr. Lujiang Yan for helping and inspiring me in the measurements with network analyzer. I would like to appreciate Prof. Darren Lipomi and Dr. Cody Carpenter for opening us the way to the haptics field, which greatly extended the horizon of our printing applications. I also appreciate Dr. Zhenghui Wu for fabricating the photodiodes and carryout of the spectroscopy measurement, which created the conditions for me to make the imaging array.

Finally, special appreciation is given to Prof. Michael Tolley, my new advisor of the future postdoctoral journey, who encouraged me so much in my previous printing projects and gave me a new opportunity to explore in the field of printing soft robotics.

The dissertation is based on the following published papers and materials being prepared for submission.

Chapter 1, in part, is a reprint of the material as it appears in *Advanced Materials*, 2021, Yichen Zhai, Zhijian Wang, Kye-Si Kwon, Shengqiang Cai, Darren Lipomi and Tse Nga Ng. The dissertation author was the primary investigator and author of this paper.

Chapter 2, in full, is a reprint of the material as it appears in *Flexible and Printed Electronics*, 2018, Yichen Zhai, Jiyeon Lee, Quyen Hoang, Dan Sievenpipper, Harinath Garudadri and Tse Nga Ng. The dissertation author was the primary investigator and author of this paper.

Chapter 3, in full, is a reprint of the material as it appears in *Advanced Materials*, 2021, Yichen Zhai, Zhijian Wang, Kye-Si Kwon, Shengqiang Cai, Darren Lipomi and Tse Nga Ng. The dissertation author was the primary investigator and author of this paper.

Chapter 4, in full, has been accepted for publication of the material as it may appear in *Advanced Intelligent Systems*, 2021, Yichen Zhai and Tse Nga Ng. The dissertation author was the primary investigator and author of this paper.

Chapter 5, in full, is currently being prepared for submission for publication of the material, Yichen Zhai, Michael Tolley and Tse Nga Ng. The dissertation author was the primary investigator and author of this paper.

Chapter 6, in part, is a reprint of the material as it appears in *Advanced Functional Materials*, 2018, Zhenghui Wu, Yichen Zhai, Weichuan Yao, Naresh Eedugurala, Song Zhang, Xiaodan Gu, Jason D. Azoulay and Tse Nga Ng. The dissertation author was the secondary investigator and author of this paper.

VITA

2013 Bachelor of Science in Microelectronics, Changchun University of Science and Technology, China

2016 Master of Science in Electrical Engineering (Robotics and Control), Stevens Institute of Technology, USA

2021 Doctor of Philosophy in Electrical Engineering (Intelligent Systems, Robotics and Control), University of California San Diego, USA

PUBLICATIONS

1 **Y. Zhai**, J. Lee, Q. Hoang, D. Sievenpiper, H. Garudadri, and T. N. Ng, A Printed Wireless Fluidic Pressure Sensor, *Flex. Print. Electron.*, vol. 3, p. 035006, 2018.

2 **Y. Zhai**, Z. Wang, K. S. Kwon, S. Cai, D. J. Lipomi, and T. N. Ng, Printing Multi-Material Organic Haptic Actuators, *Adv. Mater.*, vol. 33, no. 19, 2021.

3 **Y. Zhai**, and T. N. Ng, Self-Sustained Robots Based on Functionally Graded Elastomeric Actuators Carrying up to 22 Times Their Body Weight, *Adv. Intell. Syst.*, accepted for publication.

4 **Y. Zhai**, M. T. Tolley, and T. N. Ng, Digital Programming of Liquid Crystal Elastomers to Achieve High-Fidelity Surface Morphing, in preparation for submission.

5 Z. Wu, **Y. Zhai**, W. Yao, N. Eedugurala, S. Zhang, L. Huang, X. Gu, J. D. Azoulay, and T. N. Ng, The Role of Dielectric Screening in Organic Shortwave Infrared Photodiodes for Spectroscopic Image Sensing, *Adv. Funct. Mater.*, vol. 28, no. 50, p. 1805738, 2018.

6 Z. Wu, **Y. Zhai**, H. Kim, J. D. Azoulay, and T. N. Ng, Emerging Design and Characterization Guidelines for Polymer-Based Infrared Photodetectors, *Acc. Chem. Res.*, vol. 51, no. 12, pp. 3144–3153, 2018.

ABSTRACT OF THE DISSERTATION

Design Guidelines of Printing Processes to Improve Electrical and Mechanical Properties for Haptics and Robotics

by

Yichen Zhai

Doctor of Philosophy in Electrical Engineering (Intelligent Systems, Robotics and Control)

University of California San Diego, 2021

Professor Tse Nga Ng, Chair

3D printing has been demonstrated as a mighty tool for fast prototyping in many fields. The fast reconfigurability, high repeatability and low cost enables itself to be accepted by everyone with general knowledge in engineering. That is, when the designs and process parameters are given, anyone would be able to simply perform the manufacturing processes. However, resulting from the immaturity of material tuning, tooling design and process control, when printing functional parts with special electrical or mechanical requirements, the printed workpieces are still not competitive comparing to the traditional works of manufacturing machines. In the desire of realizing printing as a production approach in professional applications, we propose this dissertation with guidelines from the hardware improvement in printers to the specific rules in modeling and printing toolpath designs in the fields of thin-film electronic devices, wearable haptic devices, and soft robotics. In the first work, we deposited silver inks with an inkjet printer for high-frequency inductive and capacitive components, which were combined into a pressure sensor to track liquid pressure with wireless readout. Then we turned our focus to extrusion printing with functional materials. For this exploration, a special hybrid printing system was build combining fused deposition modeling (FDM) and pneumatic extrusion printing, as well as functions in force tracking, shear force control and UV curing. The pneumatic printing apparatus was optimized to process an organic actuator material, liquid crystal elastomer (LCE), in order to control the mesogen alignment. As applications, incorporating with silver extrusion inks, two LCE haptic interfaces were demonstrated—including a tactile number-display surface and a kinesthetic glove. To demonstrate the application in robotics, soft LCE actuators and printed rigid exoskeleton parts were integrated into a self-sustained moving robot, which performs autonomous motion under constant light sources with a high payload-carrying ability. We also studied the actuation range of LCE with respect to the quantitive shear control during printing processes, which proved that printed LCE structures are advantageous in topological surface reconstruction. An example of human face model reconstructed by LCE was displayed, showing higher fidelity than other existing works. Details of all our works in the modifications to the printing setups and design rules of the fabricated devices are given in this dissertation, which provide guidelines not only in the flexible electro-mechanical devices we have been focusing on, but also inspirations to the researches in all the digital manufacturing fields as we wish.

Chapter 1

Introduction

1.1 Background and motivation of printing devices in haptics and robotics

Emerging additive manufacturing techniques such as digital printing provide the capability to fabricate multi-scale and multi-material designs with high precision and throughput. Digital printing is amenable for integrating multiple materials and architecting functionally gradient materials to increase the design space for versatile motion, and can achieve free-form designs for customization of interfaces. The versatility and reconfigurability of printing processes are advantageous for fabricating integrated organic robots and haptic interfaces.

The desired feature resolution and material requirements will dictate the selection of suitable printing methods, which are classified into three common broad categories—inkjet, extrusion, and photo-patterning. Inkjet and extrusion are nozzle-based methods. Inkjet is a non-contact printing process, where the nozzles do not touch the surface being printed on and is tolerant of rough surfaces. In contrast, extrusion is a contact process with the nozzles directly depositing materials over top surfaces and requires accurate control of the distance between nozzles and surfaces. Lastly, photo-patterning uses light to crosslink polymers or sinter materials together. Below the process principles, advantages, and drawbacks of each technique are presented.

Schematic drawings of the inkjet printing process are shown in Figure 1.1(a). These techniques comprise both the conventional approach and the electrohydrodynamic (EHD) extension. In conventional inkjet, a driving voltage waveform is applied to the piezoelectric stack in the nozzle, which triggers an acoustic or pressure wave in the ink reservoir to eject a droplet with a volume proportional to the nozzle orifice diameter, typically on the order of picoliter in volume. The ink formulations can be tuned to incorporate electronic materials; for example, semiconductors [1] and conductive electrodes [2] have been deposited by inkjet to fabricate circuits [3], [4]. The resolution of the printed feature depends on the volume of ink droplets and their interaction with the substrate, [5], [6] and the typical resolution is tens of micrometers. To further improve feature resolution, inkjet printing can be modified into an EHD format, in which a high voltage pulse is applied between the nozzle and substrate, generating a high electric field that induces a cone-shaped meniscus at the nozzle and ejects droplets considerably smaller than the nozzle orifice. The resolution can be below 10 μm. Moreover, The fast evaporation of such small droplets enables it to printed metallic pillars and 3D interconnects [7].

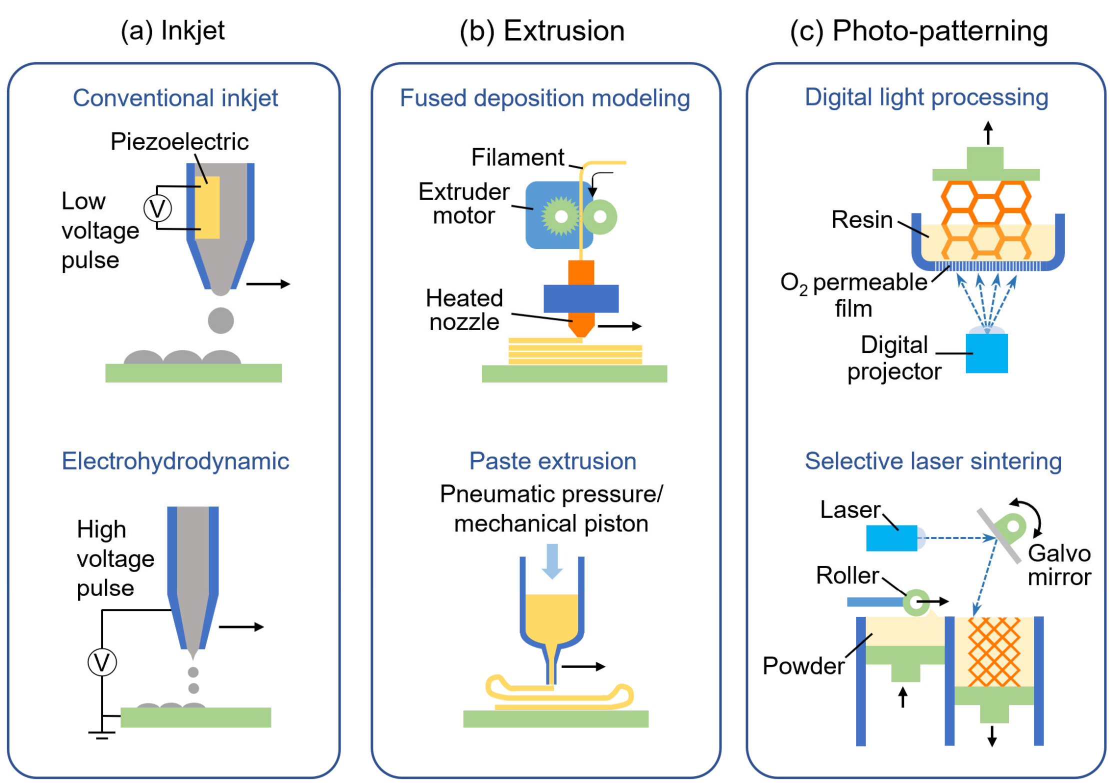

Figure 1.1: Digital printing techniques. (a) Inkjet and electro-hydrodynamic (EHD) printing. (b) Fused deposition modeling (FDM) and pneumatic extrusion printing. (c) Digital light processing (DLP) and selective laser sintering (SLS).

Extrusion processes, as shown in Figure 1.1(b), can pattern materials from prepolymers or melts in wide viscosity range (10 to 104 Pa·s). Printable materials include thermoplastic solids and composite pastes. In a commonly used technique known as fused deposition modeling (FDM), solid filaments are melted inside a heated nozzle, and the melt is extruded onto the substrate. When the thermoplastic cools below its glass transition temperature, it solidifies to form slices that constitute a 3D structure. For composite pastes or prepolymer gels, extrusion is regulated by applying pneumatic pressure or mechanical force to push the material through the nozzle. The desired flow characteristics is reached by adjusting the paste viscosity, concentration, shear moduli, and nozzle temperature. The extrusion of polymeric materials usually requires heating inside the nozzle to lower the viscosity and minimize the resistance to extrusion. Upon exiting the nozzle, the material cools and its viscosity increases, which minimizes or prevents spreading. For paste mixtures, the organic solvent dries shortly in air after extrusion, leaving the solid contents on the stacked structure. The resolution of the features printable by extrusion is similar to the inner diameter of the nozzle, or slightly larger due to lateral spread of the printed materials, and is typically on the order of below one millimeter.

Extrusion is amenable to a diverse range of materials and is the most commonly used method for printing different materials on the same platform. For conductive structures, the possible material choices include polymer composites percolated with conductive particles, [8], [9] or liquid metal alloys such as eutectic indium gallium [10]–[12] that can be patterned into mesoscale structures due to a spontaneous surface oxide upon extrusion. Functional devices ranging from energy storage [13] to optoelectronics [14] have been made by extrusion.

Broadly speaking, light-based patterning techniques are categorized as either light-induced polymerization or light-power sintering, as depicted in Figure 1.1(c). Generally, each layer is patterned by illumination that locally crosslinks a volume of photocurable material. [15], [16] Following crosslinking of the previous layer, a new layer of liquid resin or powder is added and photo-patterned, and the process is repeated to build up the structure layer by layer. In stereolithography and selective laser sintering, [17] a digitally controlled galvo-mirror directs a laser beam to solidify the resin, or to melt powder, respectively. The powder can be metallic or polymeric. The schematic diagram on the bottom in Figure 1.1(c) shows a critical aspect of the process, in which a thin layer of powder is pushed by a roller into the working tank. The laser then selectively sinters the desired pattern on the surface. Subsequently, the roller spreads another thin layer of powder for patterning the next layer.

Currently, photo-patterning is ideally suited for printing mechanical structures, inkjet is likewise for printing thin-film electronics, and extrusion has been used for patterning both electronic and mechanical structures, albeit at a lower resolution than the other two techniques. In each type of printing, the patterning and solidification process define the resolution of printed features and the type of materials to which it is amenable. [18], [19]

In our research, inkjet, electrohydrodynamic, FDM and pneumatic extrusion printing techniques are used for different fabrications. Inkjet was used to print thin film electrical devices such as transistors, inductors and capacitors. To achieve the best electrical performance, the conductive ink, substrate and detailed printing process require adjustment. For example, in high frequency applications, the surface of the printed conductor should be smooth, while the short drying time of ink leads to unsmooth surface. Such issues can be improved by special process design. Pneumatic extrusion was used to print a highly viscos functional actuator material, liquid crystal elastomer (LCE). In order to collaborate with the material, the extrusion setup requires modifications such as high-pressure air supply control in fast response and heating of the ink. Also, the printing toolpath requires specific controls to effectively apply shear force on the printed workpiece for mesogen alignment. Meanwhile, the continuity and smoothness at the end points of paths need to be controlled. In a completed device, the yield and performance depend on the whole fabrication line. Our motivation is to improve the setups and optimize the digitally controlled processes for higher capability in manufacturing devices.

1.2 Design of printing systems and processes for devices

A PSjet inkjet printer was used to fabricate electrical devices. We evaluated different conductive silver inks on different substrates, and tested different curing conditions for precise patterns. MATLAB programs were written to design the patterns of wireless resonators, which include an inductor coil and a thin-film porous capacitor. Different printing sequences were studied to generate smooth surface for better high frequency performance. A comparison of different toolpaths designed in MATLAB is shown in Figure 1.2, with corresponding printing results. The patterns were printed with Novacentrix silver ink on glossy paper substrate, where the water solvent dries fast after printing. By tuning the printing sequences of the infilled pattern, the drying sequence of ink can be controlled, and the smoothness of the surface can be improved. Finally, a printed wireless pressure sensor was tested in liquid environment, showing an ability to track heart pulses in blood pressure range. This work is introduced in Chapter 2.

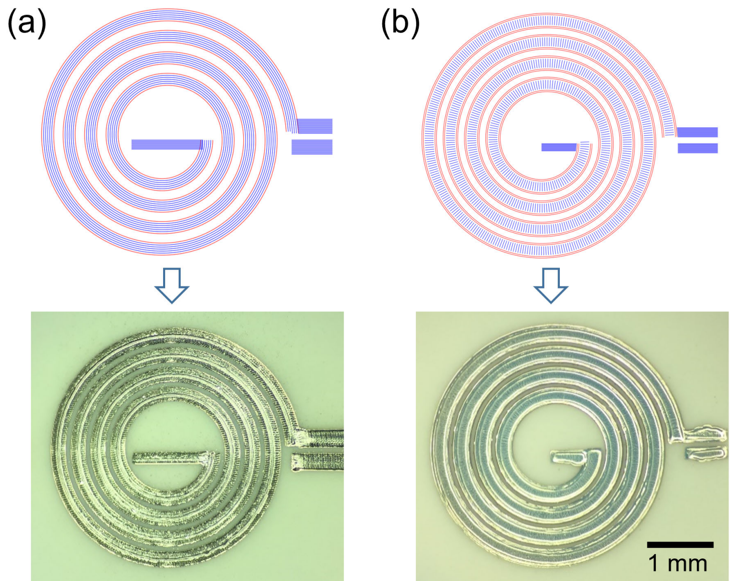

Figure 1.2: Different toolpath designs in MATLAB and printing results by inkjet. (a) Parallel infill sequence. (b) Vertical infill sequence.

To print with LCE, we built a new printing setup. The printer was modified from a commercial FDM printer, Raise3D N2. We added customized parts on the printing head assembly, in order to hold two pneumatic extrusion syringes. The parts were printed from temperature-resistant polycarbonate in high precision. The pneumatic power is supplied by an air compressor, and regulated by two dispensers. We investigated the two choices of extrusion power sources—pneumatic and mechanical piston, and found that pneumatic extrusion leads to less delay at start points and minimized leakage after the end points. This is because the pneumatic pressure supply is able to provide sharp step increase and decrease. In contrast, due to the elastic modulus of the syringe and gel material, mechanical piston needs a period to accumulate or release the pressure in viscos fluid for extrusion or stopping. The delayed period is in the order of seconds, which is often shown as large amount of leakage after extrusion. Besides air supply equipment, the circuit and firmware of the printer was modified to output extrusion signal to the two dispensers, to trigger the extrusion through two syringe needles. On one of the extrusion syringes, there are two customized heaters which control the temperature of the syringe and needle respectively [Figure 1.3 (a) and (b)], in order to reduce the viscosity of LCE for higher extrusion flow rate. Each heater has a corresponding temperature sensor attached, and PID logic was used for precise temperature control. In most 3D printers, the homing of Z axis level is usually a hard issue. To print actuators with precise layer height control, we added a load cell on the print head assembly [Figure 1.3(c)], which is able to track the vertical force on the printing nozzle. As a result, during lowering the Z level of the print head, when the nozzle contacts the substrate, the force will be sensed by the load cell, and a signal will be sent to the motion controller of the printer to mark the Z homing position. To cure LCE after extrusion, 365 nm UV light is required. Four high power UV LEDs were attached around the printing nozzle region [Figure 1.3(b)], with the cooling components for heat dissipation [Figure 1.3(a)]. For all the added functions, we made a controller to process the signals and calculations [Figure 1.3(d)].

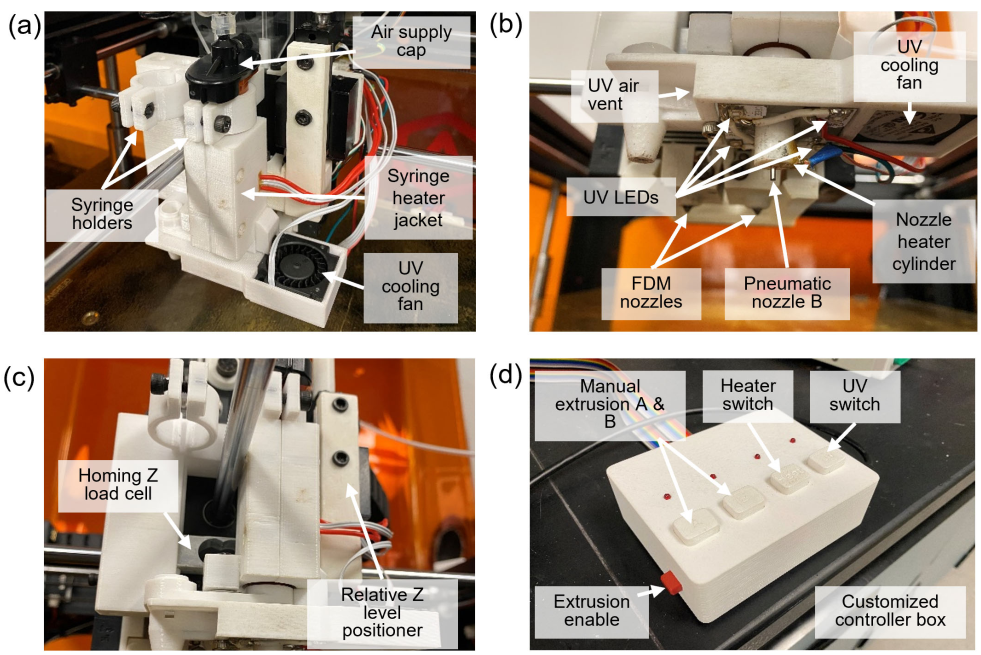

Figure 1.3: Pneumatic print head assembly and controller. (a) Syringe holders and heating jacket on the assembly. (b) Detailed nozzle region, including two FDM and two pneumatic nozzles, UV LEDs and a nozzle heater. (c) Load cell to assist leveling Z and positioner to adjust relative height between FDM and pneumatic nozzles. (d) Controller to process and monitor the added functions.

Besides the hardware modification, MATLAB programs were also designed for the generation of printing patterns and operation procedure. The programs are able to calculate desired pattern with geometric parameters, and output corresponding G-code file for the whole process. The printing procedure such as toolpath control, infill, shear direction and endpoints controls are all optimized in the codes. Examples of pattern designs and printed results are shown in Figure 1.4. The printed directions of the actuators were tuned for specific actuation directions in Figure 1.4(a), and multiple materials were deposited on the same structure to form the heating components in (b). The pneumatic printer was used for the works presented in Chapter 3-5 based on different applications. A full operation manual of the printer is included as Appendix A.

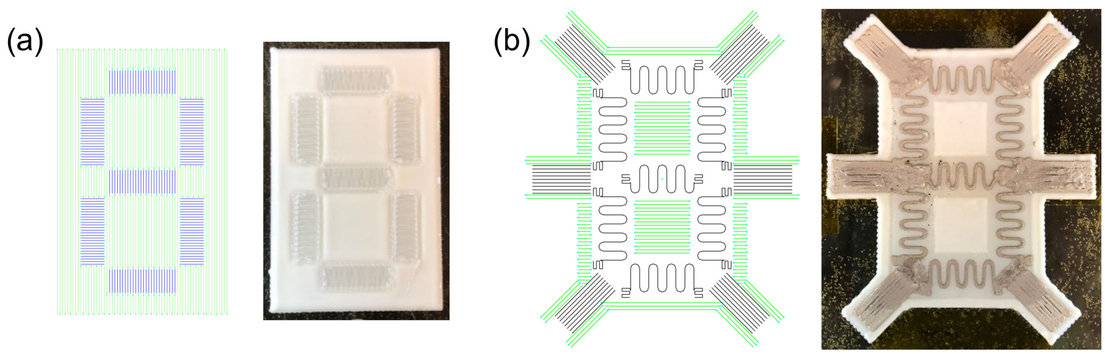

Figure 1.4: Designs of extrusion printed patterns by MATLAB and corresponding printed results. (a) LCE actuators for tactile display. (b) Silver heaters for tactile display.

Chapter 3 presents two kinds of haptic actuators fabricated by combined FDM and pneumatic extrusion printing. LCE in different domain controls was used in the actuator units and base. Thermoplastic Polyurethane (TPU) was used as spacer to assist the actuators. A tactile surface is designed to display numbers for touching sensation, and a kinesthetic actuator is able to apply force on the joints of fingers. The stress-strain characteristics are provided, showing that LCE is a suitable material in compact haptic applications.

To study the relationship between the shear stress during printing and the actuation strain of LCE samples, we made a setup with corresponding date processing codes to track the shear force as shown in Figure 1.5. The substrate is supported by a load cell, therefore, the horizonal force applied on the printed trace from the nozzle is captured by the load cell in real time. In the test, LCE samples were printed under different shear stresses, and the actuation strains of each sample were measured after fabrication. The result shows that the control of horizontal shear outside of printing nozzle and actuation strain of the sample are monotonically corelated, which proved that the alignment strength can be controlled by printing. The detailed data and results are discussed in Chapter 4.

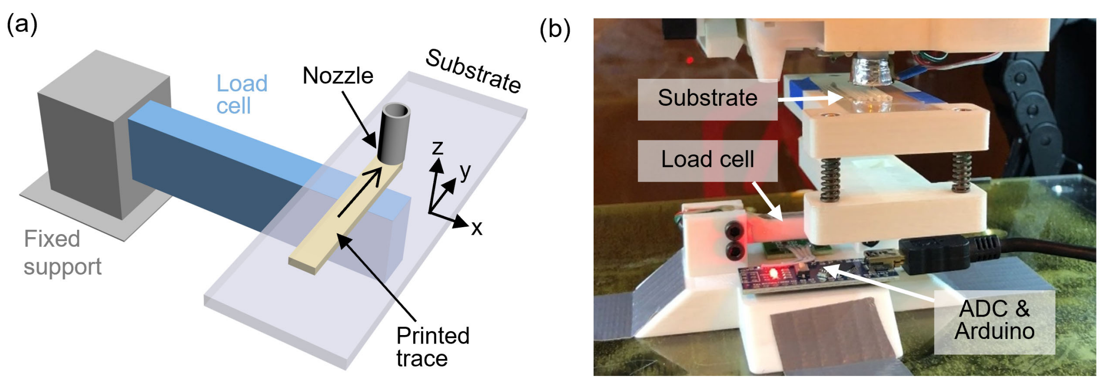

Figure 1.5: Shear force tracking setup. (a) Schematic. (b) Photograph demonstration during printing.

Besides the printing shear control, Chapter 4 demonstrated a self-sustain moving robot combining FDM printed exoskeleton and pneumatic printed LCE actuators. A printed LCE actuator collaborated with a LCE spring component ensured the two-way actuation and recovery movements. A special ratchet and a flapping shade fulfilled the automatic thermal-mechanical work processes in repeated cycles, and further achieved continuous movement of the robot. The robot is able to move under constant light input, and is able to carry a payload 22 times its bodyweight. The engineering drawings of the robot are included as Appendix B.

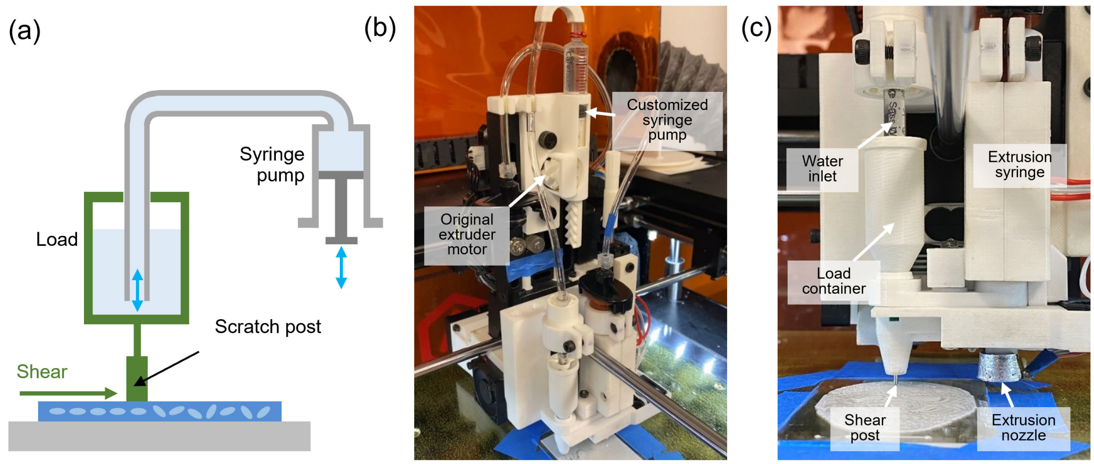

Figure 1.6: Post shear setup for aligning LCE. (a) Schematic. (b) Full view of the assembly. (c) Close-up view of the post and nozzle region.

With the shear force tracking system, we have proved that the shear stress applied on the printed LCE trace form the extrusion nozzle can monotonically control the alignment strength of the sample. However, in the printed samples, the toolpath traces usually need to be in parallel through the whole surface in order for close-packed infill, and the alignment of the material is bound to the trace direction. These limitations prevent the printing process to generate freeform alignment for complex actuation patterns. To decouple the alignment pattern from the constrains of printing, we designed a digital shear system as shown in Figure 1.6, in which a shear post is used to scratch an unaligned LCE film for freeform aligning directions and magnitudes. A water load is attached on top of the post and a digital syringe pump is used to adjust the load. With the load pressure and shear velocity controlled in real time, the magnitude of alignment can be varied continuously. As a demonstration of this setup, we designed a multi-layered LCE film structure with different shear patterns on each. When some of the layers perform linear contraction and the others stay in original state, the film structure performs a bending actuation. The magnitude of the bending curvature can be controlled by the aligning strength of the actuating layers. An algorithm was designed to calculate the curvatures of a human face model, and the shear setup was used to reproduce this model on a LCE film, which as a result shows 84.5% similarity. The fidelity of this surface reconstruction technique exceeds all the previous researches in the same type. Details of this work is reported in Chapter 5.

Chapter 6 demonstrates other applications of printing and electrical controllers. One is a shortwave infrared imaging array using 3D printed mechanical components for taking image and programmable controllers to switch the pixels with control logic. The other application is a printed passive haptic device using regular printing filament. The device has integrated heaters and temperature sensors. The temperature can be controlled to generate different feelings of stiffness. A special control logic was designed to carry out both the heating and measuring functions.

Appendix A is the operation manual of the pneumatic printing system we built.

Appendix B shows the engineering drawings of the self-sustained robot in Chapter 4.

Chapter 1, in part, is a reprint of the material as it appears in *Advanced Materials*, 2021, Yichen Zhai, Zhijian Wang, Kye-Si Kwon, Shengqiang Cai, Darren Lipomi and Tse Nga Ng. The dissertation author was the primary investigator and author of this paper.

1.3 References

1 T. N. Ng, D. E. Schwartz, P. Mei, S. Kor, J. Veres, P. Bröms, and C. Karlsson, “Pulsed voltage multiplier based on printed organic devices,” Flex. Print. Electron., vol. 1, no. 1, p. 15002, doi: 10.1088/2058-8585/1/1/015002.

2 Y. Yoshida, H. Wada, K. Izumi, and S. Tokito, “Highly conductive metal interconnects on three-dimensional objects fabricated with omnidirectional ink jet printing technology,” Jpn. J. Appl. Phys., vol. 56, p. 05EA01, 2017, doi: 10.7567/JJAP.56.05EA01.

3 X. Guo, Y. Xu, S. Ogier, T. N. Ng, M. Caironi, A. Perinot, L. Li, J. Zhao, W. Tang, R. A. Sporea, A. Nejim, J. Carrabina, P. Cain, and F. Yan, “Current Status and Opportunities of Organic Thin-Film Transistor Technologies,” IEEE Trans. Electron Devices, vol. 64, no. 5, pp. 1906–1921, 2017.

4 T. N. Ng, D. E. Schwartz, P. Mei, B. Krusor, S. Kor, J. Veres, P. Bröms, T. Eriksson, Y. Wang, O. Hagel, and C. Karlsson, “Printed dose-recording tag based on organic complementary circuits and ferroelectric nonvolatile memories,” Sci. Rep., vol. 5, no. August, p. 13457, 2015, doi: 10.1038/srep13457.

5 K. N. Al-Milaji, R. R. Secondo, T. N. Ng, N. Kinsey, and H. Zhao, “Interfacial Self-Assembly of Colloidal Nanoparticles in Dual-Droplet Inkjet Printing,” Adv. Mater. Interfaces, vol. 5, no. 10, p. 1701561, 2018, doi: 10.1002/admi.201701561.

6 D. Soltman and V. Subramanian, “Inkjet-Printed Line Morphologies and Temperature Control of the Coffee Ring Effect,” Langmuir, vol. 94720, no. 9, pp. 677–683, Mar. 2008, doi: 10.1021/la7026847.

7 B. W. An, K. Kim, H. Lee, S. Kim, Y. Shim, D. Lee, J. Y. Song, and J. Park, “High-Resolution Printing of 3D Structures Using an Electrohydrodynamic Inkjet with Multiple Functional Inks,” pp. 4322–4328, 2015, doi: 10.1002/adma.201502092.

8 T. Kim, R. Trangkanukulkij, and W. S. Kim, “Nozzle Shape Guided Filler Orientation in 3D Printed Photo-curable Nanocomposites,” Sci. Rep., vol. 8, no. 1, p. 3805, 2018, doi: 10.1038/s41598-018-22107-0.

9 N. Matsuhisa, D. Inoue, P. Zalar, H. Jin, Y. Matsuba, A. Itoh, T. Yokota, D. Hashizume, and T. Someya, “Printable elastic conductors by in situ formation of silver nanoparticles from silver flakes,” Nat. Mater., vol. 16, no. 8, pp. 834–840, Aug. 2017, doi: 10.1038/nmat4904.

10 M. D. Dickey, “Stretchable and Soft Electronics using Liquid Metals,” Adv. Mater., vol. 29, p. 1606425, 2017, doi: 10.1002/adma.201606425.

11 J. Wang, G. Cai, S. Li, D. Gao, J. Xiong, and P. S. Lee, “Printable Superelastic Conductors with Extreme Stretchability and Robust Cycling Endurance Enabled by Liquid-Metal Particles,” Adv. Mater., vol. 30, no. 16, p. 1706157, 2018, doi: 10.1002/adma.201706157.

12 C. Ladd, J. So, J. Muth, and M. D. Dickey, “3D Printing of Free Standing Liquid Metal Microstructures,” pp. 5081–5085, 2013, doi: 10.1002/adma.201301400.

13 S. H. Park, M. Kaur, D. Yun, and W. S. Kim, “Hierarchically Designed Electron Paths in 3D Printed Energy Storage Devices,” Langmuir, vol. 34, no. 37, pp. 10897–10904, 2018, doi: 10.1021/acs.langmuir.8b02404.

14 S. H. Park, R. Su, J. Jeong, S. Z. Guo, K. Qiu, D. Joung, F. Meng, and M. C. McAlpine, “3D Printed Polymer Photodetectors,” Adv. Mater., vol. 30, no. 40, p. 1803980, 2018, doi: 10.1002/adma.201803980.

15 B. E. Kelly, I. Bhattacharya, H. Heidari, M. Shusteff, C. M. Spadaccini, and H. K. Taylor, “Volumetric additive manufacturing via tomographic reconstruction,” Science (80-.)., vol. 363, no. 6431, pp. 1075–1079, 2019, doi: 10.1126/science.aau7114.

16 P. Wang, D. B. Berry, Z. Song, W. Kiratitanaporn, J. Schimelman, A. Moran, F. He, B. Xi, S. Cai, and S. Chen, “3D Printing of a Biocompatible Double Network Elastomer with Digital Control of Mechanical Properties,” Adv. Funct. Mater., p. 1910391, 2020, doi: 10.1002/adfm.201910391.

17 S. Liu, M. C. Yuen, and R. Kramer-Bottiglio, “Reconfigurable electronic devices enabled by laser-sintered liquid metal nanoparticles,” Flex. Print. Electron., vol. 4, no. 1, p. 015004, 2019, doi: 10.1088/2058-8585/aafa3b.

18 X. Wang, M. Jiang, Z. Zhou, J. Gou, and D. Hui, “3D printing of polymer matrix composites : A review and prospective,” Compos. Part B, vol. 110, pp. 442–458, 2017, doi: 10.1016/j.compositesb.2016.11.034.

19 K. S. Kumar, P. Chen, and H. Ren, “Review Article A Review of Printable Flexible and Stretchable Tactile Sensors,” vol. 2019, 2019.

Chapter 2
A printed wireless fluidic pressure sensor

2.1 Abstract

An inkjet-printed inductor–capacitor (LC) resonator is demonstrated for wireless monitoring of pressure in aqueous environments. The sensing mechanism is based on a compressible capacitor that modulates the LC circuit resonant frequency depending on the applied pressure. The trace conductivity and geometric designs of inductors are improved to increase mutual inductive coupling between the sensor and the readout coil. The dielectric porosity in the capacitive sensors are tuned to enhance pressure sensitivity. The encapsulated sensor showed a linear response to pressure between 30 and 170 mmHg (4–23 kPa) with respect to atmospheric pressure and a resolution of 3 mmHg. The sensor temporal response is up to 6 Hz and capable of capturing typical heart-pulse waveforms as a proof-of-concept demonstration.

2.2 Introduction

Wireless monitoring of physiological pressure is highly desirable for preventing failure of implanted prosthetic grafts. For example, prosthetic vascular shunts are prone to clogging in patients undergoing renal hemodialysis, but monitoring procedures using ultrasound or x-ray angiograms are costly and not suitable for frequent use to enable early detection of failing grafts [1]. Wireless telemetry based on inductor–capacitor (LC) resonators [2]–[6] provides convenient monitoring of the grafts, in which sensor signals are measured through inductive coupling with an external reader. Passive LC resonator circuits are limited in transmission distances but can be used for subcutaneous grafts [1], [7] that are typically less than 2 cm from the skin surface. The LC resonators occupy a smaller footprint and are simpler to fabricate than active devices for integration with mechanically flexible, space-constrained grafts.

In this work we demonstrate a printed LC resonator to measure hemodynamic pressure. The pressure sensing component is a compressible capacitor, such that the capacitance increases under pressure and in turn modulates the resonance frequency of the LC resonator. There are other pressure sensing devices based on resistive [8]–[12] or piezoelectric mechanisms, [13] but wireless detection of the corresponding resistance change or induced voltage requires a more complex circuit than the LC resonator. Prior research on polymeric capacitive pressure sensors [14]–[19] used micro-structures in dielectric materials to improve sensitivity. By using templates, the dielectric structural geometry is tuned to change its elastic moduli for various pressure sensing applications. However, the sensors were porous and not designed to work in liquid condition. Here we incorporate encapsulation and develop an fabrication process with inkjet printing, which reduces processing steps compared to conventional micro-electromechanical systems (MEMS) fabrication and allows rapid, reliable prototyping on flexible substrates. We designed a new method of integration that separately fabricated planar inductor pattern and porous foam capacitor are simply combined by gluing between the dielectrics. We demonstrate printing toolpaths and an empirical model used to optimize the wireless coupling between the sensor and the readout inductor coils for maximal reading distance.

2.3 Results and discussion

2.3.1 Fabrication process and optimization of printing

As shown in Figure 2.1, the LC resonator consists of an inductor and two capacitors with microstructured dielectrics designed to enhance the pressure-induced change in capacitance. The two capacitors are connected in series through a common electrode. This configuration eliminates the need for an interconnect via between the top capacitor electrode layer to the inductor layer, thus simplifying fabrication compared to a single capacitor design. The key processing parameters that improve inductor and capacitor characteristics are discussed below, while details of the fabrication procedure are provided in the experimental section.

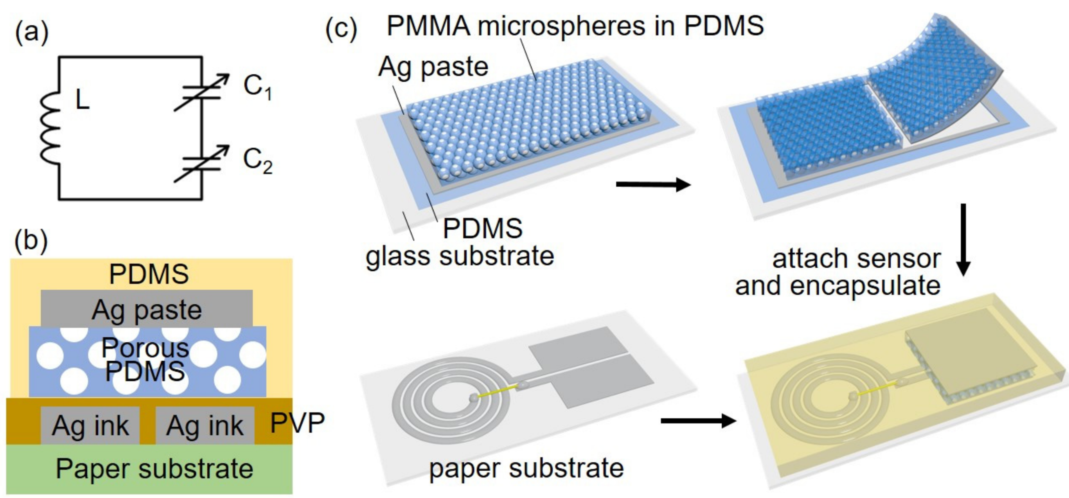

Figure 2.1: Structure and fabrication process of wireless pressure sensor. (a) Schematics of the LC resonator. (b) Cross-sectional view of the capacitive pressure sensing structure. (c) Schematics of the fabrication process.

The inductor is patterned by printing silver ink on a flexible paper substrate, and the printhead toolpath affects ink reflow and the resulting conductor trace profile [20]–[22]. Based on the geometric inductance expressions from [22], we make the inductor a four turn Archimedean

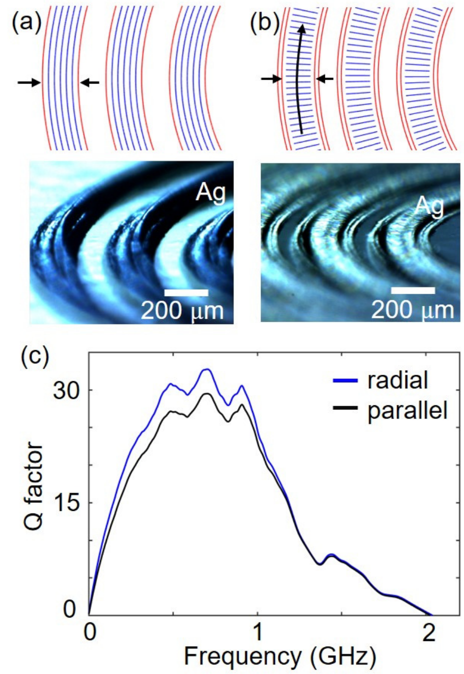

Figure 2.2: Printer toolpath in different sequences, corresponding printed silver features, and Q factors. (a) Parallel sequence. (b) Radial sequence. (c) Comparison of inductor quality factors when printing is done with radial or parallel toolpath.

spiral with an outer diameter of 8.1mm, trace width of 210 μm, and thickness of 10 μm, expecting an inductance of 196 nH in frequency range below 10 MHz. When inkjet printing on the paper surface, each Ag droplet forms a dot with diameter about 50 μm and thickness around 1.5 μm. Thus, multiple printing passes are required to fill out the spiral pattern and build up the trace thickness. The printer toolpath starts with defining the edges of each trace. Then two different sequences of ink deposition are characterized in Figure 2.2. For the parallel toolpath, when a new line is being printed, the ink droplets land on the side of a previous line that has already dried, leading to a stacked morphology. In contrast, for the radial toolpath, the line segments are short and new ink is added before the previous line dries, allowing ink reflow that results in a smooth surface. Figure 2.2(c) shows the measured inductor quality factor $Q=\omega L/R$, where ω is the angular frequency and R is the trace resistance at a specific frequency. The Q of the inductor made with radial sequence is better than the one with parallel sequence, because the radial toolpath enables a smooth conductor surface that reduces electron scattering and trace resistance.

2.3.2 Calibration of pressure sensor

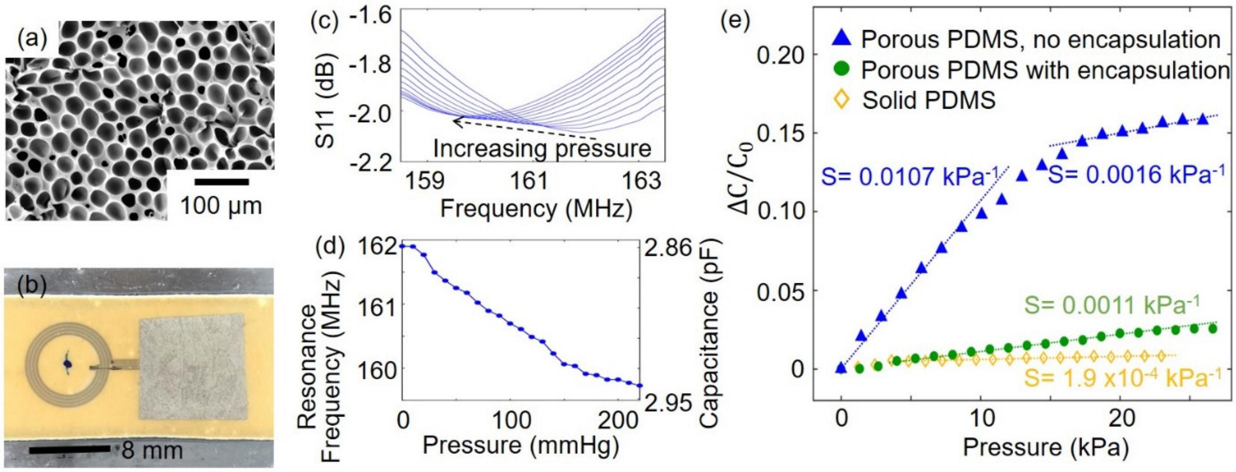

Figure 2.3: Porous structure and response calibration of the pressure sensor. (a)Scanning electron micrograph of the porous PDMS dielectric. (b) Photograph of the encapsulated LC resonator. (c) Reflection coefficient versus resonance frequency at a reading distance of 3mmbetween the readout coil and encapsulated LC resonator. The applied pressure on the sensor is increased from 0 mmHg, in increments of 20 mmHg, with respect to atmospheric pressure. (d) Resonance frequency and capacitance versus applied pressure, extracted from part (c). (e) Relative capacitance versus pressure for sensors with different dielectrics or encapsulation.

The pressure sensing capacitors are made with a porous elastomer for measurement between 30 and 170 mmHg, or 4 and 23 kPa, with respect to atmospheric pressure; this range spans the blood pressure values for children and adults. The elastomer polydimethylsiloxane (PDMS) solution is mixed with sacrificial polymethyl mathacrylate (PMMA) microspheres. After annealing, the film is submerged in dichlorobenzene, which does not damage the crosslinked PDMS but dissolve away the PMMA microspheres to leave behind pores in the dielectric (Figure 2.3). The estimated air-void volume is 55% of the film, based on the solid content ratio of PDMS to PMMA. This approach [16], [18] to form micro-pores increases the capacitance change compared to a solid dielectric, because the elastic modulus is decreased in porous films. The integrated LC resonator is encapsulated with PDMS to seal the edges of the capacitor and prevent environmental liquids from flowing into the porous dielectric.

By inductive coupling, power is transmitted wirelessly from a readout coil to the sensor coil and induces resonance in the sensor circuit. The sensor resonant frequency fs is related to the sensor's inductance L and capacitance C by [3]

$$f_s = \frac{1}{2\pi\sqrt{LC}} \tag{2.1}$$

The readout system records the power reflection over the input frequency spectrum. At the readout-coil terminals, the input reflection coefficient S11 is lowest near the sensor resonant frequency where the sensor absorbs the most power from the readout coil. The frequency at the S11 minimum depends on sensor L, C by [23]

$$f_{s11min} = \left(1 + \frac{1}{8Q^2} + \frac{k^2}{4}\right) f_s \tag{2.2}$$

where k is the geometry-dependent coupling coefficient between 0 (no coupling) and 1 (maximum coupling). [3], [4] Since $1 + \frac{1}{8Q^2} + \frac{k^2}{4}$ <<1 in normal circumstances, we can justify equating f_{S11min} to f_s. Upon applying pressure to the sensor inside a water chamber, the resonant frequency shifts to lower values [Figure 2.3(c)]. The corresponding capacitance versus applied pressure is calculated from Equation 1 with a measured *L*= 337 nH at 162 MHz, as shown in Figure 2.3(d). The initial capacitance C_0 is 2.86 pF for our pressure sensor with a total area of 8 x 8 mm^2. The calculated capacitance is the total capacitance of the LC circuit loop, including parasitic capacitance between inductor turns and contributions from adhesion layers that are not sensitive to pressure. Hence the capacitance sensitivity to pressure is lower in the integrated wireless LC resonator than in discrete capacitive sensors.

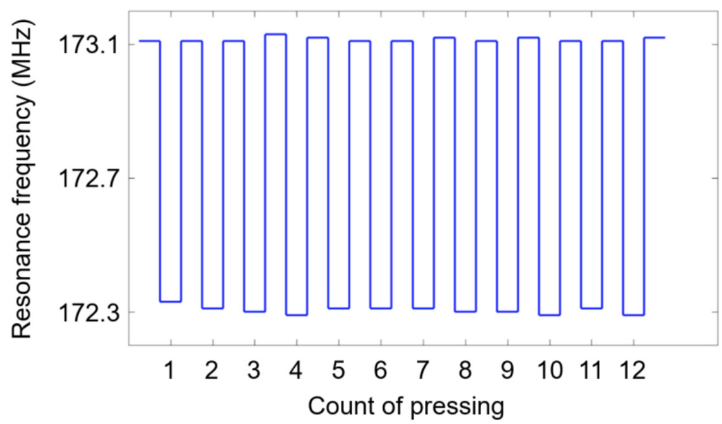

Figure 2.4: Repeatability test under 40 mmHg pressure over 12 cycles.

The sensitivity of a capacitive sensor is defined as $S=\delta(\Delta C/C_0)/\delta P$, where $\Delta C=C(P)-C_0$ is the capacitance change at an applied pressure P, with respect to the initial capacitance. The sensitivity values are denoted in Figure 2.3(e). To demonstrate the elastic property of the PDMS porous foam, we measured the sensor response under 40 mmHg mechanical pressure over 12 cycles, and the repeatable response is shown in Figure 2.4. Previous works have also shown that PDMS foam capacitors have high repeatability without hysteresis over 1000–15000 cycles [14], [16], [17]. The sensors with porous PDMS show better sensitivity by at least an order of magnitude than the one with un-structured dielectric. The LC resonator needs an encapsulation for stable operation in liquids, but the encapsulation significantly reduces the sensitivity at low pressure range <15 kPa (or <112 mmHg). Without encapsulation, the air inside the dielectric can readily escape as pressure is applied, while in the encapsulated device the volume is less compressible due to trapped air. Previous work [24] has improved sensitivity by using additional air reservoirs at the expense of sensor dimensions.

For high pressure range >15 kPa or >112 mmHg, the unencapsulated sensor saturates as the air voids are diminished, reducing the elasticity of the dielectric and in turn lowering sensitivity.

The sensitivity of the capacitive pressure sensors here is low compared to other non-sealed sensors, because air gap between dielectric and electrode in prior work [14]–[18] can increase sensitivity. The response of the un-structured device matches well with the mechanical modulus as measured in [25]. Several aspects, such as sealing under partial vacuum and reducing thicknesses of the top electrode and encapsulation layers to increase electrode displacement, can potentially improve performance in the future. Nonetheless, at the current sensitivity level of 0.011 MHz mmHg−1 and a background noise of 0.03 MHz, the integrated LC resonators are capable of resolving 3 mmHg, sufficient for blood pressure monitoring in prosthetic graft applications.

2.3.3 Wireless readout range

To determine the wireless readout range, the S11 response is measured as the reading distance d between the sensor and the readout coil is raised (Figure 2.5). At very close distance where the coupled power transfer between the readout and sensor coil is high, the S11 shows sharp resonance response, with the readout-coil impedance at 1.608 + j25.888 Ω at 177 MHz as measured in air. The inductive coupling is decreased with increasing reading distance, and the readout coil S11 is -0.162 dB at *d* = 12 mm and reaches the reading distance limit. The real part of readout-coil input impedance at resonance frequency is $Re(Z_{in}) = 2\pi f_s L_r k^2 Q$, where Lr is the readout-coil inductance. The coupling factor k is distance dependent and approximated [4] by $k = r_s^2 r_r^2 / ((d^2 + r_r^2)^{3/2} \sqrt{r_s r_r})$ for the case $r_s < r_r$, where r_s is the sensor-coil radius and r_r is the readout-coil radius. This expression indicates how longer reading distance changes the input impedance Z_{in} and in turn the magnitude of S11. The readout-coil resonant frequency f_{S11min} is not significantly affected by reading distance, for k is typically small <0.35 and thereby $f_{S11min} \sim f_s$ (Equation 1.2).

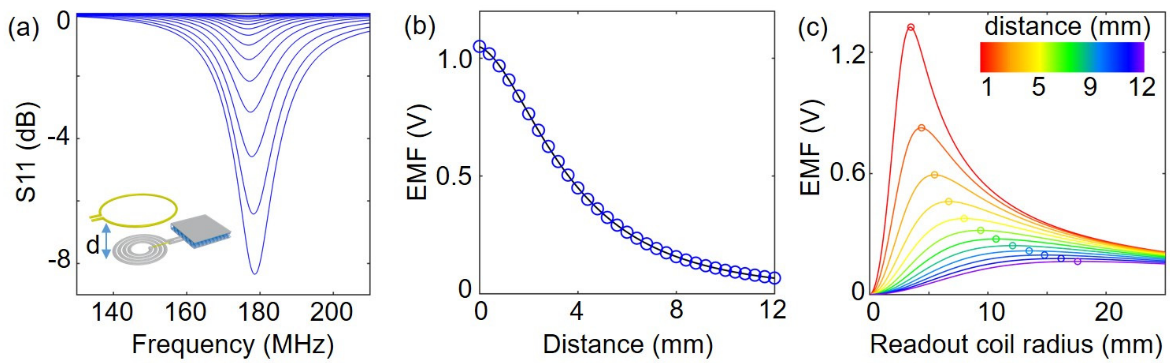

Figure 2.5: Wireless response at different distances. (a) Reflection coefficient versus frequency, as the distance d between the sensor and the readout coil is varied from being in contact to 12mmapart, in steps of 1 mm. The inset shows the measurement setup. (b) Electromotive potential induced on the sensor versus reading distance, for a readout coil with radius of 5.3 mm. The line is a fit to the electromotive force (EMF) function derived in the Section 2.3.4. (c) Electromotive potential EMF(d, r_r) induced on the sensor coil with a radius of 4mmversus readout coil radius r_r. The set of curves shows the results as reading distance is increased from 1mm(red) to 12mm(blue).

The S11 magnitude at resonant frequency is converted to an induced electromotive force using $EMF = \sqrt{P_{dissipate} \times R} = \sqrt{P_{total}(1 - 10^{S_{11}/10})R}$, where P_{total} =10 mW is the root-mean-square output power of the vector network analyzer into the readout coil and R = 129.1 Ω at d = 0 mm and R = 120.5 Ω for d > 4.4 mm. In Section 2.3.4 a mathematical expression is derived from magnetic flux relations to describe EMF(r_r, d) as a function of the reading distance and the readout-coil radius. The derived function fits well to the EMF data over the range of reading distances in Figure 2.5(b). Using a sensor-coil radius of 4 mm, the EMF(rr, d) function is plotted in Figure 2.5(c) to show the inter-related effect of readout-coil radius and reading distance. As the readout-coil radius increases, the induced EMF on the sensor reaches maximum at a longer reading distance. This function indicates that if we intend the reading distance to be farther, the radius of the readout coil should be wider; on the other hand, at close reading distances, a smaller readout-coil radius is better for inducing higher EMF and stronger signals.

Moreover, the environment around the sensor can affect its capacitance and resonance frequency. For example, in Figure 2.5(a), the distance response measurement was taken in air without a load, and the resonance frequency was about 178 MHz. In Figure 2.3(c), the pressure measurement was taken with the same sensor in water. The resonance frequency lowered to 162 MHz without a load. As the sensor environment changed from air to water, the capacitance increased in the space around the sensor, because water has a higher dielectric constant than air. Thus, the frequency range can be shifted due to the sensor environment. Nonetheless, within aqueous environments, the encapsulated sensor shows consistent signals in response to pressure changes.

2.3.4 Wireless readout model fitting

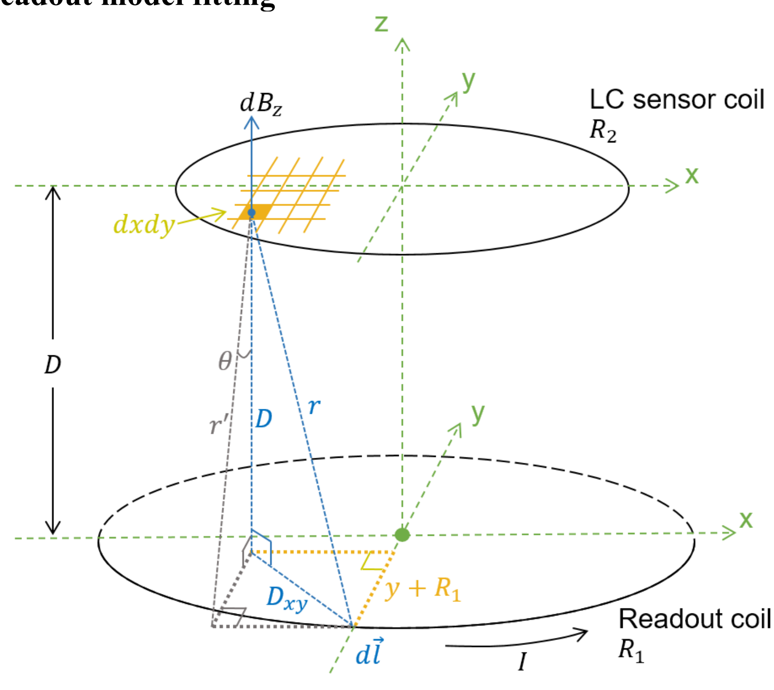

Figure 2.6: Geometric structure of wireless measurement.

The following model was derived to calculate the electromotive force (EMF) on the sensor coil as the distance varies between the readout coil and the inductor-capacitor (LC) sensor coil.

The magnetic flux with respect to the geometry of the coils is shown in Figure 2.6. The readout coil is shown as circle R_1. One turn of the LC sensor coil is shown as circle R_2. The two coils are parallel to each other, and they are aligned to the same central axis, with the origin being the center of R_1. The distance between the coils is D. A current I flows through $d\vec{l}$ in R_1. An area element $dxdy$ on surface of R_2 is randomly selected with coordinate (x, y, D). r is the distance between $d\vec{l}$ and $dxdy$, which is determined by $r^2 = {D_{xy}}^2 + D^2 = x^2 + (y + R_1)^{\,2} + D^2$, where x and y are the coordinates of $dxdy$ and y is negative in this coordinate system. The blue vertical line D is from $dxdy$ to the plane of R_1. θ is the projection angle between vertical line D and r'. By Ampere's right-hand rule, the direction of magnetic field at $dxdy$ generated by $d\vec{l}$ is perpendicular to the plane spanned by r' and $d\vec{l}$, pointing upward and outward. It is also the direction of magnetic flux density $d\vec{B}$ at $dxdy$.

To calculate the magnetic flux, we need the z-axis component of $d\vec{B}$ perpendicular to the surface $dxdy$. The z-axis component is $dB_z = dB\, sin\,\theta$. Biot-Savart law is used to calculate the magnetic flux density due to a wire loop carrying current and written as

$B = \frac{\mu_0 I}{4\pi}\int_C \frac{d\vec{l} \times \vec{r}}{|\vec{r}|^3}$, where C is the wire loop, I is the current on the wire loop, and μ_0 is the vacuum permeability. If only the length element $d\vec{l}$ is considered rather the whole loop, the differential form of the formula is

$$dB = \frac{\mu_0 I}{4\pi}\frac{dl}{r^2} \tag{2.3}$$

The z-axis component of dB is

$$dB_z = \frac{\mu_0 I}{4\pi}\frac{dl}{r^2}\sin\theta \tag{2.4}$$

and is the magnetic flux density at $dxdy$ generated by $d\vec{l}$ along z-axis. The magnetic flux $d^3\phi$ through surface $dxdy$ generated by $d\vec{l}$ is

$$d^3\phi = dB_z dxdy \tag{2.5}$$

Therefore, the magnetic flux $d\phi$ through the whole surface of R_2 generated by $d\vec{l}$ is calculated by the double integral over the area of R_2,

$$d\phi = \int_Y \int_X dB_z \, dxdy = \frac{\mu_0 I}{4\pi} \int_Y \int_X \frac{dl}{r^2} \sin\theta \, dxdy \tag{2.6}$$

The magnetic flux ϕ through the surface of R_2 generated by the whole circular wire R_1 is obtained with another integral over the perimeter of R_1,

$$\phi = \frac{\mu_0 I}{4\pi} \int_L \int_Y \int_X \frac{\sin\theta}{r^2} dxdydl = \frac{\mu_0 I}{4\pi} \int_0^{2\pi R_1} \int_{-R_2}^{R_2} \int_{-\sqrt{{R_2}^2 - y^2}}^{\sqrt{{R_2}^2 - y^2}} \frac{\sin\theta}{r^2} \, dx \, dy \, dl$$

$$= \mu_0 I R_1 \int_{-R_2}^{R_2} \frac{(y + R_1) tan^{-1}\left(\sqrt{\frac{{R_2}^2 - y^2}{(y + R_1)^2 + D^2}}\right)}{(y + R_1)^2 + D^2} \, dy \tag{2.7}$$

One of the integrals cannot be solved with analytical solution. In the above formula, I is the alternating current on R_1 and is a function of time t. The time derivative of flux ϕ is the electromotive force (EMF) induced on the sensor coil:

$$EMF(t) = \frac{d\phi}{dt} = \mu_0 R_1 \frac{dI}{dt} \int_{-R_2}^{R_2} \frac{(y + R_1) tan^{-1}\left(\sqrt{\frac{{R_2}^2 - y^2}{(y + R_1)^2 + D^2}}\right)}{(y + R_1)^2 + D^2} \, dy \tag{2.8}$$

In our experiment, the network analyzer measured the ratio of the effective values (root-mean-square values). There the following model considers only effective values of EMF rather than the real-time transient value. In the above formula, I is a sine function of time t, so the derivative $\frac{dI}{dt}$ can be expressed as $\frac{dI(t)}{dt} = \omega I(t - \frac{p}{4})$, where ω is the circular resonance frequency of the LC oscillator, p is the period at the resonance frequency, and $t-\frac{p}{4}$ is an independent variable of function I to indicate the phase shift of a quarter period. The effective value of $\frac{dI}{dt}$ is ωI_{eff}, where I_{eff} is the effective value of current on R_1. Therefore, the effective value of EMF is

$$EMF_{eff} = \mu_0 R_1 \omega I_{eff} \int_{-R_2}^{R_2} \frac{(y+R_1)tan^{-1}\left(\sqrt{\frac{{R_2}^2 - y^2}{(y+R_1)^2 + D^2}}\right)}{(y+R_1)^2 + D^2} dy \tag{2.9}$$

Based on this function, the relationship between EMF and distance D is

$$EMF(D) = \beta_3 \beta_1 \sum_{n=1}^{4} \int_{-\beta_{2n}}^{\beta_{2n}} \frac{(y+\beta_1)tan^{-1}\left(\sqrt{\frac{{\beta_{2n}}^2 - y^2}{(y+\beta_1)^2 + (D+\beta_4)^2}}\right)}{(y+\beta_1)^2 + (D+\beta_4)^2} dy \tag{2.10}$$

where $\beta_{2n} = \beta_2 - 0.16 - 0.32n$.

In this model, $\beta_1 \sim \beta_4$ are four parameters that can be checked by regression fitting to the measured results in Figure 2.5(b). β_1 is the radius of the readout coil. β_2 is the outer radius of the four-turn sensor coil in an Archimedean spiral. β_{2n} is the average radius of the nth turn coil, in which the spacing between turns is 0.32 mm. β_3 is the coefficient that corresponds to $\mu_0 \omega I_{eff}$. β_4 is an offset in the distance from the readout coil, because physically the thickness of the encapsulation in the sensor leads to a small gap between the readout coil and the sensor coil, so the gap needs to be corrected in the regression.

Using nonlinear fitting in MATLAB to fit the experiment results in Figure 2.5(b) to the function $EMF(D)$, the β parameters are estimated as follows,

$\hat{\beta}_1 = 5.73$ mm (nominally 5.3 mm);

$\hat{\beta}_2 = 3.41$ mm (nominally 4 mm);

$\hat{\beta}_3 = 0.61\ V$,

$\hat{\beta}_4 = 0.30$ mm (nominally 0 mm);

The fit values of the sensor and readout inductor coils are slightly different (less than 15%) from the nominal design values due to fabrication tolerances.

If we set parameter β_1 as an independent variable of the radius of readout coil R_1, EMF becomes a function of both R_1 and D. Substituting the other three β parameters into the formula, the EMF function is

$$EMF(R_1, D) = \hat{\beta}_3 R_1 \sum_{n=1}^{4} \int_{-\hat{\beta}_{2n}}^{\hat{\beta}_{2n}} \frac{(y + R_1)tan^{-1}\left(\sqrt{\frac{\hat{\beta}_{2n}^{\ 2} - y^2}{(y + R_1)^{\ 2} + \left(D + \hat{\beta}_4\right)^2}}\right)}{(y + R_1)^{\ 2} + \left(D + \hat{\beta}_4\right)^2} dy \qquad (2.11)$$

where $\hat{\beta}_{2n} = \hat{\beta}_2 - 0.16 - 0.32n$.

The function $EMF(R_1, D)$ is plotted with D varying from 1 mm to 12 mm in Figure 2.5(c). For each curve there is a peak EMF value, when the signal-to-noise ratio of the measurement will reach the maximum. Given a certain reading distance *D*, the value of R_1 that corresponds to the EMF maximum is the optimal size for the readout coil, and we can use the above function to design the size of readout coil depending on the desired reading distance.

2.3.5 Dynamic pressure measurements

Dynamic pressure measurements are taken to characterize the response time of the encapsulated LC resonator inside a water-filled compartment (Figure 2.7). Pressure pulses are applied by motor-driven plunger, to cycle the applied pressure between 80 mmHg and 120 mmHg. This range is typical for blood pressure in healthy adults. Our printed sensor closely tracks the pressure as reported by a commercial barometer. Under a step change in pressure [Figure 2.7(c)], the rise and fall time of our LC resonator is 0.133 ± 0.033 second, and thus the sensor is capable to sample up to 6 Hz, which is more than enough for physiological monitoring since the maximum heart rate should be below 200 beats per minute or 3.3 Hz. A pressure profile that is similar to a heartbeat with systolic and diastolic blood pressure changes is applied and accurately recorded by the printed sensor in Figure 2.7(d). The next step for this wireless telemetry development is to characterize the printed sensor response in lossy environment such as inside biological tissues. Moreover, with the small form factor and scalability, multiple sensors working operating at different resonant frequencies can be used together to detect pressure changes or flow along a fluidic path.

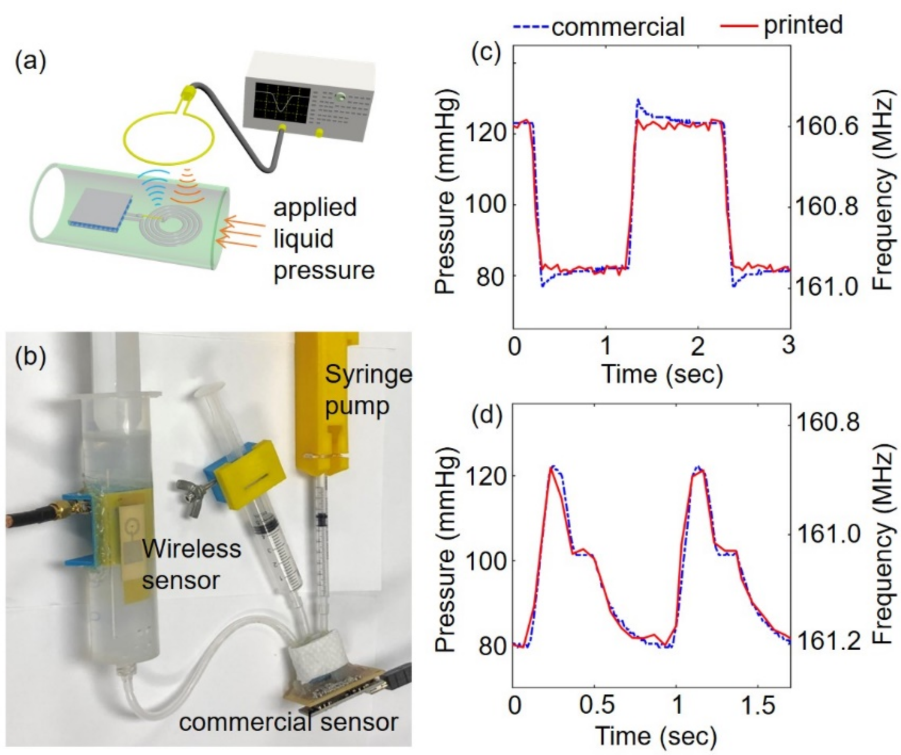

Figure 2.7: Dynamic pressure measurement setup and results. (a) Schematic and (b) Photograph of the dynamic pressure measurement where the encapsulated LC resonator is inside a water-filled compartment. Temporal response of the sensors when (c) changing pressure in abrupt steps and (d) applying a pressure profile that emulates heart pulses

2.4 Summary

In summary, this work achieved an inkjet-printed wireless pressure sensor working in water environment. We improved printing toolpaths and tuned the dielectric porosity in the capacitive sensor to realize a LC resonator that can resolve 3 mmHg with respect to atmospheric pressure. We also derived the optimal readout coil radius in relation to mutual inductive coupling at a certain reading distance. The sensor showed a linear response to pressure between 30 mmHg to 170 mmHg, with a sensitivity of 0.011 MHz/mmHg. The sensor temporal response is up to 6 Hz and capable of capturing the details of typical heart-pulse pressure profile as a proof-of-concept demonstration.

2.5 Experimental section

2.5.1 Fabrication of LC sensor

Nanoparticle silver ink (Novacentrix Metalon JS-B40G) was printed using piezoelectric inkjet [20], [21], [26], [27] (Fujifilm Dimatix DMP2800) on a paper substrate (Epson glossy photo paper) to pattern the four-turn inductor coil and the capacitor electrodes. After the ink was dried, polyvinylphenol (PVP, Aldrich) was spincoated to form a ~3 μm film over the Ag pattern to prevent delamination. The PVP solution consisted of 0.5 g PVP and 0.1 g of methylated polymelamine cross-linker in 5.4 g of propylene glycol monomethyl ether acetate solvent. The sample was annealed on a hot plate at 180 °C for 25 min. Parts of the PVP layer were mechanically scraped away to open via holes, and a piece of gold wire was used as a crossover interconnect to bridge one lead of the inductor coil to a capacitor electrode. The wire was connected to the electrodes by filling the vias with Ag ink.

A stretchable electrode coated with porous polydimethylsiloxane (PDMS) dielectric was prepared on a glass substrate prior to being transferred and bonded with the electrodes on the paper substrate. To fabricate the stretchable electrode [28], PDMS (Sylgard 184) was diluted with hexane in 1:2 ratio by weight, and spincoated on glass substrate as a buffer layer. The PDMS buffer layer was cured at 120 °C for 10 min. PDMS was mixed with silver paste (Ercon E2414 Ag/ AgCl ink) in 1:7 weight ratio, and the mixture was blade coated onto the buffer layer of PDMS. The sample was cured at 120 °C for 30 min to form a Ag electrode ~60 μm in thickness. For the porous dielectric layer, polymethyl methacrylate (PMMA) microspheres with a diameter distribution of 27–32 μm (Cospheric PMPMS-1.2) was mixed with PDMS and hexane in 3:2:2 ratio by weight. The suspension was spincoated on the Ag electrode and heated at 100 °C for 1 h to obtain a dielectric film ~75 μm in thickness. After the PDMS was fully cross-linked by the thermal curing, the sample was placed in dichlorobenzene for 48 h to dissolve the PMMA microspheres, which left behind voids and hence the PDMS became a porous dielectric.

A piece of the Ag electrode with PDMS porous dielectric was cut, in order to be bonded to the paper substrate with the complementary capacitor electrodes and the inductor coil. The bonding process used a diluted PDMS solution (1:2 PDMS:hexane by weight) as the glue, which was spincoated at 2500 rpm for 2 min over the paper substrate. Subsequently the porous film was attached to the paper substrate and cured at 100 °C for 1 h under the weight from a piece of glass slide to facilitate even contact and securely bond the two parts together. Finally, a PDMS solution (2:1 PDMS:hexane by weight) was spincoated at 800 rpm for 2 min to encapsulate the LC resonator. The structure was annealed at 100 °C for 1 h to complete the encapsulation process.

2.5.2 Characterization procedure

The impedance of individual inductors and capacitors was measured using a microwave probe (GGB Industries model 40A-GSG-250-DP) connected to a vector network analyzer (Agilent 8753ES). The S11 input reflection coefficient was measured using a one-turn readout coil with a diamater of 10.6 mm, with a resonance frequency of 162 MHz when sample was in water. The inductance of the readout coil is 337 nH at 162 MHz. The root mean square output power of the vector network analyzer was nominally 10 mW into the readout coil. The readout coil is placed parallel to the inductor of the LC resonator, with the coil centers aligned to each other during measurement. Pressure pulses are applied using a home-built motor-controlled system, where three syringes were connected together (Figure 2.7). The LC resonator was placed inside a water-filled syringe, and the compartment pressure was continuously monitored by a commercial barometer (Infineon Technologies Analog Absolute Pressure Sensor KP236N6165). The other syringes were filled with air to adjust pressure. The second syringe's plunger compressed air in the system, and upon reaching a baseline pressure the plunger was locked in position. The third syringe was used as a pump such that the plunger was driven by a stepper motor to apply pressure pulses. The motor and the commercial barometer were controlled and read by a microcontroller (Arduino Nano). The LC resonator was read wirelessly by the same one-turned readout coil described above, with the reading distance fixed at 3 mm. The vector network analyzer sampled at 16 Hz or 24 Hz. After sweeping frequency to track the resonant frequency f_{S11min}, the network analyzer was set to measure the S11 magnitude at 1 MHz higher than the resonant frequency. At a fixed frequency, we assumed that relative changes in S11 magnitude were correlated to a lateral shift of the S11 characteristics and extrapolated the S11 values to resonant frequency and capacitance by equation (1.1). Other telemetry methods [3] that directly measure resonant frequency are available, but here we chose the relative measurement due to the limited sampling rate in our off-the-shelf analyzer.

Chapter 2, in full, is a reprint of the material as it appears in *Flexible and Printed Electronics*, 2018, Yichen Zhai, Jiyeon Lee, Quyen Hoang, Dan Sievenpipper, Harinath Garudadri and Tse Nga Ng. The dissertation author was the primary investigator and author of this paper.

2.6 References

1 J. H. Cheong, S. Sheung, Y. Ng, X. Liu, R. Xue, H. J. Lim, P. B. Khannur, S. Member, K. L. Chan, A. A. Lee, K. Kang, L. S. Lim, C. He, P. Singh, W. Park, and M. Je, "An Inductively Powered Implantable Blood Flow Sensor Microsystem for Vascular Grafts," *IEEE Trans. Biomed. Eng.*, vol. 59, no. 9, pp. 2466–2475, 2012.

2 L. Y. Chen, B. C. K. Tee, A. L. Chortos, G. Schwartz, V. Tse, D. J. Lipomi, H. S. P. Wong, M. V. McConnell, and Z. Bao, "Continuous wireless pressure monitoring and mapping with ultra-small passive sensors for health monitoring and critical care," *Nat. Commun.*, vol. 5, p. 5208, 2014, doi: 10.1038/ncomms6028.

3 Q.-A. Huang, L. Dong, and L.-F. Wang, "LC Passive Wireless Sensors Toward a Wireless Sensing Platform: Status, Prospects, and Challenges," *J. Microelectromechanical Syst.*, vol. 25, no. 5, pp. 822–841, 2016, doi: 10.1109/JMEMS.2016.2602298.

4 C. C. Oliveira, A. T. Sepúlveda, N. Almeida, B. L. Wardle, J. M. Da Silva, and L. A. Rocha, "Implantable flexible pressure measurement system based on inductive coupling," *IEEE Trans. Biomed. Eng.*, vol. 62, no. 2, pp. 680–687, 2015, doi: 10.1109/TBME.2014.2363935.

5 Q. Tan, T. Luo, S. Member, T. Wei, J. Liu, L. Lin, J. Xiong, and A. S. Design, "A Wireless Passive Pressure and Temperature Sensor via a Dual LC Resonant Circuit in Harsh Environments," vol. 26, no. 2, pp. 351–356, 2017.

6 J. Kim, Z. Wang, and W. S. Kim, "Stretchable RFID for wireless strain sensing with silver nano ink," *IEEE Sens. J.*, vol. 14, no. 12, pp. 4395–4401, 2014, doi: 10.1109/JSEN.2014.2335743.

7 M. W. A. Khan, S. Member, T. Björninen, L. Sydänheimo, and L. Ukkonen, "Remotely Powered Piezoresistive Pressure Sensor : Toward Wireless Monitoring of Intracranial Pressure," vol. 26, no. 7, pp. 549–551, 2016.

8 J. Shintake, E. Piskarev, S. H. Jeong, and D. Floreano, "Ultrastretchable Strain Sensors Using Carbon Black-Filled Elastomer Composites and Comparison of Capacitive Versus Resistive Sensors," *Adv. Mater. Technol.*, p. 1700284, 2018, doi: 10.1002/admt.201700284.

9 S. S. Lee, A. Reuveny, J. Reeder, S. S. Lee, H. Jin, Q. Liu, T. Yokota, T. Sekitani, T. Isoyama, Y. Abe, and Z. Suo, "A transparent bending-insensitive pressure sensor," *Nat. Nanotechnol.*, vol. 11, no. May, pp. 472–478, 2016, doi: 10.1038/nnano.2015.324.

10 N. Luo, J. Zhang, X. Ding, Z. Zhou, Q. Zhang, Y. T. Zhang, S. C. Chen, J. L. Hu, and N. Zhao, "Textile-Enabled Highly Reproducible Flexible Pressure Sensors for Cardiovascular Monitoring," *Adv. Mater. Technol.*, vol. 3, no. 1, pp. 1–8, 2018, doi: 10.1002/admt.201700222.

11 T. Jung and S. Yang, “Highly stable liquid metal-based pressure sensor integrated with a microfluidic channel,” *Sensors*, vol. 15, no. 5, pp. 11823–11835, 2015, doi: 10.3390/s150511823.

12 X. P. Zhou, R. S. Deng, and J. Y. Zhu, “Three-layer-stacked pressure sensor with a liquid metal-embedded elastomer,” *J. Micromechanics Microengineering*, vol. 28, no. 8, 2018, doi: 10.1088/1361-6439/aac13c.

13 K. S. Ramadan, D. Sameoto, and S. Evoy, “A review of piezoelectric polymers as functional materials for electromechanical transducers,” *Smart Mater. Struct.*, vol. 23, no. 3, p. 033001, 2014, doi: 10.1088/0964-1726/23/3/033001.

14 S. C. B. Mannsfeld, B. C. K. Tee, R. M. Stoltenberg, C. V. H. H. Chen, S. Barman, B. V. O. Muir, A. N. Sokolov, C. Reese, and Z. Bao, “Highly sensitive flexible pressure sensors with microstructured rubber dielectric layers,” *Nat. Mater.*, vol. 9, no. 10, pp. 859–864, 2010, doi: 10.1038/nmat2834.

15 J. Kim, T. N. Ng, and W. S. Kim, “Highly sensitive tactile sensors integrated with organic transistors,” *Appl. Phys. Lett.*, vol. 101, no. 10, p. 103308, 2012, doi: 10.1063/1.4751354.

16 S. Kang, J. Lee, S. Lee, S. G. Kim, J. K. Kim, H. Algadi, S. Al-Sayari, D. E. Kim, D. E. Kim, and T. Lee, “Highly Sensitive Pressure Sensor Based on Bioinspired Porous Structure for Real-Time Tactile Sensing,” *Adv. Electron. Mater.*, vol. 2, no. 12, 2016, doi: 10.1002/aelm.201600356.

17 Y. Joo, J. Yoon, J. Ha, T. Kim, S. Lee, and B. Lee, “Highly Sensitive and Bendable Capacitive Pressure Sensor and Its Application to 1 V Operation Pressure-Sensitive Transistor,” pp. 1–10, 2017, doi: 10.1002/aelm.201600455.

18 O. Atalay, A. Atalay, J. Gafford, and C. Walsh, “A Highly Sensitive Capacitive-Based Soft Pressure Sensor Based on a Conductive Fabric and a Microporous Dielectric Layer,” vol. 1700237, pp. 1–8, 2018, doi: 10.1002/admt.201700237.

19 S. Chen, B. Zhuo, and X. Guo, “Large Area One-Step Facile Processing of Microstructured Elastomeric Dielectric Film for High Sensitivity and Durable Sensing over Wide Pressure Range,” 2016, doi: 10.1021/acsami.6b05177.

20 D. Soltman and V. Subramanian, “Inkjet-Printed Line Morphologies and Temperature Control of the Coffee Ring Effect,” *Langmuir*, vol. 94720, no. 9, pp. 677–683, Mar. 2008, doi: 10.1021/la7026847.

21 N. Graddage, T. Chu, H. Ding, C. Py, A. Dadvand, and Y. Tao, “Inkjet printed thin and uniform dielectrics for capacitors and organic thin fi lm transistors enabled by the coffee ring effect,” *Org. Electron.*, vol. 29, pp. 114–119, 2016, doi: 10.1016/j.orgel.2015.11.039.

22 S. Ready, F. Endicott, G. L. Whiting, T. A. Ng, E. M. Chow, and J. P. Lu, "3D printed electronics," in *International Conference on Digital Printing Technologies*, 2013, pp. 9–12.

23 S. S. Mohan, M. Hershenson, S. P. Boyd, and T. H. Lee, "Simple Accurate Expressions for Planar Spiral Inductances," vol. 34, no. 10, pp. 1419–1424, 1999.

24 N. Xue, S. Member, S. Chang, J. Lee, and S. Member, "A SU-8-Based Microfabricated Implantable Inductively Coupled Passive RF Wireless Intraocular Pressure Sensor," vol. 21, no. 6, pp. 1338–1346, 2012.

25 H. Y. Lee and B. Choi, "Sensors and Actuators A : Physical Theoretical and experimental investigation of the trapped air effect on air-sealed capacitive pressure sensor," vol. 221, pp. 104–114, 2015.

26 I. D. Johnston, D. K. McCluskey, C. K. L. Tan, and M. C. Tracey, "Mechanical characterization of bulk Sylgard 184 for microfluidics and microengineering," *J. Micromechanics Microengineering*, vol. 24, no. 3, p. 035017, 2014, doi: 10.1088/0960-1317/24/3/035017.

27 T. N. Ng, D. E. Schwartz, P. Mei, B. Krusor, S. Kor, J. Veres, P. Bröms, T. Eriksson, Y. Wang, O. Hagel, and C. Karlsson, "Printed dose-recording tag based on organic complementary circuits and ferroelectric nonvolatile memories," *Sci. Rep.*, vol. 5, no. August, p. 13457, 2015, doi: 10.1038/srep13457.

28 T. N. Ng, D. E. Schwartz, P. Mei, S. Kor, J. Veres, P. Bröms, and C. Karlsson, "Pulsed voltage multiplier based on printed organic devices," *Flex. Print. Electron.*, vol. 1, no. 1, p. 15002, doi: 10.1088/2058-8585/1/1/015002.

29 K. Wang, U. Parekh, T. Pailla, H. Garudadri, V. Gilja, and T. N. Ng, "Stretchable dry electrodes with concentric ring geometry for enhancing spatial resolution in electrophysiology," *Adv. Healthc. Mater.*, vol. 6, no. 19, p. 1700552, 2017, doi: 10.1002/adhm.201700552.

Chapter 3
Printing Multi-Material Organic Haptic Actuators

3.1 Abstract

Haptic actuators generate touch sensations and provide realism and depth in human-machine interactions. A new generation of soft haptic interfaces is desired to produce the distributed signals over large areas that are required to mimic natural touch interactions. One promising approach is to combine the advantages of organic actuator materials and additive printing technologies. This powerful combination can lead to devices that are ergonomic, readily customizable, and economical for researchers to explore potential benefits and create new haptic applications. In this chapter, we focus on the challenges and potential solutions associated with integration of multi-material actuators, with an eye toward improving the fidelity and robustness of the printing process. We then report our progress in achieving compact, light-weight haptic actuators by using an open-source extrusion printer to integrate different polymers and composites in freeform designs. We demonstrate two haptic interfaces—a tactile surface and a kinesthetic glove—to show that printing with organic materials is a versatile approach for rapid prototyping of various types of haptic devices.

3.2 Introduction

Haptic technologies interact with users through the sense of touch, generating sensations to help people in manipulation tasks and provide information of their surroundings in virtual or augmented reality. [1]–[5] Haptic systems that can realistically recreate touch sensations will greatly impact our professional and personal lives in many areas including teleoperation, simulation training, communication, and immersive entertainment. Yet, the utility of haptics is currently limited; moreover, it is challenging to produce the large-area, distributed signals required to mimic natural touch.

It would be desirable for haptic actuators to generate large ranges of forces and displacements over short time scales, in a compact form factor in the case of wearable haptics. This dynamism is required because the structures such as the skin and elements of the musculoskeletal system are highly stretchable. Moreover, they are teeming with mechanosensory neurons that can perceive sub-micron surface features and macroscale displacements, with reaction times in milliseconds. [3], [5] Thus, to accommodate this dynamism and sensitivity, an exceptionally versatile suite of materials and tools is required to realize the entire range of haptic perception.

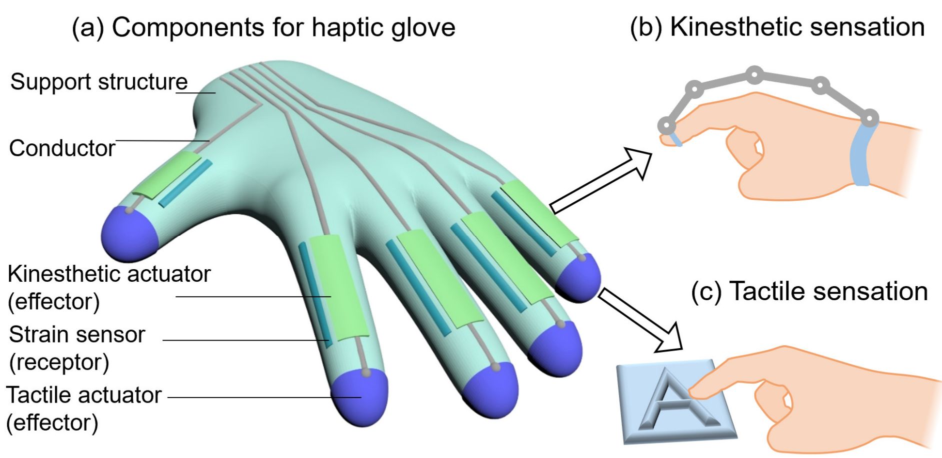

Figure 3.1: Concept of a compact haptic feedback glove. (a) Components for a haptic glove. Depiction of (b) kinesthetic sensation and (c) tactile sensation.

Haptic perception can be divided into two parts: the tactile and kinesthetic senses. [6]–[8]

A compact haptic glove with coordinated tactile and kinesthetic actuators is depicted in Figure 3.1. The tactile sense involves the nerve endings in the skin to detect contact, texture, and vibration [Figure 3.1(b)]. The kinesthetic sense is the awareness of the body position and involves structures located in the musculoskeletal system to sense force and motion [Figure 3.1(c)]. For example, to emulate the feeling of grasping a cup, a haptic system would need to trigger both tactile and kinesthetic senses. That is, pressure would be applied on the fingers to indicate contact, and other actuators located at the joints of the fingers would stiffen to produce resistance against moving into the space occupied by the cup. In comparison to visual or auditory inputs aiming at localized organs of eyes and ears, haptic systems require distributed inputs covering the body. The complexity involved to simulate haptic signals over large area, with sufficient spatial and temporal resolution and high dynamic range, has been a considerable challenge and thus presents exciting research opportunities.

Emerging additive manufacturing techniques such as digital printing provide the capability to fabricate multi-scale, multi-material designs with high precision and throughput. In an actuator, multiple materials are required to connect mechanical and electronic function. For instance, electrical conductors are incorporated with the mechanical structure, in order to apply stimuli such as voltage or heat to trigger actuation. Digital printing is amenable for integrating multiple materials and architecting functionally gradient materials to increase the design space for versatile motion. [9], [10] The versatility and reconfigurability of printing processes are advantageous for fabricating integrated organic haptic interfaces, as will be showcased in this chapter.

In this chapter, a discussion on integration challenges and potential solutions with regard to printing multi-material actuators is first presented in Section 3.3. In Section 3.4, we present our progress with two demonstrations: (i) a compact tactile surface and (ii) a light-weight kinesthetic glove, both of which are electrically programmable, without the need of heavy auxiliary equipment like air compressors required for pneumatic devices. These proof-of-concept devices were fabricated by printing liquid crystal elastomer as the material used for actuation, along with soft electrical conductors [11], [12] and other non-actuated structural components. We found that our approach was able to afford a form factor that is more conformal and portable than prior demonstrations. In Section 3.5, we conclude with our opinions on the future prospects of organic haptic technologies.

3.3 Challenges and their potential solutions with regard to printing multi-materials haptic actuators

The problem of achieving the desired functionalities is dependent on the ability to heterogeneously integrate materials with different mechanical and electrical properties. For example, soft, organic actuators may require structural materials with different rigidities (to complement actuating elements with structural supports), or to harness snap-through instabilities [13], [14] and increase the motion speed and output forces. As a mechatronic device, the haptic actuators with electrical controls can leverage widely accessible integrated circuits, but this aspect adds new integration challenges, such as how to form robust electrical connections and to maintain stable electrical performance under mechanical stress. The complexity of a multi-material system can make the fabrication process difficult, and new development to improve printing techniques will be essential for rapid prototyping to test new concepts. Moreover, for any human-machine interface, safety is a paramount consideration, and we will discuss designs to ensure operation within safe limits. Below we group the aforementioned challenges into four topics and present potential solutions, as listed in Table 3.1.

Table 3.1: Design and fabrication challenges in printing multi-materials actuators

Design and Fabrication Challenges	Potential Solutions
Delamination or buckling due to mismatch in materials moduli	• Incorporate elasticity gradient between rigid and flexible components to relieve stress • Incorporate cuts, kirigami designs, or hooked structures between interfaces • Use bonding materials at interfaces, e.g., a mixture of the component materials
Integration of electronic and mechanical functionalities	• Use composites, such as elastomers mixed with conductors to mitigate conductor cracks • Place sensors, actuators, and controller chips on different substrates, then laminate or use photo-cross-linkers to bond components
Fidelity of printed structures in replicating digital design	• Optimize deposition by adjusting the flow rate, layer height, line-overlap ratio, and printing speed and trajectory • Adjust time delay at printing start-points to ensure adequate filling; control flow at end-points to prevent materials leakage • Track printed features and tune printing parameters in real-time
Safety of human-actuator interactions	• Operate with real-time feedback control to cut power when safety limits are exceeded • Encapsulate with insulating materials to avoid electrical and thermal contacts

3.3.1 Mismatch in moduli

In actuators comprising multiple materials, the adhesion and mechanical moduli between material interfaces are important factors affecting structural integrity. When there is a large mismatch of mechanical moduli, the material stacks do not deform homogeneously upon actuation, resulting in interfacial stress. The stress may cause delamination or buckling of materials, or result in cracks when the stress exceeds the strength. Instead of abrupt, high-stress interfaces, the design of the structure can be adjusted to incorporate an elasticity gradient to alleviate interfacial stress, e.g., by using auxetic architectures [15] or tuning the ratios of base to cross-linker in materials to gradually change the mechanical moduli at interfaces.

Alternatively, the challenge of maintaining structural integrity upon deformation can be addressed by geometric designs. For example, designs inspired by kirigami [16] use cuts in bendable but not stretchable films to fold and form 3D actuators. Serpentine patterns [17] are often used to enhance the stretchability of interconnects. A simple bonder could be a mixture or suspension of the materials at the interface. With more advanced material design, an adhesive that can form crosslinking bonds to both materials at an interface can be applied to joint materials. [31]

In addition, to bond materials without the need of adhesives, an effective solution is to design hooked structures. Similar to riveting in metalwork, the structural components have portions that intersect or interlock to hold the pieces together. We used this interlocking mechanism in the demonstration of a haptic surface shown in Figure 3.3. Specifically, in the actuator segments, we incorporate open slots in one material [indicated as green parts in Layer 2 of Figure 3.3(a)] such that the second material (blue parts) would penetrate through the slots to connect the layers above and beneath the through-hole and fasten the first material in place. The geometric designs to relieve structural issues may also be applicable for electrical components as discussed below.

3.3.2 Integration of electronic and mechanical functionalities

In haptic devices, flexible conductors are needed as conductive interconnects, or to serve as resistive sensors (e.g., for sensing temperature or strain) or triggers for actuation (e.g., for joule heating or electrical bias). Silver nanoparticle paste is often used for its high flexibility, conductivity and compatibility with printing. However, conductive traces made of silver nanoparticles can crack and delaminate when stretched. To combat this issue, a simple solution is to mix a small amount (usually less than 20%) of the structural organic material into the conductive paste. The organic content in the conductive mixture will bond to the surrounding polymer structures, to prevent crack in the conductive traces and still provide high conductivity.

In addition to interconnects, electronic integrated circuits are important for realizing haptic feedback. However, many electronic components, such as programmable silicon controllers, cannot be fabricated by direct printing and require additional integration steps. These electronic components are usually rigid, and during actuation they can be displaced due to poor adhesion. A common method to tackle this integration challenge is to assemble the electronic components on a separate flexible substrate, and then embed the flexible electronic substrate into the neutral plane or on an un-movable part of the structure. [20] Another approach is to print a buffer elastomer to encapsulate the rigid chips and gradually release stress between rigid and soft materials to mitigate high-stress interfaces. [21]

3.3.3 Fidelity of printing process

The ability to digitally design and rapidly print integrated actuators is powerful for haptic research and applications. The most common technique for printing soft actuators is based on extrusion of organic materials and composites. While extrusion of pastes is versatile and compatible with many types of materials, it requires precise control of the extrusion flow rate in coordination with a well-designed tool-path (often written in G-code for computer-aided manufacturing), in order to faithfully construct the digital sketch. Optimizing the printing tool-path, along with post-processing treatments, can significantly improve the workpiece fidelity to the intended design. Common approaches to achieve overhanging structures involve the use of sacrificial supporting structures that can be cut or dissolved away after fabrication, and chemical or mechanical polishing can be used to reduce surface roughness of the workpiece.

Here, we provide some suggestions to achieve better results in processes based on extrusion.

Specifically for pneumatic printing, the extrusion flow rate is affected by multiple parameters including air supply pressure, nozzle dimension, and ink viscosity. To calibrate the flow rate, extrusion is run for a time period, and the weight of extruded material is measured. Then, the nozzle tool-path motion, i.e., the movement velocity of the printing nozzle, should be tuned depending on the extrusion flow rate. We use the following formula to adjust the traveling velocity of the nozzle:

$$v = \frac{m}{\rho t} \cdot \frac{1}{\phi(1-\lambda)h} \tag{3.1}$$

where v is the nozzle velocity, m is the measured weight and t is the time period of the extrusion calibration, ρ is the density of the material being extruded, ϕ is the inner diameter of the nozzle, λ is overlap ratio between neighboring traces, and h is the desired height of the printed layer. This calculation is used to ensure that the right amount of material is deposited to fill the designed volume without over- or under-extrusion, as either would create defects manifested as bulges or voids, respectively, in the printed structures. If the extrusion flow rate changes over time, the nozzle velocity needs to be adjusted. In the future, it would be desirable to incorporate automated feedback control [22] that tracks the printed features and tunes the printing velocity in real-time.

Another aspect of tool-path optimization is to compensate for under-filling at the start and over-filling at the end of a printing path. Because of the high viscosity of extrusion inks, the flow of ink is delayed in time with respect to the starting time of the air pressure supply. Thus, after initiating air supply, a delay in hundreds of milliseconds should be implemented before moving the nozzle away from the starting point, to ensure enough material is deposited at the starting point. At the end point, as the air pressure is removed, there should also be a similar delay period to stabilize the flow. We also move the nozzle to areas outside of the workpiece for several millimeters at high speed (>80 mm/s) and high acceleration (1000 mm/s^2). The high shear rate during this sudden motion will cut off the continuity of the extruded strand, and avoid undesired residual ink being deposited on the workpiece surface.

Lastly, the printing tool-path can be divided according to the desired resolution; for example, in regions where there are no complicated features, the tool path of the printhead can be in coarse resolution and speed up the printing. The tool-path design is an active area of research, and we expect more advances in printing algorithms in the near future to improve the fidelity of printed devices to their digital designs.

3.3.4 Safety in haptic applications

Soft polymeric materials are great candidates for human-machine interfaces as they have similar mechanical properties as biological tissues. Nevertheless, there are safety issues to be considered in haptic applications, in case of malfunction. In actuators with electrical controls, such as dielectric actuator (DEA) and LCE devices, the voltage or current supply to the actuator must be isolated from human contact. Moreover, it must have control logic to shut off power when the safety threshold is exceeded.

In particular for thermally driven actuators like shape memory polymers (SMP) and LCE, it is recommended that the surface temperature of the device ≤60°C, which is the temperature that a human can touch for up to 5 s without sustaining a burn (ASTM C1055, the Standard Guide for Heated System Surface Conditions that Produce Contact Burn Injuries). Increasing the thickness of the thermal insulation layer is an option to provide protection from thermal runaway. For actuators with an integrated heater, there can be problems arising from over-heating due to cracks in the heater. The resistance around the cracks will be much higher than in other conductive regions, and the voltage drop will be highest around the cracks, causing concentrated heat density and potentially burn the local area. To mitigate this risk, there can be real-time tracking of heater resistance to identify cracks and shut off the power supply when necessary.

For a common closed-loop system using proportional-integral-derivative (PID) controller, if an extreme event occurs like a sudden change in temperature or malfunctioning of the temperature sensor, the PID control may over-shoot or stay constantly on, leading to the possibility of overheating. To avoid accidental overheating, the safety control logic should be designed as the highest priority to cut off power to the heater, if a sensor temperature exceeds a preset safety value. If the sensor itself malfunctions, it will show up as either an open or short circuit at the sampling node; identifying such events will be critical, so that power can be terminated for safety. The above discussion is not comprehensive, but at least they are easy steps to ensure safe operation of thermally driven actuators within research settings.

3.4 Printed Organic Haptic Devices

Additive printing methods have been used to fabricate individual parts to be assembled into a haptic system. Many of the printed haptic devices were based on pneumatic actuation, including pneumatic haptic gloves [23], [24] and a tactile array [25] that combines pneumatic chambers with a SMP membrane to form a large, flexible reconfigurable surface. Below we demonstrate haptic devices using another actuation mechanism based on thermally driven polymers that enable a compact form factor. The prototypes are printed by extrusion, which allows us to directly deposit multiple materials and build entire haptic structures on automated printer platforms.

We demonstrate two examples of haptic interfaces, targeting tactile or kinesthetic senses. The main actuating material is LCE, and the actuation mechanism is based on temperature control through integrated resistive heaters. The haptic device designs incorporate non-actuating structural elements that convert the linear deformation of LCE to morph in curvilinear motion. The electronic and structural materials are patterned through a modified extrusion printer, with two pneumatic nozzles (one for LCE, another for conductive paste), two fused filament nozzles (for thermoplastic polyurethane structures), and a built-in UV light for polymer crosslinking. The fabrication method is an automated process flow customizable by digital controls; therefore, the procedures can be easily repeated and scaled with affordable 3D printers.

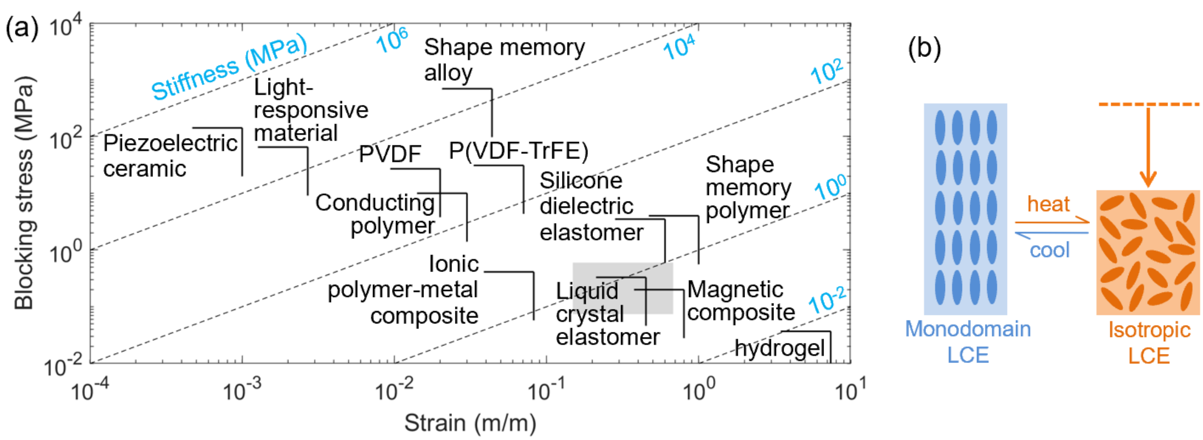

Figure 3.2: Blocking stress-strain of LCE compared to other actuator materials. (a) Range of blocking stress and actuation strain for various actuator materials. The values are from Refs. [39]–[41]. (b) Thermal actuation mechanism of LCE.

We choose LCE as the actuator material for our haptic devices, because LCE shows similar mechanical characteristics as human muscles as seen in Figure 3.2(a). The process of aligning the liquid crystals, namely mesogen domains, in LCE is critical to its actuation performance. In LCE slabs in the aligned state, when heat is applied as a stimulus, the slab will change into the isotropic phase and shrink along the aligned direction, generating force and mechanical work, as illustrated in Figure 3.2(b). There are multiple methods to align liquid-crystalline materials. Common alignment techniques are plate shearing or surface rubbing, [26] which are widely adopted in liquid crystal display industries, or mechanical stretching followed by UV-activated cross-linking to fix the orientation of the mesogens. [27]

In extrusion printing, the shearing force at the nozzle temporarily aligns the LCE in the liquid-crystal phase. [28] Then, in this mono-domain state, the LCE is cross-linked by UV light to permanently set the alignment of the mesogen. Without UV crosslinking, the mono-domain alignment would gradually disappear after 1 to 2 hr, with the LCE turning into poly-domain by environmental thermal energy. In our research, we often purposely deposit LCE without alignment as non-actuating elements of the structure. To do this, the extruded LCE is heated to 80°C, which disrupts the alignment of the mesogen and puts the material into isotropic phase. They turn into a poly-domain state after cooling to the ambient temperature. When crosslinked in the poly-domain state, the LCE will not actuate, since the randomly oriented mesogens do not move coherently. Thus, with the same LCE material, there is the option to process LCE either as an actuating component or an anchoring structural element, and the following demonstrations leverage the LCE tunability to meet both functions.

3.4.1 Compact tactile surface

Morphable tactile surfaces have been demonstrated for applications such as Braille display [29] and smart skins. [30] However, prior tactile surfaces have been limited to small coverage due to the complexities of fabrication and the need for bulky auxiliary components, particularly with fluidic actuators. Here we prototype a compact, flexible tactile surface that is scalable to large area by printing. This tactile surface is based on the concept of a 7-segment display. [31] The surface morphology is changed by varying the raised height of electronically programmable segments to form patterns for tactile perception.

Structural design and electronic control of the printed LCE tactile surface

Figure 3.3(a) is an exploded view of the printed tactile surface, and Figure 3.3(b) is a photograph of the integrated device. The material combinations and geometric layouts for each layer are depicted in Figures 3.3(a) and 3.3(c). The detailed fabrication procedure is described in the Section 3.6.2. Layer 1 is a poly-domain LCE film that serves as a surface smoothing layer to encapsulate the device. In Layer 2, thermoplastic polyurethane (TPU) is deposited in the areas for the 7-segment actuator bars, while the remaining areas are filled in with poly-domain LCE. Layer 3 is the only layer with the active actuation material; mono-domain LCE is printed on top of the TPU areas, surrounded by poly-domain LCE. The alignment of mono-domain LCE is parallel to the width, i.e., the short edge, of each rectangular actuating bar. When actuated, the bar width will shrink and affect deformation of the surface. In Layer 4, conductive silver composite is patterned to be serpentine resistive heaters, to thermally activate the actuation of selected segments. There are six contact nodes to connect the heaters to external driver circuits. Layer 5 is another poly-domain LCE film that supports the heater wires and is the bottom encapsulation for the whole device.

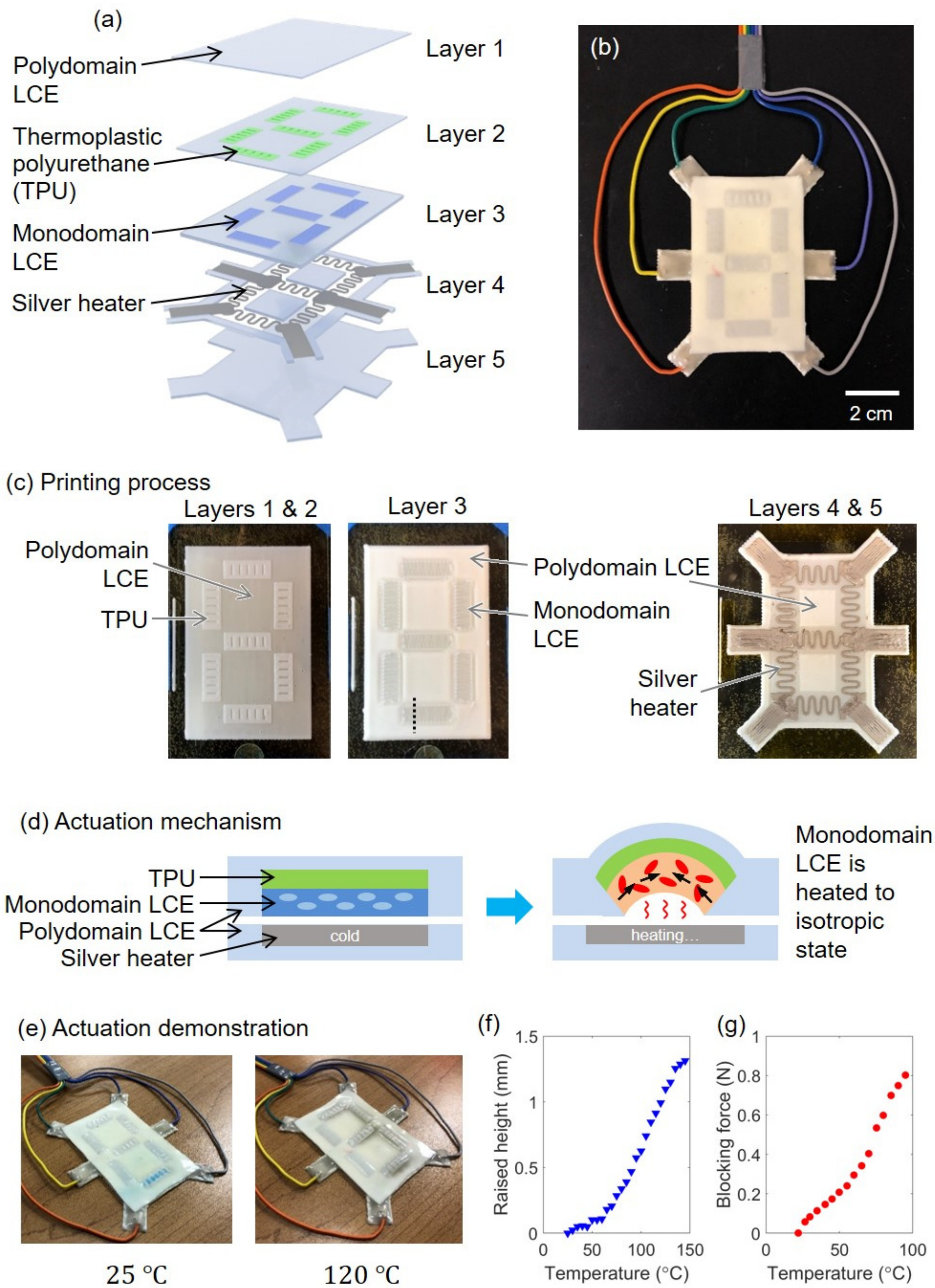

Figure 3.3: Structure and fabrication process of tactile surface. (a) Exploded view and (b) photograph of the printed tactile display. (c) Photographs of the printed layers during the extrusion printing process. (d) Cross-sectional view across an actuator segment, illustrating the actuation mechanism as temperature increases. The position of the cross-section is marked by the black dashed line in the part (c, Layer 3) photograph. (e) Demonstration outputting the number "3" as corresponding segments are heated to 120 ℃. (f) The raised height and (g) the blocking force of an actuator segment at different temperatures.

To power the tactile surface, electrical wires are connected to the six contact electrodes on Layer 4, and the wire inputs are controlled by discrete transistor switches. When a certain segment is selected to actuate, two wire switches are turned on, to supply dc power to the corresponding heater. The heater resistance is about 2 Ω, and the voltage is adjusted to achieve 3 Watts power on each heater, which can heat an actuator to more than 150°C. When multiple segments are required to actuate together, the transistors switch on in sequence to ensure the same heating duty cycle for all the selected heaters.

Tactile surface operation

Figure 3.3(d) illustrates the actuation mechanism of tactile surface, shown as a cross-sectional view across the width of an actuator segment. The heater at the bottom does not move, whereas the actuator on top is free. The actuator layer is bonded to the bottom heater layer, but only in areas (not depicted in the cross-sectional diagram) away from the 7-segment actuators to leave space to accommodate the changes in shape. Inside each actuator bar, the layers of TPU and mono-domain LCE are tightly bonded together. The upper TPU layer is a bendable but incompressible structure. When the mono-domain LCE is heated, it shrinks in the horizontal direction with contraction stress. However, because the top TPU material is incompressible, there is a vertical stress gradient, with the top of the actuator bar restrained to its original length while the LCE contracting at the bottom. Therefore, the TPU-LCE actuator bar deform to an arch shape, raised up in the middle and bent downward at the sides. This design is similar to another work using DEA [32] that leveraged stress gradient to form bumps, and here the operational voltage is 3 V, which is much lower than DEAs. The TPU-LCE combination converts LCE's linear contraction to surface morphological changes, and the 7-segment interface is electronically programmable to output different numbers as relief patterns in the Supplemental Video 1 (https://onlinelibrary.wiley.com/doi/abs/10.1002/adma.202002541).

Figure 3.3(e) shows an example of the tactile surface actuated to raise a number “3” pattern. When the heaters are powered on, in about 1 minute, the segments are heated from room temperature to 120°C, as measured by an infrared camera monitoring the top surface. The change in peak height at the actuator segment with respect to surrounding non-actuated regions is measured against the surface temperature in Figure 3.3(f). A maximum height of 1.3 mm is observed at 150°C. Figure 3.3(g) exhibits the blocking force of one unit constrained at 0 mm height. A maximum blocking force of 0.83 N is reached at 100°C. However, obviously for safety, we would not operate at such high temperature. It was shown that people can differentiate surface heights on the order of micrometers. [3] The surface temperature should be limited to below 60°C, which would raise the tactile surface by a few hundred micrometers, enough morphological changes for a user to sense, based on the perception thresholds of users. Moreover, to operate well within the temperature range for skin contact, the tactile surface can be adjusted by using LCE that actuates at lower temperature and/or adding thicker heat isolation layer in the future.

In our tactile surface which is relatively large in area, thermal interference between different units is not observed. However, the spatial resolution in an array may eventually be limited by the heat gradient distribution. Heat from an actuated unit can spread to neighboring units and may interfere with their operation. The manipulation and concentration of heat flux using metamaterial cells [33] may be needed in order to direct thermal conduction and in turn improve the resolution of tactile arrays.

3.4.2 Light-weight kinesthetic glove

Kinesthetic gloves driven by fluidic pressure actuators [23], [34] have shown high output force and fast response, but the bulky exoskeletons reduce user movement and comfort. Recent works aim to improve the form factor of kinesthetic gloves, to make them compact by using slim electrostatic brakes [35] or materials with tunable stiffness. [36] These devices apply damping resistance to finger joints and operate only reactively. That is, a person must initiate movement to feel the dampening effect, as the device cannot actively move the finger joint but only adjust the countering resistance. To enable a kinesthetic glove that actively applies force on the user's body, here we demonstrate a light-weight actuator based on LCE, to take advantage of the flexbility and compactness of printed LCE integrated structures.

Structural design of the LCE actuator for kinesthetic feedback

Figure 3.4(a) shows the kinesthetic actuator consisting of three printed layers. The top and bottom layers are extruded as mono-domain LCE. For the middle layer, conductive silver composite is extruded to pattern the heater traces, and the areas around the heater are filled by LCE. Two pieces of copper wires are embedded in the middle layer to connect the heater loop to an external power supply. In Figure 3.4(a), the LCE in the light blue regions is aligned parallel to the long edge of the actuator, whereas in the dark blue regions, the LCE is aligned parallel to the short edge. The perpendicular alignment directions between the dark and light blue regions reduce the axial movement of the copper wires with respect to the heater traces, to avoid disconnection in the electrical path upon actuation. ADC power supply is used to power on the integrated heater to raise the actuator temperature and control actuation.

Characterization of the printed LCE actuator

The actuator characteristics is determined in terms of temperature, stress, and strain, as shown in Figure 3.4(b). Figure 3.4(c) show photographs of the integrated LCE actuator contracted to different lengths at various temperatures. The characterization procedure is described in Section 3.6.5. The actuator strain is defined as $(L_0\text{-}L)/L_0$, where L_0 is the original length at room temperature and L is the length at a certain temperature and applied stress, and L= L_0-L. In Figure 3.4(b), the stress-strain measurements at a constant temperature are indicated in one color. Raising the device temperature increases the output stress and strain. The y-intercept is the blocking stress, which is the maximum force per unit area that the actuator is able to generate. At 120°C, the actuator in Figure 3.4(b) shows a blocking stress of 255 kPa (equivalent to 7 N force). The actuator dimensions are 70 mm in length, 12 mm in width, and 2.2 mm in thickness. The stored stress is released and reduced when the actuator is allowed to contract in length, reaching the maximum strain at the x-intercept where no load is applied to the actuator. This actuator at 120°C is capable of outputting 18 mJ of work (force F multiplied by displacement d), which corresponds to lifting up against gravity a load of 370 grams by a distance of 5 mm.

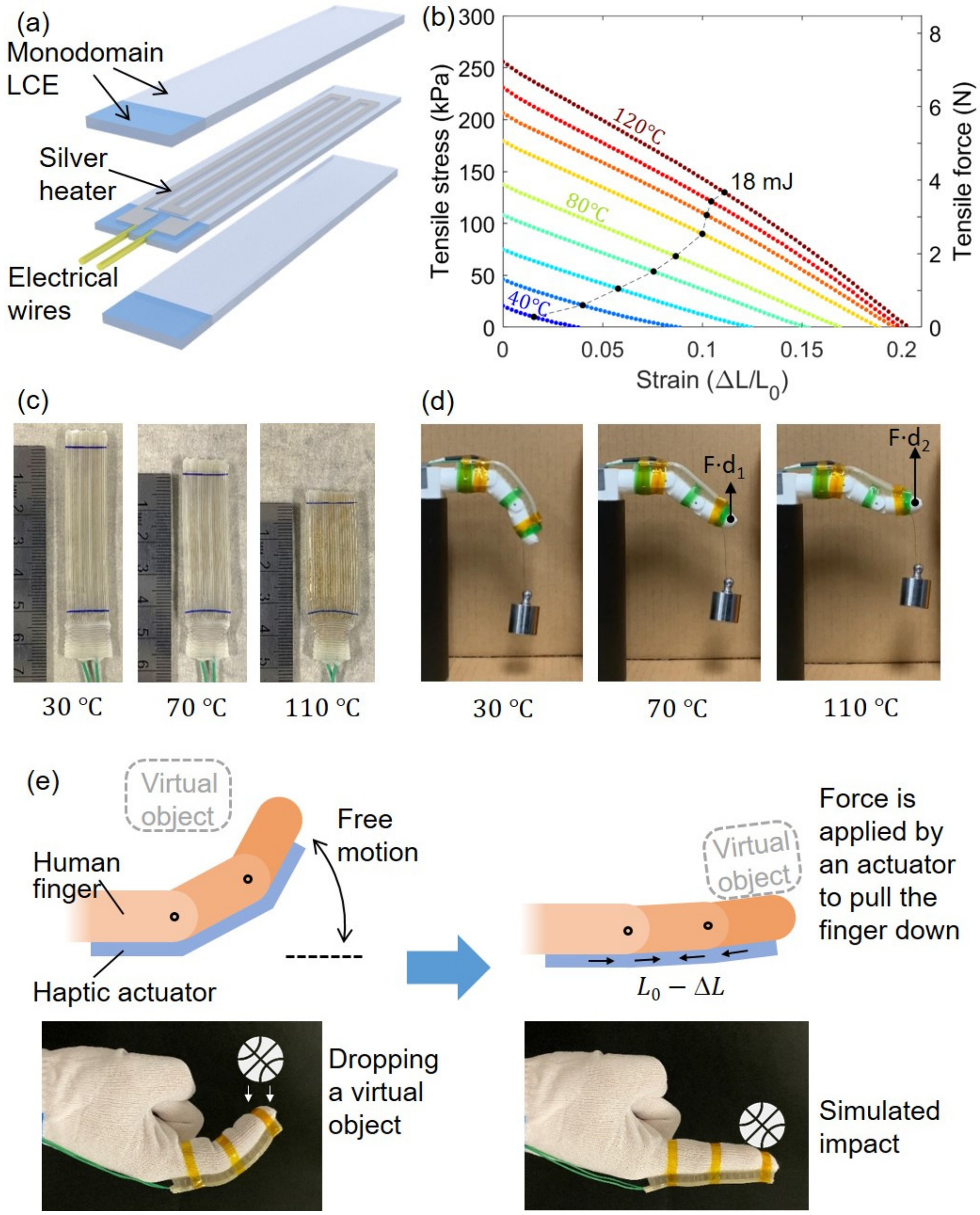

Figure 3.4: Structure and fabrication process of kinesthetic actuator. (a) Exploded view of the printed kinesthetic actuator. (b) Output stress-strain characteristics of the printed kinesthetic actuator at different temperatures, in steps of 10°C. The maximum work output is marked as a black point on each curve. (c) Photographs of the kinesthetic actuator when heated to different temperatures with no load. The ruler's numbers are in centimeter unit. The actuator dimensions are 70 mm in length, 12 mm in width, and 2.2 mm in thickness. (d) Demonstration of actuation on a finger model. A 50 g weight is lifted by the actuator to different distances, depending on the control temperatures. (e) Tensile force on the finger is applied by the actuator to generate a kinesthetic sensation, to mimic the impact from an object in virtual reality.

To demonstrate the work that the LCE actuator can do, we attach the actuator onto a model finger as shown in Figure 3.4(d). A 50-gram weight is hung on the fingertip. As the actuator is heated, the LCE contracts and lifts up the fingertip. A video of this demonstration is included as Supplemental Video 2 (https://onlinelibrary.wiley.com/doi/abs/10.1002/adma.202002541). At 70°C, the actuator lifts the finger with the 50-gram weight by 9.2 mm, corresponding to a work output of 4.5 mJ. This level of work output is generally sufficient for haptic interfaces.

The response time of thermally driven LCE actuator is limited by the heat flux exchange speed. The energy required to heat the actuator from room temperature to the actuation temperature can be estimated by $Q = c*m* \ T$, where c is the specific heat capacity of the LCE (~1 J g^{-1} K^{-1}), m is the mass of the LCE actuator (2 grams), and T is the temperature difference between the unheated and heated states. Therefore, the required thermal energy is estimated to be 150 J for heating the actuator from 25°C to 100°C. When the power passing through the printed silver heater is limited to <5 Watts as done in the above example, the heating and actuation process takes at least 30 s. This calculation assumes no heat loss and homogeneous heating. A potential method to accelerate the LCE response time is to use a high-power heater; for instance, with a 50 W heater, the temperature can be raised in 3 s if heat dissipation into the environment is minimized. In such design, the heater controller must be responsive to precisely control the temperature and input energy to avoid overheating. Conversely, the cooling process also restricts the actuator response speed. As natural cooling is slow, convection or thermoelectric cooler might be used to accelerate cooling. Overall, device geometries that maximize heat transfer would be beneficial to improve the actuator speed.

Mechanism to emulate kinesthetic sensation on a finger

To use the LCE actuator to offer kinesthetic feedback, we attach the actuator to the dorsal side of a fabric glove, with a 3 mm thick PDMS buffer pad to provide thermal insulation between the LCE actuator and the glove and ensure that the fabric temperature is always below 60°C. With the LCE at room temperature, the actuator is at original length. A person wearing the kinesthetic glove can move one's finger freely, as shown in the left column of Figure 3.4(e). In virtual reality, this scenario corresponds to the feeling that the finger is not in contact with any virtual object, and so the finger joints would feel no resistance to movement. To change the kinesthetic perception, the LCE actuator is heated to shrink its length, which pulls the finger to straighten up and restricts its free movement, as depicted in the right column of Figure 3.4(e). This output force creates a sensation in the finger that it is pressed down by a virtual object. This actuation mechanism is able to simulate the impact of a virtual object on the user, because the LCE actuator can actively apply force in addition to passive damping of joint motion. For example, when a virtual ball is dropped onto the finger, the physical dynamics can be imitated by a rapid force pulling back the finger. We envision that the active force from the LCE glove can recreate the sensation of holding an object that moves, such as the feel of a wiggling virtual pet for entertainment or the impression of softness and resistance of the various tissues in virtual surgical training.

3.5 Conclusion

To advance a new generation of soft haptic interfaces, one promising approach as presented in this progress report is to combine the advantages of organic actuator materials and additive printing technologies. This powerful combination can lead to devices that are ergonomic, readily customizable, and economical for everyone to explore potential benefits and create new haptic applications. Here we discuss our progress in achieving compact, light-weight haptic actuators by using an open-source extrusion printer to integrate different polymers and composites in freeform designs. We demonstrated two examples, a tactile surface and a kinesthetic glove, to show that printing with organic materials is a versatile approach to rapidly prototype various types of programmable haptic interfaces.

In the development of organic haptic actuators, we encountered fabrication challenges in the printing process and in materials compatibility. In particular, improvements in printing tool-path control, such as optimizing the extrusion height and the travel speed of nozzles to compensate for over- or under-extrusion, were implemented to raise the fidelity of printed structures to their digital blueprints. With regard to the issue of materials compatibility, delamination and cracking at materials interfaces were key problems. We compensated for poor adhesion by using mechanical hooking designs. And, specifically for electronic materials, we mixed the conductive silver ink with a small amount of the structural material. The conductive ink would bond with the surrounding structural material, and thus the conductive traces remained robustly bonded during actuation. Potentially our solutions to the above printing challenges would be relevant for other similar works on additive manufacturing of multi-material structures.

In applying organic materials to haptic applications, we note there are properties that need further improvement. Specifically for thermally actuated materials such as LCE and SMP, the key bottlenecks are the response speed and the operational temperature. Regarding the response speed, the actuation transition currently takes several to tens of seconds to complete, because the heat flow is slow and restricted by the efficiency of the integrated heater/cooler in the actuator. More effective heat transfer structures are needed for these thermally driven materials to reach better response speed, targeting millisecond transitions to be comparable to motor-driven haptic devices. The combination of rigid supports with soft actuators can also be designed to harness snap-through instabilities [13], [14] in order to increase the motion speed.

Regarding the operational temperature, currently most LCE materials require temperatures much higher than 60°C to shift from liquid-crystal to isotropic phase. Usually a thick thermal insulation layer is used so that the surface temperature is lowered to a safe level for skin contact. However, a better approach will be to adjust the formulations of LCE so that the phase transition temperature can be lowered. [37] A recent study has successfully reduced the LCE phase transition temperature by more than 30 ℃ through tuning the mesogen and spacer moieties. [38] With a low transition temperature, the heat required for LCE actuation is greatly reduced, ensuring thermal safety. In addition, as the phase transition requires less energy transfer, the LCE actuators will show faster response speed and consume less power. With the blooming communities of ingenious researchers working on high-performance organic actuators and printing technologies, we believe that the aforementioned issues are solvable, and the use of organic haptic interfaces, maybe extending to a whole-body suit, will be technologically possible to offer immersive haptic experiences in the future.

3.6 Experimental section

3.6.1 Formulation of extrusion inks

Liquid crystal elastomer (LCE) ink: LCE ink was synthesized from monomers, using 0.02 mole of 1,4-bis-[4-(3-acryloyloxypropyloxy) benzoyloxy]-2-methylbenzene (RM257, 98.8%, Wilshire technologies) and 0.0175 mole of 2,2′-(ethylenedioxy) diethanethiol (95%, Sigma-Aldrich) were dissolved in 50 mL dichloromethane. A polymerization catalyst, 0.2 g dipropylamine, was also added into the solution. The feed ratio of the two monomers was 8:7, and the degree of polymerization was expected to be 8. The solution was stirred for 16 hours at room temperature, to allow the monomers to polymerize into oligomers by Michael addition reaction. The overnight stirring time ensured sufficient reaction. Afterwards, 0.06 g 2-hydroxy-4′-(2-hydroxyethoxy)-2-methylpropiophenone, which was a photo initiator with 365 nm UV response, was added to the solution. Then the solution was heated with stirring to 90 ℃ in a heating mantle (Mtops DMS632) to evaporate the solvent. In about 30 minutes, the viscosity become high, and the magnetic stir bar was removed. The ink was in a round bottom flask connected to a vacuum pump and heated to 110 ℃ for 16 hours to remove the residual solvent. During heating, the flask was covered by aluminum foil to avoid photo-induced cross-linking by lights in the room. After solvent evaporation, the LCE ink was loaded into a 10 mL dispensing syringe. A hot air gun was used to heat the flask (around 220 ℃) to reduce the ink viscosity in order for it to flow out. Then the dispensing syringe was held vertically and heated in an oven to 80 ℃ for 16 hours, to settle and de-gas the LCE ink.

Silver conductive ink for the tactile surface: 10 g Ag/AgCl ink (Ercon E2414) was centrifuged at 700*g for 80 minutes. Then about 50% by volume or 20% by weight of the solvent was separated and removed from the original ink. The centrifuged silver ink was mixed with

PDMS (Sylgard 184, with the curing agent added in 10:1 ratio) in a ratio of 4:1 by weight. The mixture was put in vacuum for 5 minutes to de-gas. Then the paste was loaded into a dispensing syringe, followed by centrifuge spinning at 700*g for 15 seconds to settle the ink.

Silver conductive ink for the kinesthetic actuator: 10 g Ag/AgCl ink (Ercon E2414) was centrifuged using the same process above. Then 300 mg LCE ink was dissolved in acetone in 1:1 ratio by weight. The LCE solution was mixed with the centrifuged silver ink in 1:2 ratio by weight. The mixture was put in high vacuum for 10 minutes to evaporate the acetone. Then the mixture was loaded into a dispensing syringe followed by centrifuging.

3.6.2 Fabrication process for the tactile surface

We have modified a commercial 3D printer (Raise3D N2) to include 2 fused deposition modeling (FDM) and 2 pneumatic extrusion heads. The Metcal DX-350 digital dispensers were used to regulate and switch compressed air supply for extrusion. To reduce the viscosity of LCE for proper extrusion, the dispensing syringe was heated to 57 ℃ and the needle nozzle was heated to 60 ℃. The air supply was tuned to 90 psi for extrusion of LCE. Eighteen-gauge dispensing needles were used as extrusion nozzles.

To form the tactile surface as shown in Figure 3.3(a) of the main text, Layers 1—3 (actuator part) were printed in one stack, while Layers 4 and 5 (heater part) were separately printed as another stack, and then the two stacks were laminated together. The total area of the surface is 60mm by 40 mm, and each actuator segment is 15 mm by 5 mm.

For Layer 1, the LCE ink was extruded to form a 0.2 mm thick film, followed by 100 ℃ hot air blowing for 1 minute to convert LCE into poly-domain phase. Then LCE ink was cured by a 3 Watts, 365 nm UV light for 10 minutes. On top of Layer 1, 0.2 mm thermoplastic polyurethane (TPU) pattern was printed by FDM nozzle, shown as green parts in Layer 2. The left photograph of Figure 3.3(c) showed the printed LCE in Layer 1 and TPU in Layer 2. There were five narrow slots on each TPU unit. LCE was printed into these slots to bond the LCE layers above and beneath TPU, to prevent the delamination between LCE and TPU. Then LCE was printed in a complementary pattern around TPU to fill Layer 2, followed by hot air blowing for 1 minute and UV curing for 10 min. To complete Layer 3, three passes of LCE was printed; the total thickness is 0.6 mm, with 0.2 mm film for each pass. In Figure 3.3(a), the blue areas were heated by 100 ℃ hot air for 1 minute and cured by UV light for 20 minutes. Then mono-domain LCE was printed in the pattern shown in dark blue. The printing was divided into 6 passes, each pass forming a film at 0.1 mm thick. The direction of printing is parallel to the short edge (width) of each rectangular bar. During the printing of mono-domain LCE, 200 mW UV light was constantly on to fix the alignment of LCE. Finally, the LCE stack was further cured by 3W UV light for 10 min, shown as the middle photograph of Figure 3.3(c).

In Layer 4, there were seven resistive heaters in thin serpentine pattern, at the positions of the 7-segment actuator bars. Each heater can be independently selected to activate the corresponding actuator. There were six endpoint nodes between all the heaters. Wide conductor strips were printed to fan out to external wires connected to the power supply. The fan-out electrodes were much wider than the trace of serpentine heaters, such that the resistance was highest at the heater traces. When an applied current passed through the close loop, the resistive heaters would heat up while the leading strips were much less heated.

The heater part was fabricated separately from Layers 1—3. To form the heater shown as right photograph in Figure 3.3(c), Layer 5 was printed first, as the base with a 0.2 mm thick poly-domain LCE. On top of Layer 5, the LCE pattern of Layer 4 was printed in two individual passes, each forming a film at 0.2mm thick. The first pass was treated with heat and UV light, while the second pass was treated by heat only and remained uncross-linked, to be used as a bonding interface to attach the top actuator and the bottom heater together in the later lamination step. The heaters and fan-out electrodes were printed with silver ink in two layers, to reach a total thickness of 0.4 mm. The air pressure to extrude silver ink was 25 psi. The structure was heated to 70 ℃ for 30 minutes to dry the solvent in the silver ink. Then a small amount of PDMS was dropped on each of the serpentine heaters for encapsulation and electrical isolation. The annealing temperature was maintained at 70 ℃ for 16 hours to fully evaporate the solvent and cure the PDMS.

The top actuator part (Layers 1—3) and bottom heater part (Layers 4 & 5) were laminated together in the sequence shown in Figure 3.3(a). The stack was treated by UV light (36 Watts 365 nm) for 30 minutes, which was for cross-linking the uncured LCE in Layer 4 to bond the top and bottom parts. Finally, electrical wires were attached onto the silver fan-out electrodes using conductive epoxy (CircuitWorks CW2400). LCE was dropped on the attachment points and cured by UV light to strengthen the connection to the electrical wires.

3.6.3 Characterization methods for the tactile surface

To measure the raised height as a function of temperature, the tactile surface was placed on a flat surface, alongside a ruler fixed perpendicular to the surface. To control the heater temperature, a DC voltage source was used to power on one actuator unit. The applied voltage was adjusted to maintain the desired temperature, which was tracked by a thermal imager (PerfectPrime IR0005). The raised height was measured by taking photographs of the actuated unit and the ruler inside the same photo frame. The pixels of the raised surface were counted, in comparison with the pixels of the ruler as a scale, to obtain a calibrated distance for the raised height metric.

3.6.4 Fabrication process for the kinesthetic actuator

To fabricate the kinesthetic actuator shown in Figure 3.4(a), the bottom layer and the middle layer were printed as one piece, and the top layer was printed as a separated piece. The two pieces were attached by lamination. The bottom layer was printed with four passes (each forming a film of 0.2 mm thickness) on a glass slide. Thus the total thickness was 0.8 mm. The mono-domain LCE in the middle layer was printed in three passes, each forming 0.2 mm thick films. During printing of LCE, 200 mW UV light was used to illuminate the workpiece in the whole process. After printing, the stack was treated under 5 Watts UV light for 10 minutes to fully crosslink the LCE. Then conductive silver ink was printed to pattern the heater. The Ag printing was divided into three passes, with a total thickness of 0.6 mm.

To print the top layer, 200 mW UV light was on during printing of the first three passes. When printing the fourth pass, UV light was turned off. This surface remained uncross-linked to serve as a bonding interface for lamination of the pieces. The whole structure was then cured under 10 Watts UV light for 20 minutes.

To cure the printed silver heater, the substrate was heated to 50 °C. The printed heater was connected to a power supply through two copper wires. The current was adjusted to maintain about 1.5 Watts heating power. The thermal cure took 16 hours. This self-heating process ensured full and even annealing of the silver ink. During the first 1 hour of heating, 10 Watts UV light was turned on to cure and bond the LCE content inside the silver ink to the outer LCE structure. This step prevented the cracking and delamination of the silver heater during actuation.

3.6.5 Characterization methods for the kinesthetic actuator

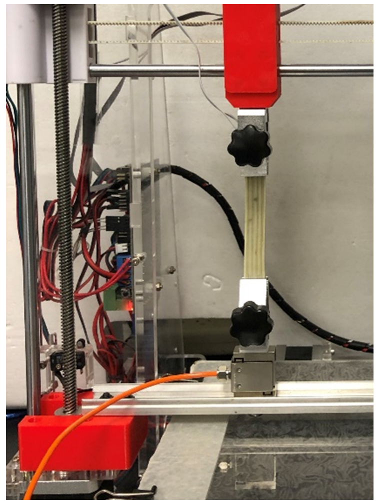

Figure 3.5: Customized programmable tensile force tester.

We modified a 3D printer frame (prusa i3) into a tensile force tester as shown in Figure S2. An S-type load cell (DY106-3kg) was attached to the tester frame, and a metal fixture was fixed to the top of the load cell. Another metal fixture was mounted on the lifting beam of the frame. The resistance value of load cell was sampled by a HX-711 AD convertor interfaced with an Arduino microprocessor. A MATLAB code was used to control the movement of tester and collect the force data as recorded by the Arduino interface.

The kinesthetic actuator was clamped between the top and bottom fixtures. A DC power supply was used to power on the integrated heater, and a thermal imager (PerfectPrime IR0005) was used to track the temperature. In the measurements, the actuator was first fixed at the original length. Then it was heated and allowed to stabilize at the desired temperature. At this time, the stress on actuator was measured as the blocking stress, shown as the y-intercept in Figure 5(b). Subsequently, the tester was controlled to allow the actuator length to contract at a speed of 0.5 mm/s. Meanwhile, the force on the load cell was recorded corresponding to each position. When the tracked force reached 0 N, it meant that the actuator reached the maximum actuation strain. This procedure provided stress-strain and work output data at a fixed temperature. The work output is the force output multiplied by the displacement distance DL. For another round of measurements at another temperature, the tester moved to stretch the actuator to its original length. The actuator was heated to the next selected temperature, and the above procedure was repeated.

Chapter 3, in full, is a reprint of the material as it appears in *Advanced Materials*, 2021, Yichen Zhai, Zhijian Wang, Kye-Si Kwon, Shengqiang Cai, Darren Lipomi and Tse Nga Ng. The dissertation author was the primary investigator and author of this paper.

3.7 References

1 H. Culbertson, S. B. Schorr, and A. M. Okamura, “Haptics: The Present and Future of Artificial Touch Sensation,” *Annu. Rev. Control. Robot. Auton. Syst.*, vol. 1, no. 12, pp. 385–409, 2018, doi: 10.1146/annurev-control-060117-105043.

2 X. Yu, Z. Xie, Y. Y. Yu, J. Lee, A. Vazquez-guardado, H. Luan, J. Ruban, X. Ning, A. Akhtar, D. Li, B. Ji, Y. Liu, R. Sun, J. Cao, Q. Huo, Y. Zhong, C. Lee, S. Kim, P. Gutruf, *et al.*, “Skin-integrated wireless haptic interfaces for virtual and augmented reality,” *Nature*, vol. 575, no. November, 2019, doi: 10.1038/s41586-019-1687-0.

3 S. Biswas and Y. Visell, “Emerging Material Technologies for Haptics,” vol. 1900042, pp. 1–30, 2019, doi: 10.1002/admt.201900042.

4 D. J. Lipomi, C. Dhong, C. W. Carpenter, N. B. Root, and V. S. Ramachandran, “Organic Haptics : Intersection of Materials Chemistry and Tactile Perception,” vol. 1906850, pp. 1–15, 2019, doi: 10.1002/adfm.201906850.

5 C. Pacchierotti, S. Sinclair, M. Solazzi, A. Frisoli, V. Hayward, and D. Prattichizzo, “Wearable Haptic Systems for the Fingertip and the Hand : Taxonomy , Review , and Perspectives,” *IEEE Trans. Haptics*, vol. 10, no. 4, pp. 580–600, 2017, doi: 10.1109/TOH.2017.2689006.

6 H. P. Saal and S. J. Bensmaia, “Touch is a team effort : interplay of submodalities in cutaneous sensibility,” *Trends Neurosci.*, vol. 37, no. 12, pp. 689–697, 2014, doi: 10.1016/j.tins.2014.08.012.

7 R. S. Johansson and J. R. Flanagan, “Coding and use of tactile signals from the fingertips in object manipulation tasks,” vol. 10, no. mAy, pp. 14–20, 2009, doi: 10.1038/nrn2621.

8 J. C. Tuthill and E. Azim, “Proprioception,” *Curr. Biol.*, vol. 28, no. 5, pp. R194–R203, 2018, doi: 10.1016/j.cub.2018.01.064.

9 P. A. G. S. Giachini, S. S. Gupta, W. Wang, D. Wood, M. Yunusa, E. Baharlou, M. Sitti, and A. Menges, “Additive manufacturing of cellulose-based materials with continuous, multidirectional stiffness gradients,” *Sci. Adv.*, vol. 6, no. 8, p. eaay0929, 2020, doi: 10.1126/sciadv.aay0929.

10 D. Raviv, W. Zhao, C. Mcknelly, A. Papadopoulou, A. Kadambi, B. Shi, S. Hirsch, D. Dikovsky, M. Zyracki, C. Olguin, R. Raskar, and S. Tibbits, “Active Printed Materials for Complex Self-Evolving Deformations,” pp. 1–9, 2014, doi: 10.1038/srep07422.

11 B. C. K. Tee and J. Ouyang, "Soft Electronically Functional Polymeric Composite Materials for a Flexible and Stretchable Digital Future," vol. 1802560, pp. 1–14, 2018, doi: 10.1002/adma.201802560.

12 J. Wang, M. F. Lin, S. Park, and P. S. Lee, "Deformable conductors for human–machine interface," *Materials Today*, vol. 21, no. 5. pp. 508–526, 2018. doi: 10.1016/j.mattod.2017.12.006.

13 J. T. B. Overveldea, T. Kloeka, J. J. A. D'Haena, and K. Bertoldia, "Amplifying the response of soft actuators by harnessing snap-through instabilities," *Proc. Natl. Acad. Sci. U. S. A.*, vol. 112, no. 35, pp. 10863–10868, 2015, doi: 10.1073/pnas.1504947112.

14 W. Fan, C. Shan, H. Guo, J. Sang, R. Wang, R. Zheng, K. Sui, and Z. Nie, "Dual-gradient enabled ultrafast biomimetic snapping of hydrogel materials," *Sci. Adv.*, vol. 5, no. 4, p. eeav7174, 2019, doi: 10.1126/sciadv.aav7174.

15 M. Kaur and W. S. Kim, "Toward a Smart Compliant Robotic Gripper Equipped with 3D-Designed Cellular Fingers," *Adv. Intell. Syst.*, vol. 1, no. 3, p. 1900019, 2019, doi: 10.1002/aisy.201900019.

16 A. M. Abdullah, X. Li, P. V. Braun, J. A. Rogers, and K. J. Hsia, "Kirigami-Inspired Self-Assembly of 3D Structures," *Adv. Funct. Mater.*, p. 1909888, 2020, doi: 10.1002/adfm.201909888.

17 C. Wang, C. Wang, Z. Huang, and S. Xu, "Materials and Structures toward Soft Electronics," vol. 1801368, pp. 1–49, 2018, doi: 10.1002/adma.201801368.

18 H. Yuk, T. Zhang, G. A. Parada, X. Liu, and X. Zhao, "Skin-inspired hydrogel-elastomer hybrids with robust interfaces and functional microstructures," *Nat. Commun.*, vol. 7, no. May, pp. 1–11, 2016, doi: 10.1038/ncomms12028.

19 D. Wirthl, R. Pichler, M. Drack, G. Kettlguber, R. Moser, R. Gerstmayr, F. Hartmann, E. Bradt, R. Kaltseis, C. M. Siket, S. E. Schausberger, S. Hild, S. Bauer, and M. Kaltenbrunner, "Engineering instant tough bonding of hydrogels for soft machines and electronics," *Sci. Adv.*, vol. 3, no. June, pp. 1–10, 2017, doi: 10.1126/sciadv.1700053.

20 Z. Suo, E. Y. Ma, H. Gleskova, and S. Wagner, "Mechanics of rollable and foldable film-on-foil electronics," *Appl. Phys. Lett.*, vol. 74, no. 8, pp. 1177–1179, 1999, doi: 10.1063/1.123478.

21 P. Mei, B. Krusor, D. E. Schwartz, T. N. Ng, G. Daniel, S. Ready, and G. L. Whiting,

"Digital Fabrication and Integrationof a Flexible Wireless Sensing Device," *IEEE Sens. J.*, vol. 17, no. 21, pp. 7114–7122, 2017.

22 R. J. M. Wolfs, F. P. Bos, E. C. F. Van Strien, and T. A. M. Salet, "A real-time height measurement and feedback system for 3D concrete printing," in *High Tech Concrete: Where Technology and Engineering Meet - Proceedings of the 2017 fib Symposium*, 2017, pp. 2474–2483. doi: 10.1007/978-3-319-59471-2_282.

23 S. Jadhav, V. Kannanda, B. Kang, M. T. Tolley, and J. P. Schulze, "Soft robotic glove for kinesthetic haptic feedback in virtual reality environments," pp. 19–24, 2017.

24 B. W. K. Ang and C. H. Yeow, "Print-it-Yourself (PIY) glove: A fully 3D printed soft robotic hand rehabilitative and assistive exoskeleton for stroke patients," *IEEE Int. Conf. Intell. Robot. Syst.*, vol. Sep, pp. 1219–1223, 2017, doi: 10.1109/IROS.2017.8202295.

25 N. Besse, S. Rosset, J. J. Zarate, and H. Shea, "Flexible Active Skin : Large Reconfigurable Arrays of Individually Addressed Shape Memory Polymer Actuators," vol. 1700102, pp. 1–8, 2017, doi: 10.1002/admt.201700102.

26 L. Liu, B. Geng, S. M. Sayed, B. Lin, P. Keller, X. Zhang, Y. Sun, and H. Yang, "Single-layer dual-phase nematic elastomer films with bending, accordion-folding, curling and buckling motions," pp. 1844–1847, 2017, doi: 10.1039/c6cc08976c.

27 C. M. Yakacki, M. Saed, D. P. Nair, T. Gong, S. M. Reed, and C. N. Bowman, "Tailorable and programmable liquid-crystalline elastomers using a two-stage thiol-acrylate reaction," *RSC Adv.*, vol. 5, no. 25, pp. 18997–19001, 2015, doi: 10.1039/c5ra01039j.

28 E. C. Davidson, A. Kotikian, S. Li, J. Aizenberg, and J. A. Lewis, "3D Printable and Reconfigurable Liquid Crystal Elastomers with Light-Induced Shape Memory via Dynamic Bond Exchange," *Adv. Mater.*, vol. 1905682, pp. 1–6, 2019, doi: 10.1002/adma.201905682.

29 J. J. Zárate and H. Shea, "Using pot-magnets to enable stable and scalable electromagnetic tactile displays," *IEEE Trans. Haptics*, vol. 10, no. 1, pp. 106–112, 2017, doi: 10.1109/TOH.2016.2591951.

30 J. H. Pikul, S. Li, H. Bai, R. T. Hanlon, I. Cohen, and R. F. Shepherd, "Stretchable surfaces with programmable 3D texture morphing for synthetic camouflaging skins," *Science (80-.).*, vol. 358, no. 6360, pp. 210–214, 2017, doi: 10.1126/science.aan5627.

31 G. Cai, J. H. Ciou, Y. Liu, Y. Jiang, and P. S. Lee, "Leaf-inspired multiresponsive MXene-based actuator for programmable smart devices," *Sci. Adv.*, vol. 5, no. 7, p. eaaw7956, 2019,

doi: 10.1126/sciadv.aaw7956.

32 U. Kim, J. Kang, C. Lee, H. Y. Kwon, S. Hwang, H. Moon, J. C. Koo, J. Do Nam, B. H. Hong, J. B. Choi, and H. R. Choi, "A transparent and stretchable graphene-based actuator for tactile display," *Nanotechnology*, vol. 24, no. 14, p. 145501, 2013, doi: 10.1088/0957-4484/24/14/145501.

33 F. Chen and D. Yuan Lei, "Experimental Realization of Extreme Heat Flux Concentration with Easy-to-Make Thermal Metamaterials," *Sci. Rep.*, vol. 5, no. March, p. 11552, 2015, doi: 10.1038/srep11552.

34 Z. Ma and P. Ben-Tzvi, "Design and Optimization of a Five-Finger Haptic Glove Mechanism," *J. Mech. Robot.*, vol. 7, no. 4, p. 041008, 2014, doi: 10.1115/1.4029437.

35 R. Hinchet, V. Vechev, H. Shea, and O. Hilliges, "DextrES : Wearable Haptic Feedback for Grasping in VR via a Thin Form-Factor Electrostatic Brake," 2018.

36 C. W. Carpenter, S. T. M. Tan, C. Keef, K. Skelil, M. Malinao, D. Rodriquez, M. A. Alkhadra, J. Ramírez, and D. J. Lipomi, "Healable thermoplastic for kinesthetic feedback in wearable haptic devices," *Sensors Actuators A Phys.*, vol. 288, pp. 79–85, 2019.

37 S. W. Ula, N. A. Traugutt, R. H. Volpe, R. R. Patel, K. Yu, and C. M. Yakacki, "Liquid crystal elastomers: An introduction and review of emerging technologies," *Liq. Cryst. Rev.*, vol. 6, no. 1, pp. 78–107, 2018, doi: 10.1080/21680396.2018.1530155.

38 M. O. Saed, C. P. Ambulo, H. Kim, R. De, V. Raval, K. Searles, D. A. Siddiqui, J. M. O. Cue, M. C. Stefan, M. R. Shankar, and T. H. Ware, "Molecularly-Engineered, 4D-Printed Liquid Crystal Elastomer Actuators," *Adv. Funct. Mater.*, vol. 29, no. 3, pp. 1–9, 2019, doi: 10.1002/adfm.201806412.

39 "http://ndeaa.jpl.nasa. gov/nasa-nde/lommas/eap/actuators-comp.pdf."

40 F. Hu, Y. Xue, J. Xu, and B. Lu, "PEDOT-Based Conducting Polymer Actuators," vol. 6, no. November, pp. 1–17, 2019, doi: 10.3389/frobt.2019.00114.

41 M. Camacho-Lopez, H. Finkelmann, P. Palffy-Muhoray, and M. Shelley, "Fast liquid-crystal elastomer swims into the dark," Nat. Mater., vol. 3, no. 5, pp. 307–310, 2004, doi: 10.1038/nmat1118.

Chapter 4

Self-Sustained Robots Based on Functionally Graded Elastomeric Actuators Carrying up to 22 Times their Body Weight

4.1 Abstract

A biomimetic strategy of combining soft actuators with an exoskeleton was applied to create untethered, self-sustained robots with high load capacity, applicable for transportation in unsupervised environments. The soft actuation components were based on liquid crystal elastomers formed into functionally graded structures by extrusion printing, which enabled a high free strain of 45.5%. The robot design included a self-sustained oscillation mechanism incorporating a novel, highly elastic spring for energy storage and impulse release. The arthropod-inspired exoskeleton structures were printed from polycarbonate with high strength to increase load-carrying capacity, or to increase moving speed by a lever mechanism that amplifies stepping distance up to 8 times. The robot achieved self-sustained locomotion, harvesting constant infrared radiation for continual power. Leveraging the strength of exoskeleton and the high stress of the actuator, the robot transported a load 22 times of its body weight. It was capable of climbing up a slope of 40 degrees and moving up to a quarter of its body length per minute with peripheral lever legs. The robot operation did not require external signaling controls or complex electronics, demonstrating the potential of this battery-free, scalable, environment-powered design with an unlimited range free from tethering constraints.

4.2 Introduction

Untethered robots that acquire energy from the ambient to produce self-sustained movement can open new avenues for realizing autonomous transporters with unlimited range. Currently many untethered robots rely on batteries [1]–[4] with limited capacities; others are wirelessly controlled by a nearby magnetic field [5]–[9] or light stimuli [10]–[16], but the robots must stay within the range of controlling signals in order to be powered. There are emerging research to generate sustained motion that does not depend on intermittent switching of external stimuli, so that the robots can harness constant environmental energy and convert it to generate locomotion free of distance constraints. Stimuli-responsive polymers such as hydrogels [17], [18] and liquid crystal elastomers [12] have been used in designs with oscillatory feedback loops, such as self-shadowing [18]–[20] or ratchet [17] mechanisms, to produce bursts of kinetic energy for propulsion. While these ingenious designs have led to self-sustained movement, the polymer robots are limited in their load-carrying capability. The soft robots are deformed by the load, and so far they can only carry loads within the same order as their own body weights [1], [14], [21]–[25], restricting their applications as transporters.

In this report, a biomimetic strategy of combining soft actuators with an exoskeleton is applied to create self-sustained robots with high load capacity. In the natural world, arthropods like leaf-cutter ants develop exoskeletons that enable them to carry loads exceeding their body weights by hundreds of times [26]. The exoskeleton provides strong supporting structures for the soft muscles to withstand the extra pressure from heavy loads. The actuating muscles are not encumbered by the weight of an internal skeletal system and can apply most of their output forces to lifting external objects. This work used heat-responsive liquid crystal elastomers (LCE) as actuating components [27]–[29]. The thermal actuation mechanism of LCE is advantageous for developing heat harvesting schemes to mimic another aspect of arthropods, in that cold-blooded insects absorb sunlight and leverage the heat to warm up for activities. Here we present design principles that harness thermal changes in LCE materials to drive an oscillating ratchet, to continually power exoskeleton robots without range limitations and demonstrate an autonomous transporter capable of carrying payloads much heavier than its own weight.

We fabricated the robots by extrusion printing [30]–[33], in which the hard components are made of polycarbonate with high strength, and the soft actuators are based on LCE with properties tuned by printing parameters. The direct printing process enables the fabrication of functionally graded structures, in particular to engineer new system-level functions beyond the bulk mechanics of component materials. Previous works have adjusted the shear stress during printing to tailor LCE mesogen alignment [30]–[32] and demonstrate free-form deformations. However, the power output of LCE actuators is hampered by the long transition time between actuation and relaxation. To accelerate LCE movement, we introduce a novel design of printed LCE springs to store and release energy in cooperation with the LCE actuator. The printed spring offers tunable elastic modulus, larger tensile breaking strength, and higher restoring force than poly-domain elastomers. This new spring component greatly expands the design space for LCE actuation, so we can realize self-oscillation in LCE systems and facilitate continuous operation similar to engine cycles. In addition to the spring and ratchet mechanism, we include a lever amplifier to increase the stepping distance in a robot stride. The robot is characterized on various hill grades, tested for its load-carrying limits, and demonstrated self-sustained locomotion under sunlight, to show the potential of this battery-free, scalable design for environment-powered actuators.

4.3 Results

4.3.1 Programming LCE mechanical properties by adjusting toolpath and shear stress

For our bioinspired robot, the artificial muscle is based on a LCE structure with two segments, one being a conventional mono-domain actuator and the other functioning as a spring. In the LCE actuator, the liquid crystal mesogens are set in alignment at room temperature. When the actuator slab is heated, the alignment is disrupted by thermal motion. The slab becomes isotropic and contracts in length as illustrated in Figure 4.1(a). The contraction is reversible; when cooled, the LCE recovers to its original shape at room temperature.

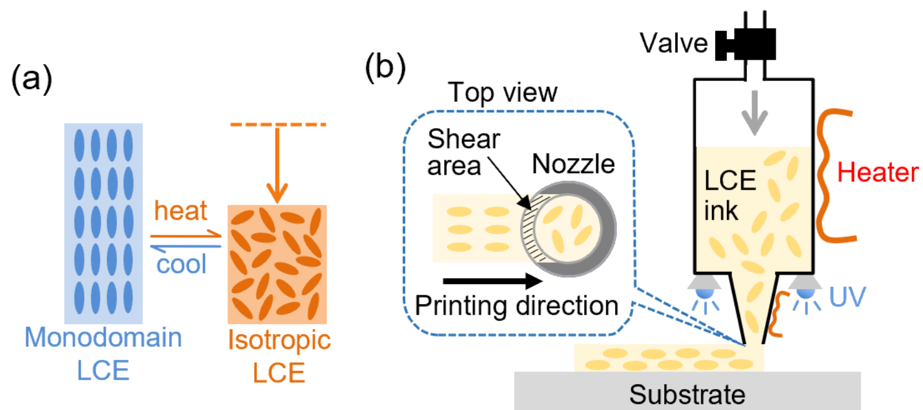

Figure 4.1: Actuation mechanism of LCE and printing setup. (a) Thermal actuation mechanism of LCE. (b) Extrusion printing to align LCE mesogens. The inset shows the area where the nozzle applied shearing force to the extruding LCE.

A common technique for aligning the mesogens is by applying a shear force on the ink during the extrusion process. Prior works showed that inside a printing nozzle, due to the difference in flow velocities at the center and around the rim, the LCE ink was sheared in a tubular distribution, resulting in better mesogen alignment in the outer shell while the inner core remained isotropic [30], [31]. To avoid uneven alignment in a filament, we modified our printing process to reduce the distance between the nozzle tip and the deposition surface, keeping the distance less than half of the inner diameter of the nozzle. As such, the extruded material was squashed by the nozzle edge as indicated by Figure 4.1(b). The moving nozzle applied a shear force parallel to the printing direction, and the shear stress generated in the LCE materials was adjusted by tuning the ink flow rate and deposition layer height. In general, faster flow rates and thinner layer heights led to a higher shear stress.

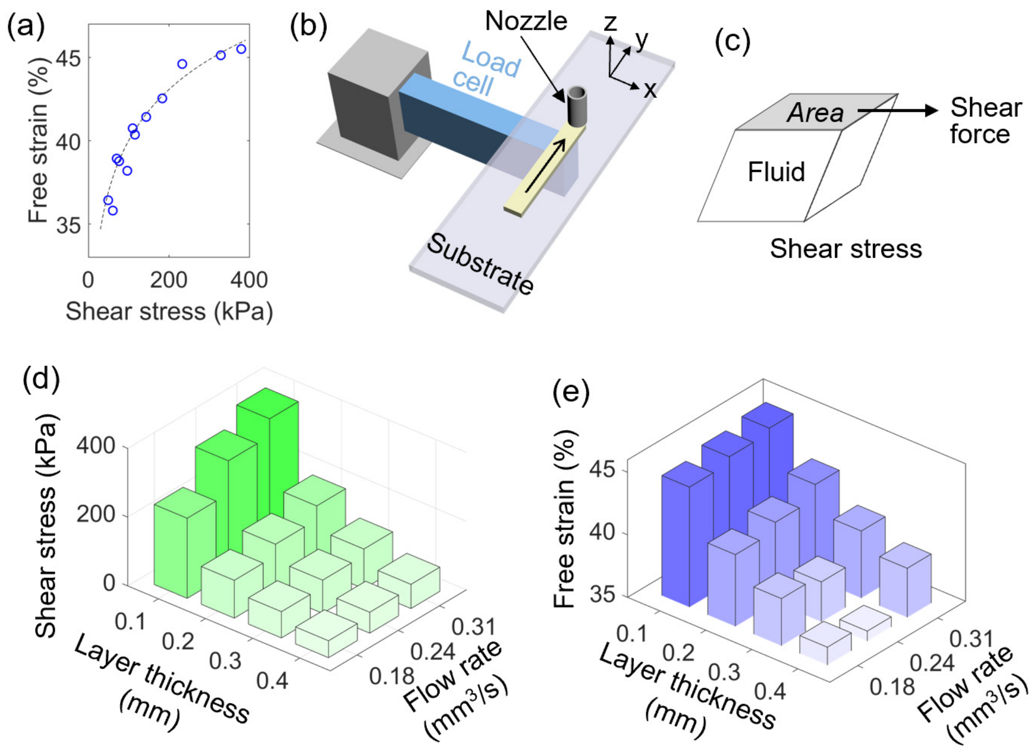

Figure 4.2: The relationships of shear stress as a function of printing parameters. (a) Free strain of LCE actuators when heated from 30°C to 130°C, as a function of shear stress at the nozzle. (b) Setup to track shear force. (c) Shear stress illustration. (d) Average shear stress during printing and (e) the resulting free strain at 100°C (right) of the LCE samples with different thicknesses and flow rates in each printing pass.

The setup in Figure 4.2(b) was used to measure the force during printing. When the nozzle printed a trace on y direction, the horizontal force applied on the trace from the nozzle was tracked by the load cell that supported the substrate. We carried out the following procedure to characterize the effect of printing parameters on the extrusion shear stress and on the LCE strain.

The supplied air pressure was tuned to 90 psi, 70 psi and 50 psi to achieve three different extrusion flow rates 0.31, 0.24 and 0.18 mm^3/s. With each flow rate, four LCE slabs were printed with single layer thicknesses of 0.1, 0.2, 0.3 and 0.4 mm respectively. The samples were printed with multiple passes to prevent a slab from curling and warping itself when it was too thin. During printing, a load cell was used to track the shear force. Then the shear stress τ was calculated by the relationship $\tau = \frac{Shear\ force}{Shear\ area}$ as shown in Figure 4.2(c), where the shear area was explained in Figure 4.1(b). The resulted shear stresses of the 12 samples were plotted in Figure 4.2(d). The free strain of each sample was characterized by taking photographs of the sample with a ruler on the side, and the lengths measured in pixels were converted to millimeters on the ruler scale. The results were shown in Figure 4.2(e). With the acquired data of shear stress during printing process and free strain of the samples, the relationship was plotted in Figure 4.2(a).

The actuators printed under increasing shear stress showed larger free strain (deformation with no load). Free strain is defined as $\sigma = (L_0 - L)/L_0$, where L_0 is the original length at room temperature and L is the final length at the actuation temperature. The dependence of free strain on printing shear stress can be empirically fitted to a logarithmic function, indicated by the dashed line in Figure 4.2(a). The function is $\sigma = 0.044\ \ln(\tau/\tau_0) + 0.197$, where τ is the shear stress and τ_0= 1 Pa is a reference value to balance the unit. With our extrusion technique, the actuator reached a maximum free strain of 45.5%, which is higher than the state-of-the-art performance for LCE [2], [30], [31].

The actuator was printed with a toolpath of parallel in-fills and designed to exhibit high contraction force and strain. However, it was limited by a slow cooling process to return to its original length. Thus, we created a spring segment which applied tension on the actuator to accelerate its recovery. There were two requirements for the LCE spring: 1) the spring dimensions should be less affected by temperature when compared to the actuator; 2) considering that the spring would be subjected to large stretching strain, it must tolerate high tensile strains before reaching the breaking point and also a high elastic modulus to store and release potential energy. We note that a poly-domain LCE, in which mesogens are not aligned, would meet the first condition, but it shows low elastic modulus and high dissipation, resulting in low elastic force and low energy storage efficiency, insufficient for our purpose of cycling the actuator back to its original position. Another option is to look for different elastomers with the desired elasticity, but here we use engineering strategies [30]–[32], [34]–[38] to tune the mechanical properties and increase the material versatility.

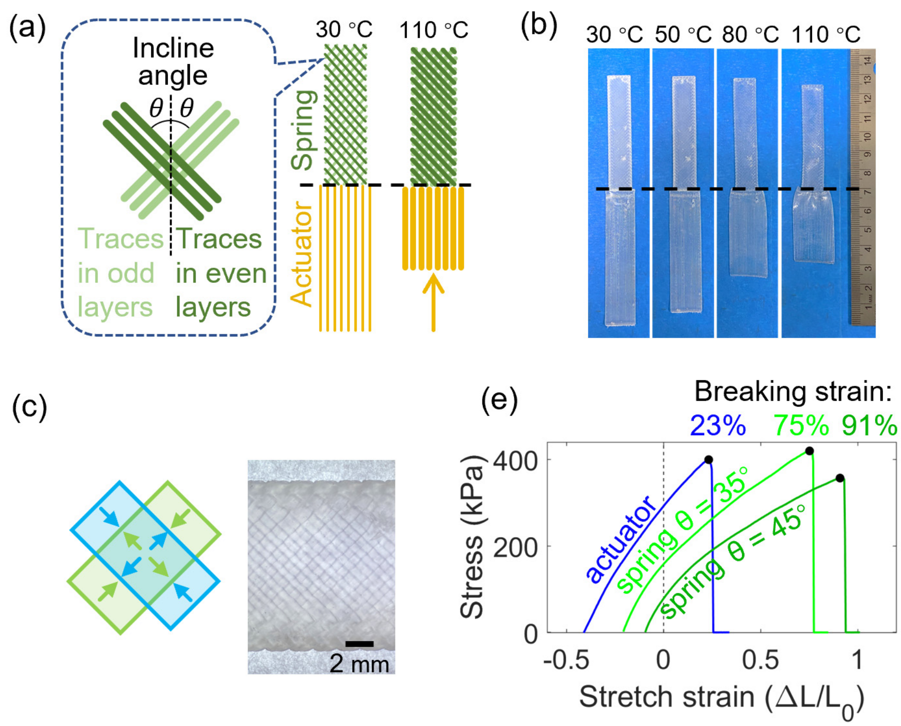

Figure 4.3: Schematics and characteristics of printed LCE actuator and spring. (a) Schematics of the printed LCE actuator and spring segments. (b)The photographs contrast the dimensional changes at different temperatures, in which the spring showed minimal strain while the actuator contracted to 45% strain. (c) Photograph of the LCE spring metastructure, and a diagram of force vectors to explain how contraction and extension were canceled out. (d) Stress-strain measurements taken at 100°C, comparing the actuator versus springs with different infill angles. The strain of 0% corresponds to the original length at room temperature.

To make a high-performance spring from LCE, we changed the printing toolpath and directed mesogen alignment to follow the incline pattern as illustrated in Figure 4.3(a). While the incline direction was the same in each layer, the direction alternated between odd and even layers, with a symmetric incline angle θ. With this meta-structure, the dimensional changes in response to heat was suppressed in the spring. When the spring was heated, the tendency for one layer to contract was offset by the pulling forces from the neighboring layers and vice versa, as visualized by the force vector diagram in Figure 4.3(c). The result was that this new spring design decoupled the thermal actuation behavior from being an inherent characteristic in mono-domain LCE structures. The printed spring was made less sensitive to heat and showed much lower contraction strain than the actuator, evident in the photographs of Figure 4.3(b), while keeping the advantage of high elasticity in mono-domain LCE.

Figure 4.1(d) compares the stress-strain characteristics of an actuator and two different springs with incline angles of 35° and 45°. The x-intercepts (negative values) indicate the free strain values measured at 100°C. Thermal actuation was reduced with an increasing incline angle in the spring, suppressed to a minimum of 10% strain at θ = 45°. In Figure 4.1(d), the black dots right before abrupt drops in stress denote the breaking stress and strain. The breaking stress of LCE actuator and springs were similar, in the range of 400 kPa. Yet the actuator broke at low tensile strain (23%), because of its thermally activated contraction which placed additional countering force to the applied tensile strain. In contrast, the spring did not have this countering force and was able to tolerate more stretching. The springs could be stretched at least 3 times longer than the actuator before breaking, and this elastic property would be an important characteristic to achieve the oscillatory mechanism for self-sustained locomotion in the following work.

4.3.2 Mechanisms to enable self-sustained locomotion

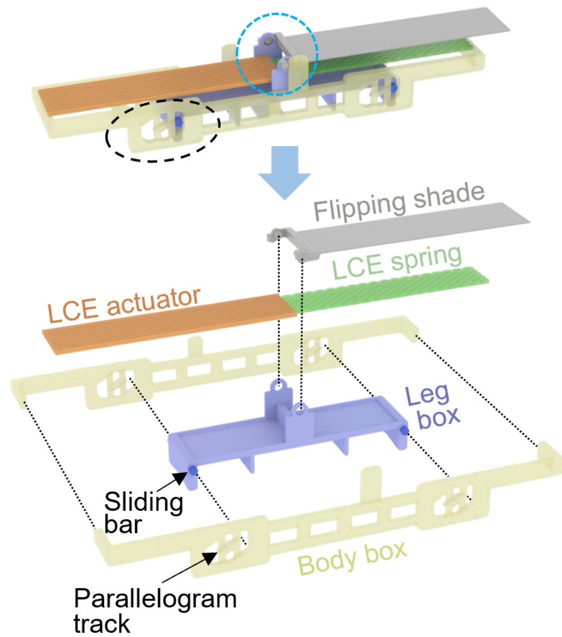

Figure 4.4: Assembly schematics and an exploded view of the printed robot. The black circle marks one of the four identical movement tracks, and the blue circle indicates the two shade hinges.

In this work, the goal was to demonstrate a self-oscillatory design that generates continual locomotion under infrared light. Figure 4.4 shows the robot structure consisting of soft LCE actuator+spring (artificial muscle) and hard polycarbonate components (exoskeleton). The key dimensions of the robot are listed in Appendix Table B.1. There were three hard components: a leg box, a body box and a flipping shade fixed at the center of the leg box through a hinge. The shade was intended to rotate between the work and return stroke, so that it would switch shading for either the spring or the actuator. At the four corners of the leg box, there were four protruding cylindrical sliding bars, drawn as a circle attached to the leg in Figure 2(b). The sliding bars on the leg box were inserted into the parallelogram tracks in the body box. Therefore, the leg box was constrained to slide around the parallelogram. The LCE actuator+spring connected the leg box to the body box. The contractive force from either the actuator or the spring would drive the relative movement between the leg box and body box.

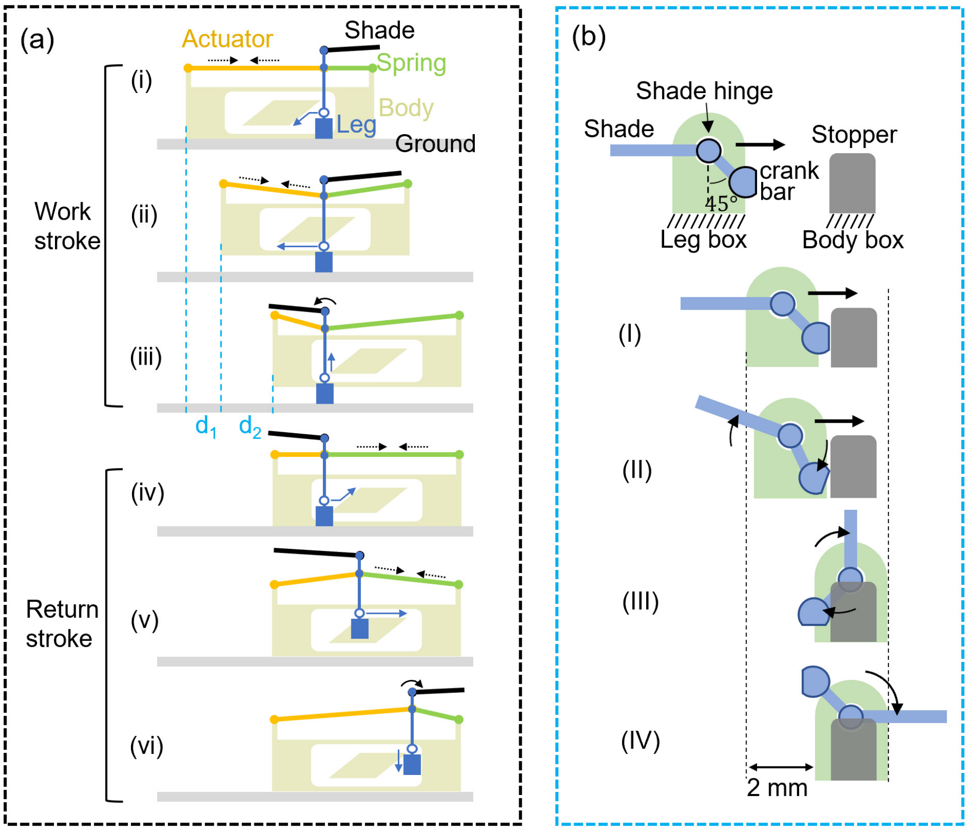

Figure 4.5: Flow charts of motion processes. (a) Flow chart of the steps in one motion cycle. (b) Flow chart of the shade flipping mechanism.

A flow chart of the movement cycle is shown in Figure 4.5(a), which zooms in on the operation at one of the four identical parallelogram tracks. Step (i) shows the standby state of the robot, in which there was minimal tension in both the actuator and the spring. The shade hovered over the spring segment, and the actuator was uncovered. If light was shone on the entire robot, the robot would proceed to step (ii) in which the actuator absorbed heat, consequently contracting and pulling to lift the body box from the ground and concurrently move the body horizontally. Between steps (i) and (ii), the horizontal moving distance of the body box was d1, defined by the parallelogram dimensions. The exposed actuator kept absorbing light energy and contracted further, pulling the sliding bar across the bottom edge of the parallelogram track. Between steps (ii) and (iii), the body box was translated farther to the right by a distance d2. The shade flipping mechanism was triggered by the movement sequence and automatically turn the shade to cover the actuator. In step (iii), the body box would drop down to contact the ground again, since the sliding bar has moved to the top edge of the parallelogram track. Steps (i) to (iii) constitute the work stroke, in which the actuator converted the absorbed heat to mechanical energy to move the body box. Meanwhile, a portion of mechanical energy is stored in the stretched spring.

Following the work stroke, steps (iv) to (vi) were carried out to complete the return stroke. The movement around the parallelogram track is similar to a ratchet. As the shaded actuator cooled down, the tension in the stretched spring pulled on the actuator to return it to its initial length. Under the spring force, the sliding bar of the leg box was guided to move right and up the parallelogram track, and the leg box is lifted above the ground in step (iv). In step (v), the sliding bar traveled across the top edge of the parallelogram, and the leg box moved to the right as driven by the spring. The shade automatically switched to the cover the spring. In step (vi), the sliding bar moved to the position where it was no longer supported by the parallelogram ledge, and the leg box dropped down onto the ground by gravity. At this moment, the robot finished one whole movement cycle and would be ready for another cycle. The total locomotion distance in one cycle was $d_1 + d_2$, traveled during the work stroke.

At the end of steps (ii) and (v), the shade should automatically flip to the opposite side in order to modulate the heating and cooling of the LCE, so that despite constant irradiation there would be oscillating actuations to transition between strokes and enable self-sustained, unsupervised movement cycles. We implemented hinges that switched the shade position according to the relative movement between the body and leg boxes, as detailed in Figure 4.5(b).

The shade hinge was attached to the center of the leg box, and there were two crank bars, one on each side of the shade. In the schematic only one side was shown, but the other side worked in a similar fashion to flip the shade in the opposite direction. The crank bar was trimmed to have a flat edge, and its position was dictated by the leg box. The crank bar would work in conjunction with the rectangular stopper attached to the body box. As the leg box carried the crank bar towards the stopper, the two structures came into contact, but the interface friction stopped movement (step I). Then, the LCE contraction continued and built up elastic energy, which eventually exceeded the threshold to overcome friction and pushed the shade and crank bar to rotate (step II). Since the friction on the arc of the crank bar was much smaller than on the flat edge, the stored elastic energy was released instantaneously, inducing an impulse force to rapidly erect the shade arm (step III). Following through due to its own rotary inertia and gravity, the shade would complete the 180° rotation, as shown in step IV.

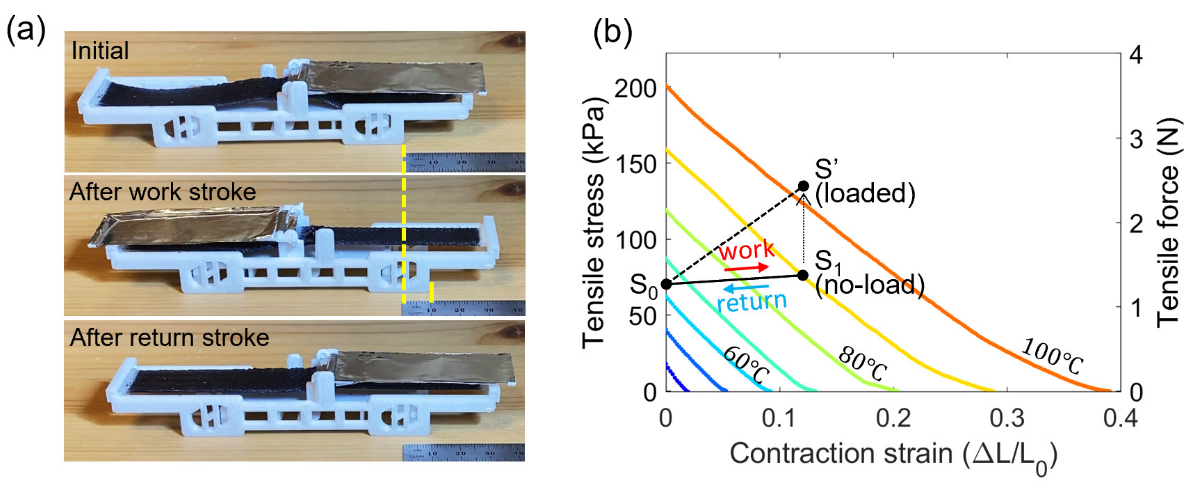

Figure 4.6: Motion cycle and energy transfer. (a) Photographs of one motion cycle. (b) Output stress–strain characteristics of the LCE actuator at different temperatures, in steps of 10 °C. The initial and actuated states of the actuator are marked as S_0 and S_1, respectively. When the robot carried a load, the actuated state changed to S'.

The photographs in Figure 4.6(a) captured the robot locomotion in one movement cycle. Under a broadband light at an intensity around 220 mW/cm^2, the robot moved about 10 mm during the work stroke, and the shade was flipped from the spring side to cover the actuator. For the 10 mm travel distance, the robot step was 8.6 mm, while an additional 1.4 mm slide was observed due to the forward launching momentum. During the return stroke, while the body box did not move, the leg box returned to the original position with respect to the body box, and the shade turned back to the spring side.

Figure 4.6(b) shows the stress-strain characteristics of the LCE actuator at different temperatures. The measurements were taken in the active output region of the actuator, thus showing only contraction strain. The blocked stress is 200 kPa at 100°C, and the blocked force of this actuator is 3.6 N. In a movement cycle, the starting state was marked as S0, corresponding to 65°C temperature and 0% strain. At the end of a work stroke, the actuator was fully actuated, marked as state S1 in the plot, corresponding to 90°C and 12.6% strain, as recorded by infrared camera and length measurements. The state of the actuator transitioned between S0 and S1, and the temperature changed between 65°C and 90°C. In the return stroke, the actuator under the shade did not need to be cooled down to room temperature. When the robot was loaded with cargo, the actuator force output must increase to lift and translate the extra payload. As a result, the actuated state shifted upwards to state S', in which the strain was still 12.6%, but the required actuation temperature and stress were increased.

4.3.3 Slope climbing test

Our robot exhibited high traction force due to the high output stress of LCE, and the LCE-exoskeleton combination offered unique capabilities for climbing steep slopes and carrying heavy payloads. Figure 4.7 demonstrates our robot climbing up a slope of 40°. After 10 successive cycles, the robot moved a distance of 70 mm, with an average step of 7 mm. This distance was shorter than the stepping distance on a flat surface, because instead of dropping straight down, the body box fell slightly backward due to the pitch angle during step (iii) of the movement cycle in Figure 4.5(a). In the example in Figure 4.7(a), the surface of the slope was coated with polydimethylsiloxane (PDMS) to prevent sliding. Nonetheless, similar climbing performance can be achieved by putting sandpaper or PDMS on the bottom surface of the robot to increase contact friction with the ground. We observed that 40° was the maximum angle that the robot could climb. For the current design, the shade rotation mechanism worked against gravity and was stuck at step (v) when the pitch angle was higher than 40°. This limit of 40° slope corresponds to a percentage grade of 83.9%. As a comparison, most common wheeled vehicles are not able to climb a slope of this grade, and the steepest paved roads are below 20°.

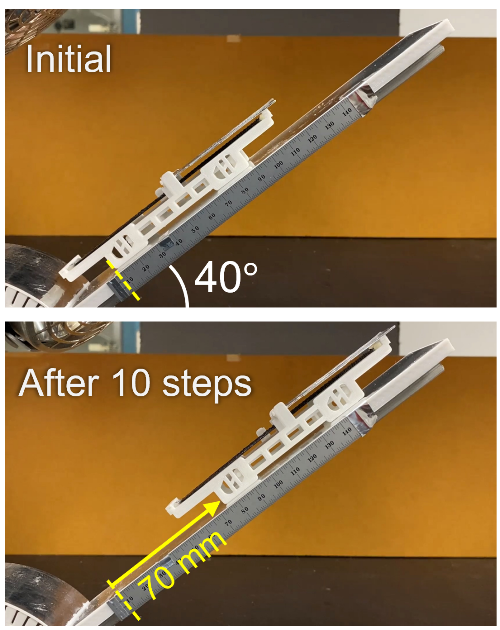

Figure 4.7: Demonstration of robot climbing a 40-degree slope.

4.3.4 Load-carrying test

The robot is already shown to be capable of carrying the solar reflector (32 g), and we further characterized its load-carrying capacity in Figure 4.8(a). The robot was able to transport a maximum mass of 311.7 g, while its body mass was 13.95 g, which accounted for the entire structure of LCE (2.51 g) and exoskeleton (11.44 g). The load-carrying ratio was 22.3 times. Under the maximum load, it traveled 10 mm per movement cycle. The load-carrying ratios of various robot designs based on soft actuators are displayed in Figure 4.8(b). The comparison included driving mechanisms using LCE [14], [15], dielectric elastomers [1], [25], magnetic elastomers [6], piezoelectric polymers [23], and pneumatically powered polymeric structures [3], [21], [22]. Here our LCE self-sustained robot showed higher load-carrying capacity than the other robots with similar body weights, demonstrating the potential of hybrid LCE-exoskeleton structures in overcoming prior load limits of LCE robots.

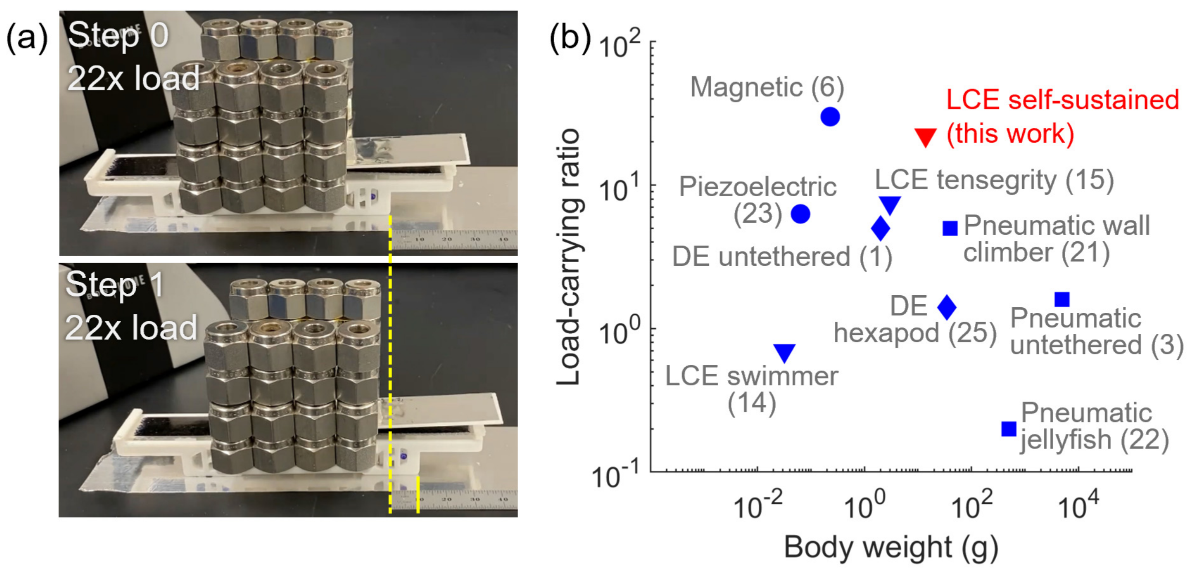

Figure 4.8: Load-carrying demonstration and comparison with other works. (a)Robot transporting a load 22 times of its body weight. (d) Comparison of load-carrying ratio versus body weight for various robot designs based on soft actuators. DE: dielectric elastomer. The numbers correspond to the listings in the Reference section.

4.3.5 Sunlight-powered locomotion

As our robot harvested infrared radiation to power the actuation cycles, we aimed to make it move with energy input only from natural sunlight, so to demonstrate the feasibility of running the robot autonomously for outdoor transportation. For indoor environments, high light power could be directed over the robot’s track, but for the outdoors, our local sunlight irradiance was measured as only ~45 mW/ cm^2 on the ground level and not powerful enough to drive the robot. Hence, we attached a set of solar reflectors on the robot to concentrate more light on the LCE region. The schematic design and photograph are shown in Figure 4.9 (a) and (b) respectively. The reflector set was designed for a solar elevation angle of 35° and concentrated the sunlight power shone on the LCE area by seven times, leading to an irradiance ~315 mW/cm^2 on the robot.

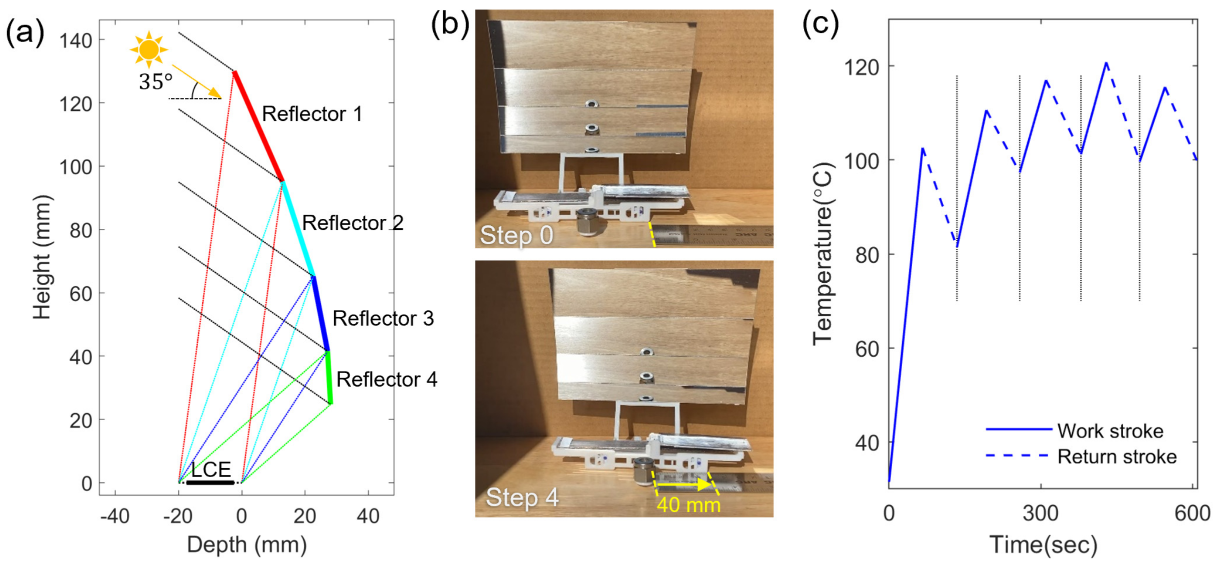

Figure 4.9: Sunlight-powered locomotion test. (a) Cross-sectional schematic of the solar reflectors. (b) Demonstration of the robot moving under outdoor sunlight. (c) Temperature changes of the actuator segment over five successive movement cycles.

With an infrared camera, the temperature of the LCE actuator was measured at the start and end time points of every stroke, as plotted in Figure 4.9(c) taken under an irradiance of 330 mW/cm^2. Starting at room temperature in the first cycle, the actuator temperature increased to 100 °C when the work stroke was completed. Then it dropped to 80 °C in the return stroke under the shade. The cycles of heating and cooling continued automatically by the shade-switching mechanism; from the third movement cycle onwards, the operating temperatures were between 100°C and 120°C. The time duration for one cycle was stabilized to 116 seconds on average. The moving speed of the robot was dependent on the light intensity. As a comparison to measurements in Figure 4.6(b) under an input power of 220 mW/cm^2, the time for one cycle was 161 seconds on average, and the temperature changed in the range of 65°C to 90°C. Higher irradiance could power the robot to work at a faster speed, but it also increased the operational temperatures. Since the LCE actuator tended to break due to high blocked stress when temperature was above 120 °C, we limited the light irradiance to below 330 mW/cm^2 to keep the operational temperature below the LCE breaking point.

4.3.6 Insect-inspired modification to amplify the step length

With the above design, the robot stepping distance was just 6% of its body length (or 12.6% of actuator length) in each movement cycle. This travel distance was constrained by the length of the parallelogram track; if the track was made longer with respect to the actuator length, the LCE contraction was insufficient to complete a stroke, and the robot was stuck. However, the LCE actuator had shown high work output to lift and transport very heavy loads compared to its body weight, indicating that there was a large portion of the actuation energy not spent on horizontal locomotion in this design. Therefore, there was room to channel more of the actuation output towards increasing the horizontal travel distance. Below we re-directed part of the actuation energy to drive a lever mechanism that extended the stepping distance, so the robot could travel farther in each movement cycle.

Inspired by insects that use long legs to move their light and small bodies, we designed an attachment with four lever legs to fit onto the robot for extending its step length. The schematics and photograph of the attachment structure are shown in Figures 4.10(a) and 4.10(b), respectively. The four lever legs were connected to the robot leg box through hinges and extended out through slots in the attachment body box, with its ledges serving as fulcrums of the lever legs. In the work stroke, as the actuator pulled the leg box towards the body box, the actuation motion simultaneously lifted up the robot body and propelled it forward, similar to the motion step (i) shown in Figure 4.5(a). Here the endpoints of lever legs provided the four contact points to the ground as seen in Figures 4.10(a). In the return stoke, the robot rested on the attachment box, and then the lever legs were lifted to return to a starting position, ready for a new cycle. This return motion avoided dragging the body backward.

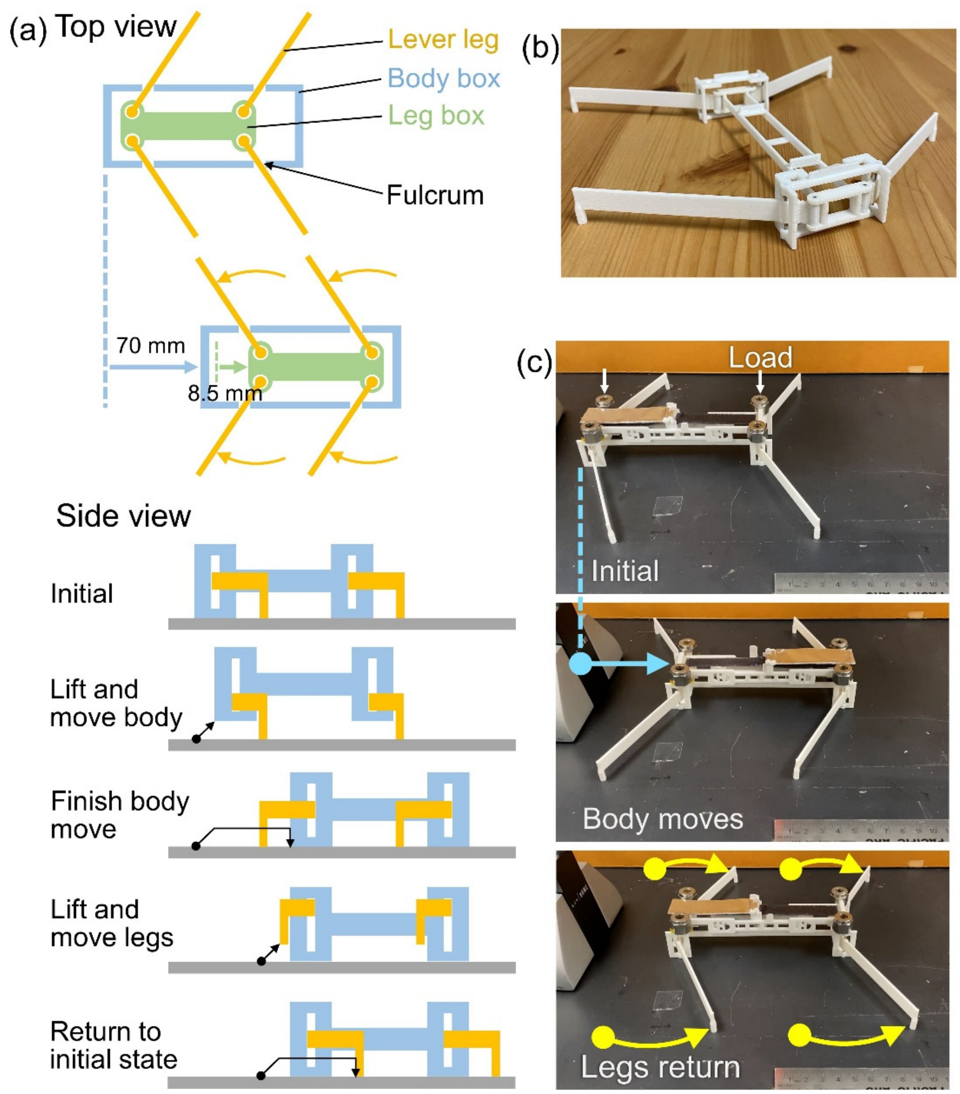

Figure 4.10: Insect-inspired locomotion. (a) Schematics of the robot equipped with lever legs to amplify the stepping distance. Top view and side view. (b) Photograph of the lever attachment. (c) Photograph of the movement sequence.

For each lever leg, the length ratio of the segments on the two sides of the fulcrum was 1:8.2, with the short segment inside and the long segment outside of the body box. By lever action, a displacement of the short segment would result in an amplified displacement of the long segment proportional to the length-ratio factor. Hence, the small 8.6 mm step in the original robot design was amplified by 8.2 times by the lever legs, for the modified robot to traverse 70 mm per step. Figure 4.10(c) shows the locomotion of the modified robot, carrying a load equal to its body mass while advancing roughly a quarter of its body length per minute.

4.4 Discussions

This work demonstrated three new concepts for LCE actuation: 1. the design of a self-sustained oscillation mechanism to store and release energy from a constant input; 2. the decoupling of mechanical properties from thermal response by tuning print toolpaths to fabricate novel, highly elastic spring components for energy storage; and 3. the use of exoskeleton structures to increase load-carrying capacity or stepping distance. The improvements in printing toolpaths enabled freeform tuning of the LCE characteristics; the printing process realized an state-of-the-art actuator, reaching a maximum free strain of 45.5% and a blocked stress of 200 kPa at 100°C. By adapting the toolpaths, the same LCE material was fabricated into a highly elastic spring with a breaking strain of 91%.

In the robot design, the exoskeleton enables both self-oscillating movements and load-supporting functions. Our robot operation did not require external signaling controls or complex electronics. Under a constant light input, the robot achieved self-sustained cycles like a heat engine, absorbing heat from light energy to do work. The features of self-sustained locomotion and high load-carrying capability show the potential for this robot design to be used for transportation in unsupervised environments. The robot is scalable in size and can be modified to increase the load capacity or moving speed by using peripheral structures such as the lever legs.

To enable repetitive oscillations, our robot used an energy storage spring to restore the actuator position after contraction, and the crank design allowed the generation of impulse energy for rapid rotation of the flipping shade. The straight chord on the hinge crank bar served as a frictional barrier to build up tension stress and store more energy before the rotation mechanism was triggered. When the activation threshold was overcome by the tension, the impulse energy released led to rapid complete rotation, so the work stroke would not be stuck when the shade is in a mid-way perpendicular state.

One key aspect of our robot was that the two-phase contraction and extension of the LCE actuator were expanded into a six-phase movement cycle through the incorporation of parallelogram tracks. The track divided the cyclic movements of the sliding bar into two different paths in the work and return strokes, so that the locomotion was in uni-directional. Such cyclic designs are commonly found in retractable pens and self-lock buttons, in which the sequential pressing and releasing of a button moved in divided paths. While such structures ensured automated cycles, part of the energy was traded off between lifting movement and forward movement of our robot.

In a movement cycle, the work of the LCE actuator was consumed in two parts, by (i) the frictional heat between components and (ii) gravitational potential energy of lifting body or leg box. Especially when the robot was heavily loaded, a large amount of potential energy was required to lift the body box. This component of energy was consumed in up and down displacement and not used for forward movement. Therefore, reducing the lift distance would be a design consideration to reduce unnecessary energy consumption and increase the load-carrying ability. The lift distance Δh was determined from $\Delta h = (H + D)/2$, where in our demonstration, H= 3 mm was the height of the parallelogram stub, D=2.5 mm was the diameter of the sliding bar, and therefore Δh=2.75 mm was the lift distance in each cycle. To reduce the energy spent on lift movement, both H and D should be reduced. However, in the current proof-of-concept design, the feature size was limited by the resolution of FDM printing; also the strength of smaller stubs for the parallelogram and sliding bar was not enough to support heavy loads. Hence to advance performance in the future, other high-precision printing methods such as stereolithography and high-strength materials for the exoskeleton can be used to scale down robots and enable very high load-carrying ratios.

In addition, it is possible to increase the robot speed. Currently the locomotion speed is limited by the heat absorption and dissipation time. As the heating and cooling processes are both related to surface areas, one design strategy is to reduce the total thickness of the LCE layers while increase their widths. As this change will maintain the same cross-sectional area, the robot will keep the same load-carrying ability. With the same heat capacity but a larger surface area, the heat transfer will be faster and the robot movement will be accelerated. Overall, the bioinspired robot in this work offers new elements of self-oscillation and structural modifications to amplify load and step size, and the strategies can be generally applicable to future locomotion robot designs.

4.5 Experimental section

4.5.1 Printing setup

A schematic of our printer is shown in Figure 1(b). It was modified from a Raise3D N2 platform, with the option to use a fused deposition modeling (FDM) nozzle and a pneumatic extrusion nozzle with compressed air supply in the range of 0~90 psi. The air supply was controlled by a dispenser with a pressure regulator and a solenoid valve. The LCE ink was stored in a dispensing syringe and extruded through an 18-gauge needle nozzle. There were heaters for the syringe and the nozzle to increase the temperature of LCE ink, in order to reduce the ink viscosity for smooth extrusion. During printing, a load cell (SEN-14728, 0.5 kgf, Digi-Key) with HX-711 ADC module was used to track the shear force. There were UV light emitting diodes mounted next to the nozzle for cross-linking the workpiece.

4.5.2 Stress-strain characterization

We attached an S-type load cell (DY106-3kg) on a 3D printer frame (prusa i3) to modify it into a programmable tensile force tester. A pair of metal fixtures was used in the tester to hold the samples. The analog feedback value from the load cell was sampled by a HX-711 AD convertor, and the data was read by an Arduino chip. A MATLAB program was used to control the movement of tester and record the force value from Arduino.

The LCE actuator or spring was clamped between the top and bottom fixtures. A 205-Watt infrared heat lamp (Bon Home Culinary Heat Lamp) was used to heat up the sample. The distance between the lamp and sample was tuned to adjust the temperature, which was tracked by a thermal imager (PerfectPrime IR0005). In the measurements, the sample was fixed at the original length. Then the temperature of the sample was controlled to the desired temperatures between 40 °C and 100 °C. When the temperature was stabilized, the readout force was the blocking force. Then the printer frame was controlled to reduce the length of the sample, meanwhile the contraction force was recorded at each length. When the contraction force reduced to zero, it means the sample reached the maximum free strain at that temperature, and one complete curve was measured. The sample was stretched by the frame to its original length, and was heated to another temperature to repeat the process for measurement of the next curve.

4.5.3 Fabrication of the robot

The dimensions of robot components are listed in Appendix Table B.1. The body box, leg box and frame of the flipping shade were printed with 1.75 mm polycarbonate filament (PC-Max) in the FDM mode. The layer thickness was set to 0.2 mm, and the global printing speed was 15 mm/s. The nozzle temperature was 270 ~ 285 °C, and the platform was heated to 110 °C. “Bottom raft” and “support everywhere” settings were used to increase the yield. To avoid wrapping of polycarbonate, the printer was enclosed to minimize air flow. The cooling fans were disabled, and aluminum foils were wrapped around the nozzle to prevent any air blown towards the printed workpiece. After printing, the raft and support structures were removed by pliers. Then the surface was polished by precision files, 320-grit sand papers, and 1000-grit sand papers. Aluminum foils were mounted for the flipping shade to block infrared radiation.

The LCE actuator and spring were printed at 90 psi, with the syringe at 55 °C, the nozzle at 60 °C, and a flow rate of 0.5 mm3/s. In each printing pass, the layer thickness was 0.1 mm, and there were 12 layers in total. The area of the actuator was 68*15 mm2, and the spring was 60*12 mm2 with traces printed in 35° incline angle. The actuator and spring were printed and connected in one piece, but the toolpaths were different in each segment. A 200 mW UV light was used to cross-link LCE during printing. After printing, the sample was cured by 10 W UV light for 5 minutes to fully cross-link. The surface of LCE components was painted black with a marker pen to increase light absorption.

The polycarbonate exoskeleton components were assembled with the LCE actuator+spring into one structure. Using instant adhesive (Loctite 495), the middle of the LCE piece was glued to the center point on the leg box, while the ends of the LCE structure were glued to the ends of the body box.

4.5.4 Light source for powering the robot

A 205-Watt infrared heat lamp (Bon Home Culinary Heat Lamp) was used as light source. The black-body temperature is 530°C, leading to a peak wavelength of ~3.6 μm. The distance between the lamp and the robot was tuned in the range of 8 ~ 13 cm to achieve a light power of 220 ~ 330 mW/cm2. The light power was measured on a piece of brass that was painted black, and we tracked the increase of temperature with a thermal imaging camera (PerfectPrime IR0005). When testing the robot, the temperature of LCE was also measured by the thermal imaging camera.

4.5.5 Slope-climbing test

In the slope climbing test, an adjustable ramp was printed with polycarbonate by FDM. The top surface was covered with a plastic mirror sheet to avoid overheating the plastic pad. The surface of the mirror was coated with polydimethylsiloxane (PDMS, Sylgard 184) to increase traction with the robot. During testing, the slope angle was increased by 5° increments, to find the limit when the robot could not complete a whole movement cycle.

4.5.6 Load-carrying test

Two cargo support plates were printed with polycarbonate and attached to the two sides of the robot with instant adhesive. Metal nuts were added on the cargo plates as loads. The weight of each nut was 9.7 g.

4.5.7 Sunlight reflector attachment

The supporting frame of the reflectors was printed with polylactic acid filaments by FDM. Plastic mirrors were attached on the frame with instant adhesive. The frame and a balancing weight were attached on two sides of the robot. The demonstration of robot locomotion powered by sunlight was carried out at noon, and the solar elevation angle was about 35°.

4.5.8 Lever leg attachment

The long lever legs and corresponding supporting components were printed with polycarbonate and attached onto the robot with instant adhesive. The rotation hinges of the legs were connected by 18-gauge rods. The mechanism of the lever legs was shown in more details in Appendix B.

Chapter 4, in full, has been accepted for publication of the material as it may appear in *Advanced Intelligent Systems*, 2021, Yichen Zhai and Tse Nga Ng. The dissertation author was the primary investigator and author of this paper.

4.6 References

1 X. Ji, X. Liu, V. Cacucciolo, M. Imboden, Y. Civet, A. El Haitami, S. Cantin, Y. Perriard, and H. Shea, "An autonomous untethered fast soft robotic insect driven by low-voltage dielectric elastomer actuators," *Sci. Robot.*, vol. 4, no. 37, 2019, doi: 10.1126/scirobotics.aaz6451.

2 Q. He, Z. Wang, Y. Wang, A. Minori, M. T. Tolley, and S. Cai, "Electrically controlled liquid crystal elastomer-based soft tubular actuator with multimodal actuation," *Sci. Adv.*, vol. 5, no. 10, pp. 1–8, 2019, doi: 10.1126/sciadv.aax5746.

3 M. T. Tolley, R. F. Shepherd, B. Mosadegh, K. C. Galloway, M. Wehner, M. Karpelson, R. J. Wood, and G. M. Whitesides, "A Resilient, Untethered Soft Robot," *Soft Robot.*, vol. 1, no. 3, pp. 213–223, 2014, doi: 10.1089/soro.2014.0008.

4 T. Li, G. Li, Y. Liang, T. Cheng, J. Dai, X. Yang, B. Liu, Z. Zeng, Z. Huang, Y. Luo, T. Xie, and W. Yang, "Fast-moving soft electronic fish," *Sci. Adv.*, vol. 3, no. 4, pp. 1–8, 2017, doi: 10.1126/sciadv.1602045.

5 H. Lee, Y. Jang, J. K. Choe, S. Lee, H. Song, J. P. Lee, N. Lone, and J. Kim, "3D-printed programmable tensegrity for soft robotics," *Sci. Robot.*, vol. 5, no. 45, pp. 1–12, 2020, doi: 10.1126/SCIROBOTICS.AAY9024.

6 E. B. Joyee, A. Szmelter, D. Eddington, and Y. Pan, "3D Printed Biomimetic Soft Robot with Multimodal Locomotion and Multifunctionality," *Soft Robot.*, vol. 00, no. 00, pp. 14–16, 2020, doi: 10.1089/soro.2020.0004.

7 C. Li, G. C. Lau, H. Yuan, A. Aggarwal, V. L. Dominguez, S. Liu, H. Sai, L. C. Palmer, N. A. Sather, T. J. Pearson, D. E. Freedman, P. K. Amiri, M. O. de la Cruz, and S. I. Stupp, "Fast and programmable locomotion of hydrogel-metal hybrids under light and magnetic fields," *Sci. Robot.*, vol. 5, no. 49, p. eabbb9822, 2020, doi: 10.1126/scirobotics.abb9822.

8 X. Yang, W. Shang, H. Lu, Y. Liu, L. Yang, R. Tan, X. Wu, and Y. Shen, "An agglutinate magnetic spray transforms inanimate objects into millirobots for biomedical applications," *Sci. Robot.*, vol. 5, no. 48, p. eabc8191, 2020, doi: 10.1126/scirobotics.abc8191.

9 Y. Kim, H. Yuk, R. Zhao, S. A. Chester, and X. Zhao, "Printing ferromagnetic domains for untethered fast-transforming soft materials," *Nature*, vol. 558, no. 7709, pp. 274–279, 2018, doi: 10.1038/s41586-018-0185-0.

10 X. Lu, S. Guo, X. Tong, H. Xia, and Y. Zhao, "Tunable Photocontrolled Motions Using

Stored Strain Energy in Malleable Azobenzene Liquid Crystalline Polymer Actuators," *Adv. Mater.*, vol. 29, no. 28, pp. 1–7, 2017, doi: 10.1002/adma.201606467.

11 H. Zeng, O. M. Wani, P. Wasylczyk, and A. Priimagi, "Light-Driven, Caterpillar-Inspired Miniature Inching Robot," *Macromol. Rapid Commun.*, vol. 39, no. 1, pp. 1–6, 2018, doi: 10.1002/marc.201700224.

12 M. Pilz Da Cunha, M. G. Debije, and A. P. H. J. Schenning, "Bioinspired light-driven soft robots based on liquid crystal polymers," *Chem. Soc. Rev.*, vol. 49, no. 18, pp. 6568–6578, 2020, doi: 10.1039/d0cs00363h.

13 H. Zeng, P. Wasylczyk, C. Parmeggiani, D. Martella, M. Burresi, and D. S. Wiersma, "Light-Fueled Microscopic Walkers," *Adv. Mater.*, vol. 27, no. 26, pp. 3883–3887, 2015, doi: 10.1002/adma.201501446.

14 C. Huang, J. A. Lv, X. Tian, Y. Wang, Y. Yu, and J. Liu, "Miniaturized swimming soft robot with complex movement actuated and controlled by remote light signals," *Sci. Rep.*, vol. 5, no. July, pp. 1–8, 2015, doi: 10.1038/srep17414.

15 Z. Wang, K. Li, Q. He, and S. Cai, "A Light-Powered Ultralight Tensegrity Robot with High Deformability and Load Capacity," vol. 1806849, pp. 1–8, 2018, doi: 10.1002/adma.201806849.

16 G. Cai, J. H. Ciou, Y. Liu, Y. Jiang, and P. S. Lee, "Leaf-inspired multiresponsive MXene-based actuator for programmable smart devices," *Sci. Adv.*, vol. 5, no. 7, p. eaaw7956, 2019, doi: 10.1126/sciadv.aaw7956.

17 B. Shin, J. Ha, M. Lee, K. Park, G. H. Park, T. H. Choi, K. J. Cho, and H. Y. Kim, "Hygrobot: A self-locomotive ratcheted actuator powered by environmental humidity," *Sci. Robot.*, vol. 3, no. 14, pp. 1–9, 2018, doi: 10.1126/scirobotics.aar2629.

18 Y. Zhao, C. Xuan, X. Qian, Y. Alsaid, M. Hua, L. Jin, and X. He, "Soft phototactic swimmer based on self-sustained hydrogel oscillator," *Sci. Robot.*, vol. 4, no. 33, pp. 1–11, 2019, doi: 10.1126/scirobotics.aax7112.

19 J. J. Wie, M. R. Shankar, and T. J. White, "Photomotility of polymers," *Nat. Commun.*, vol. 7, p. 13260, 2016, doi: 10.1038/ncomms13260.

20 A. Kotikian, C. McMahan, E. C. Davidson, J. M. Muhammad, R. D. Weeks, C. Daraio, and J. A. Lewis, "Untethered soft robotic matter with passive control of shape morphing and propulsion," *Sci. Robot.*, vol. 4, no. 33, pp. 1–11, 2019, doi: 10.1126/scirobotics.aax7044.

21 Y. Tang, Q. Zhang, G. Lin, and J. Yin, “Switchable Adhesion Actuator for Amphibious Climbing Soft Robot,” *Soft Robot.*, vol. 5, no. 5, pp. 592–600, 2018, doi: 10.1089/soro.2017.0133.

22 A. Joshi, A. Kulkarni, and Y. Tadesse, “FludoJelly: Experimental study on jellyfish-like soft robot enabled by soft pneumatic composite (SPC),” *Robotics*, vol. 8, no. 3, 2019, doi: 10.3390/robotics8030056.

23 Y. Wu, J. K. Yim, J. Liang, Z. Shao, M. Qi, J. Zhong, Z. Luo, X. Yan, M. Zhang, X. Wang, R. S. Fearing, R. J. Full, and L. Lin, “Insect-scale fast moving and ultrarobust soft robot,” *Sci. Robot.*, vol. 4, no. 32, 2019, doi: 10.1126/scirobotics.aax1594.

24 G. Gu, J. Zou, R. Zhao, X. Zhao, and X. Zhu, “Soft wall-climbing robots,” vol. 2874, no. December, pp. 1–13, 2018.

25 C. T. Nguyen, H. Phung, T. D. Nguyen, H. Jung, and H. R. Choi, “Multiple-degrees-of-freedom dielectric elastomer actuators for soft printable hexapod robot,” *Sensors Actuators, A Phys.*, vol. 267, no. October, pp. 505–516, 2017, doi: 10.1016/j.sna.2017.10.010.

26 V. Nguyen, B. Lilly, and C. Castro, “The exoskeletal structure and tensile loading behavior of an ant neck joint,” *J. Biomech.*, vol. 47, no. 2, pp. 497–504, 2014.

27 C. Wang, K. Sim, J. Chen, H. Kim, Z. Rao, Y. Li, W. Chen, J. Song, R. Verduzco, and C. Yu, “Soft Ultrathin Electronics Innervated Adaptive Fully Soft Robots,” *Adv. Mater.*, vol. 30, no. 13, p. 1706695, 2018, doi: 10.1002/adma.201706695.

28 R. S. Kularatne, H. Kim, J. M. Boothby, and T. H. Ware, “Liquid crystal elastomer actuators: Synthesis, alignment, and applications,” *J. Polym. Sci. Part B Polym. Phys.*, vol. 55, no. 5, pp. 395–411, 2017, doi: 10.1002/polb.24287.

29 S. W. Ula, N. A. Traugutt, R. H. Volpe, R. R. Patel, K. Yu, C. M. Yakacki, S. W. Ula, N. A. Traugutt, R. H. Volpe, R. R. Patel, K. Yu, S. W. Ula, N. A. Traugutt, R. H. Volpe, R. R. Patel, K. Yu, and C. M. Yakacki, “Liquid crystal elastomers : an introduction and review of emerging technologies Liquid crystal elastomers : an introduction and review of emerging technologies,” vol. 0396, 2018, doi: 10.1080/21680396.2018.1530155.

30 A. Kotikian, R. L. Truby, J. W. Boley, T. J. White, and J. A. Lewis, “3D Printing of Liquid Crystal Elastomeric Actuators with Spatially Programed Nematic Order,” *Adv. Mater.*, vol. 30, no. 10, pp. 1–6, 2018, doi: 10.1002/adma.201706164.

31 Z. Z. Wang, Z. Z. Wang, Y. Zheng, Q. He, Y. Wang, and S. Cai, “Three-dimensional

printing of functionally graded liquid crystal elastomer," *Sci. Adv.*, vol. 6, no. 39, 2020, doi: 10.1126/sciadv.abc0034.

32 Y. Zhai, Z. Wang, K.-S. Kwon, S. Cai, D. J. Lipomi, and T. N. Ng, "Printing Multi-Material Organic Haptic Actuators," *Adv. Mater.*, 2020, doi: 10.1002/adma.202002541.

33 M. Kaur, T. H. Kim, and W. S. Kim, "New Frontiers in 3D Structural Sensing Robots," *Adv. Mater.*, p. 2002534, 2021, doi: 10.1002/adma.202002534.

34 Y. J. Tan, G. J. Susanto, H. P. Anwar Ali, and B. C. K. Tee, "Progress and Roadmap for Intelligent Self-Healing Materials in Autonomous Robotics," *Adv. Mater.*, p. 2002800, 2020, doi: 10.1002/adma.202002800.

35 K. Kwon and T. Nga, "Author ' s personal copy Improving electroactive polymer actuator by tuning ionic liquid concentration," *Org. Electron.*, vol. 15, no. 1, pp. 294–298, 2014, doi: 10.1016/j.orgel.2013.11.026.

36 N. Li, N. Eedugurala, D. S. Leem, J. D. Azoulay, and T. N. Ng, "Organic Upconversion Imager with Dual Electronic and Optical Readouts for Shortwave Infrared Light Detection," *Adv. Funct. Mater.*, p. 2100565, 2021, doi: 10.1002/adfm.202100565.

37 A. Vohra, K. Schlingman, R. S. Carmichael, and T. B. Carmichael, "Membrane-Interface-Elastomer Structures for Stretchable Electronics," *Chem*, vol. 4, no. 7, pp. 1673–1684, 2018, doi: 10.1016/j.chempr.2018.04.019.

38 Y. Zhai, J. Lee, Q. Hoang, D. Sievenpiper, H. Garudadri, and T. N. Ng, "Printed Wireless Fluidic Pressure Sensor," *Flex. Print. Electron.*, vol. 3, p. 035006, 2018.

Chapter 5

Digital Programming of Liquid Crystal Elastomers to Achieve High-Fidelity Surface Morphing

5.1 Abstract

Morphable surfaces will enable adaptive systems, but their resolution and freeform tunability have been limited by fabrication methods. This work presents a freeform patterning platform and its toolpath algorithms to enable high-resolution surface morphing of liquid crystal elastomers (LCE). A scratch post applying adjustable pressure and shear velocity was demonstrated to align LCE nematic domains in programmable gradients, offering the ability to locally tune the workpiece actuation strain and bending curvature radii from 1.8 mm to 14.4 mm. Two algorithms to calculate the patterning toolpaths for multi-layer structures are compared to determine the optimization criteria in examples of printed dome and human face models. The actuated human face model reached a maximum of 84.5% in structural similarity index measure when compared to the original design, showcasing the high fidelity and reconfigurability of this platform for fabricating complex morphable LCE structures.

5.2 Introduction

Shape morphing structures provide additional degrees of freedom in the geometries and functionalities of adaptive optics and electronics [1]–[3], robotic systems and camouflages [4], [5], and human-computer interfaces [6], [7]. Liquid crystal elastomers (LCE) are one type of soft materials demonstrated to achieve topological transformations via contracting, bending, twisting, and periodical deformations upon photonic or thermal actuation [8]–[16] changing from a flat state into a three-dimensional (3D) shape and vice versa in reverse deformations [17], [18]. For example, the complex contours of a human face model had been reconstructed in a continuous LCE film [19] and in enveloping surfaces of open meshes using kirigami and origami designs [3], [20]–[22]. However, better fidelity of the actuated LCE surface to the original design is desired, but the current design algorithms and fabrication procedures are limiting the pattern resolution and actuation response in morphable LCE surfaces.

To enable thermal actuation and shape shifts, LCE mesogens must be aligned to form monodomains that would change their orientations upon heating, thereby tuning strain and stress within the structure. Common methods to align LCE use molds or guides to direct the mesogen orientation based on photo-alignment [8]–[11] or catalyst-directed processes [23]–[25], but these techniques are restricted to patterning single layers and cannot adjust strain magnitudes within a multilayer structure. Alternatively, digital extrusion printing applies shear stress to align LCE mesogens by adjusting the nozzle travel velocity and height with respect to the substrate [16], [26], [27]. Since the alignment process is coupled with the material dispensing step, the extrusion rate must be dynamically tuned at high precision, which is challenging with high viscosity materials like LCE and thus the patterning resolution is limited.

In this report, we present a novel approach to align LCE mesogens in multilayer structures with freeform tunability and demonstrate high-resolution morphable surfaces. We have developed a patterning platform that decouples materials deposition and alignment processes, affording digital controls through a scratch post that applies variable pressure and shear velocity to locally tune mesogen domains. As this alignment process enables precise adjustment of strain gradients in LCE structures, we have concurrently improved the algorithms that translate the target actuation forms into patterning toolpaths. Prior works on morphable surfaces calculated the contraction areas in different regions to induce out-of-plane deformations leading to three-dimensional (3D) topography [10], [13], [19]. In contrast, the work below shows that using the criterion of surface curvature is more accurate than mapping contraction areas to reproduce complex features. We compared two methods of curvature calculations to optimize toolpath algorithms, and we fabricated examples of printed dome and human face models to demonstrate the reconfigurability and resolution of this platform for freeform patterning of morphable LCE.

5.3 Results

5.3.1 Controlling actuation curvatures of LCE

Figures 5.1(a) and (b) show the setup for local alignment of LCE domains using a scratch post mounted on a three-axis stage. The scratch post was a metal cylinder placed under a water chamber, and a programmable syringe pump would move water in or out of the chamber to adjust the load on the post, which in turn changed the pressure applied on the LCE workpiece. For the experiments in this report, individual layers of 0.2 mm thick LCE were deposited by a pneumatic extrusion printer, and any alignment from the extrusion process was erased by heating the layer to ~120°C with a hot air gun. This step initialized each layer to a polydomain state. Then the scratch post was put in contact with the LCE surface, and as the post was dragged on the uncured LCE, the horizontal shear force directed LCE mesogens to reorient from polydomains to the monodomain state. The mesogens maintained its alignment for a couple of hours, a sufficiently long time for the entire surface layer to be patterned and subsequently crosslinked by a UV light to permanently set the alignment. This process was repeated for multi-layer structures, with the option to incorporate different alignment patterns for each layer.

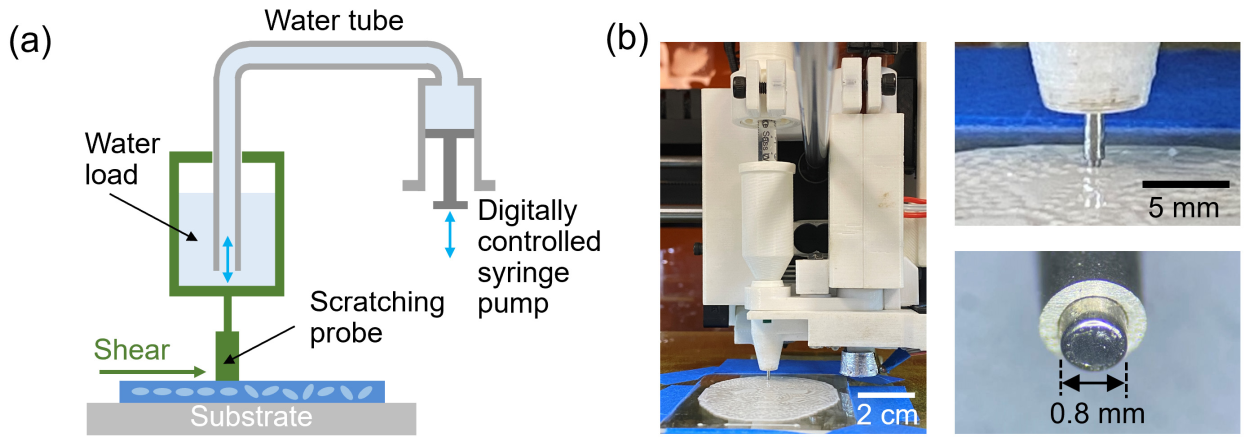

Figure 5.1: Post shear setup. (a) A schematic of the LCE alignment platform. (b) Photograph of the scratch post connected to a water chamber that varies the scratch load (left). Zoom-in side view (top right) and bottom view (bottom right) photographs of the scratch post.

The schematics in Figure 5.2(a) illustrate the thermal actuation of LCE samples with the bottom two layers in weak or strong alignment, covered by two layers of polydomain films. Upon heating, the aligned layers contract while the dimensions of polydomain layers remain unchanged. As a result, the actuated structure bends into an arc and curls to a smaller radius (higher curvature) with stronger mesogen alignment. This bending mode is enabled by the multilayer design and extends the actuation of LCE beyond in-plane deformations. The photographs in Figure 5.2(b) display the bending radii of three actuated samples sheared at the same velocity but under different loads. The actuation curvature increased as the alignment process was carried out under larger loads.

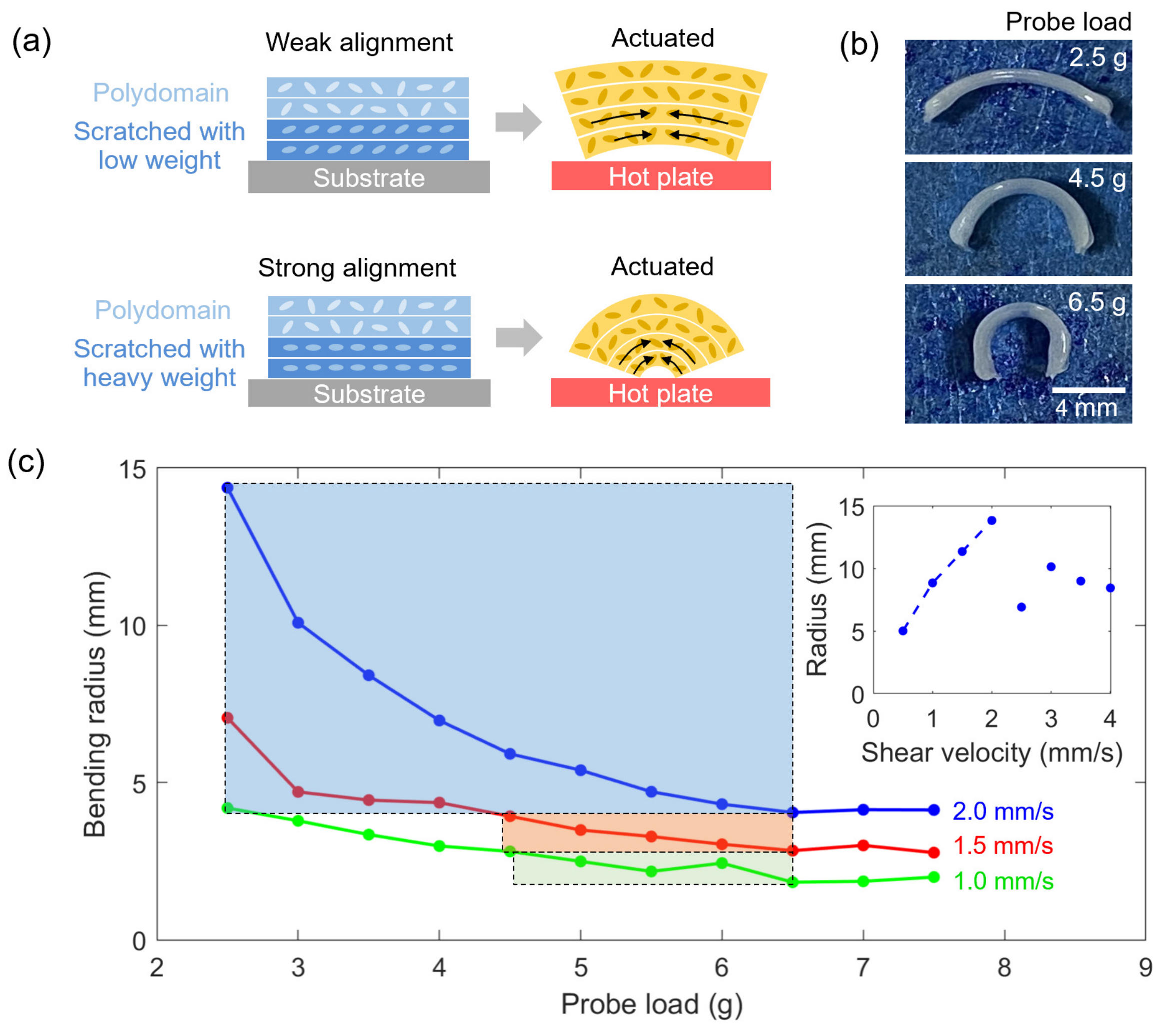

Figure 5.2: Calibration of curvature as a function of shear velocity and post load. (a) Illustrations of LCE domains processed under different scratch loads to control bending curvatures upon thermal actuation. (b) Photographs of thermally actuated LCE samples scratched under various loads at a post velocity of 1.5 mm/s. The actuation temperature was 150°C. (c) Actuation curvature as a function of the scratch load and the scratch post velocity. The inset shows actuation curvatures versus post velocities at a fixed load of 2.4 grams. The colored shadowed areas indicate the control regions we selected to use in surface reconstruction designs.

The extent of mesogen alignment and the corresponding actuation strain were adjusted by varying the shear velocity and pressure applied by the scratch post. Figure 5.2(c) shows the bending radius of actuated samples as a function of post load and shear velocity during the alignment process. The bending radii were tunable to encompass a wide range from 1.8 mm to

14.4 mm. When the load on the scratch post was increased to higher than 6.5 g, the bending radius reached saturation. When the shear velocity was varied between 0.5 mm/s to 2 mm/s at a fixed load, there was a monotonic correlation that higher velocity led to an increasing radius. As the scratch post moved faster, it induced weaker mesogen alignment; and if the post velocity exceeded 2 mm/s, the post intermittently lost contact with the LCE surface, resulting in poor alignment as manifested in the irregular trend for velocity >2 mm/s as observed in the Figure 5.2(c) inset. To ensure well-controlled alignment, we set the control parameters within the shadowed regions in Figure 5.2(c). For a target actuation curvature within the control boundaries, our tooling algorithm would select the corresponding shear velocity and load based on the calibration in Figure 5.2(c).

5.3.2 Comparing toolpath designs based on curvature directions

In our patterning approach, the alignment direction of LCE mesogens was oriented along the moving direction of the scratch post. Hence there is one main axis of alignment (namely, a single curvature tangent) for each location on a monodomain LCE surface. Meanwhile, on three-dimensional (3D) structures such as spheres and domes, the surface curvatures at each location may differ depending on directions. To determine the optimal curvature directions for patterning the LCE alignment axis, we compare two approaches as illustrated in Figure 5.3(a). The schematics include examples at different sampling locations. The bars drawn at each location indicate the magnitudes of local curvature in their respective directions. The curvature is defined as the reciprocal of the bending radius; therefore, a longer bar represents a smaller radius on account of a higher bending force upon LCE actuation. The red bar denotes the maximum curvature at a sampling location, while the blue bar represents the curvature perpendicular to the inclined direction (azimuth on horizontal plane) of the local surface.

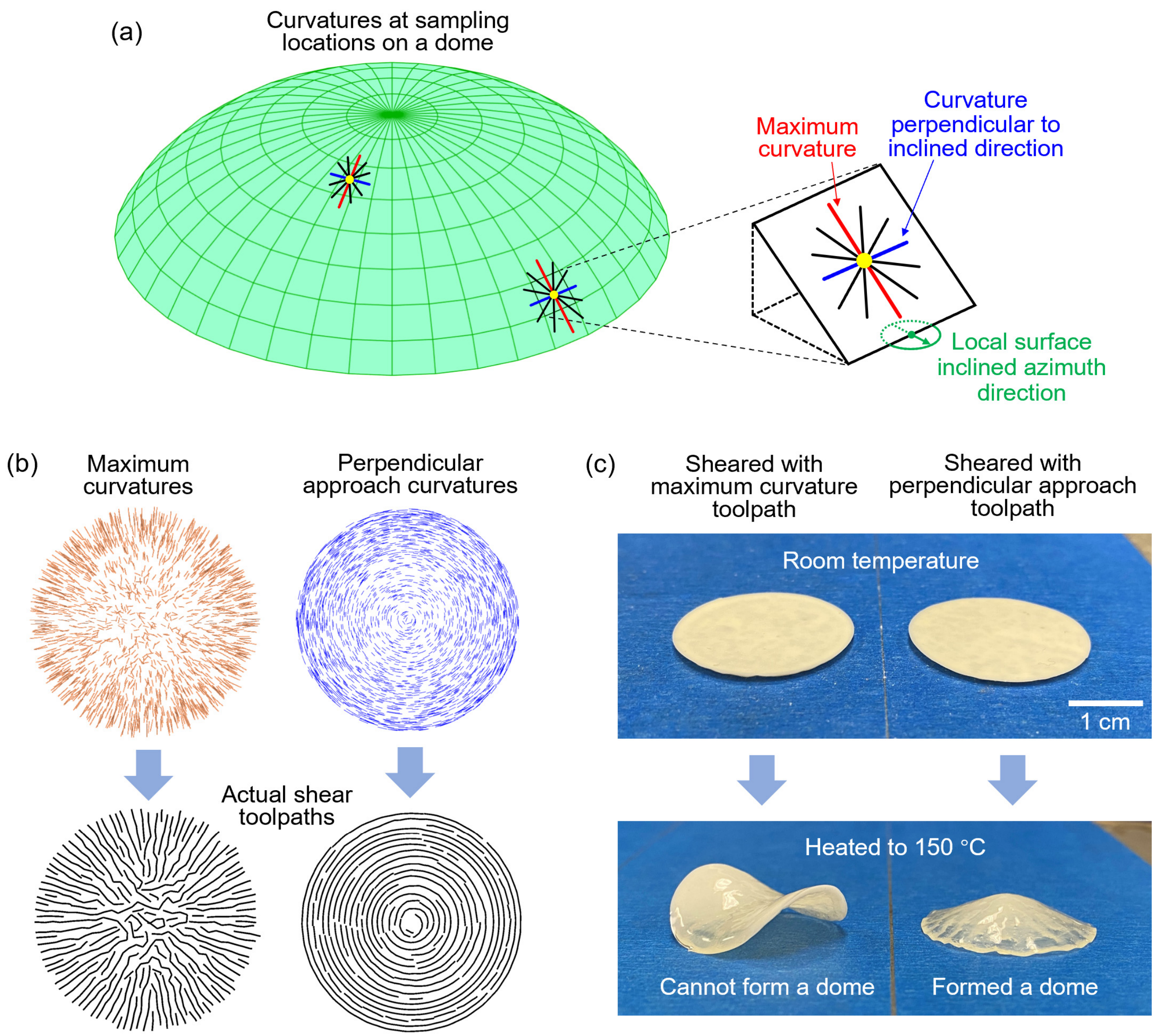

Figure 5.3: Toolpath based on different curvature directions. (a) An illustration of curvatures at different sampling locations on a dome surface (the display grid not drawn to scale). At each sample point (yellow dot), the bar lengths indicate the magnitudes of curvature in specific directions. The red bar show the direction of maximum curvature, and the blue bar points in the direction perpendicular to the inclined direction of local surface. (b) For the dome example, local maximum curvatures (red) and curvatures perpendicular to surface inclined directions (blue). The black lines indicate the calculated toolpaths for the scratch post. (c) Photographs of LCE samples sheared with toolpaths based on the local maximum (left) or the perpendicular approach (right).

We started with a simple target to pattern a LCE stack that would transform into a dome upon thermal actuation. We computed two sets of toolpaths for the scratch alignment process, one based on the maximum curvature direction and another one according to the perpendicular counterpart. In the maximum curvature approach, the toolpaths were mostly in radial directions, while in the perpendicular approach, they were consisted of arc segments [Figure 5.3(b)]. Note that this significant separation of patterns in the two different approaches only happen to the cases that the dome is more oblate (e.g., vertically compressed) than a perfect spherical dome. If the dome is vertically sharper than a spherical dome, both approaches lead to circular toolpaths. Samples were patterned with the two toolpath designs, and upon thermal actuation at 150 ℃ in Figure 5.3(c), only the sample patterned with the perpendicular approach was able to form a dome, while the other sample based on the maximum curvature direction formed an unexpected saddle shape. This result pointed out that, to form a dome, there should be material contraction along circular contours in addition to curvature formation, and the perpendicular approach for toolpath computation offered this contraction control better than the maximum curvature method.

To demonstrate the ability of our alignment platform to pattern complex freeform surfaces, we targeted the fabrication of LCE stacks that would morph into a human face, which is fundamentally a combination of multiple domes. For example, the face contour is a large dome, and facial features such as the lips are two stretched domes, the nose is a triangular dome, and the eye sockets are two concave domes. As such, a toolpath design based on the perpendicular approach is promising for this face model demonstration. On account of the complexities of a face model, we developed the following algorithm to generate patterning toolpaths that optimize the fidelity of actuated samples to the intended design.

5.3.3 Tool path generation

To generate freeform toolpaths for our LCE alignment platform, the computation algorithm involved three main steps as shown in Figure 5.4(a). The first step was to calculate the local curvature direction and magnitude at sampling points on the target shape. The second step was to map the positions of the sampling points from the 3D shape to a flat surface using a method that compensates for area distortions. In the last step, the calculations from the first two steps were brought together to determine the toolpath for the scratch post, translating the local curvatures into scratch trajectory, velocity, and load to be implemented on the alignment platform.

Step 1: Calculating local curvature direction and magnitude

For an arbitrary 3D surface to be reconstructed from an actuated LCE stack, for example the face model in our demonstration, we started with the target shape and created a point cloud to represent that 3D surface. The target surface was filled with points such that no more than 0.1 mm was between any two adjacent points, for our design intended to be in the few cm2 range. The 0.1 mm point distance was determined by the resolution of our process considering the size of the scratch post, and it is independent from the scale of the model. We deleted the edges of the 3D model and only used the point cloud for calculations, as shown in Figure 5.4(b). Starting from a sampling point P1, on the selected curvature direction, we estimated the corresponding curvature magnitude using two neighboring points, labeled as P2 and P3, about 2 mm away from P1. As shown in Figure 5.4(b), the radius of curvature at point P1 was determined from the circumcircle of the triangle formed by the three points. The actual distances between the three points were calculated from their coordinates and labeled l_1, l_2 and l_3. The radius of curvature was calculated by the following formulas:

Semi-perimeter of $\triangle P_1P_2P_3$:

$$l = \frac{l_1 + l_2 + l_3}{2} \tag{5.1}$$

Area of $\triangle P_1P_2P_3$:

$$S = \sqrt{l(l - l_1)(l - l_2)(l - l_3)} \tag{5.2}$$

Radius of circumcircle:

$$r = \frac{l_1 \times l_2 \times l_3}{4S} \tag{5.3}$$

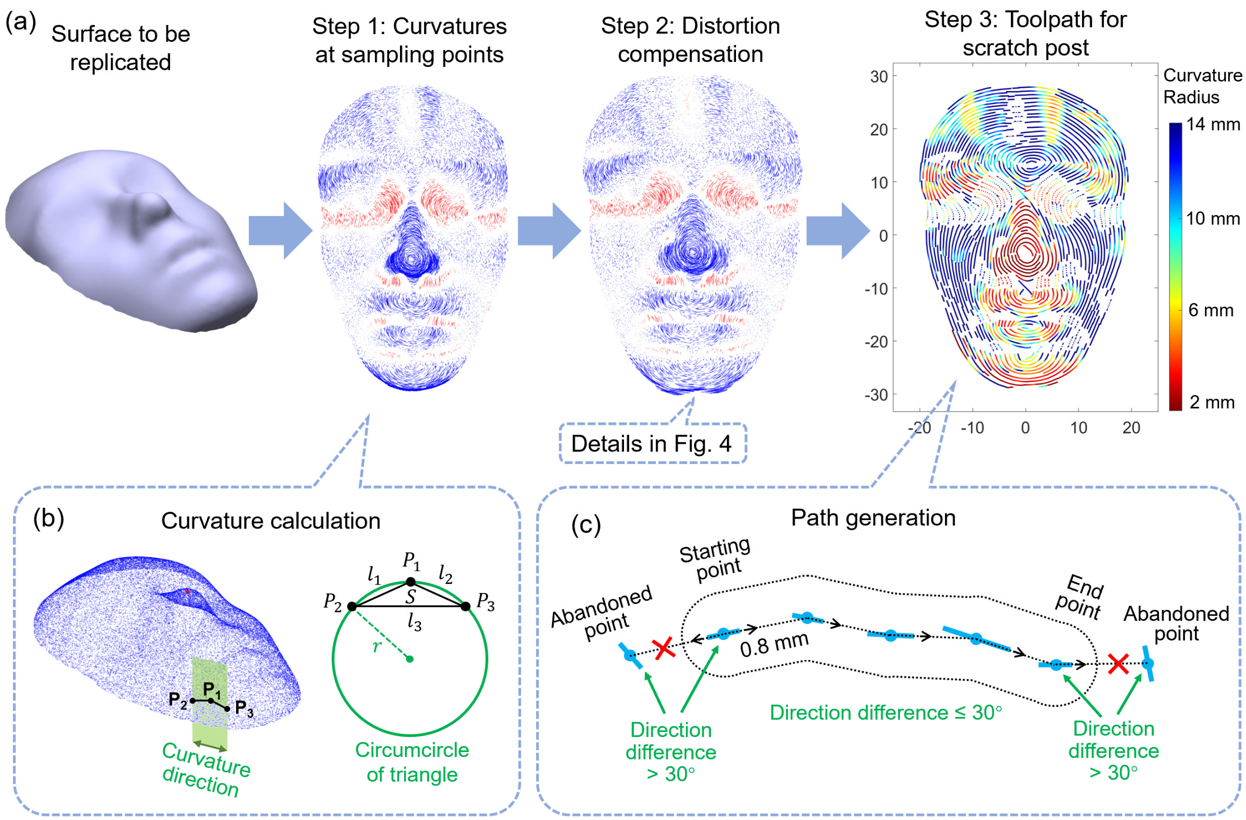

Figure 5.4: Procedure of tool path generation. (a) Process to generate toolpath for patterning the desired 3D surface. In Step 1 and 2, the blue and red colors indicate convex and concave curvatures, respectively. The magnitude of curvature is indicated by the length of each bar. In the toolpath diagram in Step 3, the solid and dashed lines represent convex and concave regions, respectively. (b) Diagram used in calculating the curvature radius at location P_1. (c) A schematic showing the clustering criterion from a group of local points to determine the start and the end of a toolpath pass.

In this method, the distance to the two neighboring points (l_1 and l_2) is approximately 2 mm, which was determined by the curvature scales on the human face 3D model. Other values from 1 mm to 4 mm were also tested and 2 mm was the optimal scale value to reproduce the curvature features. To find the maximum curvature direction, this calculation is repeated with 180 bidirectional directions around P1 in 1° interval, while in the perpendicular approach, the process is executed only once on the pre-selected direction. For our toolpath algorithm, we used the curvature direction based on the perpendicular approach, namely taking the direction perpendicular to inclined azimuth direction of the local surface. In Figure 5.4(a) Step 1, the bars were vectors pointing in the curvature directions calculated form the perpendicular approach, and the bar length represented the magnitude of curvature (1/r) at each sampling point. The blue bars marked the convex surfaces, and the red bars marked the concave regions.

Step 2. Mapping a 3D surface onto a 2D plane and compensating for distortions

In projecting the desired 3D model onto a 2D plane, the relative positions of patterning segments should be shifted as illustrated in Figure 5.5(a). In 3D, the segmentation grid of x-y axes were set in equal spacings. Yet when we flattened the model contours, the segmentation lengths along the x-y axes would no longer be equal but rather depend on slope integrals along the z-axis. For example, a segment with a sharp z-slope would be projected to a long segment (i), and a shallow z-slope to a corresponding short segment at (ii) in Figure 5.5(a). The traditional method to correct such changes is through finite element analysis (FEA). Instead of using computationally intensive FEA, below we present a simple and accessible algorithm to correct the area distortions which can be processed by general mathematical programming tools such as MATLAB.

Our process of segment mapping and distortion compensation is shown in Figures 5.5(b) to 4(f). In the first step, the target 3D model in the form of point cloud was set to a x-y grid. Within the boundaries of each grid, all the cloud points were fit to a plane with the least square regression. The intersection of the fit plane with the grid axes was a parallelogram. These parallelogram blocks are shown in Figure 5.5(b). In the second step, the incline angle of each parallelogram block was computed, and the blocks were rotated to remove the incline with respect to the x-y plane. The side view and the top view after rotation are shown in Figures 5.5(c) and (d), respectively. Because the sizes of the parallelogram blocks were the same as or larger than the original grid blocks, there were overlaps between the blocks as seen in Figure 5.5(d). In the third step, the blocks were translated to eliminate the overlaps which extended the area coverage. For a corner block, the translation involved aligning the shared vertices between this block and the neighboring center block. Meanwhile for an edge block, the translation was implemented to align the mid-point of the edge shared with its neighboring block.

After translation of all the blocks surrounding the central one, the result is shown as the left diagram in Figure 5.5(e). In the fourth step, to fill the gaps between the blocks, the vertices in blocks sharing the grid intersection were merged together by calculating the geometric mean positions, as indicated by the blue circles in Figure 5.5(e). Lastly, steps 3 and 4 were repeated from the block at the global peak to the edges of the whole mesh in loops. The central block at the global peak was found by locating the block highest on the z axis. In each repetition loop, the blocks were first translated based on the inner loop, followed by stitching all the shared vertices. The final result after compensating for area distortions is shown in the right diagram of Figure 5.5(f), which shows the extended areas in the x-y plane compared to the outline of the initial 3D mesh (blue line). Our process here accounted for the additional LCE materials needed to raise the surface and create contours in the z-axis. Finally, the positions of points in the 3D cloud were mapped to the corresponding coordinates projected on the x-y plane, and the local curvature is displayed with distortion compensation in the Step 2 diagram of Figure 5.5(a).

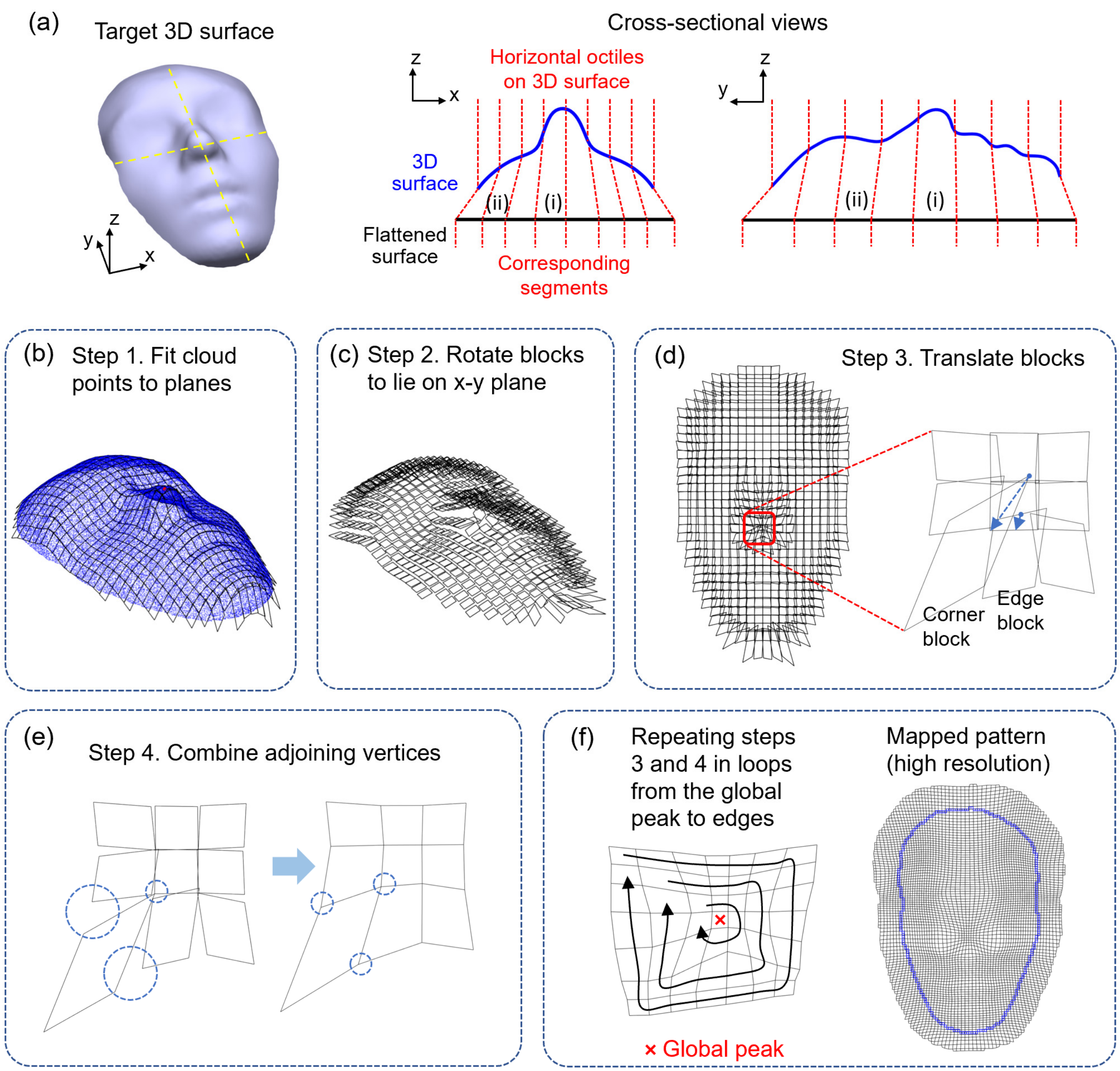

Figure 5.5: Distortion compensation process that maps a 3D surface to a flattened plane. In part (a), The cross-sectional views correlate the 3D grid to expanded plane segments at the location denoted by the two yellow dashed lines. In part (f), the outline of the original mesh of the 3D face surface is shown in blue, and the final mesh projected onto a 2D plane is shown in black.

Step 3. Translating curvature information into scratch post toolpath

The algorithm to translate the local curvatures into toolpath trajectories is illustrated in Figure 5.4(c). To generate a path, the starting location was a randomly selected point in the point cloud. Then using the local curvature vectors from Step 2 of Figure 5.4(a), the algorithm transversed according to the vector direction from the starting point to both ends of the vector in a step size of 0.8 mm, which was chosen to match the diameter of the scratch post. Upon completing the transverse steps, two cloud points located closest to the stepping endpoints were selected. The curvature directions of these newly selected points were retrieved and compared with that of the first point. If the curvature directions differed by ≤ 30°, the new point location would be added into the path. Otherwise, the new point location would be dismissed, and the toolpath trajectory would terminate at this location. In Figure 5.4(c), the point to the left of the first point was not included, while the point to the right was selected as the second point for this path. The selection of trajectory points was repeated according to this method until the process is terminated on both ends. That is, when the differences in curvature direction between the trajectory endpoints and the next preliminary points were greater than 30°, the trajectory of this particular toolpath was completed. Each toolpath would have a linewidth of 0.8 mm which was the scratch post diameter, as marked by the dashed contour in Figure 5.4(c). To prevent other trajectories from overlapping and overwriting the same areas, the algorithm would delete all the cloud points within the linewidth contour upon the completion of a trajectory, so that new paths would be generated only from points outside of existing paths.

In generating toolpath trajectories, the algorithm first accounted for the curvature direction at each sampling point as discussed above. Subsequently, the algorithm incorporated the target curvature magnitudes by controlling the velocity and load of the scratch post, according to the calibration in Figure 5.2(c). The resulting toolpath map for our face model is shown in Figure 5.4(c). For each trajectory, the spatial changes in the curvature magnitude are denoted by the color scale. In addition, the solid lines indicate paths to form convex surfaces, while the dashed lines show concave regions. To control the LCE actuation to either a convex or concave shape, the algorithm would align the bottom two layers of the 4-layer LCE structures to achieve convex curvatures, or conversely scratch the top two layers for concave surfaces, while leaving the other remaining layers in an unaligned polydomain state.

5.3.4 Actuation results

We processed LCE samples with the toolpath algorithm in Figure 5.4, and photographs of the workpieces at room temperature and at 150 ℃ are shown in Figure 5.6. Upon heat actuation, the LCE samples transformed from a flat film to a 3D surface reproducing the human face model. We examined our two strategies to generate toolpaths, by comparing the patterning results based on the perpendicular approach and the local maximum curvature approach in Figure 5.6(a) (sample 1) and 5(b) (sample 2), respectively. The actuated sample in Figure 5.6(a) showed more distinctive features than the one in Figure 5.6(b). Also, the latter sample mainly bent along the x-direction while the bending along the y-direction was limited, which was similar to the saddle outcome in Figure 5.3(c).

To quantify the degree in similarity of the actuated samples to the target model, the topography of actuated samples were captured via a 3D scanner as shown in the upper row of Figure 5.6(c). Then the topography measurements were transferred to grayscale images (104*168 pixels) based on the z-axis value at each pixel, shown in the lower row of Figure 5.6(c). The similarities between the images were calculated by structural similarity index measure (SSIM), which assessed the fidelity of image and video processing [28]. On the reference target and sample images, a pair of 9×9 windows were generated at corresponding positions, which were marked as r and s, respectively. The SSIM value between the two windowed images was calculated by

$$SSIM(x,y) = \frac{\left(2\mu_x\mu_y + C_1\right)\left(2\sigma_{xy} + C_2\right)}{\left(\mu_x^2 + \mu_y^2 + C_1\right)\left(\sigma_x^2 + \sigma_y^2 + C_2\right)} \tag{5.4}$$

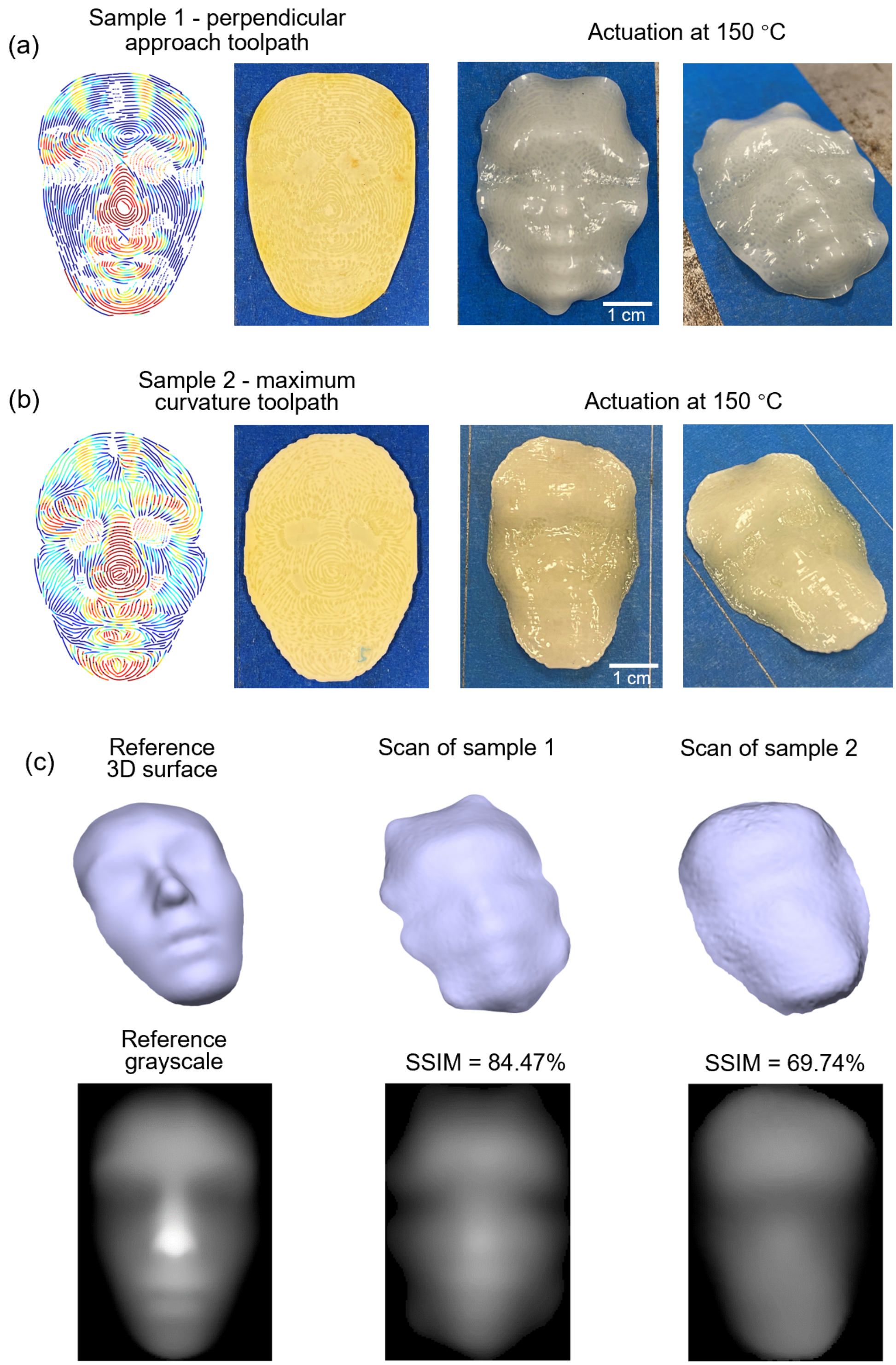

Figure 5.6: Toolpath diagrams and photographs of LCE samples patterned according to (a) the perpendicular approach and (b) the local maximum curvature approach. The flat films at room temperature morphed into 3D face structures upon actuation by heating at 150 °C. (c) Comparison of the reference 3D surface and the two actuated samples. The first row shows 3D scan results, and the second are grayscale images with their corresponding structural similarity indices.

where μ_r and μ_s were the means of the two windows, σ_r and σ_s were the variances of the windows, σ_{rs} was the covariance, and C_1, C_2 were constants and both set to zero in our work. The windows were shifted through the whole images and the overall SSIM value was determined by the mean value from all the window pairs. In this calculation, we only counted the common areas—if in one window there were non-zero values, yet the corresponding window had all zeros, the SSIM from this pair of windows was not counted in the mean. Finally, the SSIM was 84.5% for sample 1 and only 69.7% for sample 2, confirming that the perpendicular approach improved fidelity for face model reconstruction.

5.4 Discussions

Our LCE mesogen alignment method and the toolpath algorithm offer freeform reconfigurability to program voxels in millimeter resolution. By programming the scratch post load and velocity, we realized a gradient of actuation strains; this ability to achieve grayscale mesogen alignment enabled a continuum of bending and linear deformations, providing more control than prior works where the LCE alignment was only in bi-states (either maximally aligned or not). In addition, our method allowed facile layer-by-layer patterning to implement precise out-of-plane bending actuation. Previously linear contraction was the main actuation mode in LCE structures. While contraction around a perimeter had been able to squeeze a LCE film into 3D shapes, such structure was not directly programmed in curvature and actuated arbitrarily between convex or concave forms. In our platform, we provided both linear contraction and bending curvature controls. The LCE structure was designed in multiple layers with different extents of mesogen alignment, in order for the workpiece to actuate in bending mode with well-defined curvatures. One clear evidence was that the lips on our face model were reproduced in the actuation state in Figure 5.6(a), which were not obvious in earlier morphing demonstrations [3], [19], showcasing that our method met the difficult challenge of patterning convex and concave regions in close proximity.

In our toolpath algorithms, we used the curvature perpendicular to the local incline for trajectory calculations. As tested, this perpendicular approach was more suited than the maximum curvature approach in forming dome-like surfaces in human faces. While the target surface was complex, capturing the curvatures with the perpendicular approach was sufficient to reconstruct the surface with fast prototyping processes, which greatly reduced the calculation iterations spent on toolpath generation. However, as shown in Figure 5.6(c), our best reconstruction SSIM was 84.5%, which still showed a loss of fidelity compared to the intended shape.

One reason for this divergence was that the actuation radius only covered the range from 1.8 mm to 14.4 mm, while among all the curvatures calculated on the 3D face model, 3% of the cloud points were lower and 41% were higher than this range. The 41% of points with a radius of curvature larger than 14.4 mm meant that the points were on a nearly flat plane. We rounded the outliers to the boundary limits and resulted in lower fidelity. A solution is to modify the scratch post load and velocity to cover a wider range of radius. Alternately, in the fabrication process, all four layers of LCE can be aligned in different patterns to enhance bending or linear actuation. For example, if the first to third layers are aligned and the rest of upper layers remain polydomain, the whole film would bend beyond the current limits. And if all four layers are scratched with the same parameters, the aligned region would undergo linear in-plane contraction. Another contribution to the fidelity loss was that some minor information of surface bending and area mapping was lost when we used the perpendicular approach to calculate toolpath trajectories. A possible improvement is to use finite element analysis to calculate all the surface bending and area mapping with a mesh denser than implemented here. Such algorithms require large amount of calculation, but theoretically they could improve the SSIM to nearly 100%.

In summary, we demonstrated a freeform LCE alignment system which transferred high-fidelity patterns with large strain gradients. The toolpath algorithm reconstructed 3D shapes by bending curvature control in multi-layered structures, expanding beyond conventional linear contraction control and the limits of single films. With the low-cost setup and easy implementation, this versatile fabrication approach opened an avenue to create high-precision, reconfigurable LCE structures in future applications.

5.5 Materials and Methods

5.5.1 Preparation of LCE ink

The LCE ink was synthesized from monomer 1,4-bis-[4-(3-acryloyloxypropyloxy) benzoyloxy]-2-methylbenzene (RM257, 98.8%, Wilshire technologies) and 2,2′-(ethylenedioxy) diethanethiol (EDDET, 90~95%, Sigma-Aldrich). The degree of polymerization of the ink was targeted to be 7~8. First, 0.04 mole of RM257 and 0.035 mole of EDDET were dissolved in 100 mL dichloromethane. Then 0.54 mL dipropylamine was added into the solution as the polymerization catalyst. The solution was stirred for 24 hours at room temperature. Subsequently, 0.11 g 2-hydroxy-4′-(2-hydroxyethoxy)-2-methylpropiophenone was added to the solution as a photo initiator. In a round bottom flask, the solution was stirred and heated to 70 °C on a heating mantle (Mtops DMS632) to evaporate the solvent. In 30 minutes, most of the solvent was removed, and then the flask was connected to vacuum and heated to 90 °C for one day to remove residual solvent and catalyst. During heating, the flask was covered by aluminum foils to avoid crosslinking induced by florescent lights in the room. After solvent evaporation, the LCE ink was loaded into a

10 mL dispensing syringe. A hot air gun set to 200 °C was used to heat the flask to reduce the ink viscosity in order for it to flow out. Then the dispensing syringe was held vertically and heated in an oven to 80 °C for 24 hours, for the ink to settle and de-gas.

5.5.2 Fabrication process

Each sample consisted of four LCE layers printed on glass substrates, with each layer extruded to be 0.2 mm in thickness. To remove alignment due to the shear force from the extrusion nozzle, each layer was heated for 1 min with a hot air gun at 120 °C to reset LCE mesogens to isotropic polydomains. Then the film was patterned by the scratch post to align mesogens according to the selected toolpath. After the alignment process, the film was cured under 10 Watts 365 nm UV light for 3 minutes to crosslink the LCE. The deposition and alignment steps were repeated for each layer.

5.5.3 3D scanning of actuated samples

The samples were heated on a hot plat at 150 °C to actuate shape morphing. The TrueDepth camera on an iPhone 11 Pro was used to scan the actuated workpiece as recorded by the "Capture" App. The scan result was a point cloud in obj format. The point cloud was then transferred to a continuous 3D mesh by the "MeshLab" program and saved as a stl file.

Chapter 5, in full, is currently being prepared for submission for publication of the material, Yichen Zhai, Michael Tolley and Tse Nga Ng. The dissertation author was the primary investigator and author of this paper.

5.6 References

1 I. Jung, J. Xiao, V. Malyarchuk, C. Lu, M. Li, Z. Liu, J. Yoon, Y. Huang, and J. A. Rogers, "Dynamically tunable hemispherical electronic eye camera system with adjustable zoom capability," *Proc. Natl. Acad. Sci.*, vol. 108, no. 5, pp. 1788–1793, 2011, doi: 10.1073/pnas.1015440108.

2 Y. Qiu, E. Zhang, R. Plamthottam, and Q. Pei, "Dielectric Elastomer Artificial Muscle: Materials Innovations and Device Explorations," *Acc. Chem. Res.*, vol. 52, pp. 316–325, 2019, doi: 10.1021/acs.accounts.8b00516.

3 J. W. Boley, W. M. Van Rees, C. Lissandrello, M. N. Horenstein, R. L. Truby, A. Kotikian, J. A. Lewis, and L. Mahadevan, "Shape-shifting structured lattices via multimaterial 4D printing," *Proc. Natl. Acad. Sci. U. S. A.*, vol. 116, no. 42, pp. 20856–20862, 2019, doi: 10.1073/pnas.1908806116.

4 T. J. Wallin, J. Pikul, and R. F. Shepherd, "3D printing of soft robotic systems," *Nat. Rev. Mater.*, vol. 3, no. 6, pp. 84–100, 2018, doi: 10.1038/s41578-018-0002-2.

5 J. H. Pikul, S. Li, H. Bai, R. T. Hanlon, I. Cohen, and R. F. Shepherd, "Stretchable surfaces with programmable 3D texture morphing for synthetic camouflaging skins," *Science (80-.).*, vol. 358, no. 6360, pp. 210–214, 2017, doi: 10.1126/science.aan5627.

6 Y. Zhai, Z. Wang, K.-S. Kwon, S. Cai, D. J. Lipomi, and T. N. Ng, "Printing Multi-Material Organic Haptic Actuators," *Adv. Mater.*, 2020, doi: 10.1002/adma.202002541.

7 Y. Liu, J. Li, S. Song, J. Kang, Y. Tsao, S. Chen, V. Mottini, K. Mcconnell, W. Xu, Y. Zheng, J. B. Tok, P. M. George, and Z. Bao, "Morphing electronics enable neuromodulation in growing tissue," *Nat. Biotechnol.*, doi: 10.1038/s41587-020-0495-2.

8 K. Fuchi, T. H. Ware, P. R. Buskohl, G. W. Reich, R. A. Vaia, T. J. White, and J. J. Joo, "Topology optimization for the design of folding liquid crystal elastomer actuators," *Soft Matter*, vol. 11, no. 37, pp. 7288–7295, 2015, doi: 10.1039/c5sm01671a.

9 Y. Guo, H. Shahsavan, and M. Sitti, "3D Microstructures of Liquid Crystal Networks with Programmed Voxelated Director Fields," *Adv. Mater.*, vol. 32, no. 38, pp. 1–10, 2020, doi: 10.1002/adma.202002753.

10 T. H. Ware, M. E. McConney, J. J. Wie, V. P. Tondiglia, and T. J. White, "Voxelated liquid crystal elastomers," *Science (80-.).*, vol. 347, no. 6225, pp. 982–984, 2015, doi: 10.1126/science.1261019.

11 Y. Xia, G. Cedillo-Servin, R. D. Kamien, and S. Yang, “Guided Folding of Nematic Liquid Crystal Elastomer Sheets into 3D via Patterned 1D Microchannels,” *Adv. Mater.*, vol. 28, no. 43, pp. 9637–9643, 2016, doi: 10.1002/adma.201603751.

12 O. D. Lavrentovich, “Prepatterned liquid crystal elastomers as a step toward artificial morphogenesis,” *Proc. Natl. Acad. Sci. U. S. A.*, vol. 115, no. 28, pp. 7171–7173, 2018, doi: 10.1073/pnas.1809083115.

13 E. C. Davidson, A. Kotikian, S. Li, J. Aizenberg, and J. A. Lewis, “3D Printable and Reconfigurable Liquid Crystal Elastomers with Light-Induced Shape Memory via Dynamic Bond Exchange,” *Adv. Mater.*, vol. 1905682, pp. 1–6, 2019, doi: 10.1002/adma.201905682.

14 Y. Zhang, Z. Wang, Y. Yang, Q. Chen, X. Qian, Y. Wu, H. Liang, Y. Xu, Y. Wei, and Y. Ji, “Seamless multimaterial 3D liquid-crystalline elastomer actuators for next-generation entirely soft robots,” *Sci. Adv.*, vol. 6, no. 9, p. eaay8606, 2020, doi: 10.1126/sciadv.aay8606.

15 Q. He, Z. Wang, Y. Wang, A. Minori, M. T. Tolley, and S. Cai, “Electrically controlled liquid crystal elastomer-based soft tubular actuator with multimodal actuation,” *Sci. Adv.*, vol. 5, no. 10, pp. 1–8, 2019, doi: 10.1126/sciadv.aax5746.

16 Y. Zhai and N. T. Ng, “Self-Sustained Robots Based on Functionally Graded Elastomeric Actuators Capable of Carrying a Payload 22 Times of Body-Weight,” *Adv. Intell. Syst.*, vol. accepted, 2021.

17 M. J. Ford, C. P. Ambulo, T. A. Kent, E. J. Markvicka, C. Pan, J. Malen, T. H. Ware, and C. Majidi, “A multifunctional shape-morphing elastomer with liquid metal inclusions,” *Proc. Natl. Acad. Sci. U. S. A.*, vol. 116, no. 43, pp. 21438–21444, 2019, doi: 10.1073/pnas.1911021116.

18 M. Barnes and R. Verduzco, “Direct shape programming of liquid crystal elastomers,” *Soft Matter*, vol. 15, no. 5, pp. 870–879, 2019, doi: 10.1039/c8sm02174k.

19 H. Aharoni, Y. Xia, X. Zhang, R. D. Kamien, and S. Yang, “Universal inverse design of surfaces with thin nematic elastomer sheets,” *Proc. Natl. Acad. Sci. U. S. A.*, vol. 115, no. 28, pp. 7206–7211, 2018, doi: 10.1073/pnas.1804702115.

20 W. Wang, “Mechanical Assembly of Thermo-Responsive Polymer-Based Untethered Shape-Morphing Structures,” *Macromol. Mater. Eng.*, vol. 305, no. 1, pp. 1–9, 2020, doi: 10.1002/mame.201900568.

21 M. T. Tolley, S. M. Felton, S. Miyashita, D. Aukes, D. Rus, and R. J. Wood, "Self-folding origami: Shape memory composites activated by uniform heating," *Smart Mater. Struct.*, vol. 23, no. 9, pp. 1–14, 2014, doi: 10.1088/0964-1726/23/9/094006.

22 A. Minori, S. Jadhav, Q. He, S. Cai, and M. T. Tolley, "Reversible actuation of origami inspired composites using liquid crystal elastomers," *ASME 2017 Conf. Smart Mater. Adapt. Struct. Intell. Syst. SMASIS 2017*, vol. 1, 2017, doi: 10.1115/SMASIS2017-3986.

23 A. S. Kuenstler, Y. Chen, P. Bui, H. Kim, A. DeSimone, L. Jin, and R. C. Hayward, "Blueprinting Photothermal Shape-Morphing of Liquid Crystal Elastomers," *Adv. Mater.*, vol. 32, no. 17, pp. 1–9, 2020, doi: 10.1002/adma.202000609.

24 A. D. Auguste, J. W. Ward, J. O. Hardin, B. A. Kowalski, T. C. Guin, J. D. Berrigan, and T. J. White, "Enabling and Localizing Omnidirectional Nonlinear Deformation in Liquid Crystalline Elastomers," *Adv. Mater.*, vol. 30, no. 35, pp. 1–6, 2018, doi: 10.1002/adma.201802438.

25 C. M. Yakacki, M. Saed, D. P. Nair, T. Gong, S. M. Reed, and C. N. Bowman, "Tailorable and programmable liquid-crystalline elastomers using a two-stage thiol-acrylate reaction," *RSC Adv.*, vol. 5, no. 25, pp. 18997–19001, 2015, doi: 10.1039/c5ra01039j.

26 A. Kotikian, R. L. Truby, J. W. Boley, T. J. White, and J. A. Lewis, "3D Printing of Liquid Crystal Elastomeric Actuators with Spatially Programed Nematic Order," *Adv. Mater.*, vol. 30, no. 10, pp. 1–6, 2018, doi: 10.1002/adma.201706164.

27 Z. Z. Wang, Z. Z. Wang, Y. Zheng, Q. He, Y. Wang, and S. Cai, "Three-dimensional printing of functionally graded liquid crystal elastomer," *Sci. Adv.*, vol. 6, no. 39, 2020, doi: 10.1126/sciadv.abc0034.

28 Z. Wang, A. C. Bovik, H. R. Sheikh, and E. P. Simoncelli, "Image quality assessment: From error visibility to structural similarity," *IEEE Trans. Image Process.*, vol. 13, no. 4, pp. 600–612, 2004, doi: 10.1109/TIP.2003.819861.

Chapter 6

Other Applications of 3D Printing and Control Processes in Electro-mechanical System Integration

6.1 Introduction

In our research works, we integrated multiple different components into experimental systems for fabrication and characterization. For example, the printing system consists of a commercial printer platform, 3D printed mechanical components, an outer Arduino controller, heaters, UV lights, multiple power supplies, nozzle force sensing components and pneumatic air supply components. Moreover, the heart pulse simulation pump and wireless readout system in Chapter 2, the tensile/compressive force tester for the LCE haptic devices in Chapter 3, the shear force tracking device in Chapter 4, and the post shear system in Chapter 5 were all in customized designs as a part of our research, which used 3D printed components and electronic controller circuits. In this chapter, we further present other system integration works using printed parts and electrical controls. An organic shortwave infrared (SWIR) photodiode array was manufactured with individual photodiodes, multiplexer control circuit and printed mechanical parts for imaging. Another application is a kinesthetic haptic device printed from regular polylactic acid (PLA) with integrated silver heater and temperature sensor. A feedback control circuit was designed to maintain the temperatures, in order to tune the stiffness of the device for haptic feelings.

6.2 Organic SWIR photodiode array for spectroscopic imaging

6.2.1 Results

SWIR imaging benefits from enhanced penetration depths[1], [2] and accuracy[3], [4] with regard to minimally invasive tissue analyses. For example, since blood and fat tissues have strong absorption features in the SWIR, ischemia[5] (inadequate blood flow) or atherosclerosis[6] (fatty deposits clogging arteries) can be readily diagnosed by SWIR spectroscopy. Figure 6.1(a) shows clear differences in transmittance between muscle and fat, especially at λ = 1210 nm. The ability to distinguish fat and muscle tissues may assist laparoscopic procedures to enhance contrast between crucial organs and surrounding tissues. As such, SWIR imaging is highly desirable, but current technologies are costly and not affordable for wide deployment. Here we demonstrate the feasibility to easily incorporate the organic photodiodes into a low-cost, scalable active-matrix array that enables spatial mapping and compositional analysis of biological tissue.

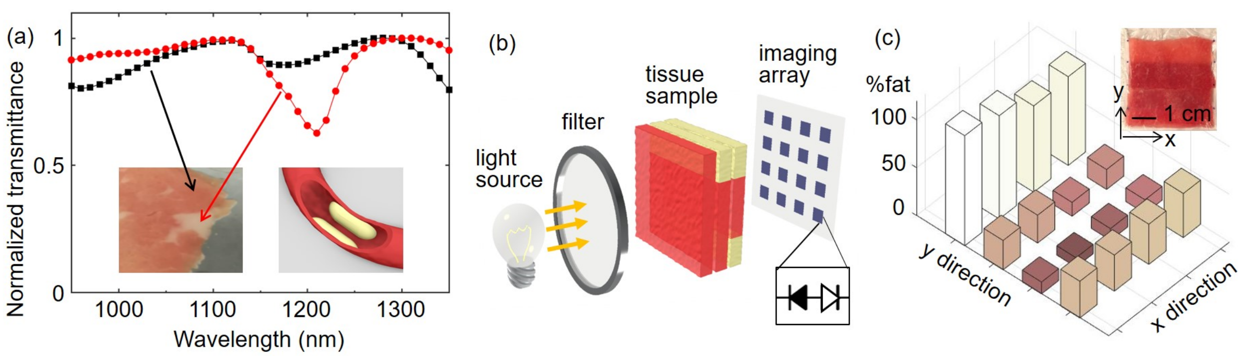

Figure 6.1: Schematic of imaging setup and results showing the contents of fat. (a) Normalized transmittance spectra of muscle (black) and fatty tissues (red). The inset schematic illustrates the scenario of fatty deposits clogging an artery. (b) Measurement setup using the organic array for SWIR spectral imaging. (c) Percentage of fatty tissue at each pixel location. The inset photograph shows the sample as seen in the visible.

Figure 6.1(b) illustrates our measurement setup for spectral imaging. To enable spatial mapping, a 4×4 active-matrix array is integrated where each pixel is comprised of an organic photodiode connected to a silicon switching diode which reduces signal cross-talk between neighboring pixels. The circuit diagram and pixel characterization are shown in Figure 6.2. To enable compositional analysis, the incident light is tuned to a narrow spectral range (10 nm of full width at half maximum) by using bandpass filters. To differentiate fatty tissues from muscle, we acquire measurements with two wavelengths, centered at λ = 1152 nm or 1200 nm. Fatty tissues display much stronger absorption at λ = 1200 nm compared to lean muscle. Meanwhile, both types of tissues show similar absorption at λ = 1152 nm, and thus signals will be normalized to this baseline at λ = 1152 nm, by calculating the transmittance ratio TR = $\%T_{1200nm}/\%T_{1152nm}$. This normalization also adjusts for the background due to water, because the transmittance of water is nearly constant in the λ range of 1150 nm to 1250 nm

For the sample in Figure 6.1(c) inset, we stack three ~1 mm thick beef slices together, to image the fat distribution under a lean muscle layer. Faint outlines of the region with high fat content on the top quarter section is observable in the visible spectrum; the fat buried in the bottom quarter region is harder to see in the visible but can be distinguished by the SWIR TR values in Figure 6.1(c). We convert the TR values to estimate the fat percentage at each pixel location by fat% = $(TR_{sample} - TR_{muscle})/(TR_{fat} - TR_{muscle})$, where the values of TR_{muscle} and TR_{fat} are measured with 3 mm thick calibration standards that are visibly only lean muscle or only fat, respectively. The measurement uncertainty is ~30% due to light scattering artifacts and variations in calibration tissues. Nonetheless, the organic array is capable of providing contrast between fat and muscle tissues and shows promise for biomedical spectral imaging applications.

6.2.2 Design and operation procedure

The circuit diagram of 4×4 array with SWIR photodiodes is shown in Figure 6.2(a). Each photodiode is individually connected to a 1N4007 switching diode in back-to-back structure. The positive poles of the two diodes are attached together. Then 16 pairs of diodes are connected to four vertical lines marked as A1~A4 and four horizontal lines marked as B1~B4. There is an electronic switch on each line to select the row and column to be connected in the loop. The switches are performed by CD4053BE analog multiplexer IC chips, and the switching logic of the chips and controlled by an Arduino nano controller. The photographs of the imaging array and the multiplexer circuit are shown in Figure 6.2 (b) and (c), respectively. The vertical and horizontal lines are connected in an outer loop through a picoammeter and a voltage source in Keithley 6487.

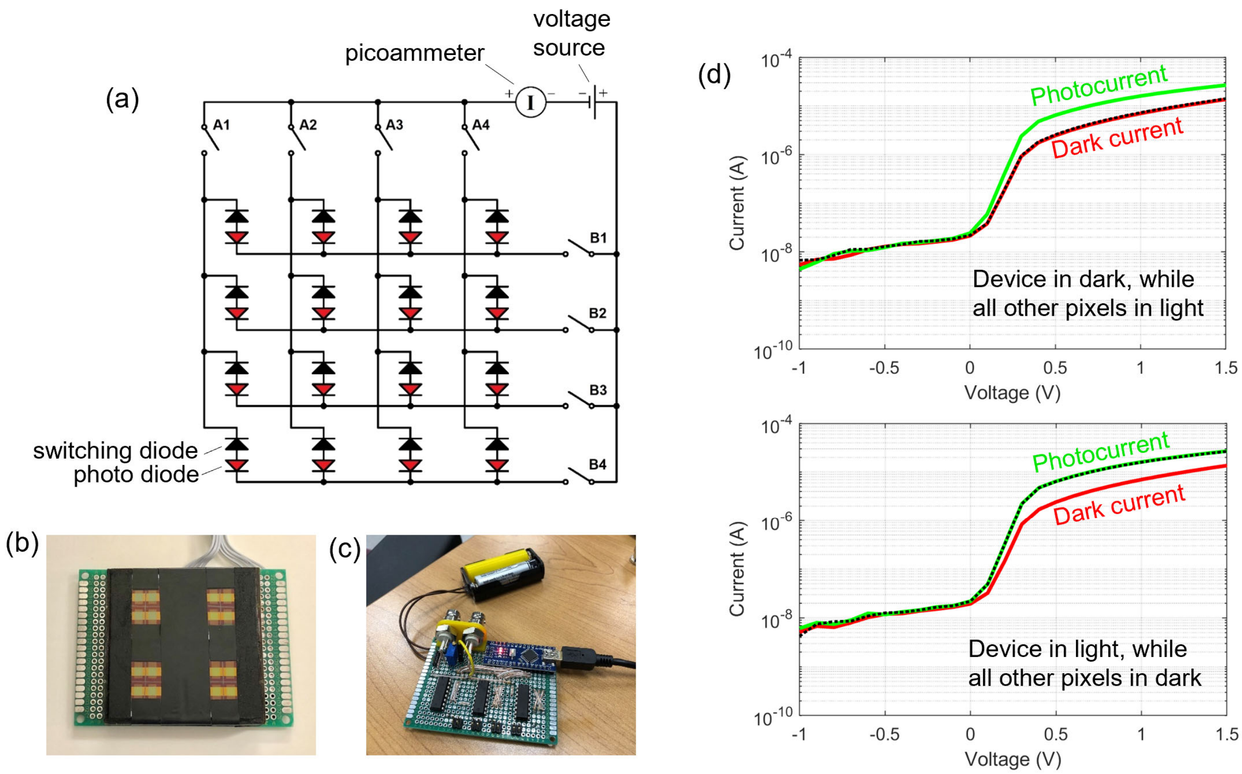

Figure 6.2: Circuit diagram, photograph, and pixel characterization of the 4 x 4 active-matrix imaging array. (a) Circuit diagram. (b) Photograph of the imaging array. (c) Photograph of the multiplexer. (d) Current-voltage characteristics of a single pixel in the array, showing minimized cross-talking current.

During measurement, each time only one switch in the vertical lines and one switch in the horizontal lines are turned on, and the single photodiode at the intersection is connected into the outer loop. The voltage source outputs 1.2 V bias totally. About 0.3 V bias is applied on the switching diode as positive bias to turn it on. The rest 0.9 V is applied on the photodiode as negative bias to increase the EQE of the device. The photo current from the photodiode is measured by Keithley 6487 picoammeter. The advantage of back-to-back diode structure in this array is that the four photodiodes sharing the same vertical or horizontal line are isolated by the switching diodes so that the crosstalk between pixels can be reduced. If there is no switching diode, when one device is being measured, the photo current generated by a neighboring photodiode could flow back through other photodiodes on the same lines and bypasses the device being measured. This extra part of current causes the interference between the measured device and the neighboring devices. The added switching diodes are able to stop the back-flow current and block the bypass.

In the current versus voltage characteristics shown in Figure 6.2(d), the red solid lines indicate the (1) minimum pixel current when all the pixels are in the dark. The green solid lines show the (2) maximum pixel current when every pixel is illuminated evenly by white light at 1.48 mW/cm2 . The black dashed line in the top panel shows the case where the pixel being measured is in the dark, while all other neighboring pixels are illuminated. The pixel current still shows similar current as the dark current (1), indicating that the switching diodes have blocked the photocurrent from neighboring pixels from flowing to the pixel under measurement. The bottom panel shows the pixel current (black dashed line) of the illuminated neighboring pixels.

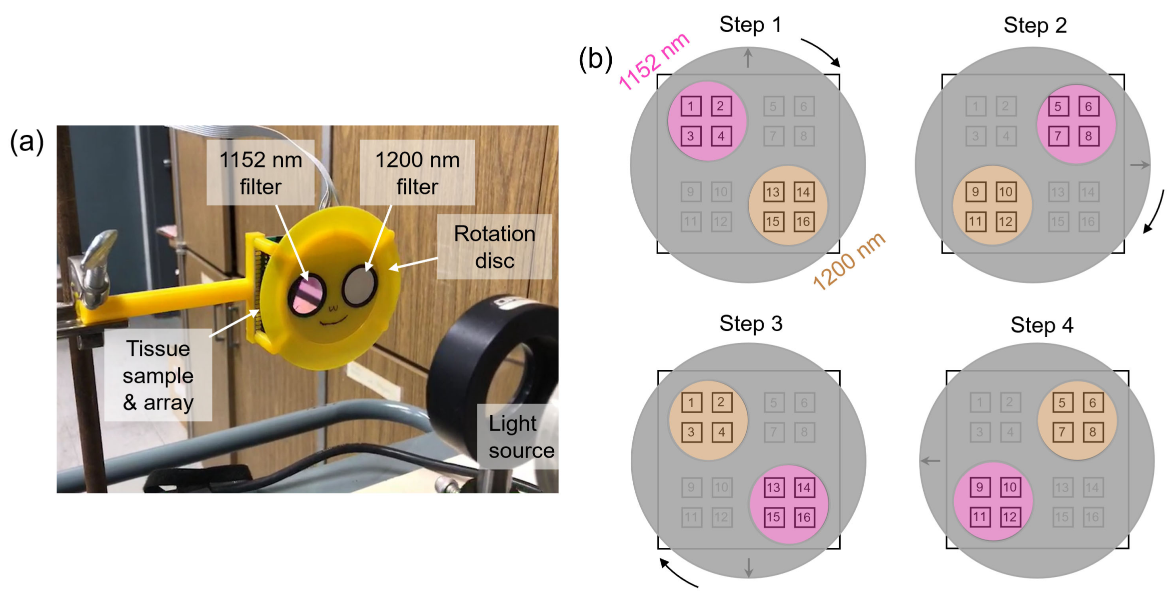

Figure 6.3: Imaging setup and operation procedure. (a) Photograph of imaging setup with 3D printed mechanical components. (b) Sequence of shifting filters during imaging process.

A photograph of the imaging setup is shown in Figure 6.3(a). Two bandpass filters at 1152 nm and 1200 nm are mounted in a rotation disc. Filtered light in narrow spectra range can pass through the filters while the light in other regions is blocked by the disc. As shown in Figure 6.2(b), our 16 pixels are separated in four regions, and the size of a single filter could cover the four pixels in one region. When the disc rotates, the filtered single wavelength light can be shifted between different regions. The stacking sequence of the filters, sample tissues and imaging array is shown in Figure 6.1(b), in which the samples are inserted between the filters and the array. The operation sequence of the imaging process is shown in Figure 6.3(b). When a sample or calibration standards was installed, all the four steps were performed to measure the transmitting photocurrent through the sample at the two wavelengths. In step 1, the 1152 nm filter covered pixels 1~4 while the 1200 nm filter covered pixels 13~16. A MATLAB program was used to command the multiplexer to connect each of these eight pixels to the outer circuit loop. Then the program controlled Keithley multimeter to apply bias voltage and measure the current through the loop. Eight current values were acquired in the program process and recorded as the photocurrents at 1152 nm or 1200 nm of the corresponding pixels. To measure the photocurrents of all the pixels in the array, the disc was rotated by 90° each time, and the program switched the multiplexer to measure the current of other eight corresponding pixels. After going through the four steps, the photocurrent at 1152 nm and 1200 nm of all the 16 pixels were measured. The values were used to calculate the transmittance ratio for imaging.

6.3 Printed haptic device in feedback control

6.3.1 Design and characterization

When thermoplastic polymers are heated, the stiffness changes significantly due to the transition from glass state to rubber state, while the polymer is still in solid form. Because of this feature, some polymers can be made into passive haptics devices with temperature control for kinesthetic feedback to human users.[7] In this work, we designed a printed haptic device with common polylactic acid (PLA) printing filament and integrated heating components. The temperature of the device is tracked by an integrated thermistor for precise feedback control. With the characterization of flexural modulus versus temperature, the feelings of stiffness can be controlled as desired.

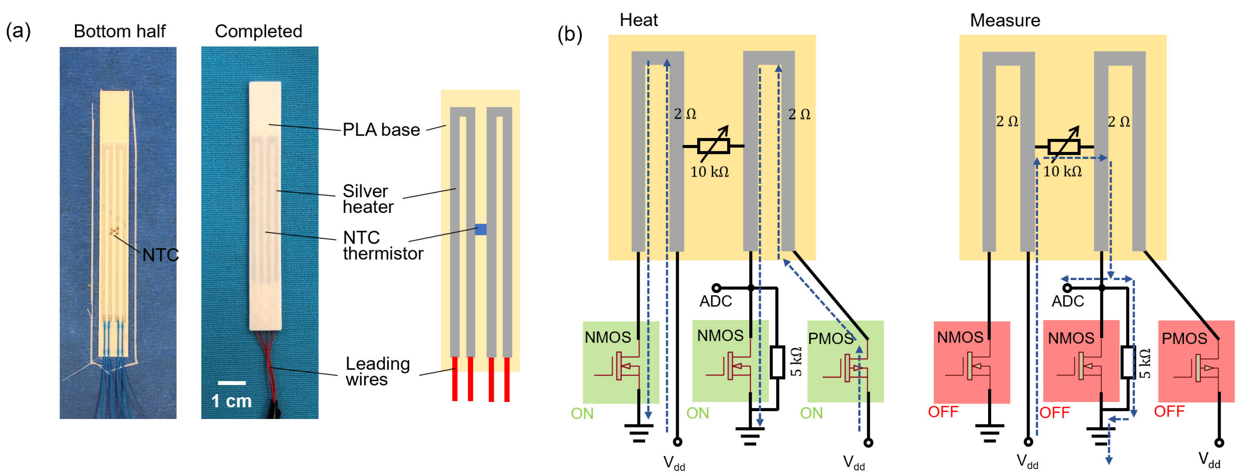

Figure 6.4: Design and control logic of printed PLA haptic device. (a) Photograph and schematic of PLA haptic device with integrated heater and thermistor. (b) Electrical diagram and control logic of heating and measuring states.

Photographs and a schematic of the printed haptic device are shown in Figure 6.4(a). In the fabrication process, first, the bottom half of the stack was printed, with pre-defined channels for two heaters. Then a NTC thermistor was inserted between the two heater channels, and four pieces of leading wires were attached to the four ports of the heaters. The heaters were fabricated by screen printing elastic silver paste into the channels. The formula of the silver paste is described in section 2.5.1 of this dissertation. After heating to dry the solvent in the silver paste, the top sealing was printed to complete the PLA device. As a novel point of this design, the temperature sensor was integrated between the two heater units, and the heaters also served as leading wires of the sensor. Therefore, without extra leading wires for the sensor, the heaters are homogenous through the whole haptic device and the heat can be evenly distributed.

To achieve precise temperature control, PID control with pulse width modulation (PWM) was used to drive the haptic device. The electrical diagram and control logic are shown in Figure 6.4(b). The device is switched by three MOS transistors to connect to the power source. The positive port of one of the heaters is regulated by a PMOS transistor, and the positive port of the other is connected to the power source directly. The negative ports of both heaters are regulated by two NMOS transistors. A $5\ \mathrm{k\Omega}$ divider resistor is used to short one NMOS, and the source electrode of the NMOS is connected to an inner analog-digital convertor (ADC) of an Arduino processor. All the gate electrodes of MOS transistors are controlled by the Arduino. The ADC was used in 16 times over sampling for 12-bit precision. In the heating state (on state of PWM), all three transistors are turned on to heat up the device, and the current path is marked with blue dashed lines. The thermistor and divider resistor are in much higher resistance compared to the heaters, so they will not affect the heating current. In the measuring state (off state of PWM), all the transistors are turned off. There is a small current through the thermistor and divider, and the voltage between them is measured by the ADC and the temperature is calculated from the voltage. In the measuring state, the current is in very low level compared to the heating state, so the negligible heat generated by this current does not affect the heat distribution.

A test of temperature control of this system is shown in Figure 6.5(a). The real-time temperature is shown in blue lines and the output PWM duty cycle is shown in green lines. At 5 second, the desired temperature was set to 55 ℃. The PWM was tuned to maximum duty cycle of 90%, and the rest 10% off cycle was used to take temperature measurements. It took 15 seconds for the device to reach and stabilize at 55 ℃. The PID control kept tuning the output power dynamically to maintain the temperature. At 35 second, the temperature was set to 45 ℃, and it took another 20 seconds to cool down to the desired temperature and then maintain. The test proved fully functional and precise temperature control of the haptic device.

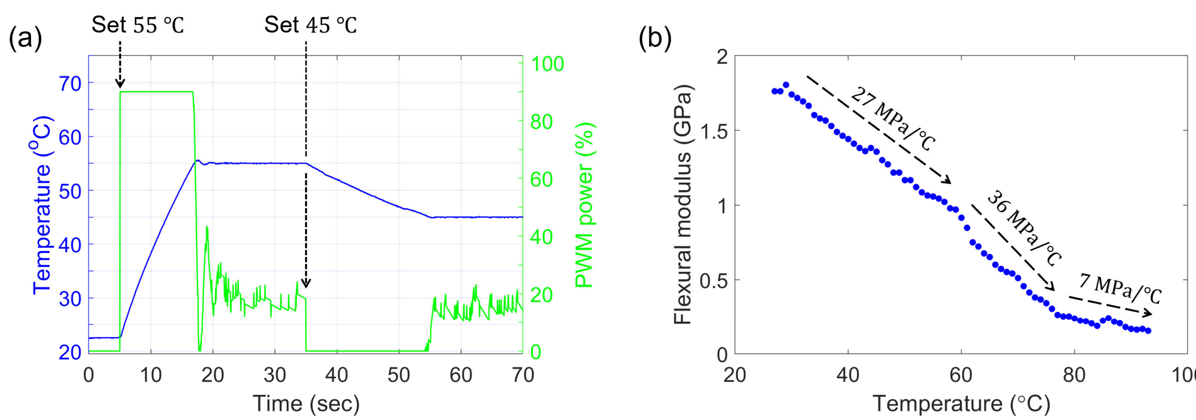

Figure 6.5: Characterization of haptic device. (a) Temperature control with desired temperature settings. (b) Flexural modulus measured at different temperature.

To characterize the stiffness at different temperatures, we measured the flexural modulus with the method given in Ref [8], in order to quantitively represent the feeling of stiffness. As shown in Figure 6.5(b), when the device was heated from 30 ℃ to 93 ℃, the flexural modulus changed from 1.8 GPa to 0.2 GPa, showing the capability to use in haptic applications for a wide range of feelings. The change of modulus can be divided into two regions by the glass transition temperature of about 60 ℃, and the changing rate is different on the two sides. When the temperature is over 80 ℃, the change of flexural modulus nearly saturated in the rubber state. With the characterized mapping between temperature and flexural modulus, the device can be used for stiffness control.

6.3.2 Haptic glove and human test

We designed a haptic glove to apply the damping resistance from the haptic device on human fingers. A human finger can bend in a wide range from 0° to nearly 180°, however, the bending of the device is limited. If the bending exceeds the maximum strain, the device could crack. To achieve haptic feeling on the whole bending range of finger, we designed a pair of unparallel four-bar linkages to connect the device to a glove. The photographs of the setup and the schematic are shown in Figure 6.6 (a) and (b), respectively. The unparallel linkage system reduces the bending angle of finger by a half, to maintain the bending deformation of the device in safe range.

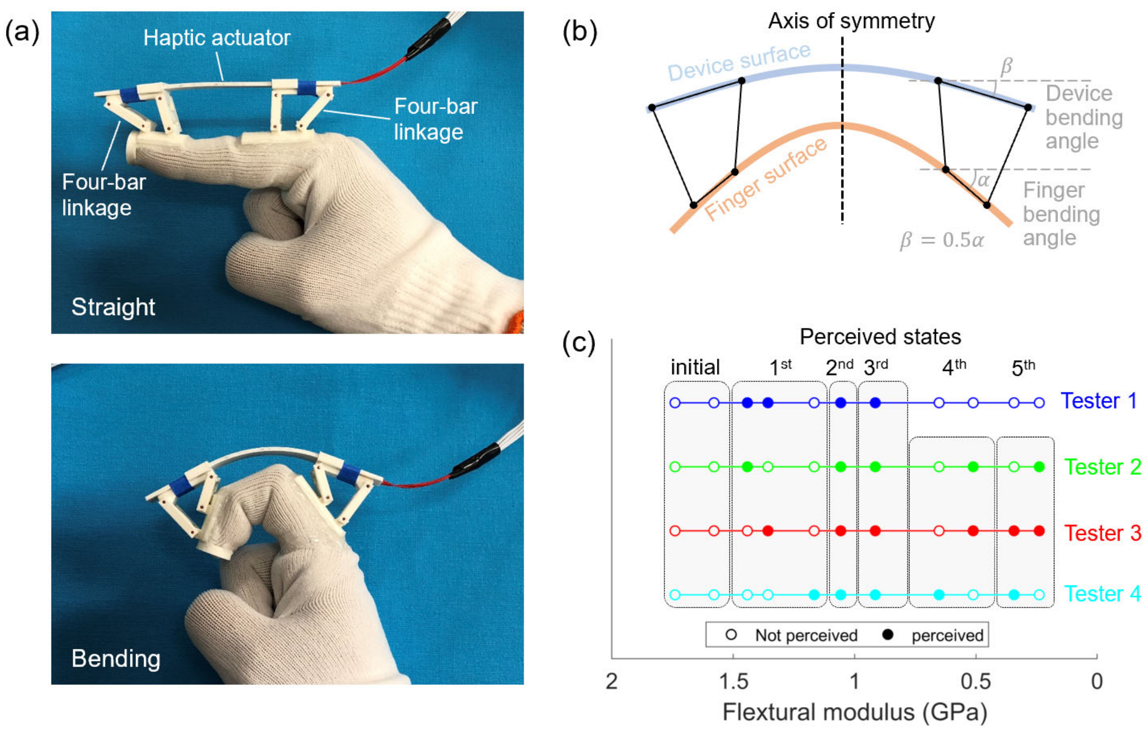

Figure 6.6: Haptic glove and human test. (a) Photographs and (b) schematic of four-bar linkages connecting the haptic device to finger. (c) Human test results with perceived stiffness states.

In the human test, we asked each of four testers to put on the haptic glove. The temperature of the device was increased from room temperature to 80 ℃ with an increment of 5 ℃. Each time when a new temperature was reached, the tester was asked to bend the finger for several times and tell if there was a feeling of less stiffness compared to the last state. If the tester felt less stiffness, the tested state was marked as perceived, otherwise marked as not perceived. The results from the four testers are shown in Figure 6.6(c), in which the temperature scale was converted to flexural modulus scale based on the results in Figure 6.5(b). As shown in the figure, most testers can perceive at least four different stiffness states, and the commonly perceived states can be divided into five regions. The results can be a reference when operating this device in real applications for different haptic feelings.

Chapter 6, in part, is a reprint of the material as it appears in *Advanced Functional Materials*, 2018, Zhenghui Wu, Yichen Zhai, Weichuan Yao, Naresh Eedugurala, Song Zhang, Xiaodan Gu, Jason D. Azoulay and Tse Nga Ng. The dissertation author was the secondary investigator and author of this paper.

6.4 References

1 O. T. Bruns, T. S. Bischof, D. K. Harris, D. Franke, Y. Shi, L. Riedemann, A. Bartelt, F. B. Jaworski, J. A. Carr, C. J. Rowlands, M. W. B. Wilson, O. Chen, H. Wei, G. W. Hwang, D. M. Montana, I. Coropceanu, O. B. Achorn, J. Kloepper, J. Heeren, *et al.*, "Next-generation in vivo optical imaging with short-wave infrared quantum dots," *Nat. Biomed. Eng.*, vol. 1, no. 4, p. 0056, 2017, doi: 10.1038/s41551-017-0056.

2 G. Hong, S. Diao, J. Chang, A. L. Antaris, C. Chen, B. Zhang, S. Zhao, D. N. Atochin, P. L. Huang, K. I. Andreasson, C. J. Kuo, and H. Dai, "Through-skull fluorescence imaging of the brain in a new near-infrared window," *Nat. Photonics*, vol. 8, no. 9, pp. 723–730, 2014, doi: 10.1038/nphoton.2014.166.

3 R. Nachabé, B. H. W. Hendriks, M. van der Voort, A. E. Desjardins, and H. J. C. M. Sterenborg, "Estimation of biological chromophores using diffuse optical spectroscopy: benefit of extending the UV-VIS wavelength range to include 1000 to 1600 nm," *Biomed. Opt. Express*, vol. 1, no. 5, p. 1432, 2010, doi: 10.1364/BOE.1.001432.

4 R. H. Wilson, K. P. Nadeau, F. B. Jaworski, B. J. Tromberg, and A. J. Durkin, "Review of short-wave infrared spectroscopy and imaging methods for biological tissue characterization", doi: 10.1117/1.JBO.20.3.030901.

5 H. Akbari, Y. Kosugi, K. Kojima, and N. Tanaka, "Detection and analysis of the intestinal ischemia using visible and invisible hyperspectral imaging," *IEEE Trans. Biomed. Eng.*, vol. 57, no. 8, pp. 2011–2017, 2010, doi: 10.1109/TBME.2010.2049110.

6 S. Shang, Z. Chen, Y. Zhao, S. Yang, and D. Xing, "Simultaneous imaging of atherosclerotic plaque composition and structure with dual-mode photoacoustic and optical coherence tomography," *Opt. Express*, vol. 25, no. 2, p. 530, 2017, doi: 10.1364/OE.25.000530.

7 C. W. Carpenter, S. T. M. Tan, C. Keef, K. Skelil, M. Malinao, D. Rodriquez, M. A. Alkhadra, J. Ramírez, and D. J. Lipomi, "Healable thermoplastic for kinesthetic feedback in wearable haptic devices," *Sensors Actuators A Phys.*, vol. 288, pp. 79–85, 2019.

8 C. Zweben, W. S. Smith, and M. W. Wardle, "Test Methods for Fiber Tensile Strength, Composite Flexural Modulus, and Properties of Fabric-Reinforced Laminates.," *ASTM Spec. Tech. Publ.*, no. 674, pp. 228–262, 1979, doi: 10.1520/stp36912s.

Appendix A

Advanced Printing System
Operation Manual

Yichen Zhai

February 2021

Chapter A.1 – Primary operations

The Advanced Printing System (APS) is a hybrid printing system with combined printing methods, including two FDM nozzles and two pneumatic extrusion nozzles. The system is modified based on a Raise3D N2 printer. The FDM printing process follows the traditional printing methods. For the operations, refer to the manuals on the website of Raise3D:

https://support.raise3d.com/list.html?cid=3&pid=218.

This manual mainly gives the process to operate with pneumatic printing. The two types of printing can be combined in one continuous printing flow. However, this is not recommended, as there will be complex calibration of the relative positions of all the nozzles and calculation of clearance. Improper work flow could potentially cause issues.

A.1.1 Compressed Air Supply

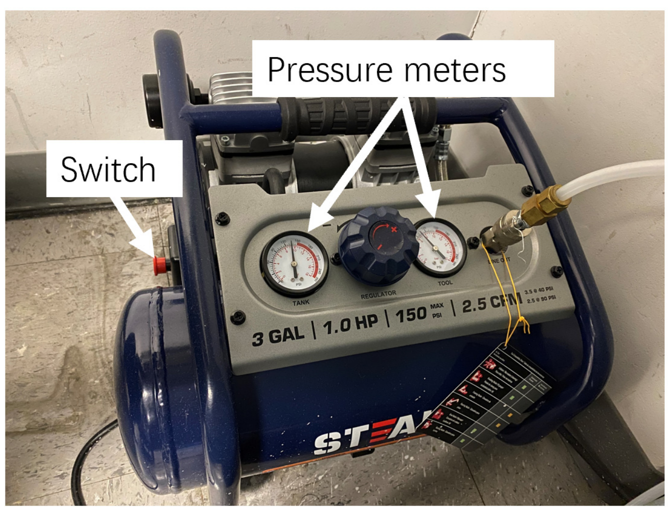

Figure A.1: Control of air compressor.

The extrusion is powered by high-pressure air supply from the air compressor, which is located at the corner on the left of the fume hood in 1512. The switch is shown as the red button in Figure A.1. Pulling out is to power on and pressing in is to power off. Regularly check the pressure meters to make sure:

The left meter is in the range of 120~150 psi (this is the inner setting of the equipment).

The right meter is in the range of 100~120 psi (this can be turned by the central regulator).

If the left value is lower than 120 psi for a long time and the pump still does not cut-in, check the switch. If the switch is already on but it still does not work, replace the compressor.

Attention: If the left value is obviously higher than 150 psi, which is in the red region, unplug immediately. DO NOT switch off and DO NOT depressurize manually. Leave the compressor free for several days to depressurize naturally, then replace it.

Attention: Always treat the compressor as a potential explosive. Always avoid heating and impact.

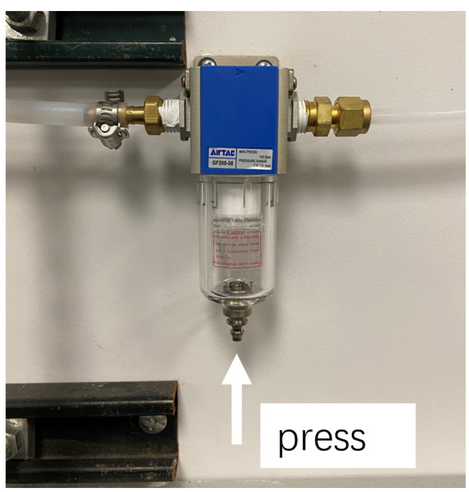

Figure A.2: Filter of compressor air.

The compressor can be regularly on. If the pneumatic printing mode is not used for months, the compressor can be powered off. However, avoid switching on and off too frequently.

The high-pressure air tube goes through a filter which is attached on wall to the left of the printer, as shown in Figure A.2. Regularly press the bottom switch to release the collected dust and moisture.

A.1.2 Powering on the Printer

The main power of the printer is controlled by the emergency stop located to the right of the printer. The added extra functions are powered through the outlets in the back, including two ports for the two dispensers, one for the pneumatic nozzle heater, one for the pneumatic syringe heater, and one for the UV light power supply. The switches are shown in Figure A.3.

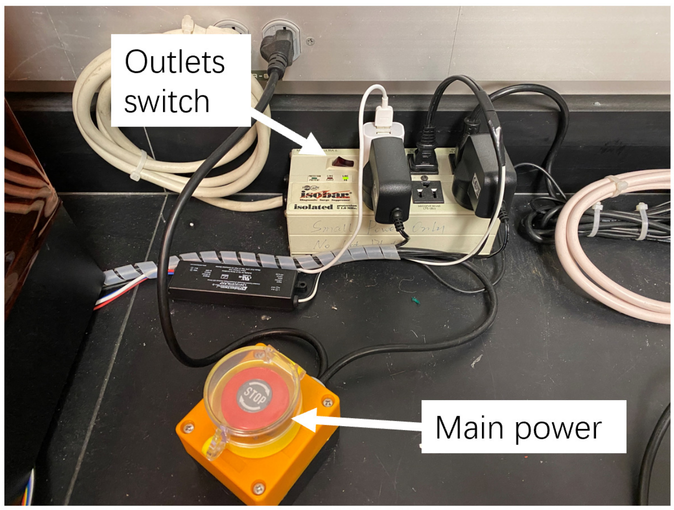

Figure A.3: Switches of the printing system.

If only FDM printing mode is used, turn on main power only by rotating the emergency stop button. To turn off, press down the stop button.

If the pneumatic printing mode is used, turn on both the main power and the outlets switch. Then turn on both the two dispensers on the left of the printer by pressing the power buttons, as shown in Figure A.4.

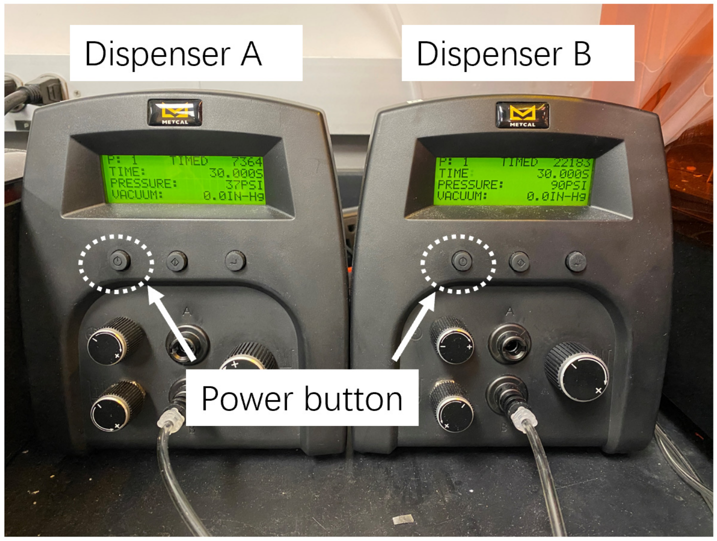

Figure A.4: Power button of dispensers.

Attention: In any cases, DO NOT keep the outlets switch on unattended especially overnight.

The dispensers contain valves and pressure regulators inside to control the air supplied to the extrusion syringe. Other operations of the dispensers are shown in Figure A.5. There are four modes, only “purge” and “timed” are used in all printing usages. Press the middle button twice to shift between the two modes. Except calibration (explained in section **A.2.5**), always keep the mode in “purge”. By turning the pressure adjusting knob, the pressure can be changed. After changing pressure, press the purge button A or B on the APS controller (shown in section **A.1.3**) to stabilize the pressure, otherwise the displayed pressure is not the real current pressure.

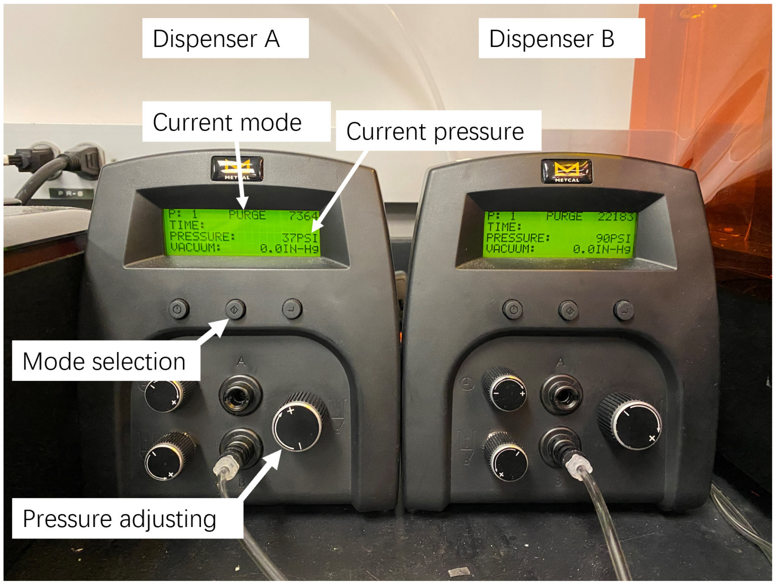

Figure A.5: Operations of dispensers.

Attention: DO NOT set any pressure higher than 90 psi.

A.1.3 APS Controller Operations

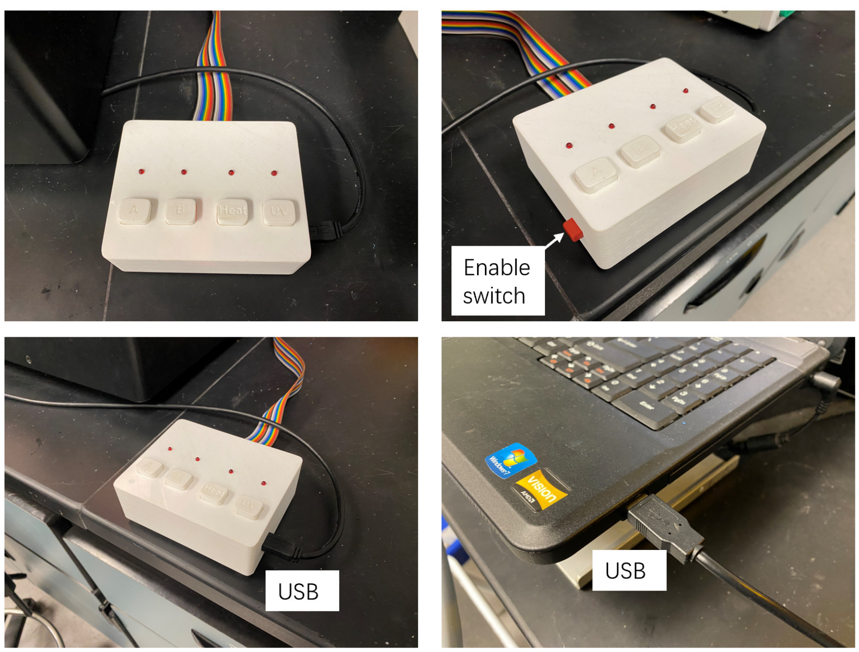

Figure A.6: Sketch of APS controller.

The APS controller is the white box shown in Figure A.6, which controls all the functions related to pneumatic extrusion, including syringe heater, nozzle heater, Z level calibration, UV light and fan, and extrusion signal to A and B dispensers.

There are four buttons with four LED indicators. The functions of the buttons from left to right are purge dispenser A, purge dispenser B, turn on/off syringe/nozzle heaters together, turn on/off UV light.

When the dispenser is set to "purge" mode, by holding the purge buttons on APS controller, the dispenser keeps purging to supply air to the syringe. When the dispenser is set to "timed", by pressing the purge button once, the dispenser will purge for the preset time period (preset to 30 sec). Note that besides pressing the physical buttons to extrude, the extrusion can also be controlled in the G-code. When commands "A1" or "B1" is executed in the G-code, the A or B dispenser will keep purging, which will be stopped by executing commands "A0" or "B0". On the left of the APS controller, there is a red enable switch button. When the button is pressed to pop-up position, the extrusion of both dispensers will be disabled. At this time, neither the purge buttons nor G-code is able to control the extrusion. This design is for the emergency situations that the nozzle leaks too much so the extrusion must be stopped immediately.

By pressing the heater button once, the heater can be shifted between on and off states. When in on state, the LED blinks when the current syringe temperature has not reached the target temperature. When it reaches, the LED will keep solid on.

By pressing the UV button once, the UV light with the fan can be shifted between on and off states. The LED keeps solid on. Note that if either the front or side door of the printer is opened, the UV light will be cut off for safety. When the door is closed, the UV light will come back again.

The values in the APS controller are set and monitored by a computer via COM serial communication. The baud rate is 250,000 bps. Before setting, check the USB connection on both sides of the APS controller and the computer. Then start the serial monitor in the sequence shown in Figure A.7.

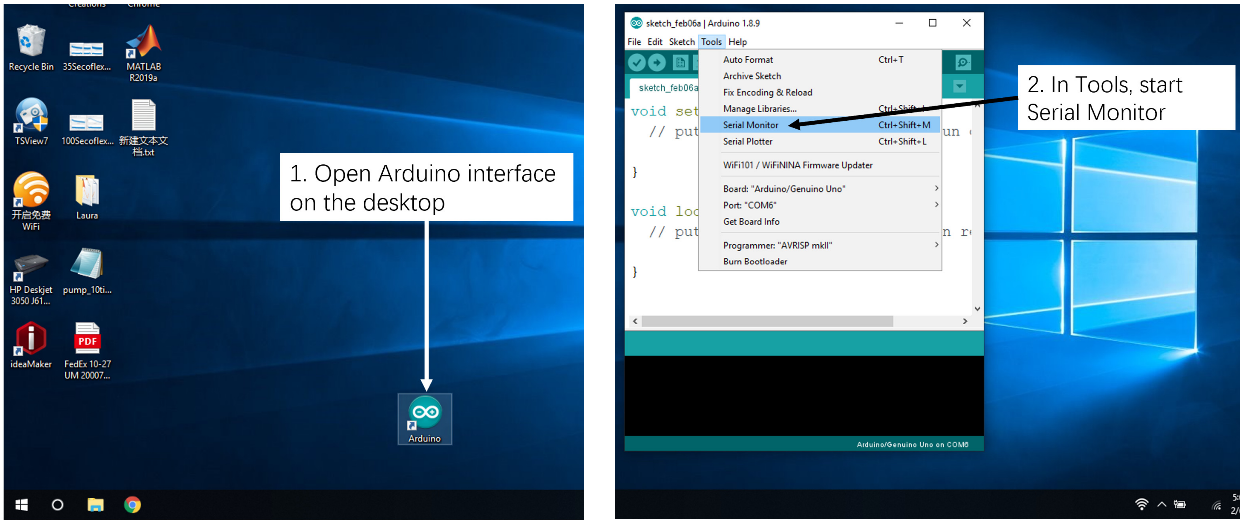

Figure A.7: Initializing serial connection.

The interface of the communication with APS controller is shown in Figure A.8.

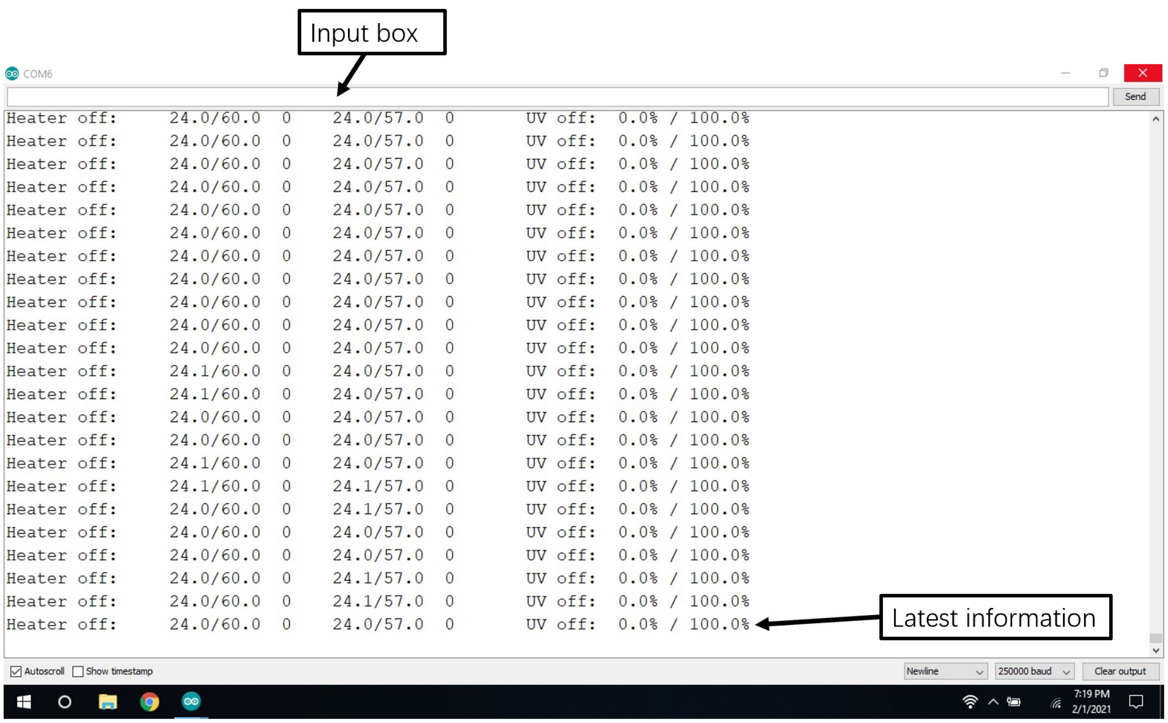

Figure A.8: Sketch of serial communication interface.

The communication is always in ASCII char format. The instructions for APS controller are limited to only numbers, which means a user only need to typed numbers in the input box to set any values and functions, but no letter is needed. The monitored information from the APS controller keeps refreshing automatically, so only the last row shows the real-time information. The details of the displayed values are explained in Figure A.9.

The explanations of all the values are shown in the next figure. When the physical buttons for heater or UV is pressed to turn on the functions, besides the LED indicators on the controller, the displayed information will also change to "Heater ON" and "UV ON", and the PWM power values will become positive integers higher than 0. The displayed states are shown in Figure A.10.

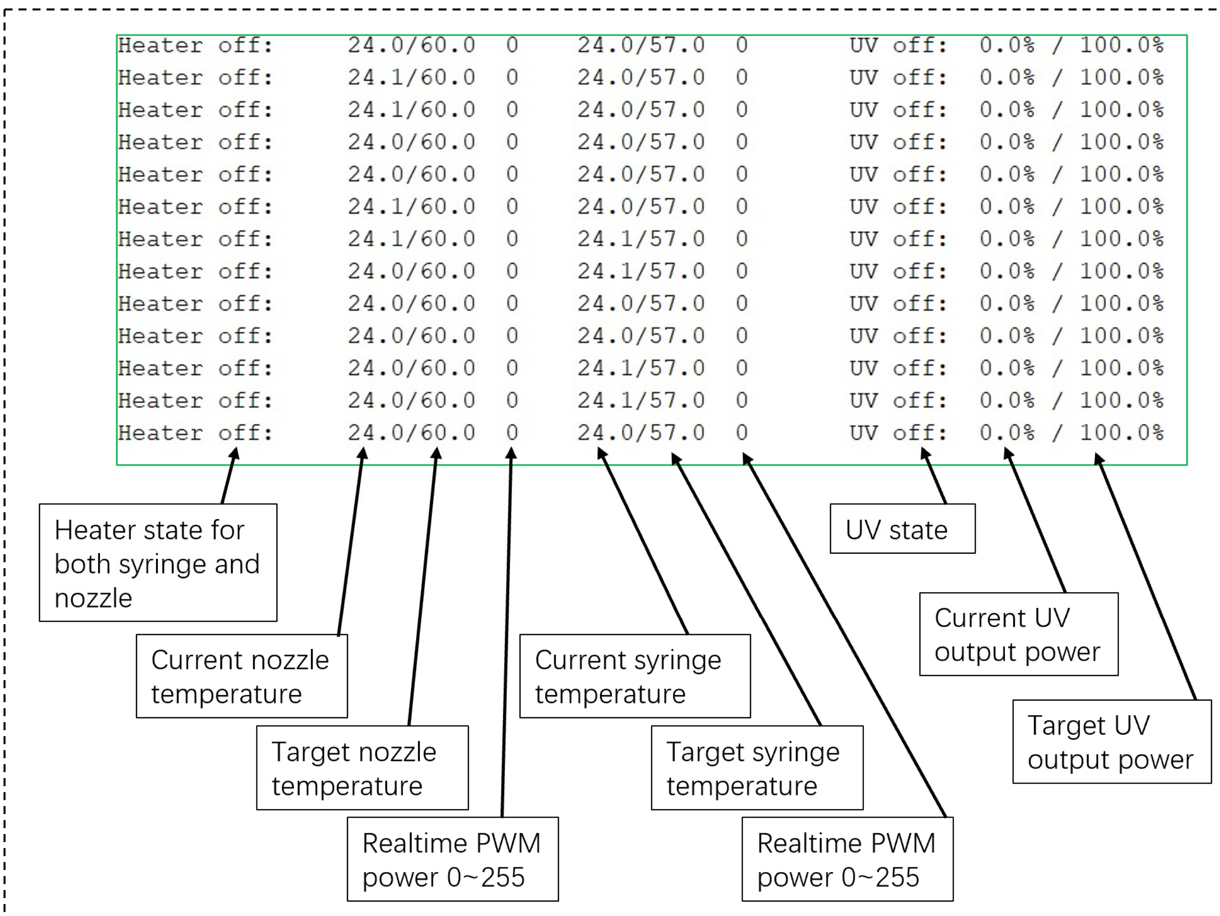

Figure A.9: Detailed explanations of serial communication interface.

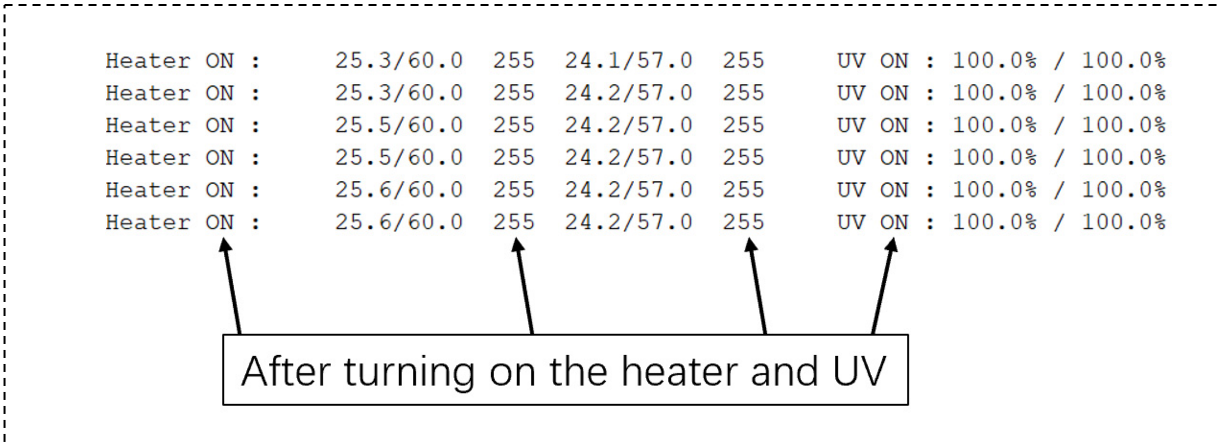

Figure A.10: Serial communication interface after turning on the heaters and UV lights.

To set any target values, type the numbers in the input box followed by the enter key. The control values are shown in Table A.1.

Table A.1: Instruction table of input values. Different ranges of input value controls different functions. Normally only the first three rows are used in most printing operations.

Values	Format	Function
0 ~ 60	integer or decimal	Set syringe heater target temperature, range 0~60 °C
100 ~ 160	integer or decimal	Set nozzle heater target temperature, range 0~60 °C
-0.1 ~ -100	integer or decimal	Set UV PWM output power, range 0%~100%
1000 ~ 1999.99	integer or decimal	Syringe heater PID, set P in 0~999.99, do not change
2000 ~ 2999.99	integer or decimal	Syringe heater PID, set I in 0~999.99, do not change
3000 ~ 3999.99	integer or decimal	Syringe heater PID, set D in 0~999.99, do not change
11000 ~ 11999.99	integer or decimal	Nozzle heater PID, set P in 0~999.99, do not change
12000 ~ 12999.99	integer or decimal	Nozzle heater PID, set I in 0~999.99, do not change
13000 ~ 13999.99	integer or decimal	Nozzle heater PID, set D in 0~999.99, do not change

-101 and -102	integer	Turn on and off showing force from nozzle load cell
5000 and 5001	integer	Turn on and off UV, the same as UV button
6000	integer	Display current PID values

Note:

1. Do not set temperatures higher than 60 °C for either nozzle or syringe heater.
2. The PWM values for UV light are in 255 levels, so the increment is about 0.4%. In this case, if the target is set to 0.3%, the output value will be rounded to 0.4%. If the target is set to 0.1%, the output value will be rounded to 0%. It is recommended to follow the increment for small values, such as 0.4%, 0.8%, 1.2%, 1.6% and 2.0%. For larger values like 5% or 10%, no need to follow.
3. The full power of the nozzle heater is 8 W, of the syringe heater is 10 W. The total consumption power of UV lights is 10 W, with a 30% ~ 40% light conversion efficiency.
4. The target temperatures and PID values are written in the EEPROM, which can be stored even the APS controller is powered off.

Chapter A.2 – Preparation for Printing

This chapter introduces how to load materials (viscos inks) into the dispensing syringe, attach syringe and substrate, initial settings in the systems before printing, and calibration of extrusion flow rate. The operations will be inside the printer. The touchable and untouchable positions in the printer will be introduced first to avoid potential damages and injuries.

A.2.1 Touchable and Untouchable Positions

Attention: Always wear gloves when operating in printing processes.

In preparation for the printing, the front door and top cover can be opened in the way shown in Figure A.11. However, during printing they should remain closed.

Figure A.11: Opening door and cover of printer.

For more convenient operations around the print head, the print head assembly can be manually moved along XY directions. However, the stepper motors have breaking torque even when they are not rotating and the head is not being moved by g-code. At this time, forced dragging will result in serious problems. The motors should be disabled first before any manual motion. The operations are demonstrated by Figure A.12 above with the following sequence.

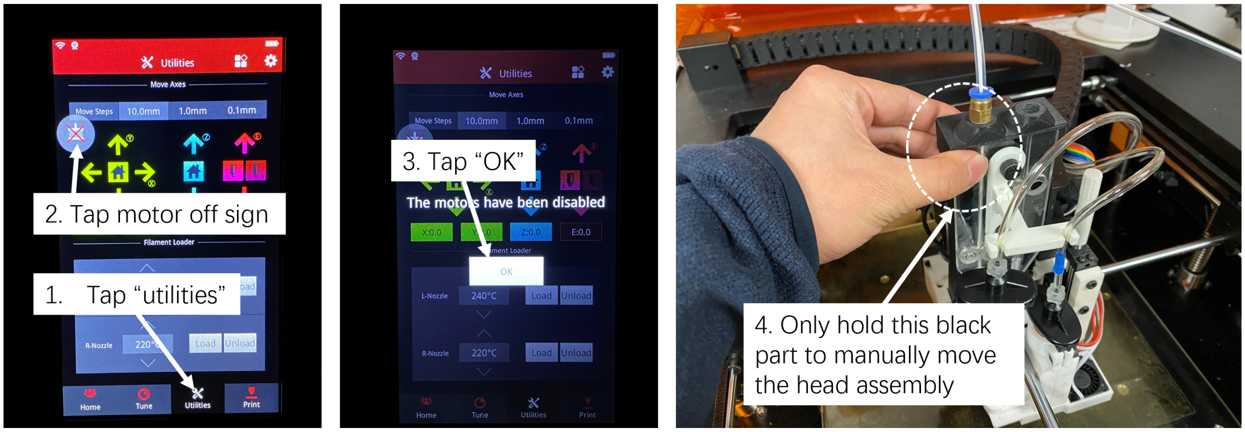

Figure A.12: Turning off stepper motors and moving print head manually.

1. On the touch screen, tap "Utilities" tab.
2. Tap the sign of motor with cross.
3. Tap "OK".
4. Manually move the head slowly by holding the position shown in the figure. Do not hold anywhere else. Avoid moving fast, since the motors will generate high voltage and damage the electric controller.

Attention: The untouchable parts in the printer are shown in Figure A.13.

1. Do not touch the two brass clips on the side door with bare hands. The electric static discharge will damage the inner circuit.
2. Do not touch the smooth rods and screw rods during printing progress, which may cause injury.
3. Do not touch the timing belts, which will affect the accuracy of printing.
4. Do not touch or drag any wires on the right side of the head assembly. The broken of any wire will cause serious malfunction or irreversible damage.

5. Do not touch the UV LED lights around the nozzle. Do not touch the nozzle heater wires. Do NEVER sense the temperatures of the FDM and pneumatic nozzles by touching.

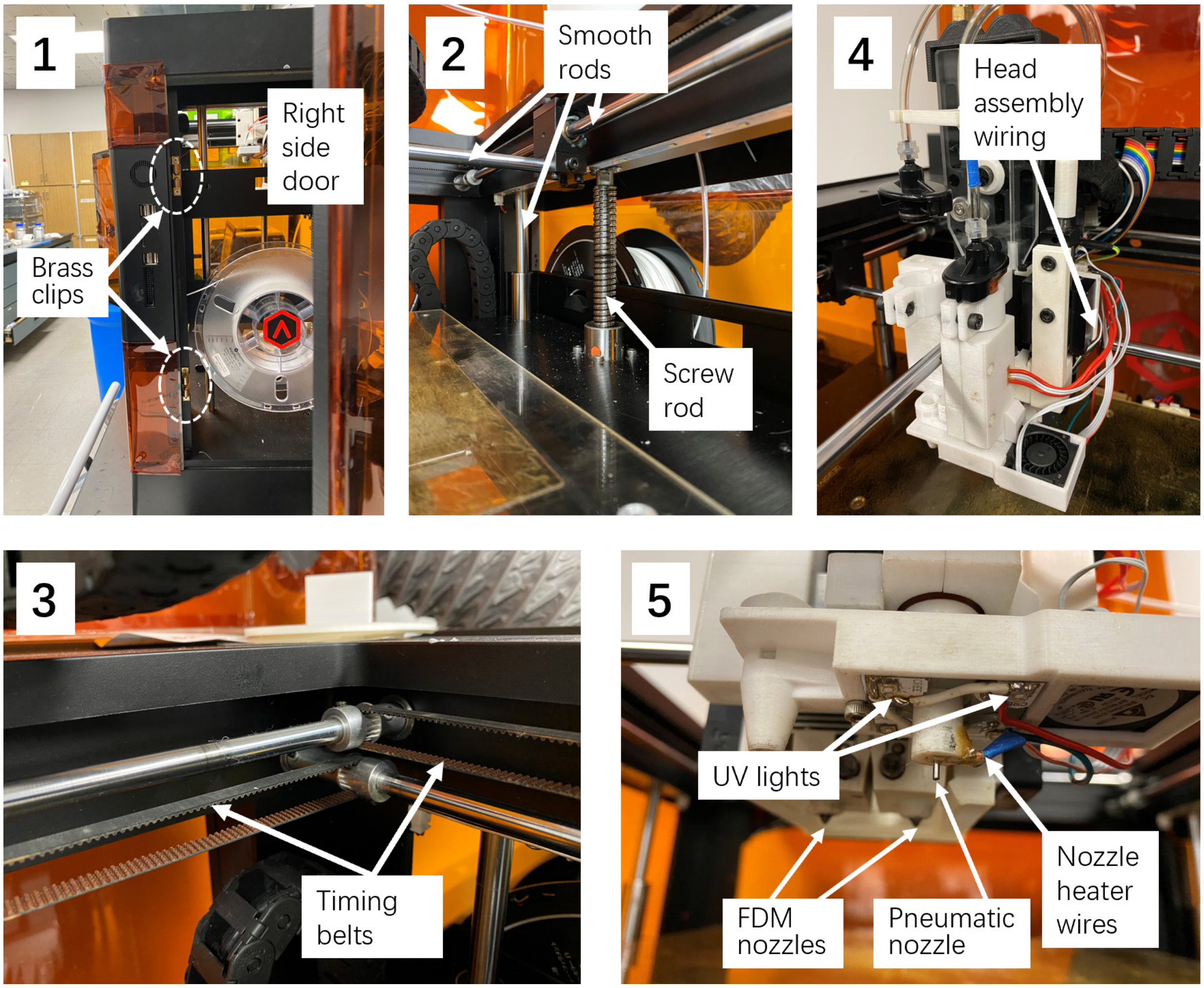

Figure A.13: Untouchable positions.

A.2.2 Loading Materials

Figure A.14 shows the parts related to dispensing syringe. Before loading any material, screw in the orange seal cap on the front side. Then pour the material into the syringe from the back opening. Try to fill the material directly into the bottom part of the syringe, and avoid stick to the inner wall in the upper part. A glass or aluminum foil funnel may help. After filling, do not put the piston wiper in. The material must be settled and degassed first. For thermal melting materials like LCE which are in extremely high viscosity (over 1 MPa·s), hold the syringe vertically in the oven for 1~3 days at 80 °C. For other gel materials with lower viscosity like PDMS, use the centrifuge.

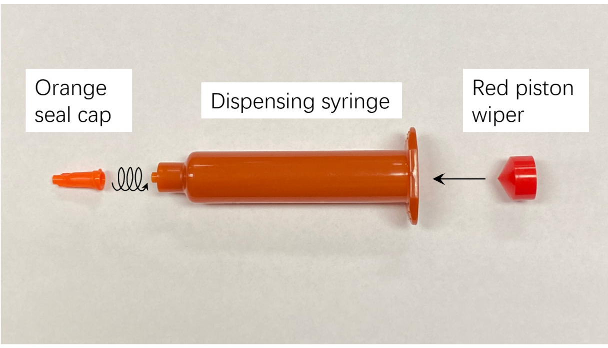

Figure A.14: Sequence to assemble dispensing syringe for storage.

Note: Single substance like PDMS can be centrifuged for long time, while centrifuging mixtures like silver paste will result in phase-separation. For mixtures, degas in vacuum first. After filled into the syringe, limit the centrifuge time within 15 sec at 2400 rpm to settle.

After settling, put the piston wiper in. The manufacturer has two kinds of piston wipers, the red one can be used for any materials especially high-viscos LCE. The white one can only be used for low-viscos materials. Use the L-ranch shown above to push it in. Squeeze all the air between the material and piston out. This requires some practice of hand operations.

Attention: The air gap must be fully squeezed out. It does not damage the hardware, but will result in flow rates completely out of control, and will ruin the printed workpiece. For materials like LCE which may contain residuals of solvent, during heating and printing, the solvent will vaporize and generate a large air gap. To avoid this, the original material has to be heated in vacuum for one day or more, then after loaded into syringe, heat again for more days to fully remove the solvent.

A.2.3 Installing Syringe

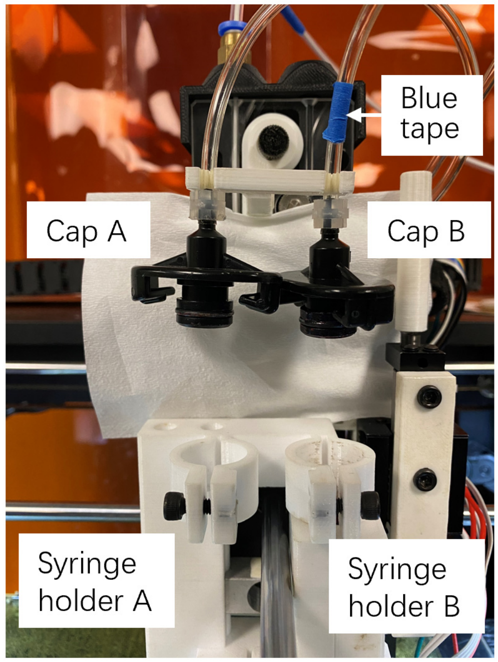

Figure A.15: Syringe holders and caps on print head assembly.

Figure A.15 above shows the print head assembly. There are two syringe caps, which are connected to the dispenser A and B respectively, and deliver the compressed air to two corresponding syringes. Cap B is marked with blue tape on the tube. In the lower part there are two syringe holders. It is recommended to always use cap A for syringe A, and cap B for syringe B. The sequence can be swapped sometimes in special situations, but not recommended. There are syringe heaters and nozzle heater on the syringe holder B, but no heater on holder A. During operation, the nozzle of syringe B is always regard as the main nozzle for coordinate calculations, and nozzle A is the extra nozzle. For the main materials like LCE and PDMS, use holder B. For other assistant materials and pollutive materials like silver paste, use holder A. If both two holders and nozzles are used together, remember to align the nozzle tips to the same Z axis level when installing the syringe.

The sequence of installing extrusion syringe is shown in Figure A.16.

1. Screw the syringe needle into the syringe and tighten. The system is designed for 18-gauge syringe needles only. Do not use any other sizes. To identify, the color of the needle hub is in green. The outer diameter is 1.27 mm and inner is 0.838 mm.
2. Fasten the corresponding syringe cap by pushing in and rotate for half-circle.
3. Check and loosen the screws which are mentioned in step 4. Then insert the syringe into the corresponding holder. Use one hand to hold the syringe cap and push down, use another hand to hold the ring of the holder or the white heater block. Do not hold the bottom UV light part. During pushing down, the resistance may be large, then rotate the syringe back and forth and push down.
4. Check if the needle is exposed by about 4 mm at the bottom. A variation of ± 1 mm is acceptable. Then tighten the screws with corresponding L-wrench shown in the figure next. If the syringe heater will be used, tighten only the two M3 screws on the heater and keep the M4 screw loosened on the holder ring. If the heater will not be used, it is in opposite way. Tighten only the M4 screw.

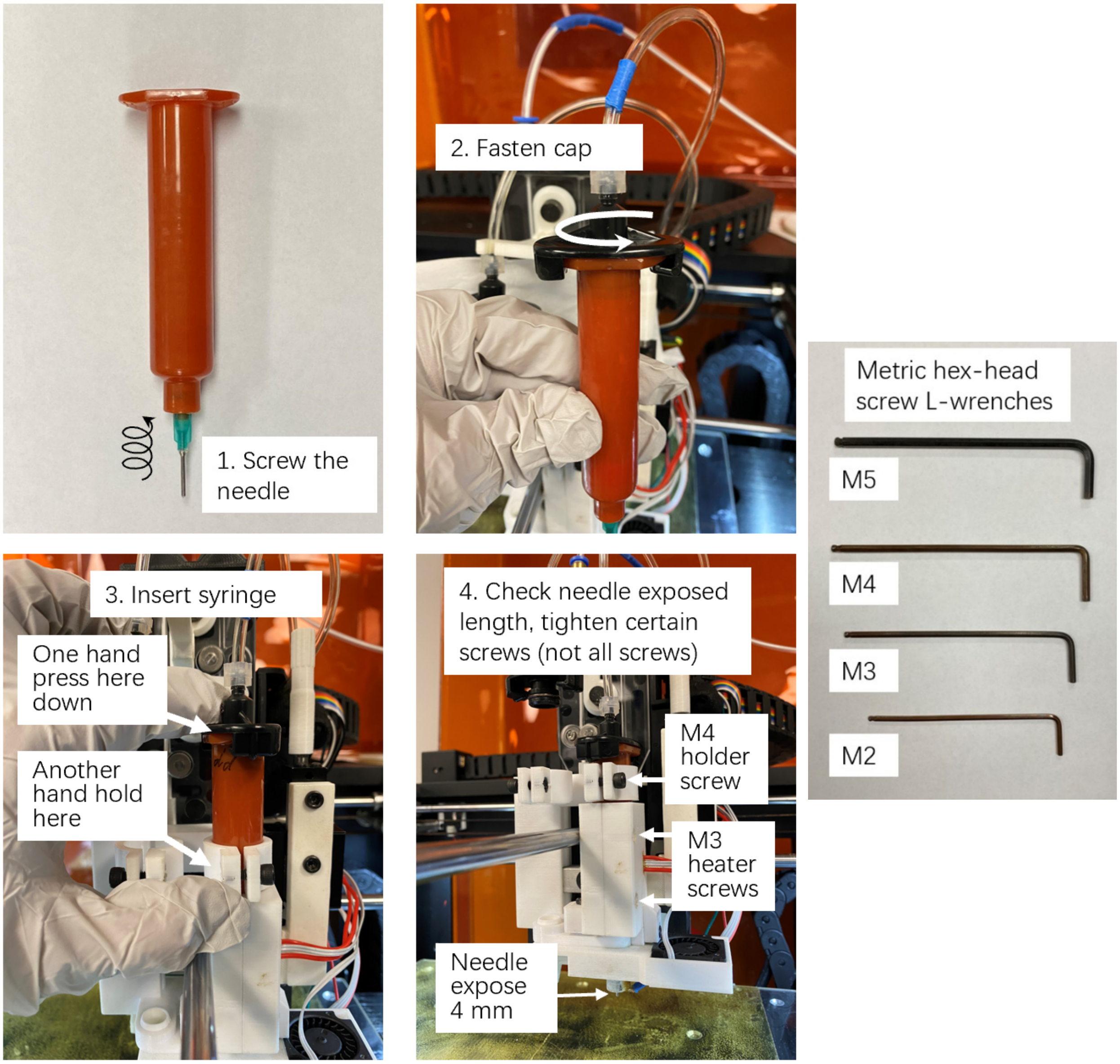

Figure A.16: Operation sequence to install syringe on print head and with different L-wrenches.

After installing the syringe, adjust the relative height between the FDM nozzles and pneumatic extrusion nozzles by rotating the positioner knob shown in Figure A.17. In this figure only nozzle B is installed, while the position A is blank. If only pneumatic printing is used, make sure the pneumatic nozzles are at least 3 mm lower than the FDM nozzles. If only the FDM nozzles are used, do not install the syringe and needle, and make sure the extrusion nozzle holder parts (the white cylinder nozzle holder) are at least 5 mm higher than the FDM nozzles. If both are used in a single printing progress (G-code file), adjust them to the same Z level.

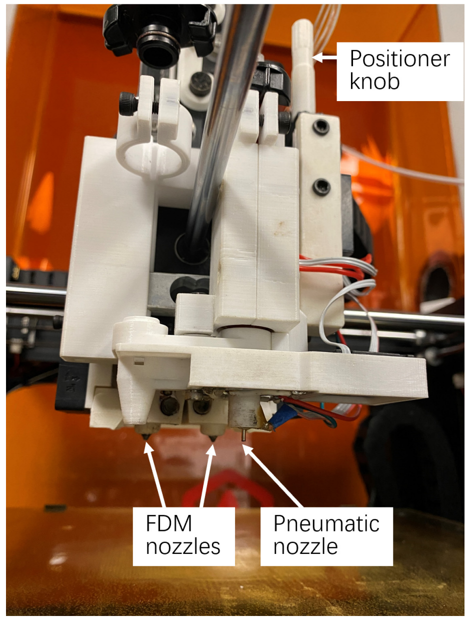

Figure A.17: Positioner to adjust the relative height position of nozzles.

A.2.4 Attaching substrate

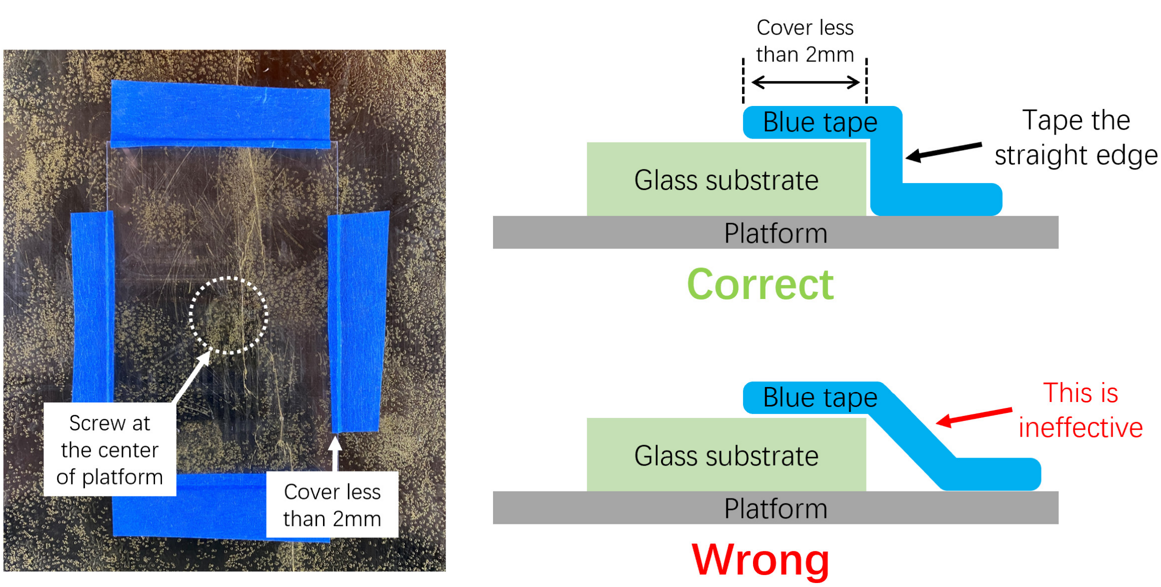

Figure A.18: Attaching glass substrate on platform.

75*50 mm glass slides are recommended as the substrate for printing. As shown in Figure A.18, there is a screw at the center of the platform, which is painted black. Align the center of glass slide to the screw, and use 3M blue mounting tape to tape all 4 edges of the glass. Do not only tape less than 3 edges, and do not only tape the corners, which are both useless to fix the substrate under the strong shear force of printing. When taping, cover less than 2 mm of the top edge of the glass. Remember to also tape the straight edge of the glass as shown in the side view schematic above, otherwise it does not provide enough force. The direction of the glass slide can be both landscape or portrait, which is based on the certain pattern design.

A.2.5 Setting printing conditions and testing flow rate

For pneumatic extrusion, the flow rate is constant and cannot be digitally controlled during printing. The flow rate is different with different materials, batches, temperature, suppling pressure and degradation of material. Before generating the printing G-code file, the flow rate has to be experimentally measured, and the value will be used in the file.

First, set the temperatures of extrusion nozzle and syringe if the material needs to be heated, the method is in **Section A.1.3**.

For LCE with DP=8, set the nozzle temperature to 55~60 °C, and set the syringe temperature to 50~55 °C. For example, in the input box of the serial monitor, type "155" followed by ENTER key to set nozzle, type "50" followed by ENTER key to set syringe.

For LCE with DP=7, set both the nozzle and syringe temperatures to 35~40 °C.

After setting temperatures, press the button "heat" on the APS controller once to turn on the heating. The LED will blink.

Attention: As shown in Figure A.19, after turning on heaters, keep looking at the two current temperatures for 10~20 seconds to see if they are increasing. The nozzle temperature increases about 20 times faster than the syringe temperature. Normally both should increase. If any of them is not increasing, check the outlets switch and check if all 5 items are plugged in. If the outlet is normal and the temperature still remains the same, it means the feedback signal from the temperature sensor is abnormal. Turn OFF the heater and switch OFF the outlets immediately!

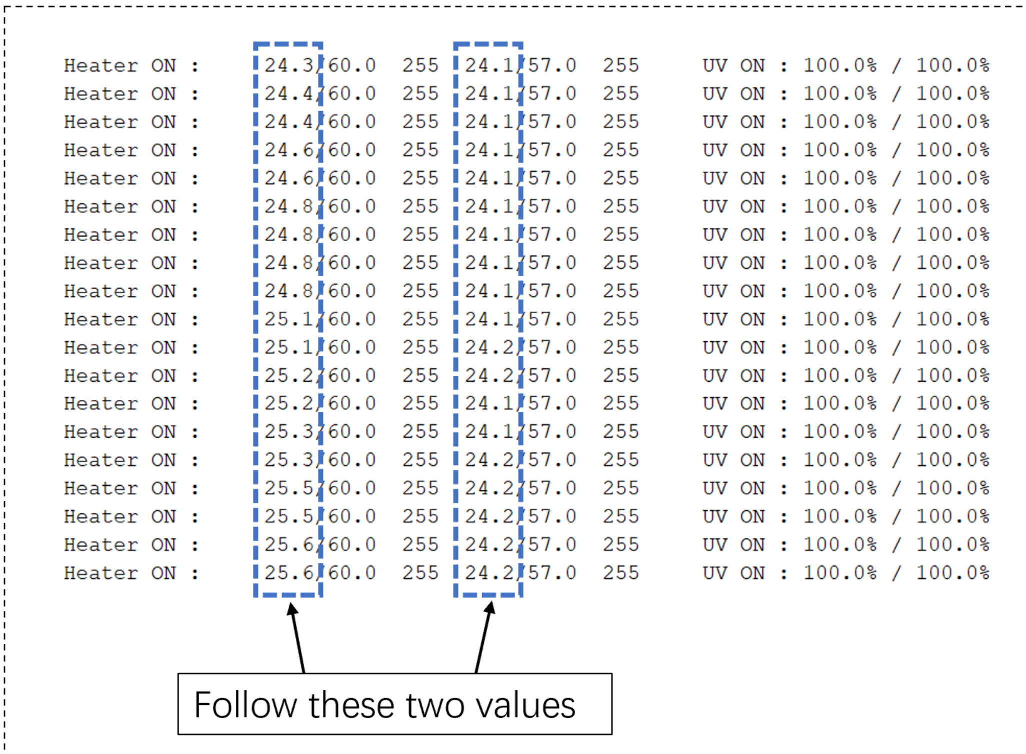

Figure A.19: Current temperatures of nozzle and syringe heaters.

After heating started, wait for 5~10 minutes to reach the target temperature. Then adjust the output pressure of the dispensers (Figure A.5). For LCE with DP=8, keep the pressure at 90 psi. For LCE with DP=7, adjust the pressure to 50 psi or lower. For non-flowing PDMS, it is also below 50 psi. Flowing PDMS (Sylgard 184) is not suitable for printing. The viscosity is too low, so the extrusion rate is too high to control.

Note that after adjusting the pressure knob, the displayed pressure does not change automatically. Short press the extrude button A or B on the APS controller once, then the displayed pressure will be updated.

The flow rate is determined by measuring the weight of extruded material in 30 seconds. Before this step, repeatedly press the extrusion button A or B on the APS controller for many times, and several seconds for each time. Use wiper to wipe away the extruded material. This is to stabilize the extrusion flow rate. Then follow the following steps and Figure A.20:

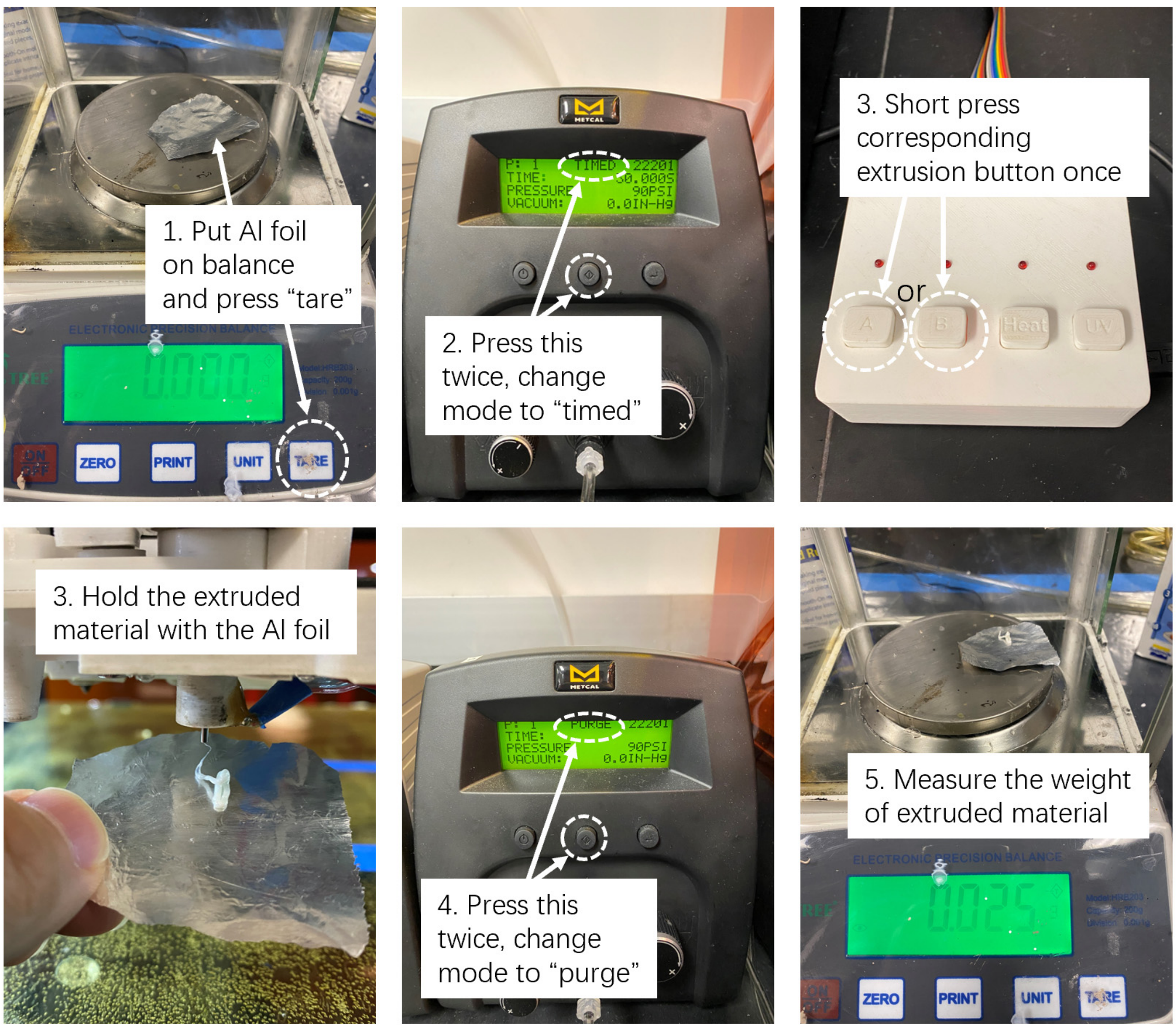

Figure A.20: Operation sequence to measure flow rate.

1. Prepare a small piece of aluminum foil, the weight is about 100 mg. Put it on the electronic

balance and press "TARE" to set the value to 0.

2. Press the mode selection button on the dispenser twice to change the mode to "timed".
3. Put the aluminum foil below the nozzle. Then short press the extrude button once. The system will keep extrude for 30 seconds automatically.
4. Press the mode selection button on the dispenser twice to change the mode back to "purge".
5. Measure the weight of the extruded material with the balance.

Attention: Do not forget step 4. Always check if the dispensers remain in "purge" mode. Failure to perform this step does not damage the system, but will ruin the printed workpiece.

Note: If LCE is accidently dropped on the platform, use wiper dipped in IPA to wipe away. IPA can reduce the stickiness of LCE but cannot dissolve it. However, do not use IPA to wipe the nozzle.

When the density of material is 1~1.2, a flow rate of 20~30 mg/30 sec is preferable. If the flow rate is too high, reduce the pressure and test the flow rate again. If the pressure is as low as 25~30 psi, and the flow rate is still obviously higher than 50 mg/30 sec, the material is not suitable for printing. If the material is very viscous, such as LCE with DP=8, and if the pressure is already set to 90 psi, a flow rate between 15~20 mg/30 sec is acceptable. However, for such situation, during printing, any fluctuation will affect the flow rate a lot, and it often tends to decrease to even lower. In such cases, the printing process should be monitored by user, and the printing feed rate should be changed along with the printing (explained in **Section 4.2**). If the flow rate is below 15 mg/30 sec at 90 psi, printing with this material is not recommended.

Chapter A.3 – Pattern Design

The printer is running with Marlin firmware. The features of Marlin are explained on this page: https://reprap.org/wiki/Marlin

The printing process is controlled by a file written in G-code. The commands of G-code are listed on this page: https://reprap.org/wiki/G-code

To comply with pneumatic extrusion function, some customized codes are added. Code "A1" and "B1" are to start the extrusion of nozzle A and B respectively, while code "A0" and "B0" are to stop the extrusion. After extrusion started, if the stop commands are not executed, the nozzles will keep extrusion.

The customized G-code file for pneumatic extrusion printing is generated by a MATLAB program. The examples of the main program and customized functions are explained in **Sections A.3.2~A.3.4**.

A.3.1 Basic Lines in the Pattern

In the design of G-code with MATLAB, the basic variable is a pattern matrix. The size of the matrix is N*4, where N is the number of the individual traces in the pattern.

```
mm=[0, 0, 5, 0;...
    0, 0.6, 5, 0.6;...
    0, 1.2, 5, 1.2;...
    0, 1.8, 5, 1.8;...
    0, 2.4, 5, 2.4];
```

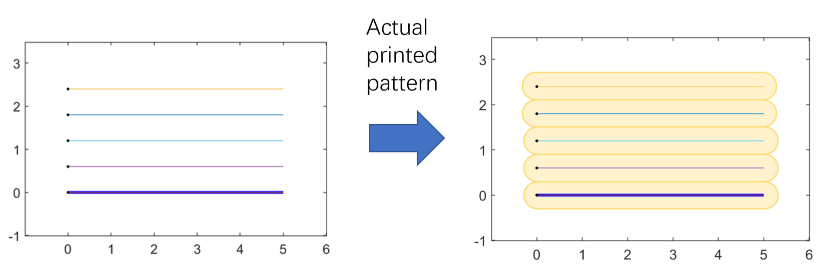

Figure A.21: Using pattern matrix to generate parallel lines.

The example in Figure A.21 is to fill a block in 5*2.4 mm size (each edge will be 0.3 mm larger, and the actual size is 5.6*3 mm). Note that with the 18-gauge needle, the distance between neighboring lines is always set to 0.6 mm, although the ID is 0.838 mm. There are five rows in the matrix. In each row, there are four values as (x1, y1, x2, y2), where (x1, y1) is the starting point and (x2, y2) is the ending point of a line. In the preview plot, the blue thick line is the first line of the pattern, and the black dot on each line marks the starting point of this line. In this file, the five lines are printing in one-way, meaning that after drawing a line from left to right, the nozzle stops extrusion, and then lifts in Z level and performs a free movement to the left-side starting point of the second line. Note that to many start/end points and free movements may blur the pattern. The matrix in Figure A.22 shows an improved pattern, which uses two-way printing pattern.

```
mm=[0,0,5,0;...
    5,0.6,0,0.6;...
    0,1.2,5,1.2;...
    5,1.8,0,1.8;...
    0,2.4,5,2.4];
```

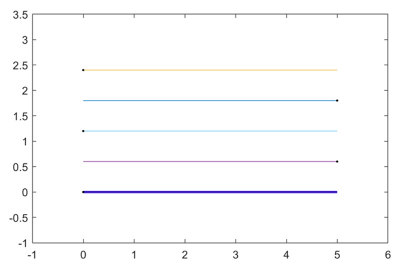

Figure A.22: Using pattern matrix to generate two-way parallel lines.

In the two-way patterns, the nozzle keeps extruding and moving from the end point of the previous line to the start point of the next line. The whole pattern is printed in back-and-forth sequences, and all the five lines are printed in one continuous path. The actual moving path is show in Figure A.23. Note that as long as the distance between the lines is 0.6 mm, there is no need to add the short vertical lines at then ends between the points. The printer will move automatically and continuously.

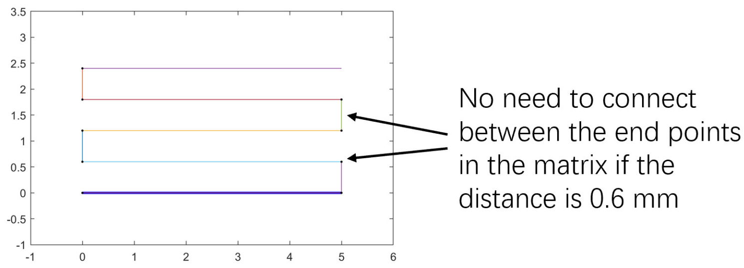

Figure A.23: Actual tool path of two-way patterns.

A.3.2 Main Program

The MATLAB codes consist two parts. The first part is to calculate a pattern matrix, which can be written either manually or by the functions. The second part is to write the G-code file. An example MATLAB program is in the attachments. Here each segment is explained in details.

```
clc;
clear;
close all;
```

Do not change. Initialize program.

```
xoff=132;
yoff=175;
```

Do not change. Offset of X and Y coordinates. When designing the pattern, the coordinates are all around the origin (0, 0), which is mapped to the center of the glass slide. However, on the actual platform, the coordinate (0, 0) is not the center but the lower left corner. This is to shift the coordinates.

```
Arate=40;
denA=2.5;

Brate=25;
denB=1.2;
```

30-second extrusion rate of nozzle A and B. Change the values to the extrusion rate tested in **Section 2.5**. For example, the 30-second extruded material was measured as 25 mg, and the material is LCE with a density of 1.2. It will be used at nozzle B position, so Brate is changed to 25, and denB is 1.2. Here nozzle A will not be used, so Arate and denA can be any values.

```
xA=-31.55;
yA=0;
```

Do not change. Offset of nozzle A with respect to nozzle B.

```
downA=0.04;
downB=0.17;
```

Z level offset due to homing-Z error and syringe thermally softened expansion error. If the syringe is heated to 55~60 °C, set the value to 0.15~0.17, so after homing Z, the nozzle will be lifted 0.15~0.17 mm higher as an updated Z home. If the syringe is not heated, set the value to 0.04~0.05. Here nozzle B will be used with LCE. It will be heated, so downB is set to 0.17.

```
Va=Arate/denA/1.05/0.1/0.6/30;
Vb=Brate/denB/1.05/0.1/0.6/30;
```

Do not change. Calculation of the printing velocity based on the extrusion rate. This velocity only corresponds to printing a trace with 0.6 mm width and 0.1 mm layer thickness. If the layer thickness is in other values, the velocity will be modified with multipliers in the functions later.

```
retreat=1.51;
retreat=retreat^2;
```

Do not change. Set threshold for the continuous movements between the end point and the next start point.

```
xb1=0+xoff;
yb1=-21+yoff;
```

Initialize the position for homing Z. Before printing, the nozzle will move to this position, lower itself to touch the platform. The touch force is measured by a load cell. Once it is in contact with the platform, it will stop and record the current Z level as zero level. The position should be selected close to the south or west edge of the glass, and should not be on the blue tape. Here it is selected as (0, -21) for nozzle B. If it is nozzle A, the nozzle A offset must be added as xa1=0+xoff-xA and ya1=-21+yoff-yA.

```
%%%%%%%%%%%%%% LCE 1 %%%%%%%%%%%%%%%

mm=[];
mm=[mm;bf(-20,-5.5,-6.6,-17.5,1,2)];
mm=[mm;bf(-6.6,17.5,6.6,-17.5,2,1)];

figure
plotpath(mm);
mm=mm+[xoff yoff xoff yoff];
LCE1=mm;
xlim([-38 38])
ylim([-25 25])
```

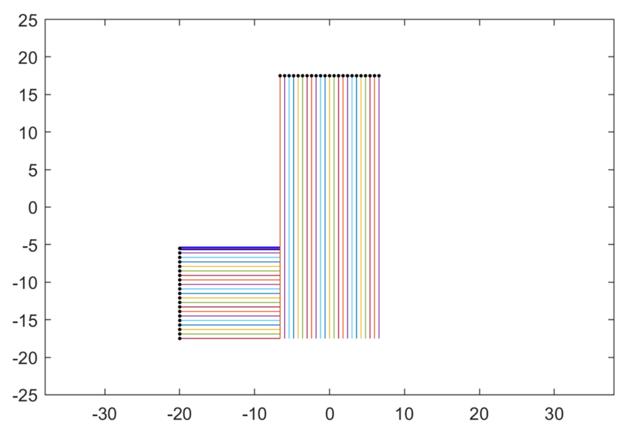

Figure A.24: Example of designing the first pattern.

Design of the first pattern. A preview of the pattern is shown in Figure A.24. mm=[] is to initialize a temporary matrix named as mm. The following lines are to add two independent basic shapes into this pattern. Function bf(-20,-5.5,-6.6,-17.5,1,2) is to generate and add the left horizontal block into matrix mm, and function bf(-6.6,17.5,6.6,-17.5,2,1) is to add the right vertical block. plotpath(mm) is a function to plot the tool path matrix automatically in the initialized figure. mm=mm+[xoff yoff xoff yoff] is necessary to shift the pattern from the origin to the center of the platform. Failure to perform this step will result in serious problem. LCE1=mm is to save the current temporary matrix to the working matrix LCE1. Note that as long as different shapes are all in the same single layer thickness and total layers, as many as individual shapes can be added in the same working matrix.

```
%%%%%%%%%%%%%% LCE 2 %%%%%%%%%%%%%%%%%%%%%%%%%
mm=[];
mm=[mm;bi2(-6.6+20,17.5,6.6+20,-17.5,1,2,55)];

figure
plotpath(mm);
mm=mm+[xoff yoff xoff yoff];
LCE21=mm;

mm=[];
mm=[mm;bi2(-6.6+20,17.5,6.6+20,-17.5,3,2,-55)];

plotpath(mm);
mm=mm+[xoff yoff xoff yoff];
LCE22=mm;

xlim([-38 38])
ylim([-25 25])
set(gcf,'Position',[300 50 500 800]);
```

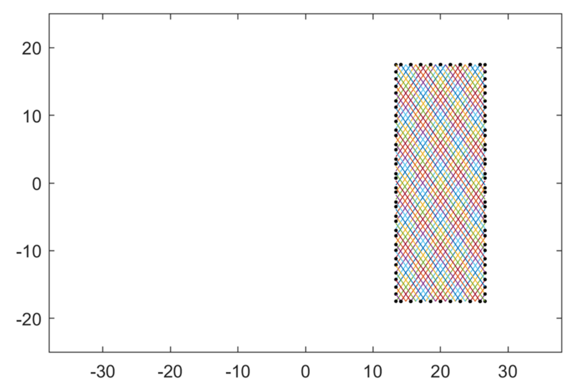

Figure A.25: Example of designing the second pattern.

This segment gives an example of a more complex pattern. Two different working matrices LCE21 and LCE22 are generated. A preview is shown in Figure A.25. The two patterns overlap at the same position. They both fill the same block, but the inclined directions are separated on odd and even number layers. In this case, although both matrices are to fill the same block, the infill are different between layers, so they should be separately saved in two matrices.

```
%%%%%%%%%%%%%%%% print  %%%%%%%%%%%%%%%%%%%%

fp = fopen(['gcode_example.gcode'],'wt');
gstart(2,2,down90,[xb1,yb1],1,fp,Vb);

for i=1:12
    layer=i*0.1;
    gcode(2,2,LCE1,layer,0.1,fp,Vb);
    gcode2ly(2,2,LCE21,LCE22,layer,0.1,fp,Vb);
end

gend([xoff,yoff],fp);
```

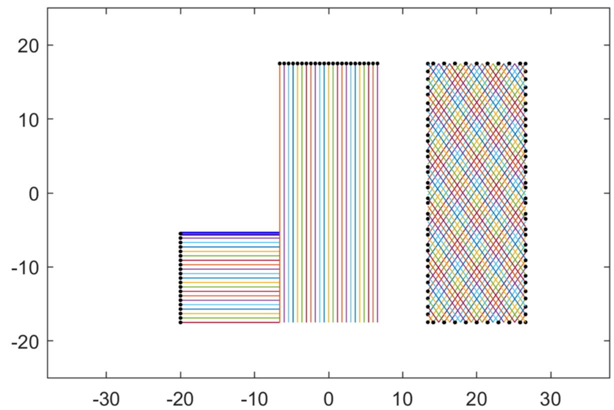

Figure A.26: Preview of the combined patterns.

This is the second part of the MATLAB codes, which is to write a G-code file with the generated patterns and initialized parameters in the first part. A preview of the whole pattern is shown in Figure A.26.

fp = fopen(['gcode_example.gcode'],'wt') is to initialize a file pointer. The file name gcode_example can be changed to anything and is recommend to change for each individual printing. However, the extension name .gcode must be added every time.

gstart(2,2,down90,[xb1,yb1],1,fp,Vb) is a function to add the initial operations into the G-code, which controls the homing Z of one nozzle, and printing of a dummy line to stabilize the liquid pressure inside this nozzle.

The for loop controls the writing of pattern in 12 layers with a single layer thickness of 0.1 mm, so in each loop, the current nozzle height should be updated with layer=i*0.1.

gcode(2,2,LCE1,layer,0.1,fp,Vb) is a function to write the left shape into the G-code file. This shape duplicates the same pattern in all the layers, and function gcode() can be used in such and most other simple cases. As a contrast, gcode2ly(2,2,LCE21,LCE22,layer,0.1,fp,Vb) is to write the right shape, which has separated patterns on odd and even layers. Function gcode2ly() is specially designed for this case.

A.3.3 Operational Functions

This section explains the customized functions used in the code which are to achieve certain operations.

plotpath(mm)

This function is used to preview the designed pattern. The input variable is a N*4 pattern matrix **mm**. The function performs operations to plot all the elements of the matrix in the initialized new figure or last figure. There is no return value.

gstart(nozzle, extruder, down, xy, direction, fp, velocity)

This function is to write the initial operations into the G-code file, which controls the homing Z of one nozzle, and printing of a dummy line to stabilize the liquid pressure inside the nozzle. There are 6 input variables and no return value. The input parameters are explained below.

nozzle

Nozzle or syringe position, the value is in {1, 2}, where 1=nozzle A, 2=nozzle B.

extruder

The dispenser used to supply air, the value is in {1, 2}, usually this equals to nozzle.

down

Z level offset adjuster, which is set at the beginning of program. If the syringe is heated, set this to 0.17. If not, set to 0.04.

xy

The position for the nozzle to touch the substrate for homing Z. This value is a 1*2 vector as [x, y], which are the x and y coordinates. Note that after each single printing, if there is still extra printing process on the same substrate, this position must be shifted, since the nozzle leaks material and will make a drop at this position, which will affect the homing next time.

direction

This controls that to which direction the dummy line is drawn. The starting point of the dummy line is 2 mm away from the homing Z position, and the length is 20 mm. The value is in {1, 2, 3, 4} where 1=east, 2=south, 3=west, 4=north.

fp

File pointer to write G-code. Here just use variable fp, but not the exact file name.

velocity

The printing velocity with 0.1 mm layer thickness. This value has been calculated at the beginning of the program based on the measured 30-second extrusion amount.

An example of this function is shown below.

gstart(nozzle,	extruder,	down,	xy,	direction,	fp,	velocity)
gstart(2,	2,	0.17,	[0+xoff,-21+yoff],	1,	fp,	Vb)

The positions of homing Z and the dummy line are shown in Figure A.27.

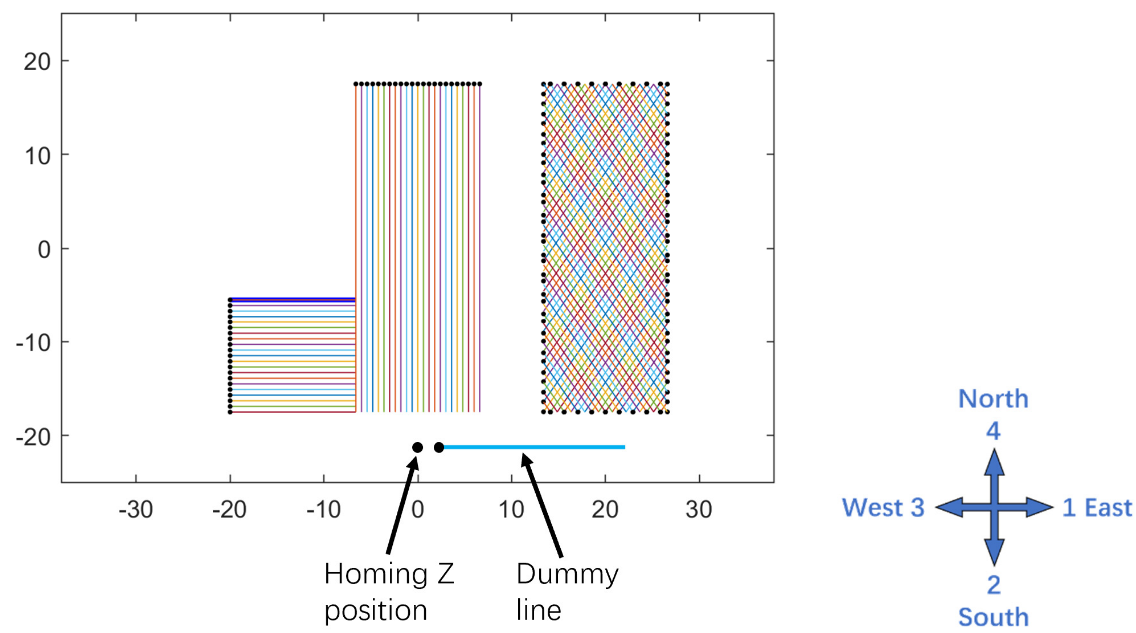

Figure A.27: The positions of homing Z and the dummy line.

gcode(nozzle, extruder, matrix, height, thickness, fp, velocity)

This function writes one layer of a simple pattern matrix into the G-code file. Usually, it is used in a for loop to perform repeated writing of different layers. There are 7 input variables and no return value. The input parameters are explained below.

nozzle

Nozzle or syringe position, the value is in {1, 2}, where 1=nozzle A, 2=nozzle B.

extruder

The dispenser used to supply air, usually this equals to nozzle.

matrix

The working pattern matrix containing the design. It should NOT be the temporary matrix. The matrix should have been shifted by xoff and yoff.

height

Current total height of Z level in millimeters.

thickness

The thickness of current layer in millimeters.

fp

File pointer to write G-code.

velocity

The printing velocity with 0.1 mm layer thickness. This value has been calculated at the beginning of the program based on the measured 30-second extrusion amount.

An example of this function is below.

gcode(nozzle,	extruder,	matrix,	height,	thickness,	fp,	velocity)
gcode(2,	2,	LCE1,	layer,	0.1,	fp,	Vb)

gcode2ly(nozzle, extruder, matrix1, matrix2, height, thickness, fp, velocity)

This function is similar to **gcode()**. The only difference is that it can separate the odd and even layers with different patterns. There is only one more input variable of the pattern matrix. **matrix1** is the pattern matrix for all the odd layers, and **matrix2** is for all the even layers. As long as other input parameters are correct, the function will determine if the current layer is odd or even automatically by the **height** and **thickness**. Note that each time when running this function, it only generates the G-code for one layer, and the pattern is either LCE21 or LCE22. To generate structures with multiple layers, it must be put in a for loop. There are 8 input variables and no return value.

An example of this function is shown below.

gcode2ly(nozzle,	extruder,	matrix1,	matrix2,	height,	thickness,	fp,	velocity)
gcode2ly(2,	2,	LCE21,	LCE22,	layer,	0.1,	fp,	Vb)

gend(xy,fp)

This function is to write the ending operations in the G-code and close the file in MATLAB. There are 2 input variables. There is no return value.

xy

After printing, the nozzle will be lifted to 25 mm Z level, and move to this position. It is a 1*2 vector with any X and Y coordinate values in the range of the platform. The central position [xoff, yoff] is recommended. Do NOT set any values larger than 250.

fp

File pointer to write G-code.

An example of this function is below.

gend(xy,	fp)
gend([xoff, yoff],	fp)

A.3.4 Pattern Filling Functions

These functions are to automatically fill shapes with designated patterns. Note that any patterns can be written manually. Using of these are to simplify the works with just parameter controls.

bf(x1, y1, x2, y2, dir1, dir2)

Block filling function for calculating the lines to fill a rectangular block. All the lines are in parallel direction with one-way printing. **x1** and **y1** are the coordinates of the upper left (northwest) vertex of the block, **x2** and **y2** are the coordinates of the lower right (southeast) vertex. **dir1** is the printing direction of the lines. **dir2** is the stacking direction of the lines. The values of the direction are in $\{1, 2, 3, 4\}$, where 1=east, 2=south, 3=west, 4=north. There are 6 input variables. The return value is a N*4 pattern matrix.

Examples of this function are shown in Figure A.28. There are four cases depending on the desired directions.

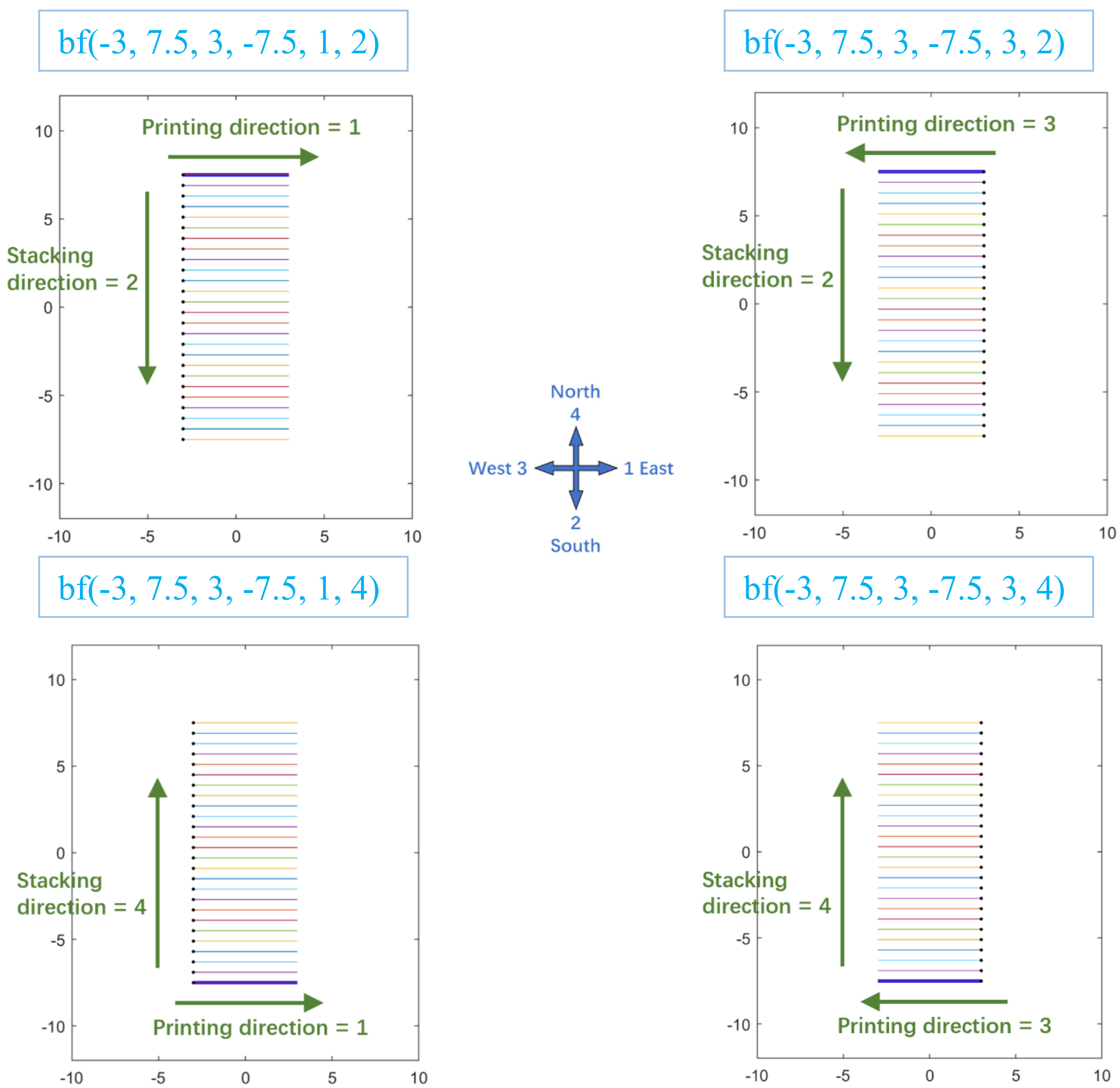

Figure A.28: Examples of block filling functions.

bf2(x1, y1, x2, y2, dir1, dir2)

Two-way block filling function to fill a rectangular block similar to bf(). The printed lines are in back-and-forth two-way directions. All the input variables are in the same definitions as bf(). Since the printing is in two directions, **dir1** here is the direction of the 1st line. **dir2** is still the stacking direction of the lines. The return value is a N*4 pattern matrix.

An example of this function is shown in Figure A.29.

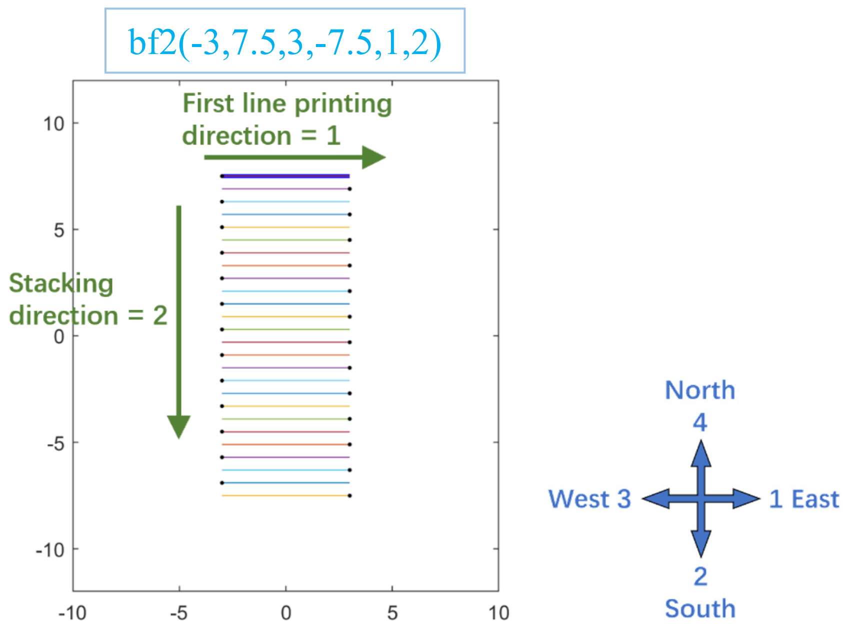

Figure A.29: An example of two-way block filling function.

bp(x1, y1, x2, y2, x3, y3, x4, y4, dir1, dir2)

Trapezoid filling function. (x1, y1), (x2, y2), (x3, y3), (x4, y4) are the four vertices. The edge (x1, y1)---(x2, y2) is parallel to the edge (x3, y3)---(x4, y4). The two unparallel edges are (x1, y1)---(x3, y3) and (x2, y2)---(x4, y4). The printing is in one-way. **dir1** is the printing direction of the lines. **dir2** is the stacking direction of the lines. Note that all the edges need not to be parallel to any axes, but the first edge must be parallel to the third edge.

An example of this function is shown in Figure A.30.

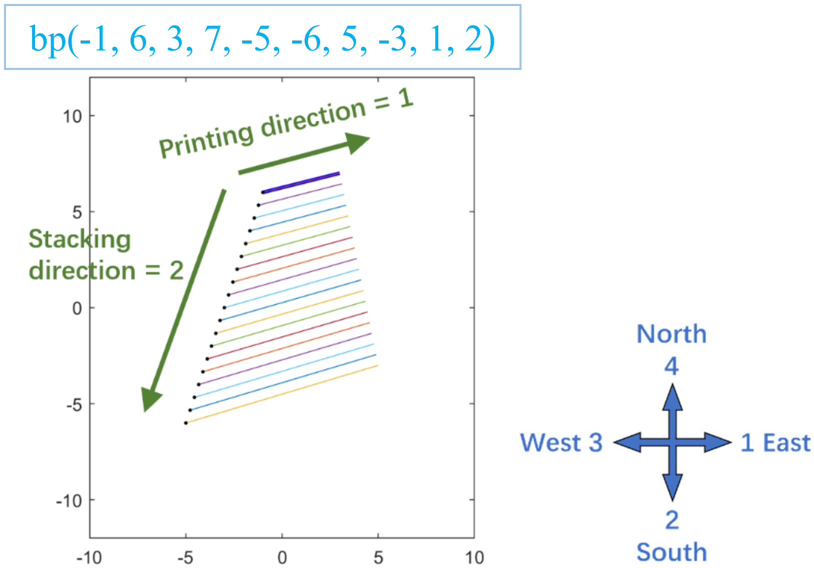

Figure A.30: An example of trapezoid filling function.

bp2(x1, y1, x2, y2, x3, y3, x4, y4, dir1, dir2)

Two-way trapezoid filling function. All the input variables are in the same definition as bp(). **dir1** is the direction of the 1st line. **dir2** is the stacking direction of the lines. The return value is a N*4 pattern matrix.

An example of this function is shown in Figure A.31.

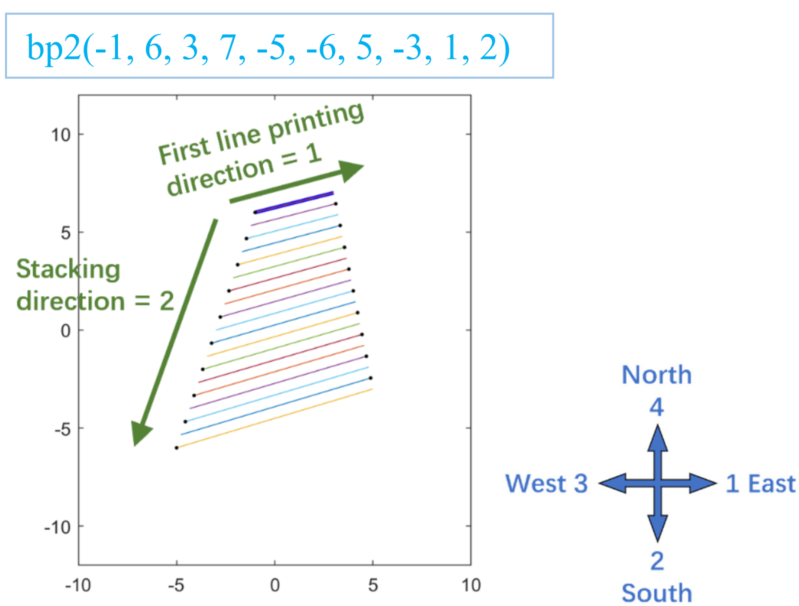

Figure A.31: An example of two-way trapezoid filling function.

bi2(x1, y1, x2, y2, dir1, dir2, angle)

Two-way block filling function to fill a rectangular block with inclined infill lines. There are 7 input variables. The first 6 are in the same definitions as bf2. The 7th variable **angle** is to control the inclined angle of the normal line. Left is positive. The return value is a N*4 pattern matrix.

Examples of this function are shown in Figure A.32.

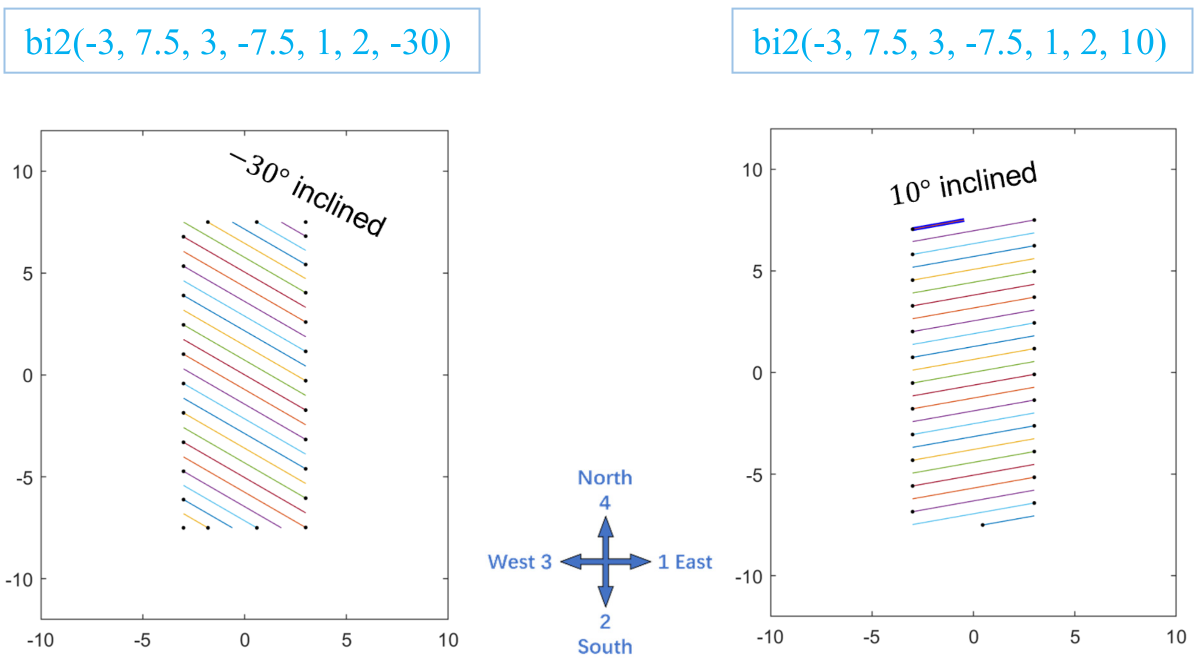

Figure A.32: Examples of two-way block filling function with inclined angles.

Chapter A.4 – Printing in Progress

A.4.1 Uploading G-code file

The printer has an individual user-interface computer running Linux kernel, so it is in parallel level as a PC that cannot be connected through a USB cable. The printing G-code file can be stored in a flash drive or SD card, and inserted into the printer for printing. However, printing from such storage devices is not recommend since the unstable connection is possible interrupt the printing process any time. The generate G-code file can be uploaded to the printer via Wi-Fi local area network and stored in the on-board flash memory.

To upload the file, first download and install the latest ideaMaker program on this website: https://www.raise3d.com/ideamaker/

The PC next to the printer is used as a virtual router to generate a wireless local area network. The printer is automatically connected to it. From the user's PC side, connect to the Wi-Fi hotspot named as “kop”. The password is 11111111.

After setting up Wi-Fi connection, open ideaMaker and perform the steps in Figure A.33 to upload the g-code file.

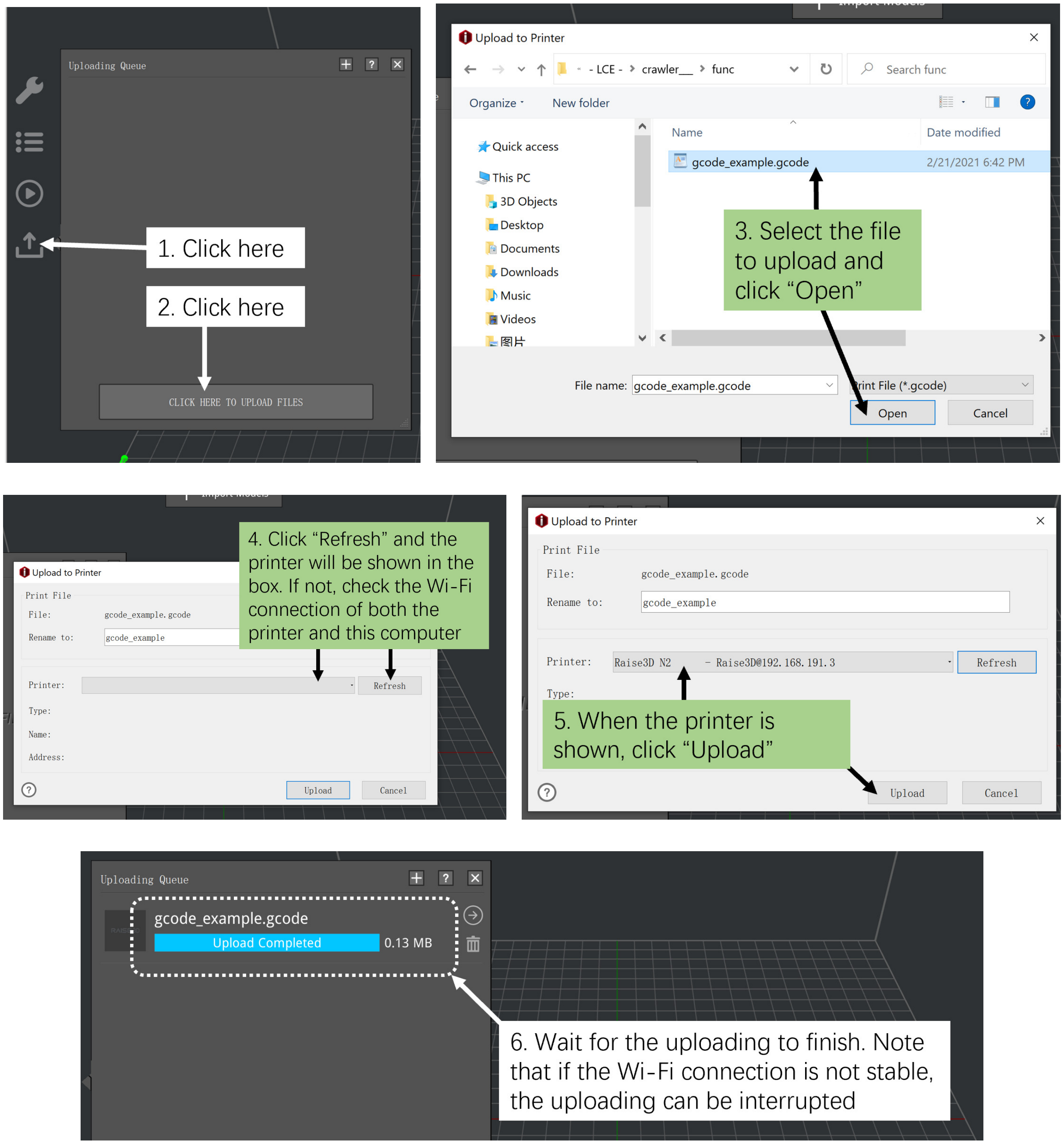

Figure A.33: Operation sequence to upload g-code files.

A.4.2 Starting printing process

If the material is LCE and requires immediate cross-linking during printing, set the UV output power to 2% by typing “-2” in serial monitor followed by ENTER key. However, do not turn on UV light at this time. If heating is needed in the printing process, keep heater on and check if the target temperatures are reached. Check if all the doors are closed, then perform the operation procedure shown in Figure A.34 on the touch screen of printer to start printing.

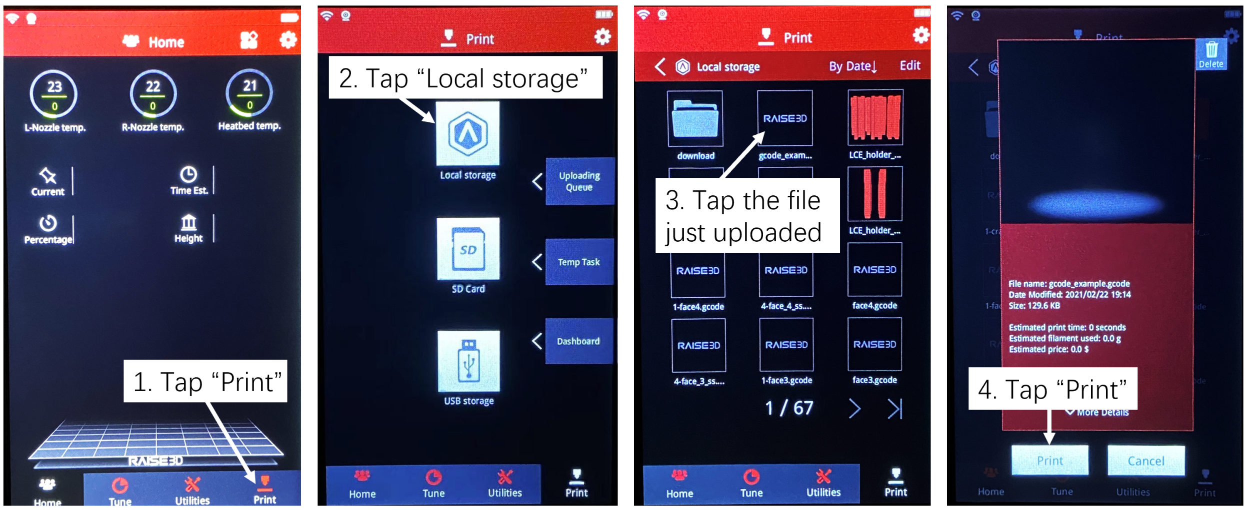

Figure A.34: Operation sequence to start printing.

Note that the due to time setting of the computer, the uploaded file may not be at the first place. Sometimes it might be on a later page.

When the printing starts, first it homes X and Y axes. Then the nozzle will move to the defined (xb1, yb1) position to home Z. During homing Z, the nozzle touches the substrate twice. First it moves down at a high speed. When getting in touch, it lifts for 1.5 mm, then moves down at a very low speed. During this process, keep looking at the position of the nozzle, since any variation may be detected by the load cell and cause a stop at a position higher than the substrate. Also, if there is malfunction in the load cell, when the nozzle contacts the substrate, it may not stop. Figure A.35 shows the contact state.

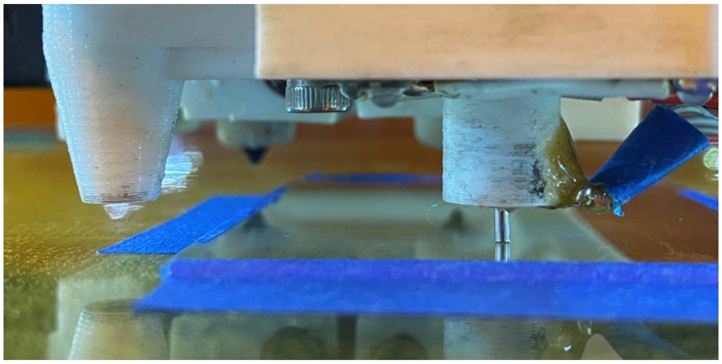

Figure A.35: Nozzle in contact state.

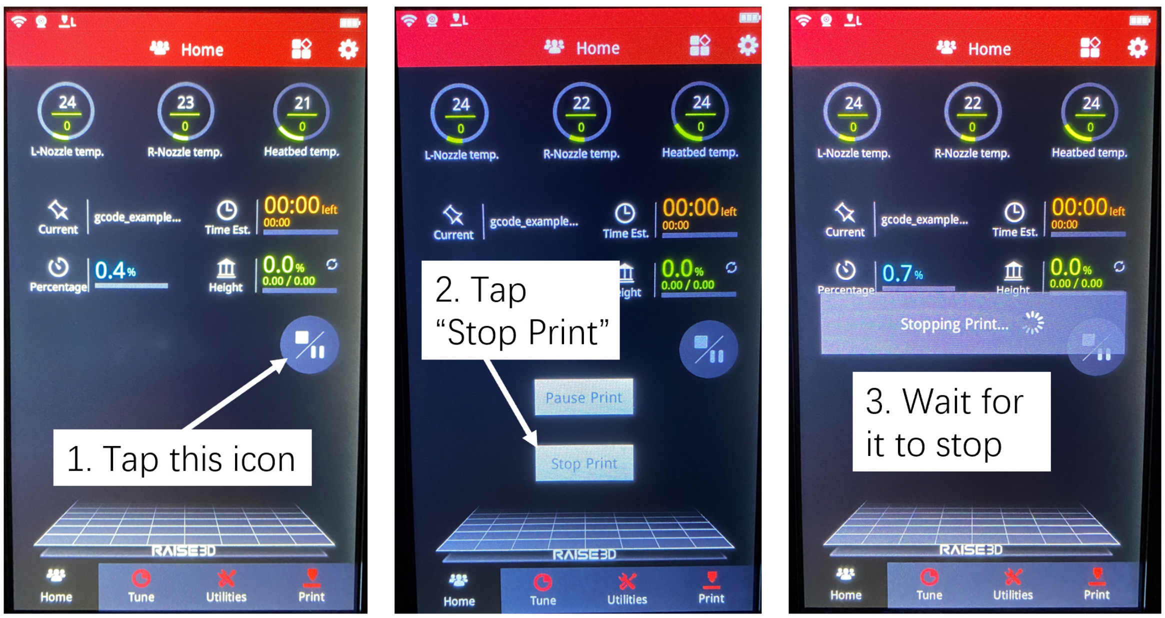

Figure A.36: Operation sequence to stop the printing process in program.

If the nozzle stops at a high position, a user should manually stop the printing process by the procedure in Figure A.36, and start the printing process again with the procedure on the previous page. Note that if the homing Z is wrongly completed and the nozzle has started extrusion for the pattern in the air, the printing process cannot be stopped immediately. It will print several more lines after initiating the stopping procedure. At this time, press the red enable switch on the left side of APS controller (Figure A.6) to cut off extrusion signal first, then stop the printing with the following procedure. This can prevent leakage of material on the substrate. Before starting the next printing, press the red enable switch again. This case often happens. There is no need to press the emergency stop.

Attention: If the nozzle is already in contact with the substrate but the printing head assembly is still moving down, PRESS the emergency stop (Figure A.3) immediately to avoid collision. This means the load cell is in malfunction and cannot feedback the force. This hardly happens but still happened once in the history.

If homing Z is successfully finished, the nozzle will start to print the dummy line. At this time, the UV can be turned on if needed in the process. To turn on UV, press the button "UV" on the APS controller once. Note that UV can only be turned on after homing Z, because the vibration of the UV cooling fan can affect the load cell and cause an interruption. During printing process, UV can be turned on and off repeatedly anytime, and the UV power can be tuned anytime. For printing LCE, UV power higher than 3% is not recommended.

Attention: After turning on UV, check if the cooling fan is working as shown in Figure A.37. If the fan is not working, turn off UV immediately, otherwise they will burn themselves.

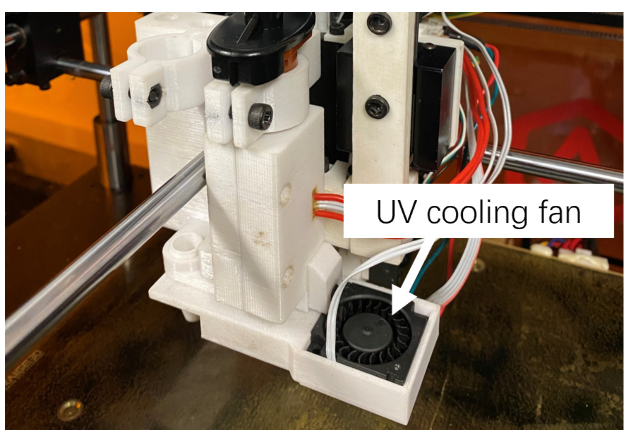

Figure A.37: UV cooling fan.

During printing in progress, repeatedly check the already printed result, in case if the viscosity of the material is not even, the extrusion rate changes and cause defects. Figure A.38 illustrates two kinds defects: over-extrusion and under-extrusion. When over extrusion happens, the extrusion rate becomes higher than expected, and the extra extruded material cause bulges. At this time, the printing speed should be increased to comply with this faster extrusion. When under extrusion happens, lack of material causes gaps between two single lines. Then the printing speed should be decreased.

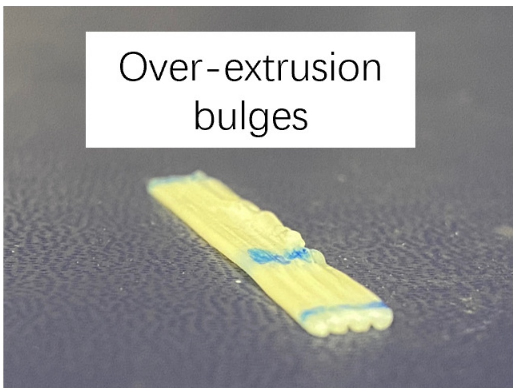

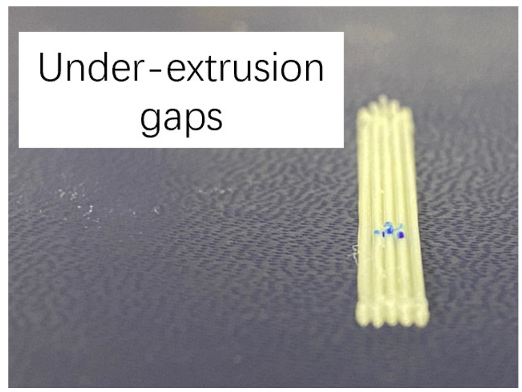

Figure A.38: Printed results with defects from over-extrusion and under-extrusion.

To change printing speed during printing, adjust the feed rate as shown in Figure A.39. For over extrusion, change the feed rate higher, such as 110 or 120. For under extrusion, change the feed rate lower, such as 90 or 80. Note that after changing the value, it may take 5 sec~2 min to update and take effect. Sometimes the printing system can forget to update the value, so it is recommended to change the value twice then it can keep that in mind. If the defect still persists after updating the feed rate, change it to further higher or lower values.

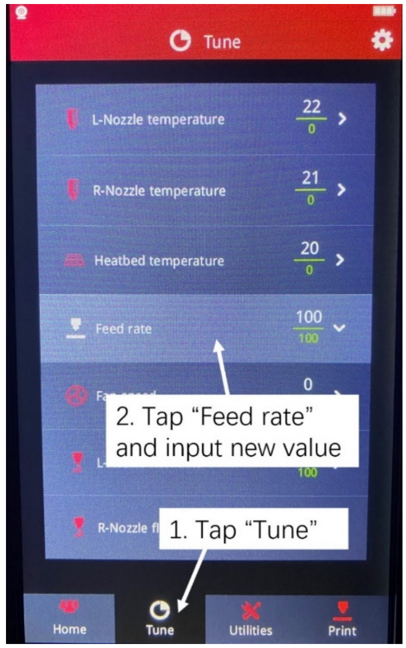

Figure A.39: Operation sequence to change printing speed.

During printing, the front door can be opened anytime, in case some defects need to be corrected manually. There is no need to turn off UV and heater. Usually some over extrusion or leaking of material can be removed by tweezers. However, gloves are always required and the only place that can be touched by tweezers is the substrate. Do not touch anywhere on the print head assembly.

A.4.3 Finishing works after printing

After printing, turn off UV immediately. If there is no other printing works, turn off the heater.

If the workpiece needs more post-treatment with UV. Turn off UV first, cover the nozzle with the black cover shown in Figure A.40. If without this cover, the reflected UV light on the platform could shine into the nozzle, and cross-link the material in the nozzle to cause a clog. After covering, change UV power to 100% and turn on UV to treat the workpiece for 1~5 minutes.

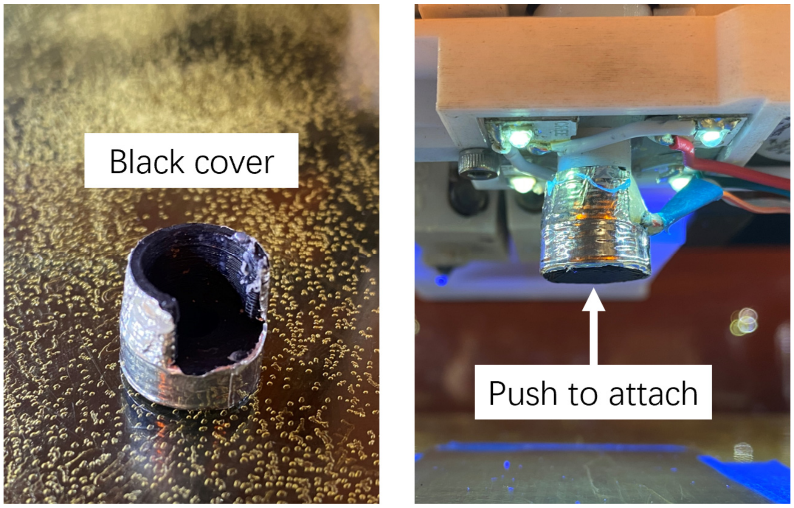

Figure A.40: Black cover to prevent UV induced crosslinking inside the nozzle.

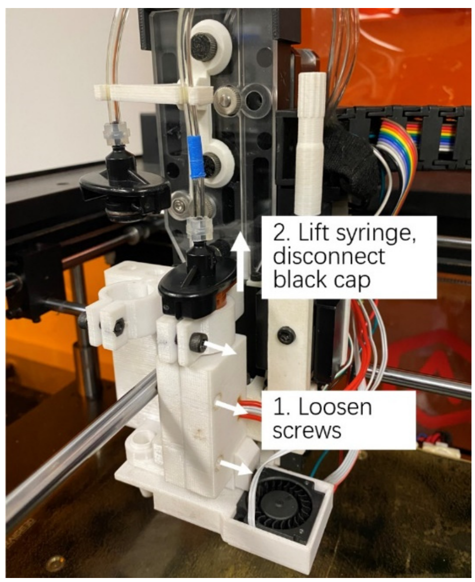

Figure A.41: Operation sequence to remove the syringe.

After all the operations, loosen all the screws on the syringe holder and heater, then lift the syringe and disconnect the black cap as shown in Figure A.41.

Turn off the two dispensers. Close the top lid and front door.

Attention: Finally, do not forget to turn off the outlets switch and main power.

Appendix B

Engineering drawings of Self-sustained Robot

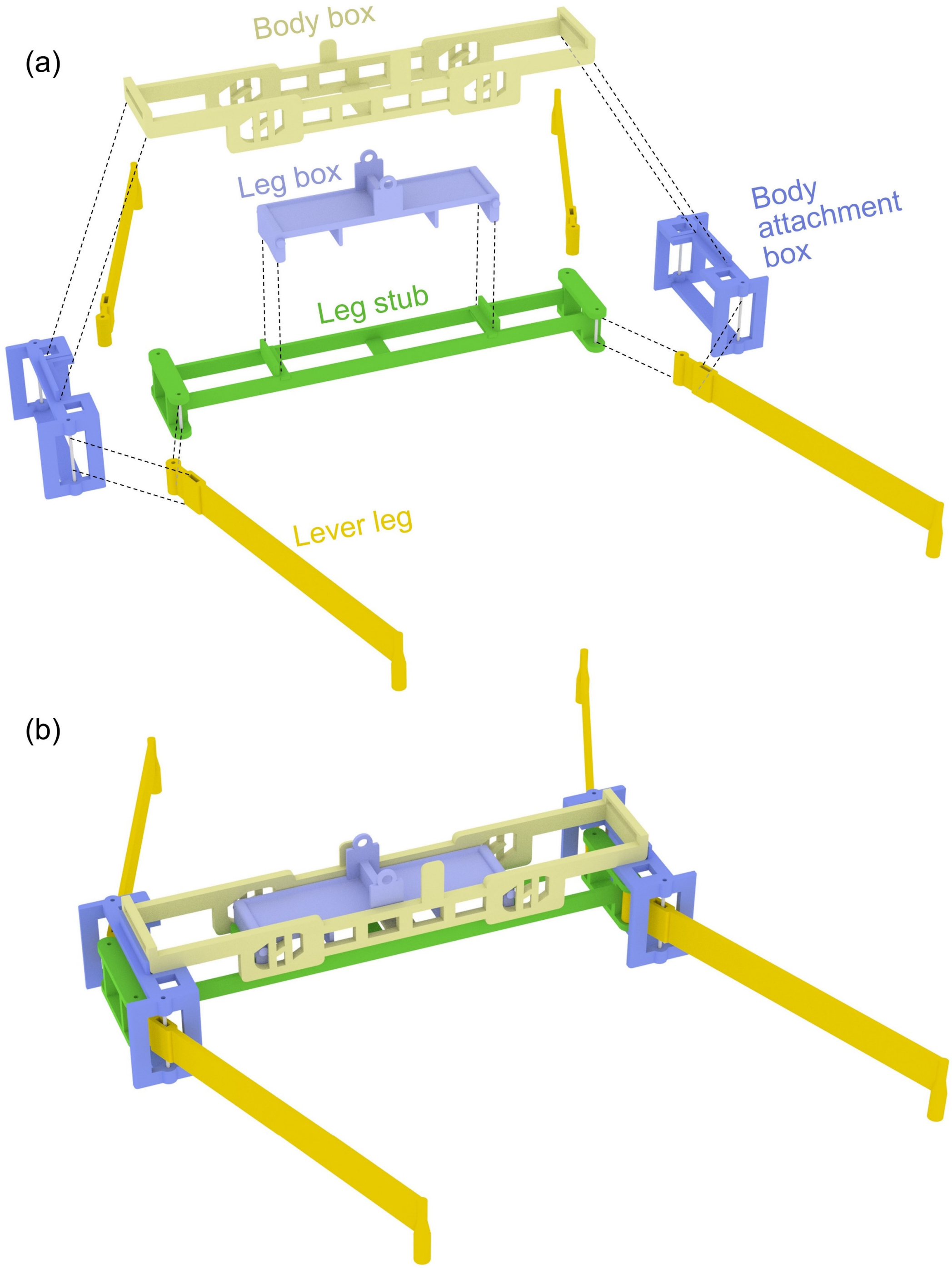

Figure B.1: (a) Explosion and (b) assembly views of insect-inspired modification of self-sustained robot. The shade and LCE components are omitted.

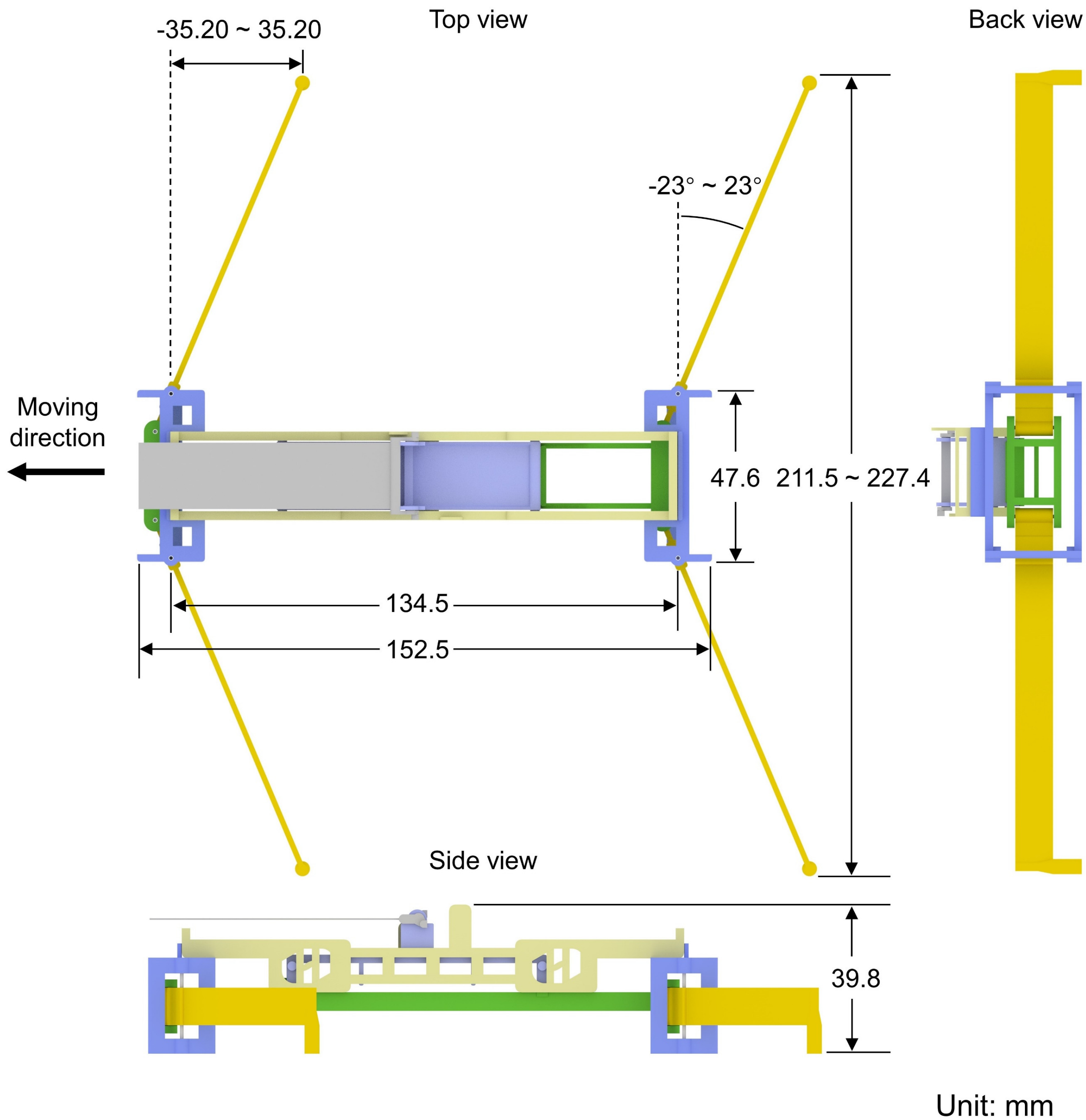

Figure B.2: Three-view schematics of insect-inspired modification of self-sustained robot. The LCE components are omitted

Table B.1: Designed dimensions of the components in self-sustained robot

Component	Dimension	Parameter (mm)
Original robot	L × W × H	134.5 × 23.4 × 23.4
Robot with lever attachments	L × W × H	152.5 × 227.4 × 39.8
LCE actuator	L × W × H	68 × 15 × 1.2
LCE spring	L × W × H	60 × 12 × 1.2
Parallelogram tracks	Length	6.1
	Height	3.0
	Top/bottom edge length	2.2
	Corner fillet amount	0.5
	Repeat distance	67.0
Sliding bars	Diameter	2.5
	Repeat distance	67.0
Flipping shade	Hinge diameter	2.5
	Radius of crank	1.91
	Diameter of crank bar	2.0
	Center to chord on crank bar	0.7 ~ 0.8
Lever legs	Effective length	100.0
	Length range inside fulcrum	10.0 ~ 10.9
	Length range outside fulcrum	89.1 ~ 90
	Repeat distance/wheelbase	134.5

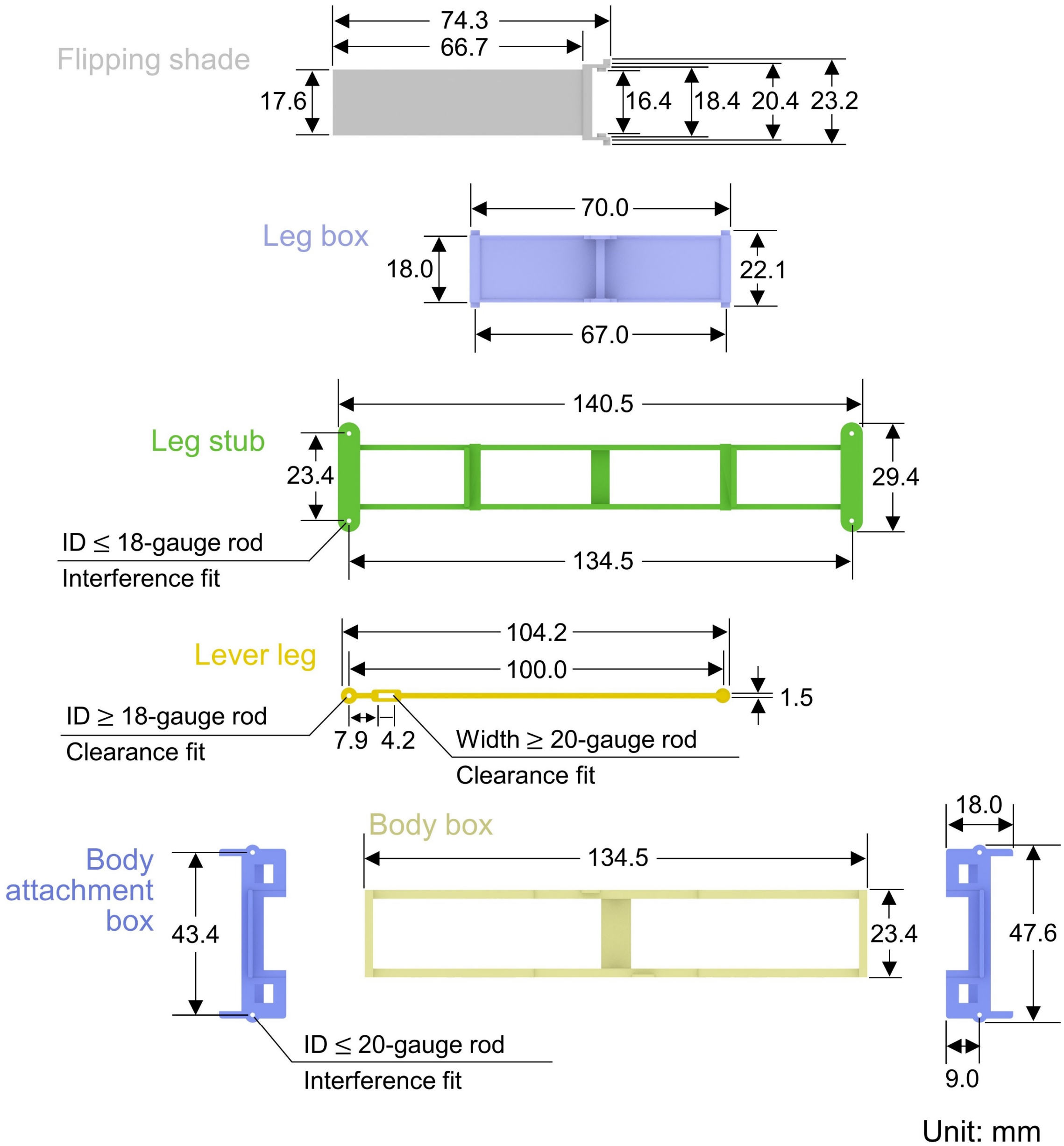

Figure B.3: Top-view schematic of the components in robot.

Four 18-gauge rods are used as shafts in the hinges of the four lever legs, which are fastened in the leg stub by interference fit, and the legs can rotate smoothly around the rod by clearance fit. Four 20-gauges rods are fastened in the body attachment boxes and inserted the slot on the lever legs, as fulcrums. The legs can slide and rotate around the fulcrums.

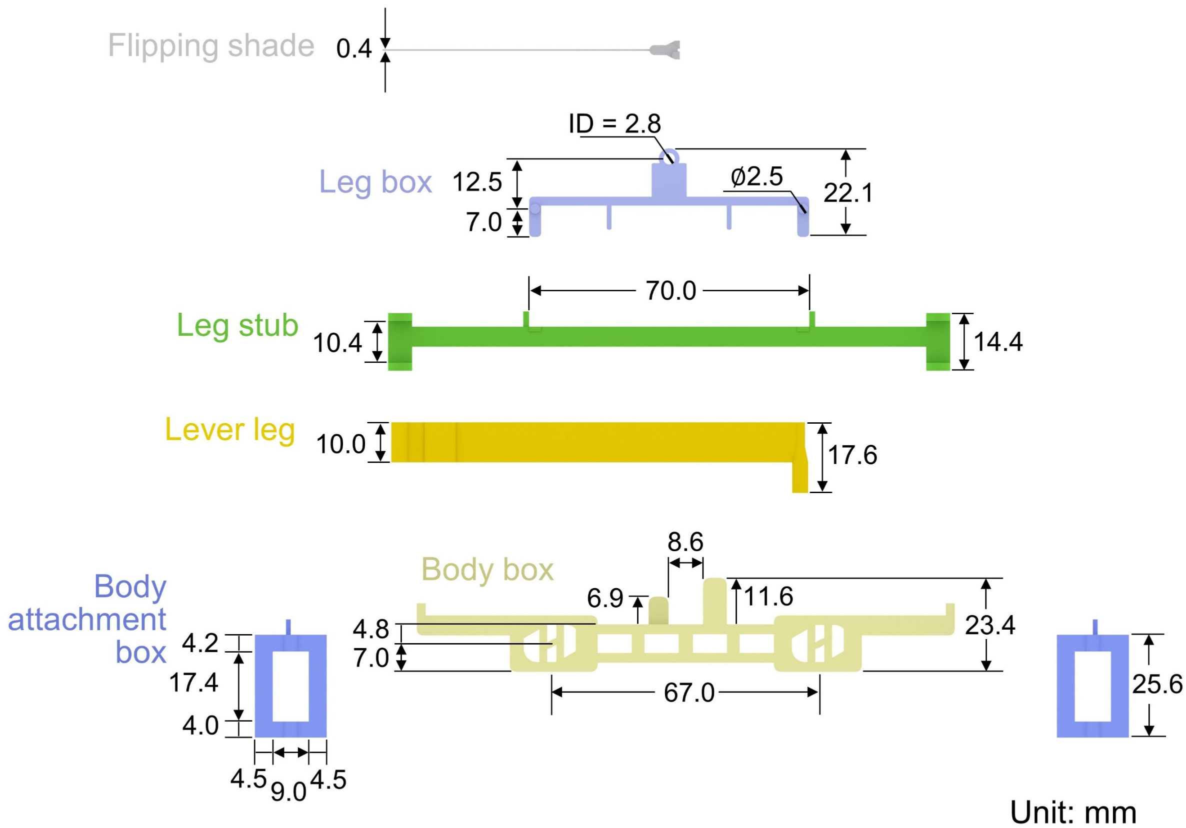

Figure B.4: Side-view schematic of the components in robot.

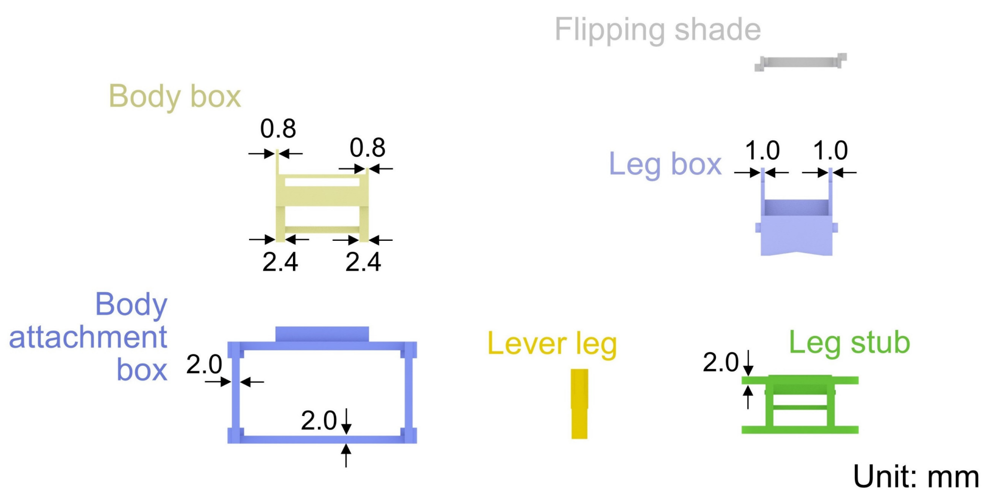

Figure B.5: Front-view schematic of the components in robot.

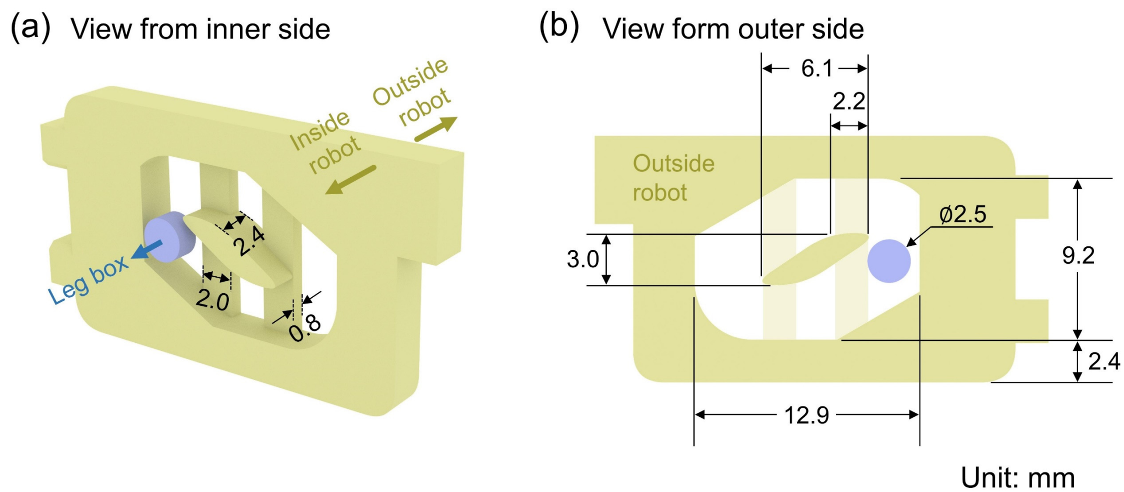

Figure B.6: Detailed views of the parallelogram track and sliding bar. (a) 3D view from the inner side of robot. (b) Schematic of the parallelogram track from outer side of robot.

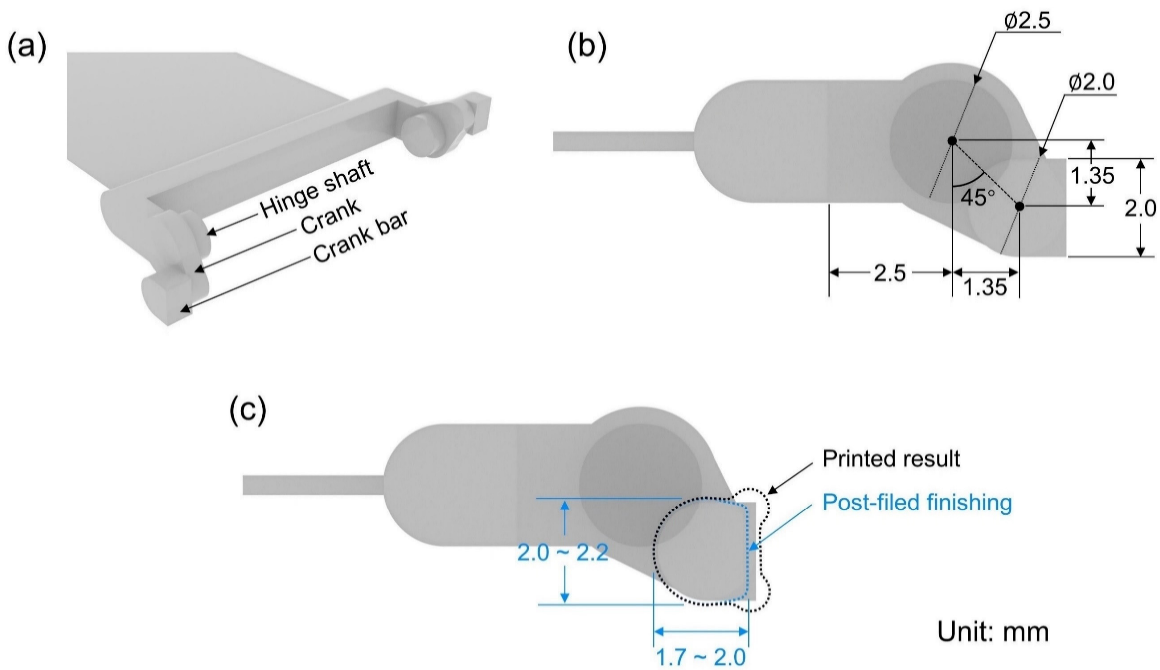

Figure B.7: Detailed views of the flapping shade. (a) 3D view. (b) Schematic of the crank structure on one side of the shade. (c) Actual printed result of the crank bar and post grinding dimensions.

The shape of crank bar is not regular and smaller than the precision that the 0.4 mm 3D printing nozzle can reach, which leads to a large error in the printed result, shown as the black dashed shape in Figure B.7 (c). After printing, the workpiece needs to be modified to the blue dashed shape with a precision file.